Departament de Teoria
del Senyal i Comunicacions
UNIVERSITAT POLITÈCNICA DE CATALUNYA

Ph.D. Dissertation

Sea Surface Salinity Retrieval Error Budget within the ESA Soil Moisture and Ocean Salinity Mission

Roberto Sabia

Advisors

Prof. Adriano Camps Carmona

Prof. Mercè Vall-llossera Ferran

Barcelona, July 2008

ACTA DE QUALIFICACIÓ DE LA TESI DOCTORAL

Reunit el tribunal integrat pels sota signants per jutjar la tesi doctoral:

Títol de la tesi: .....

Autor de la tesi: .....

Acorda atorgar la qualificació de:

- ☐ No apte
- ☐ Aprovat
- ☐ Notable
- ☐ Excel·lent
- ☐ Excel·lent Cum Laude

Barcelona, …… de/d'…..…….. de .....….

El President

.....
(nom i cognoms)

El Secretari

.....
(nom i cognoms)

El vocal

.....
(nom i cognoms)

El vocal

.....
(nom i cognoms)

El vocal

.....
(nom i cognoms)

A mia Nonna Pia

Table of Contents

List of Figures

Fig. 7.12 Sample results showing the different Sun impact by applying (top) or not (bottom) the cancellation algorithm using first Stokes parameter in restricted configuration. Sun is at its minimum estimated value.

Fig. 7.13 Sample results showing the different Sun impact by estimating its brightness temperature at its minimum (top) and maximum (bottom) value, using first Stokes parameter in non- restricted configuration.

Fig. 8.1 Sample SEPS outputs, at Y-pol (left) and X-pol (right), using 1/2 ° resolution OCCAM data.

Fig. 8.2 Sample L2 outputs with OCCAM data at 1/4° resolution. Right column: zoom of the original *SSS* and *SSS* error, respectively.

Fig. 8.3 Original (left) and retrieved (right) L3 *SSS* maps, for a 1° (top), 1/2° (mid) and 1/4° (bottom) OCCAM data resolution.

Fig. 8.4 Level 3 error statistics for a 1° (top left), 1/2° (top right) and 1/4° (bottom) OCCAM data resolution.

Fig. 8.5 Sample SEPS outputs in the new zone at Y-pol using 1/4° resolution OCCAM data.

Fig. 8.6 Sample L2 outputs in the new zone with OCCAM data at a 1/4° resolution.

Fig. 8.7 Original (left) and retrieved (right) L3 *SSS* maps, for a 1° (top), 1/2° (mid) and 1/4° (bottom) OCCAM data resolution.

Fig. 8.8 L3 error statistics in the new zone for a 1° (top left), 1/2° (top right) and 1/4° (bottom) OCCAM data resolution.

List of Tables

List of Acronyms

AF-FOV - Alias-Free Field Of View

AMIRAS - Airborne MIRAS

AVHRR - Advanced Very High Resolution Radiometer

CMS - Centre de Météorologie Spatiale

DDM - Delay-Doppler Maps

ECMWF - European Centre for Medium-range Weather Forecast

ENSO - El Niño-Southern Oscillation

ESA - European Space Agency

FOV - Field Of View

FROG - Foam, Rain, Oil spills and GPS-reflections

GHRSST-PP - Global High Resolution Sea Surface Temperature - Pilot Project

GLONASS - GLObal'naya NAvigatsionnaya Sputnikovaya Sistema

GMF - Geophysical Model Function

GNSS-R - Global Navigation Satellite Systems-Reflections

GODAE - Global Ocean Data Assimilation Experiment

GPS - Global Positioning System

IEM - Integral Equation Method

IFREMER - Institut Français de Recherche pour l'Exploitation de la Mer

ISEA - Icosahedron Snyder Equal Area

IFOV - Instantaneous Field Of View

KM - Kirchhoff Model

L2PP - Level 2 Prototype Processor

LAURA - L-band AUtomatic RAdiometer

MIRAS - Microwave Imaging Radiometer by Aperture Synthesis

MSS - Mean Square Slope

MWF - Mean Wind Field

NATC - North Atlantic Thermohaline Circulation

NIR - Noise Injection Radiometer

NCEP - National Centre for Environmental Predictions

NOCS - National Oceanography Centre, Southampton

OCCAM - Ocean Circulation and Climate Advanced Modeling

PSU - Practical Salinity Units

ROI - Region Of Interest

SAF/OSI - Satellite Application Facility/Ocean and Sea Ice

SBAS - Satellite Based Augmentation Systems

SMOS - Soil Moisture and Ocean Salinity

SEPS - SMOS End-to-End Performance Simulator

SPM - Small Perturbation Model

SSA - Small Slope Approximation

SSS - Sea Surface Salinity

SST - Sea Surface Temperature

SWH - Significant Wave Height

TEC - Total Electron Content

TSM - Two Scale Model

UPC - Universitat Politècnica de Catalunya

WISE - WInd and Salinity Experiment

WOA - World Ocean Atlas

Executive Summary

Satellite oceanography has become a consolidated integration of conventional *in situ* monitoring of the oceans. Accurate knowledge of the oceanographic processes and their interaction is crucial for the understanding of the climate system. In this framework, routinely-measured salinity fields will directly aid in characterizing the variations of the global ocean circulation. Salinity is used in predictive oceanographic models, but no capability exists to date to measure it directly and globally.

The European Space Agency's Soil Moisture and Ocean Salinity (SMOS) mission aims at filling this gap through the implementation of a satellite that has the potential to provide synoptically and routinely this information.

A novel instrument, the Microwave Imaging Radiometer by Aperture Synthesis, has been developed to observe the sea surface salinity (SSS) over the oceans by capturing images of the emitted microwave radiation around the frequency of 1.4 GHz (L-band). SMOS will carry the first-ever, polar-orbiting, space-borne, 2-D interferometric radiometer and will be launched in early 2009.

Like whatsoever remotely-sensed geophysical parameter estimation, the retrieval of salinity is an inverse problem that involves the minimization of a cost function. In order to ensure a reliable estimation of this variable, all the other parameters affecting the measured brightness temperature will have to be taken into account, filtered or quantified. The overall retrieved product will thus be salinity maps in a single satellite overpass over the Earth. The proposed accuracy requirement for the mission is specified as 0.1 ‰ after averaging in a 10-day and 2ºx2º spatio-temporal boxes.

In this Ph.D. Thesis several studies have been performed towards the determination of an ocean salinity error budget within the SMOS mission. The motivations of the mission, the rationale of the measurements and the basic concepts of microwave radiometry have been described along with the salinity retrieval main features.

The salinity retrieval issues whose influence is critical in the inversion procedure are:

- Scene-dependent bias in the simulated measurements,
- Radiometric sensitivity (thermal noise) and radiometric accuracy,
- L-band forward modeling definition,
- Auxiliary data, sea surface temperature (SST) and wind speed, uncertainties,
- Constraints in the cost function, especially on salinity term, and
- Adequate spatio-temporal averaging.

A straightforward concept stems from the statement of the salinity retrieval problem: different tuning and setting of the minimization algorithm lead to different results, and complete awareness of that should be assumed. Based on this consideration, the error budget determination has been progressively approached by evaluating the extent of the impact of different variables and parameterizations in terms of salinity error.

The impact of several multi-sources auxiliary data on the final SSS error has been addressed. This gives a first feeling of the quantitative error that should be expected in real upcoming measurements, whilst, in another study, the potential use of reflectometry-derived signals to correct for sea state uncertainty in the SMOS context has been investigated.

The core of the work concerned the overall SSS Error Budget. The error sources are consistently binned and the corresponding effects in terms of the averaged SSS error have been addressed in different algorithm configurations.

Furthermore, the results of a salinity horizontal variability study, performed by using input data at increasingly variable spatial resolution, are shown. This should assess the capability of retrieved SSS to reproduce mesoscale oceanographic features.

Main results and insights deriving from these studies will contribute to the definition of the salinity retrieval algorithm baseline.

Chapter 1
Introduction

1.1 Earth Observation and Climate Change

Remote sensing from space-borne platforms has experienced an extensive development over the last decades until becoming nowadays a reliable and established methodology of scientific research and an efficient procedure to routinely measure and monitor the Earth.

Thanks to the concomitant development of cutting-edge hardware technology and powerful software processing techniques, Earth observation has reached an unprecedented level of accuracy and applicability within a broad range of disciplines, spanning from meteorology to agriculture mapping, from cartography to urban monitoring and risk management, and from oceanography to climatology. The common framework of the different applications is the so-called retrieval, or "inverse problem", in which the desired parameter of interest is recovered starting from some observed satellite variables. The continuous refinement of these processing techniques has increased the range of applications, and currently almost every geophysical parameter is sensed by satellite instruments.

The most prominent advantage of the remote sensing technology is the synopticity of the measurements over a defined spatial zone, with frequent temporal coverage of the observed scenes and, according to the sensor used, an accuracy/sensitivity from moderate to excellent.

Within this framework, satellite oceanography has become a consolidated integration of conventional *in situ* monitoring of the oceans and advanced remote sensing capabilities provide unprecedented opportunities for monitoring, studying, and forecasting the ocean environment [Robinson, 1994]. In this discipline, the remoteness and harsh weather conditions of the dynamically important regions of the world make the benefits of a synoptic, all-weather satellite measurement self-evident [Lagerloef et al., 1995].

Since climate change and its socio-economical implications are increasingly topical, the oceanographic applications are nowadays ultimately oriented to gather information on processes related to the global warming and the climate.

1.2. Salinity Science Objectives

Accurate knowledge of both atmospheric and oceanographic processes, and their interaction, is crucial for an adequate understanding of the climate system. Within this framework, data collection of salinity fields will allow proper estimations of the annual and inter-annual variability of the distribution of salt.

Ocean circulation is mainly driven by the momentum and water/heat fluxes through the atmosphere-ocean interface, which can be traced by observation of Sea Surface Salinity (*SSS*) [Swift and McIntosh, 1983]. In addition, salinity together with sea temperature determines the density of seawater; the colder and saltier the water, the denser the mass.

In some regions (e.g. the Arctic), salinity fosters the formation of deep water, which is the process that triggers the so-called thermohaline circulation. This "conveyor belt"-like circulation (Fig. 1.1) is an important component of the Earth's heat redistribution engine, and crucial in regulating the weather and climate [Lagerloef, 2000].

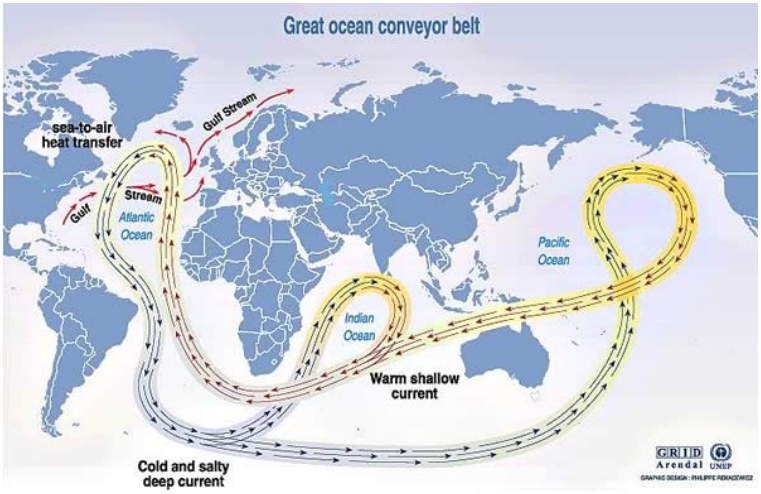

Fig. 1.1 "Conveyor Belt": the overall oceanic system that regulates the redistribution of heat all over the Earth [UNEP website].

Salinity variability is correlated with the net evaporation minus precipitation (E-P) budget (Fig. 1.2), being the water flux through the sea surface layers, as it will be discussed, critical for density stratification and for the definition of the mixed layer depth [Delcroix et al., 1996].

Variations in salinity, in fact, influence the near-surface dynamics of tropical oceans, where rainfall modifies the buoyancy of the surface layer and thus the ocean-atmosphere heat fluxes. Therefore, salinity fields and their seasonal and inter-annual variability are at the same time tracers and constraints on the water cycle and on the coupled ocean–atmosphere models. Salinity variations are related, furthermore, to river run-off and to the processes of seawater freezing and melting.

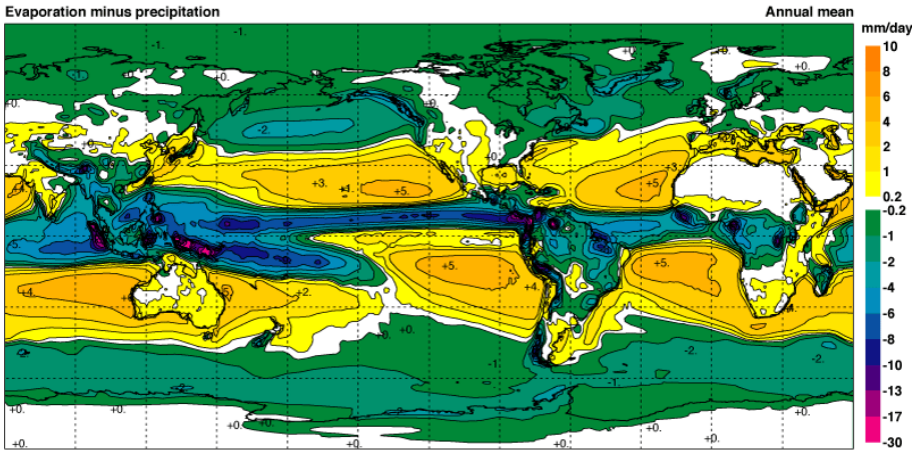

Fig. 1.2 Global Evaporation minus Precipitation (E-P) budget [ECMWF website].

Over most of the global oceans there is a lack of *in situ* salinity time series, and only a small fraction of the ocean is sampled on a regular basis. Accordingly, the major outcome of a satellite mission monitoring *SSS* would thus be to provide global, synoptic and routinely-measured salinity fields.

The existing database is very sparse in both time and space to resolve some key oceanographic processes, with almost 25% of a one-degree squared ice-free ocean devoid of measurements, whilst 73% has fewer than ten samples [Bingham et al., 2002; Koblinsky et al., 2003]. Figure 1.3 underlines the inhomogeneous distribution of surface salinity observations.

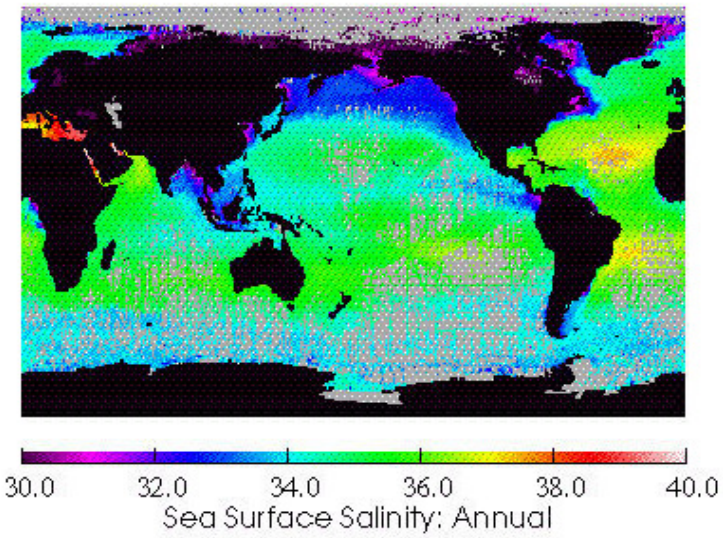

Fig. 1.3 Estimated annual mean salinity field. Gray areas represent absence of data [Levitus et al., 1998].

The most classical way to move around the lack of salinity data is based on temperature-salinity (T/S) correlations, due to the conservation of density in a given water mass [Emery and Wert, 1976]. Unfortunately, this T/S relationship is far from universal and becomes very uncertain at the surface, because of air-sea exchanges [Michel et al., 2005]. As a matter of fact, this dearth of

salinity measurements may result in major discrepancies between modeled and observed surface currents.

On the other hand, unlike other oceanographic variables, until now it has not been possible to measure salinity from space [ESA SMOS Brochure, 2004]. While nowadays ocean circulation models already assimilate sea surface temperature and altimeter-derived sea surface height from satellites, for salinity they still depend on relaxation to climatological values (Fig. 1.4).

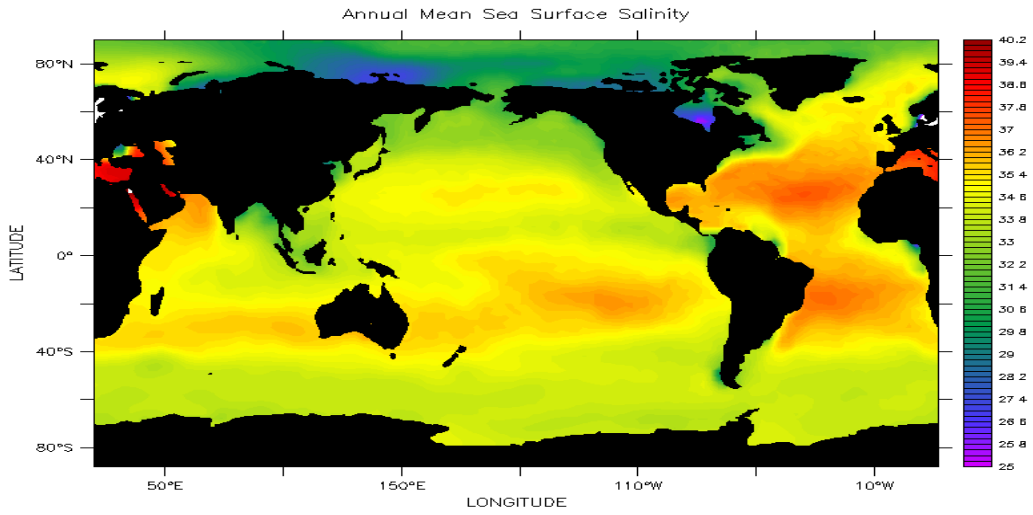

Fig. 1.4 World climatologic salinity as from [Levitus, 1982].

1.3. Prospective Benefits of Remotely-Sensed *SSS*

Global measurements of *SSS* will directly aid in characterizing and understanding the current variations in global ocean circulation [Berger et al., 2002], and will provide insights on the relationships and feedback between oceans and climate. Several phenomena extremely relevant for large-scale oceanography and climatic studies can benefit from a space-borne observational approach.

Remotely-sensed *SSS* estimates major outcomes can be summarized as follows [Font et al., 2004]:

- Improve monitoring of sea surface salinity variability, to better understand and characterize its spatial and temporal distribution in the surface of the oceans.
- Monitor large-scale salinity events, including ice melting, major river runoff, or monsoons. In particular, tracking inter-annual ocean salinity variations in the North Atlantic Thermohaline Circulation (NATC) is vital to long time scale climate prediction and modeling.

- Improve seasonal to inter-annual ENSO (El Niño - Southern Oscillation) climate predictions, involving the use of ocean salinity data to initialize and improve coupled climate forecast models.

Satellite *SSS* will help in modeling the role of freshwater flux in the formation and maintenance of tropical Pacific barrier layers [Font et al., 2008] and would improve estimates of ocean rainfall (surface freshwater flux balance). Besides, evaporation minus precipitation budget is difficult to measure accurately over the ocean, so global maps of *SSS* would provide a constraint on estimates of this balance on a global scale.
Summarizing, synoptic *SSS* estimations will be crucial in the near future, both to investigate the ocean-atmosphere interactions and to initialize the coupled numerical models forecasting and predicting the extent of the climate change.

1.4 Soil Moisture and Ocean Salinity (SMOS) Mission

As discussed, even though *SSS* is used in predictive atmospheric and oceanographic models, no capability exists to date to measure it directly and globally.
The Soil Moisture and Ocean Salinity (SMOS) mission aims at filling this gap through the implementation of a satellite (Fig. 1.5) that has the potential to provide synoptically and routinely this information, addressing the links among the water cycle, the ocean circulation and the climate.
Its objective is to provide global and frequent soil moisture and sea surface salinity maps. Both variables are crucial in weather, climate and extreme-event forecasting and they will be provided on spatial and temporal scales compatible with applications in the fields of climatology, meteorology and large scale hydrology [Silvestrin et al., 2001]. SMOS will thus make available the long needed measurements of surface soil moisture and sea surface salinity to foster new research in these fields. Nevertheless, in this Ph.D. thesis it will be uniquely dealt with salinity retrieval. As a secondary objective, SMOS will also provide observations over regions of snow and ice, contributing to the studies of the cryosphere.

Fig. 1.5 SMOS Y-shaped instrument artistic view [ESA SMOS website].

The SMOS satellite, which will be launched in early 2009, was selected by the European Space Agency (ESA) as an Earth Explorer Opportunity missions within the wider frame of the ESA Living Planet Program.

Two main general classes of Earth Observation missions have been identified: Earth Watch and Earth Explorer. The Earth Explorer missions encompass a new strategy for observing the Earth from space; missions are designed to address critical and specific issues that have been raised by the scientific community whilst demonstrating breakthrough technology in observing techniques. Earth Explorer missions are, in turn, split in two categories: the so-called "core" missions and the "opportunity" missions [SMOS SRD, 2002]. Unlike the core missions, the opportunity missions are smaller and more focused on a specific issue, and aims at demonstrating the feasibility of emerging technologies.

ESA's water mission SMOS is thus a technology demonstration project. It was selected for feasibility studies in May 1999 by ESA's Program Board for Earth Observation. Since then, a successful Phase A feasibility study (2000-2001) and a Phase B (2002) for further definition and critical breadboarding have been completed (the Phase B payload design was completed in October 2003). Approval for full implementation was given in November 2003. Phase C/D started in mid-2004. The Critical Design Review of the payload took place in November 2005 [EO Portal website].

SMOS will use passive microwave remote sensing techniques from space with the aim of picking up the electromagnetic energy emitted by the Earth's surfaces. An important aspect of this mission, as said, is that it will demonstrate a new measuring technique by adopting a completely different approach in the field of observing the Earth from space. A novel instrument has been developed, with the capability of observing both soil moisture and ocean

salinity by capturing images of emitted microwave radiation around the frequency of 1.4 GHz (L-band). SMOS will carry the first-ever, polar-orbiting, space-borne, 2-D interferometric radiometer (Fig. 1.6).

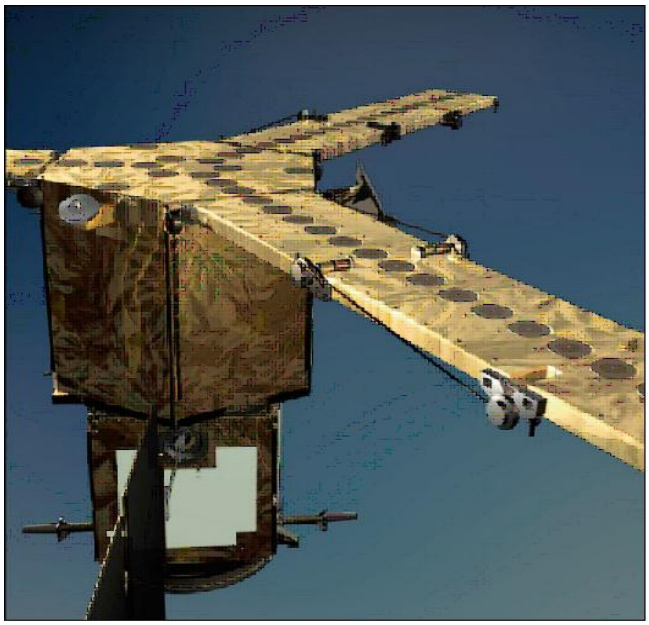

Fig. 1.6 SMOS payload [ESA SMOS website].

The SMOS unique payload is the Microwave Imaging Radiometer by Aperture Synthesis (MIRAS), whose characteristics and features will be described in the next chapter.

1.4.1 SMOS Mission Specifications and Requirements

SMOS has a Sun-synchronous polar dawn-dusk circular orbit. Orbit altitude is 763 km, the inclination is 98,4° with 06.00 hrs local solar time at ascending node, and the latitude coverage is at least ±80°. The launch of the SMOS spacecraft is planned on a Rockot launch vehicle from Plesetsk, Russia. The minimum foreseen lifetime is 3 years, in order to cover at least two seasonal cycles.

Temporal resolution is 3 days revisit time at Equator. Spatial resolution spans from 32 km at its best up to 100 km in the field of view (FOV) swath edge. The FOV is limited to a hexagon-like shape about 1000 km across called the "alias-free zone" (Fig. 1.7).

Considering the spatial resolution constraints, the overall goal for *SSS* retrieval from SMOS data is to meet the Global Ocean Data Assimilation Experiment (GODAE) optimized requirement for open ocean *SSS*. The pilot experiment GODAE aimed at demonstrating the feasibility of real-time global ocean modeling and data assimilation systems, both in terms of their implementation and their utility [Smith and Lefèbvre, 1997]. Following recommendations of the Ocean Observing System Development Panel, the proposed GODAE accuracy requirement for

satellite *SSS* is specified as 0.1 psu (practical salinity units) for a ten-day and 2°x2° resolution for global ocean circulation studies. Considering the exploratory nature of the *SSS* measurement with SMOS, the GODAE open-ocean requirement represents a technically challenging and demanding objective.

Incomplete knowledge of the image reconstruction errors that will be discussed in the next chapter, their correlation characteristics, and calibration stability represent uncertainties in the capability of SMOS to achieve these requirements, particularly at higher latitudes where the sensitivity to *SSS* is lower because of the lower *SST*. However, it will be possible to average data over 30 days or longer periods for many climate studies.

Monthly averages over 1°x1° boxes would give data comparable to the standard climatologies [Levitus et al., 1994], but with time dependence, which is not available from current climatologies.

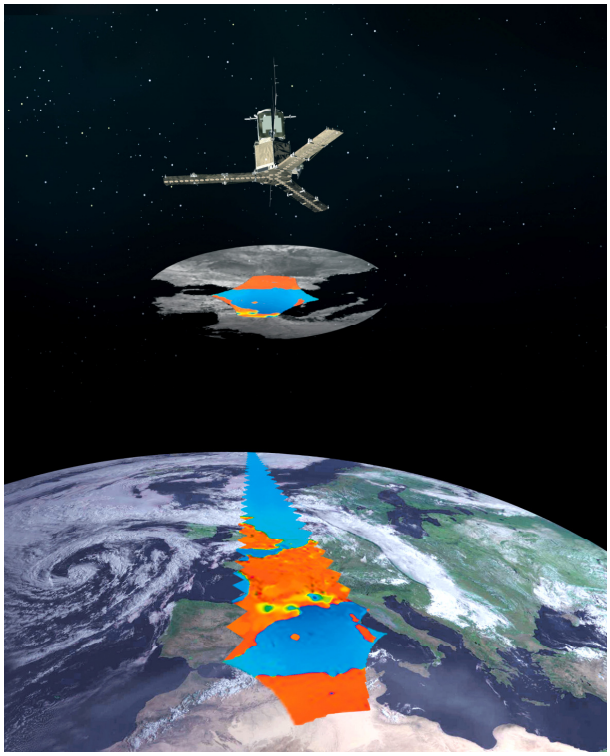

Fig. 1.7 SMOS observation geometry. The field of view is limited to a hexagon-like shape about 1000 km across called the “alias-free zone”.

1.4.2 SMOS Data Overview and Processing Chain

The following mission data products definitions have been specifically tailored to the SMOS mission [ESA SMOS website]:

- SMOS Raw Data.

These are SMOS Payload data in their original format comprised of instrument observations data and housekeeping telemetry, as received from the satellite.

- SMOS Level 0 Data Products.

These are SMOS Payload data in so-called Source Packets. They are chronologically sorted by Source Packet type: Observation Data and Housekeeping Telemetry.

- SMOS Level 1A Data Products.

These are the SMOS reformatted and calibrated data in engineering units. Level 1A products are physically consolidated in pole-to-pole time-based segments. Scientific SMOS Level 1A products are the so-called 'Calibrated Visibilities'.

- SMOS Level 1B Data Products.

The SMOS Level 1B products are the output of the image reconstruction of the SMOS observation measurements and consist of Fourier Components of the brightness temperature maps in the antenna polarization reference frame.

- SMOS Level 1C Data Products.

Since Level 1B products are arranged as snapshots and not geographically sorted, SMOS Level 1C products constitute reprocessed Level 1B geographically sorted, that is, swath-based brightness temperature maps.

- SMOS Level 2 Data Products.

Level 2 products are of two separate types:

  - Soil Moisture swath-based maps
  - Ocean Salinity swath-based maps

Global maps will be produced in the next processing step (Level 3 data).

1.5 Chapters' Overview and Thesis Structure

The Ph.D. Thesis plan is arranged as follows. In Chapter 2 the rationale and the Physics behind the measurements to illustrate the link between the geophysical parameter of interest (*SSS*) and the observed variable will be analyzed. Likewise, several details of the instrument onboard will be given, backing up these technical specifications with basic concepts of microwave radiometry, and some further notions on microwave radiometry by aperture synthesis. Besides, the theoretical modeling and field experiments to understand the relationship between the Brightness Temperature and the geophysical variables will be described.

Chapter 3 covers the current state of the art of the mission, stressing recent insights and results, and concerning especially on salinity retrieval issues, providing an overview of the different characterizations of the retrieval algorithm.

Chapter 4, in turn, describes the simulation software tools available to perform the entire salinity processing chain, namely, the SMOS End-to-End Performance Simulator (SEPS) and the Level 2 Ocean Salinity processor. Relevant features and capabilities of these tools will be described.

Chapter 5 includes the results of a retrieved salinity sensitivity study, in which the impact of several multi-source different auxiliary data of Sea Surface Temperature (*SST*) and wind speed (U_{10}) on the final error have been addressed. This gives a first feeling of the quantitative *SSS* error that should be expected in real upcoming measurements.

Chapter 6 is conceived as the follow-on of the previous study, whereas the potential use of GNSS-R (Global Navigation Satellite Systems-Reflections) derived signals to correct for sea state uncertainty in the SMOS context has been investigated.

Chapter 7 is the core of the entire Ph.D. Thesis, and deals with the overall *SSS* Error Budget; all the relevant error sources are listed and consistently binned, and therefore the corresponding effect in terms of the *SSS* error is addressed in different algorithm configurations. This study partially includes the previous ones with the aim of providing a quantitative impact factor of each parameter involved in the process, with the ultimate objective of tackling these effects once the satellite will be flying.

Chapter 8 shows the results of a *SSS* horizontal variability study, performed by using input data at increasingly variable resolution, and assessing the capability of retrieved *SSS* to reproduce interesting oceanographic features.

Chapter 9 summarizes the conclusions, the main findings and final remarks of the overall study, paving the way for future work whose main issues are envisaged.

Chapter 2
The SMOS Mission and the Rationale of the Measurements

In the previous chapter, a comprehensive view of the need for satellite salinity estimations and the motivation of the SMOS mission have been detailed. Being SMOS' single payload an interferometric radiometer by aperture synthesis, in this chapter some basic concepts on thermal radiation and microwave radiometry are provided.
The rationale and the Physics behind the measurements will be described afterwards, followed by some results concerning the theoretical modelization of the signal, or gathered by means of field experiments. Finally, some technical specifications of the MIRAS instrument will be given as well as a brief overview of the main concepts of the interferometric radiometry by aperture synthesis.

2.1 Basic Concepts on Microwave Radiometry

2.1.1 Thermal Radiation

Passive remote sensing using radiometric techniques has experienced an extensive growth in both technology and applications in the last decades. Radiometry is the field of science and engineering devoted to the measurement of the thermal electromagnetic energy radiated by the bodies. All material media (gases, liquids, solids and plasma) at a finite absolute temperature radiate electromagnetic energy over the entire electromagnetic spectrum.
The emission of radiation is caused by transition of electrons from higher to lower energy levels. The collision probability is a function of the density of the particles and the kinetic energy of their random motion. Hence, an increase of the absolute temperature of a body corresponds to an increase of the intensity of the energy radiated by the body itself.
A radiometer is a high sensitivity and precise instrument capable of measuring low levels of radiation emitted by a body or a target scene.

2.1.2 Planck's Blackbody Radiation's Law

A blackbody is an idealized perfectly opaque material that absorbs all the incident radiation from all directions at all frequencies. When the thermodynamic equilibrium is reached at

physical temperature T_o, it is also a perfect emitter. It radiates all the incident power isotropically, otherwise the energy absorbed would indefinitely increase its temperature.

The unpolarized blackbody radiation follows the Planck's radiation law [Ulaby et al., 1982], and its behavior is shown in Fig. 2.1 for different temperatures of the emitting body:

$$B_f = \frac{2 \cdot h \cdot f^3}{c^2} \cdot \frac{1}{e^{hf/kT_o} - 1}, \tag{2.1}$$

whereas:

B_f is the spectral brightness (brightness per unit bandwidth), [W m^{-2} sr^{-1} Hz^{-1}]

f is the frequency [Hz],

h is the Planck's constant (h = 6.63·10^{-34} J·s)

k is the Boltzmann's constant (k = 1.38·10^{-23} J·K^{-1}),

T_o is the absolute physical temperature in K, and

c is the speed of light (c = 3·10^{8} m s^{-1}).

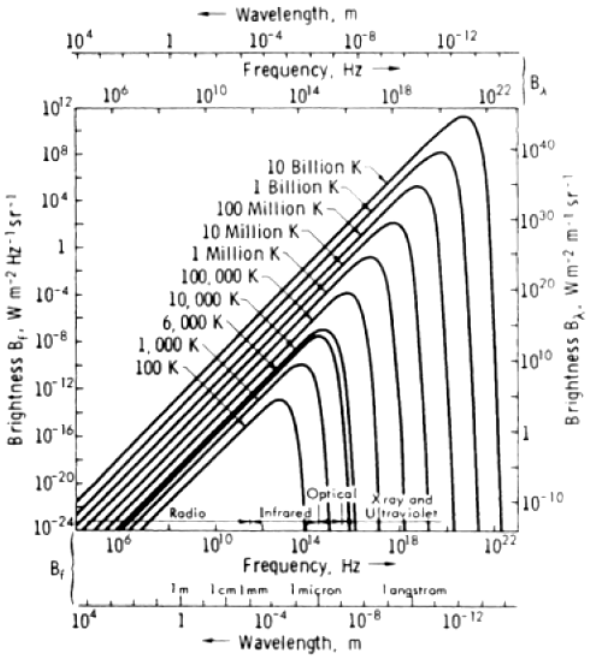

Fig. 2.4 Planck's radiation law [Ulaby et al., 1982, p. 193].

At microwave frequencies, the exponent hf/kT_o in the denominator of Planck's law is far smaller than 1, and therefore, a Taylor's approximation can be used to simplify the Eqn. 2.1. At low microwave frequencies, the Rayleigh-Jeans law can be used as good approximation of the Planck's law, and can be written as:

$$B_f \approx \frac{2 \cdot f^2 \cdot k \cdot T_{phys}}{c^2} = \frac{2 \cdot k \cdot T_{phys}}{\lambda^2}, \tag{2.2}$$

being $\lambda = c / f$ the wavelength.

In a large part of the microwave spectrum, the error committed by the Rayleigh-Jeans' approximation is negligible, and thus the expression given in Eqn. 2.2 will be used from now onwards. An important characteristic of this approximation is that exhibits a linear relationship between the spectral brightness density and the physical temperature (Fig. 2.2).

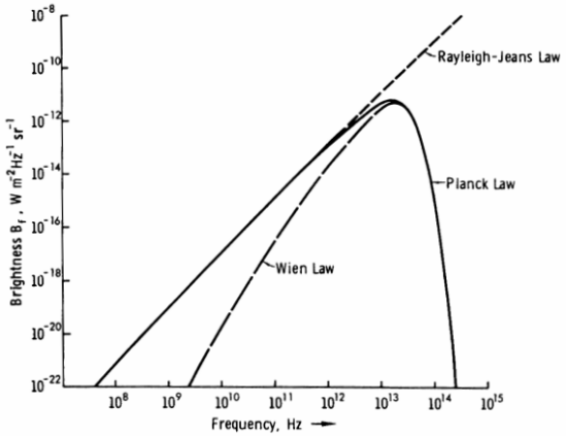

Fig. 2.5 Comparison of Planck's law with its low-frequency (Rayleigh-Jeans law) and high-frequency (Wien's law) approximations at 300 K [Ulaby et al., 1982, p.198].

2.1.3 Power-Temperature Correspondence

The power received by an antenna placed inside a blackbody (Fig. 2.3) at a constant physical temperature T_o, with a bandwidth small enough to assume that the spectral brightness density does not change over the frequency range is:

$$P_{bb} = k \cdot T_o \cdot B, \tag{2.3}$$

where the subscript *bb* stands for blackbody.

Equation 2.3 shows a linear relationship between the physical temperature of a body and the power collected by an antenna. The same expression was derived by Nyquist (Eqn. 2.4) for the available power at the terminals of a resistance at a physical temperature T_o. This implies that, for an ideal receiver of bandwidth B, the antenna delivers the same power of a resistance at a temperature T_A, which is called the antenna temperature (Fig. 2.3):

$$P_n = k \cdot T_o \cdot \mathrm{B}\,. \tag{2.4}$$

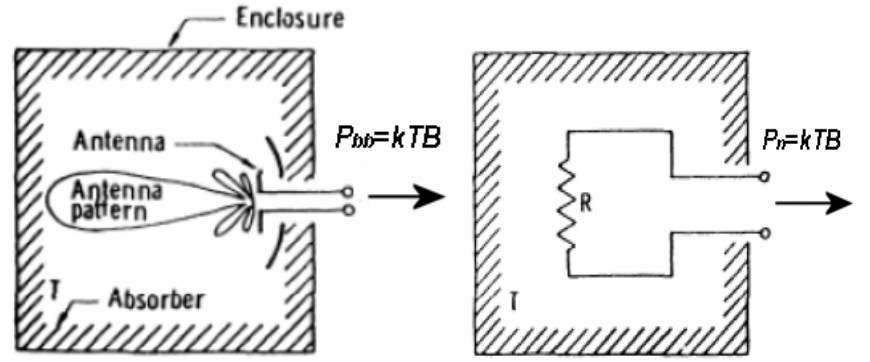

Fig. 2.6 The power delivered by: (a) an antenna placed inside of a blackbody enclosure of temperature T is equal to the power delivered by (b) a resistor maintained at the same physical temperature [Ulaby et al., 1982, p. 199].

2.1.4 Gray-Body Radiation

Unlike the blackbodies, real materials (called gray-bodies) do not necessarily absorb all the incident energy upon them, part of which being reflected, and thus emit less energy than the blackbodies. Gray-bodies are associated to the definition of two quantities, the brightness temperature $T_B(\theta,\varphi)$ and the emissivity $e(\theta,\varphi)$. Equation 2.5 shows the relationship between these two quantities:

$$e(\theta,\phi) = \frac{B(\theta,\phi)}{B_{bb}} = \frac{T_B(\theta,\phi)}{T_o}\,, \tag{2.5}$$

where B_{bb} is the brightness of the blackbody at a temperature T_o.

The emissivity is a dimensionless parameter ranging from zero (for perfect reflectors, e.g. metals) to unity (for perfect blackbodies), and it is polarization-dependent. As a consequence, the brightness temperature of a real semi-infinite dielectric material is always smaller than its physical temperature.

2.1.5 Apparent Temperature

The apparent temperature (T_{AP}) is an equivalent temperature related to the amount of brightness incident over the antenna, $B_i(\theta,\varphi)$:

$$B_i(\theta,\phi) = \frac{2 \cdot k}{\lambda^2} \cdot T_{AP}(\theta,\phi) \cdot B \,. \tag{2.6}$$

In remote sensing applications, the T_B of the surface is measured by an antenna far away (Fig. 2.4). In this case, the apparent temperature T_{AP} is the relevant parameter and it depends on:

- The brightness temperature of the surface under observation (T_B),
- The atmospheric upward radiation (T_{UP}),
- The atmospheric downward radiation scattered over the surface (T_{SC}), and
- The atmospheric attenuation (L_a).

Assuming a scattering-free atmosphere the apparent brightness temperature can be written as follows:

$$T_{AP} = T_{UP} + \frac{1}{L_a} \cdot (T_B + T_{SC}) \,. \tag{2.7}$$

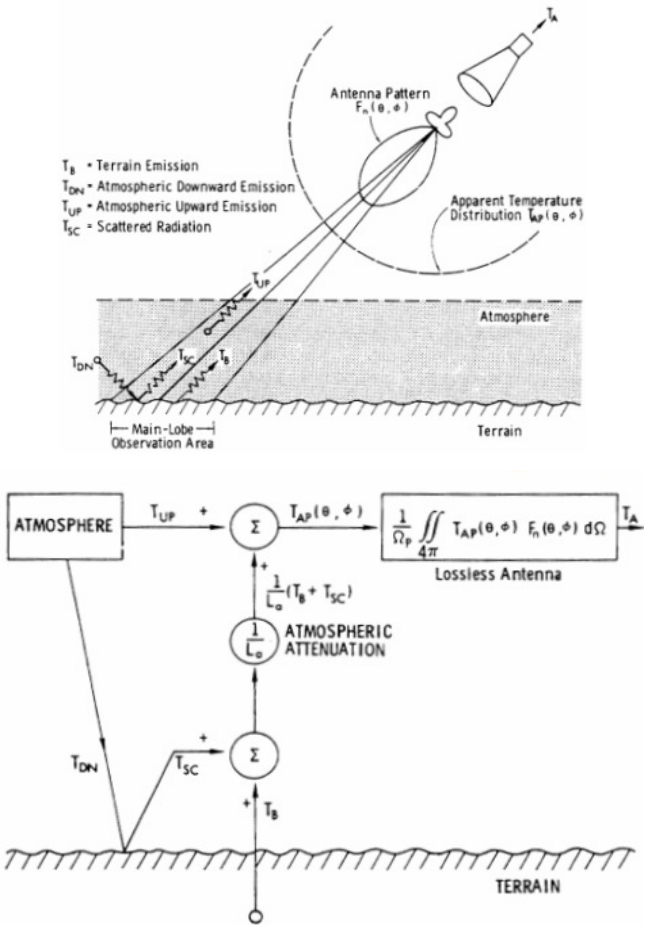

Fig. 2.4 Relationship between the antenna temperature T_A, the apparent temperature T_{AP} and the brightness temperature T_B [Ulaby et al., 1982, p. 202].

From Eqn. 2.7, when the atmospheric losses are high, the apparent temperature is almost equal to the atmospheric upward temperature, T_{UP}. This happens at high frequencies or at the absorption windows of some gases. If the brightness temperature of the Earth's surface has to be measured, it is necessary to operate at frequencies characterized by low atmospheric attenuation. In the frequency range from 1 GHz to 10 GHz losses for a cloud-free atmosphere are very small and the radiation passing through the atmospheric layer is barely attenuated [Ulaby et al., 1982, p. 203] (Fig. 2.5)

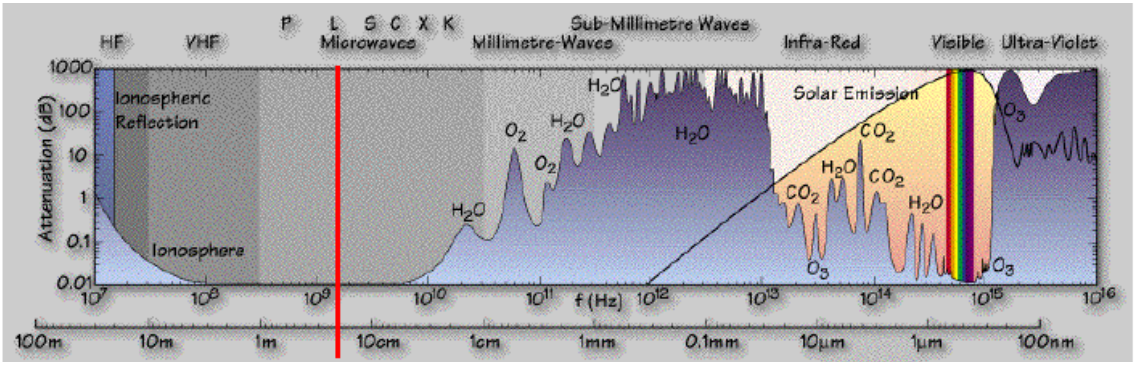

Fig 2.5 Atmospheric transmission in the whole frequency spectrum [Envisat website].

According to Fig. 2.4 and taking into account the normalized antenna pattern $F_n(\theta,\varphi)$ and having normalized by the pattern solid angle Ω_p, the antenna temperature is given by:

$$T_A = \frac{1}{\Omega_p}\iint_{4\pi} T_{AP}(\theta,\phi)\,|\,F_n(\theta,\phi)\,|^2\,d\Omega\,. \qquad (2.8)$$

2.2 Physics of the Measurements

Once the basic principles of microwave radiometry have been described, along with the definition of the brightness temperature, it is possible to deal with the physics behind the SMOS measurements, thus linking the parameter observed by the sensor (T_B, or a related magnitude), with the desired geophysical parameter: the salinity.

2.2.1 L-band Microwave Radiometry and Dielectric Constant of Seawater

Unlike visible and infrared sensors, the sensors operating at microwave frequencies have the advantage of being nearly independent from the cloud coverage and solar presence (even if the presence of rain cells may be an issue). Other technologies (millimeter-wave frequency

radiometry, optical sensing…) suffer deficiencies due to vulnerability to cloud cover and/or various perturbing factors [Kerr et al., 2001].

Figure 2.6 represents the relative normalized brightness temperature sensitivity to different parameters between 0 and 40 GHz. The dependence on salinity increases with decreasing frequency; hence, low microwave frequencies are needed to detect changes in salinity.

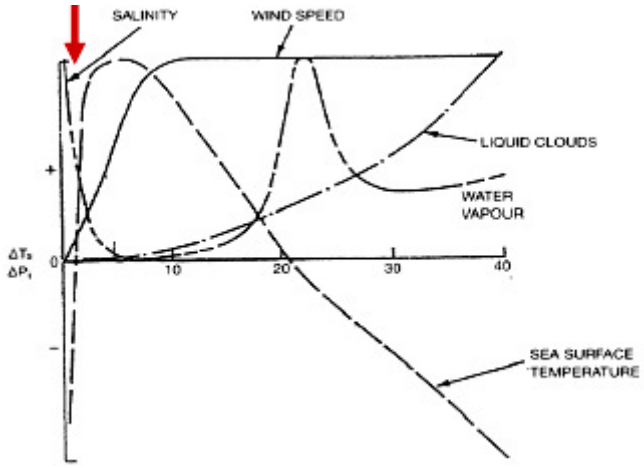

Fig. 2.6 Normalized brightness temperature sensitivity to different geophysical parameters [Font and Camps, 2008].

The spectral window at L-band (1400–1427 MHz, 21cm wavelength) is the lowest frequency band set aside for passive use only and provides with modern radiometers sufficient sensitivity for salinity remote sensing. The conditions for sea surface salinity retrieval from space [Swift and McIntosh, 1983] are achieved, providing the sensitivity of T_B to *SSS* is optimum, whilst atmospheric effects are almost negligible.

As it was said in the previous section, T_B is related to the emissivity through:

$$T_B(\theta, p) = e(\theta, p) \cdot T_{ph}, \tag{2.9}$$

where T_{ph} is the physical temperature of the body, in this case the ocean scene.

For a flat surface, from energy conservation considerations, the emissivity can be written as follows:

$$e(\theta, p) = 1 - R(\theta, p), \tag{2.10}$$

where $R(\theta, p)$ is the Fresnel power reflection coefficient at p polarization (p=horizontal and vertical). For a plane surface, the Fresnel coefficient is dependent on the incident angle θ, and on the complex dielectric constant of sea water, ε_r:

$$R_H = \left| \frac{\cos\theta - \sqrt{\varepsilon_r - \sin^2\theta}}{\cos\theta + \sqrt{\varepsilon_r - \sin^2\theta}} \right|^2 , \tag{2.11}$$

$$R_V = \left| \frac{\varepsilon_r \cos\theta - \sqrt{\varepsilon_r - \sin^2\theta}}{\varepsilon_r \cos\theta + \sqrt{\varepsilon_r - \sin^2\theta}} \right|^2 . \tag{2.12}$$

The complex dielectric constant (or permittivity) of the sea water is dependent on temperature and on the concentration of salt. It can be calculated at any frequency within the microwave band from the Debye's expression [Debye, 1929]:

$$\varepsilon_r = \varepsilon_\infty + \frac{(\varepsilon_s - \varepsilon_\infty)}{1 + j\omega\tau} - j\frac{\sigma}{\omega\varepsilon_0}, \tag{2.13}$$

in which ε_∞ is the electrical permittivity at very high frequencies, ε_s is the static dielectric constant, τ is the relaxation time, σ is the ionic conductivity, and ε_0 is the permittivity of free space. The three parameters ε_s, τ and σ are functions of the temperature and salinity of sea-water.

The brightness temperatures measured by the radiometer are thus linked to salinity through the dielectric constant (or the conductivity) of the sea water. At a specific frequency, the dielectric constant for seawater depends on both *SSS* and *SST* [Klein and Swift, 1977]. In principle, it is possible to obtain *SSS* information from L-band passive microwave measurements as long as the other factors influencing T_B can be accounted for.

2.2.2 Brightness Temperature Sensitivity

Despite the nearly optimal conditions to retrieve salinity from L-band microwave radiometry, the sea surface salinity signature on the brightness temperature and the dynamic range related to *SSS* variations are still relatively small. Thus, over the oceans very high sensitivity and accuracy are required.

Figure 2.7 shows the brightness temperature as a function of sea surface temperature, at different salinities in case of a flat surface and nadir incidence angle. It underlines how the sensitivity to *SSS* decrease as the *SST* gets cooler, making the salinity retrieval in cold ocean areas even more challenging.

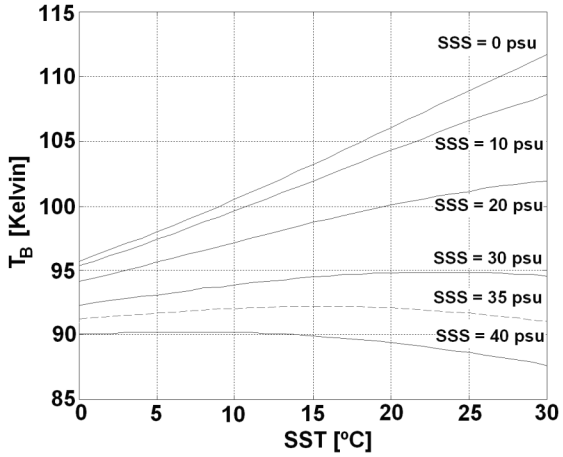

Fig. 2.7 Dependence of the brightness temperature at nadir with *SSS* and *SST* [Camps et al., 2003a].

The sensitivity of the brightness temperature T_B at L-band to *SSS* has been thoroughly characterized. For instance, at nadir the sensitivity is 0.5K/psu for a sea surface temperature of 20 °C decreasing to 0.25K/psu for an *SST* of 0 °C.

On average, this sensitivity varies between 0.2 and 0.8 K/psu depending on the *SST*, the incidence angle and polarizations [Yueh et al., 2001] (Fig. 2.8). These sensitivities pose demanding requirements on the performance of the instrument, on the calibration procedure, and on the definition of the geophysical parameter retrieval scheme.

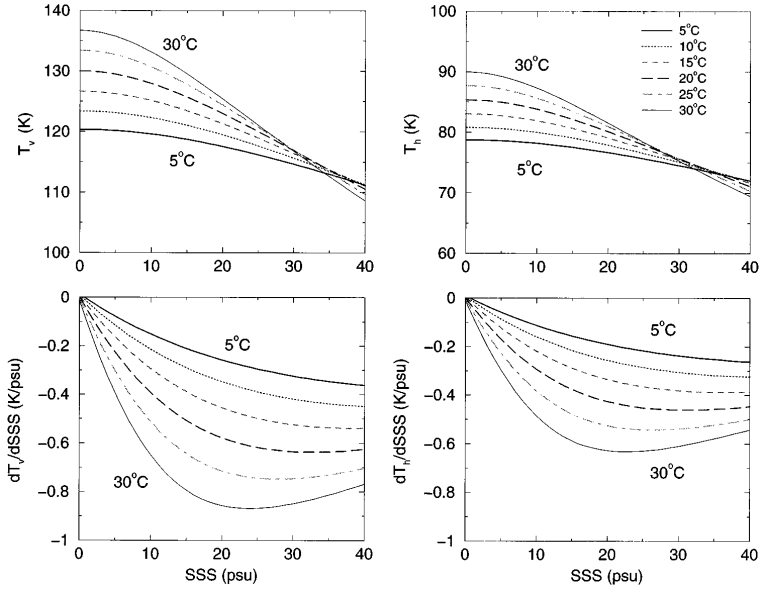

Fig. 2.8 Sensitivity of brightness temperature to water salinity at 40° incidence angle.
The two upper panels plot *Th* and *Tv* versus the salinity at six water temperatures. The two lower panels plot the derivatives to indicate the sensitivity to *SSS* [Yueh et al., 2001].

At 1.4 GHz the penetration depth of the electromagnetic radiation is only 1 cm, which means that salinity remote sensing is referred to a thin film of the sea surface layer. Due to the low sensitivity, and the spatial resolution that can be expected with a space-borne microwave interferometric radiometer (as will be discussed further on), it is not possible to obtain *SSS* data for mesoscale or regional studies. However, as mentioned, several phenomena extremely relevant for large-scale and climatic studies can benefit from these upcoming measurements.

2.2.3 Factors Influencing the Brightness Temperature Determination

To ensure that the data derived from the SMOS mission are correctly converted into salinity estimates, many other effects that influence the signal need to be carefully quantified [ESA SMOS Brochure, 2004]. The rationale is that it is possible to retrieve *SSS* from microwave measurements as long as whichever variable influencing the brightness temperature signal is properly taken into account, in order to avoid that its variation could hide the salinity dependence.

At L-band, the T_B over the ocean mainly depends on three variables: the sea surface salinity to be measured, the sea surface temperature, and the sea roughness, which is the largest contributor to the deviations of the brightness temperature with respect to the flat sea model [Font et al., 2004].

Sea surface roughness is the major geophysical error source, as it can modify the T_B measured by several Kelvin depending on the incidence angle and it can be even larger than the salinity-induced change itself.

Unlike the US/Argentinean Aquarius/SAC-D mission [Le Vine et al., 2007], SMOS does not carry any active instrument (scatterometer) to determine roughness simultaneously with the measurement, and in most cases the SMOS satellite overpasses will not coincide with other satellite sensors (radars) providing simultaneously this information over the same swath. Auxiliary information will thus be needed to correct for this effect.

The auxiliary variables that are generally used to parameterize the surface roughness and the sea state are the 10 m height wind speed (U_{10}), as the most widely available data source (despite the relationship between the latter and the sea surface geometry is not straightforward), the significant wave height (*SWH*) [Camps et al., 2004a], or both [Gabarró et al., 2004a].

Uncertainties in the required auxiliary parameters themselves may induce errors in the retrieval procedure, hampering reliable salinity estimations, as it will be seen in the next chapters.

In summary, the variables that influence the brightness temperature signals such as the sea surface temperature, the sea surface roughness (wind-driven waves, swell, currents, rain, oil spills etc.) and the presence of foam must be properly accounted for in order to retrieve the sea surface salinity with the prescribed accuracy.

2.2.4 Perturbations in the Measurement of the Brightness Temperature

As it was said in the previous section, the surface brightness temperature accounts only for the observed scene natural emission. The apparent brightness temperature reaching the radiometer antenna includes other perturbing phenomena such as atmospheric and ionospheric effects, and the downwelling cosmic, galactic, Sun and Moon noises scattered over the surface [Ulaby et al., 1982].

Figure 2.9 represents a sketch of the perturbing noises present in the radiometric measurements. The atmospheric effects have been already discussed, while in the next two subsections the ionospheric and galactic noises will be dealt with.

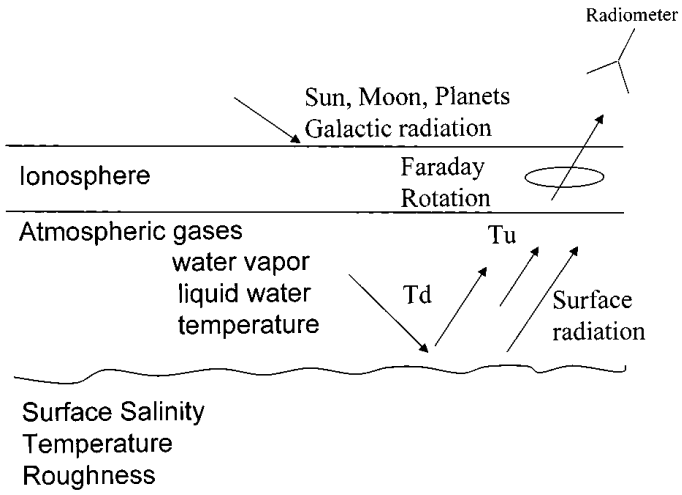

Fig. 2.9 Perturbing noise sources that influence the sea surface microwave radiation [Yueh et al., 2001].

2.2.4.1 Faraday and Geometric Rotations

Faraday rotation is based on the rotation of the plane of polarization of the electromagnetic waves propagating through an ionized medium in the presence of a magnetic field (the ionosphere). According to [Skou, 1981], the mean rotation value can be estimated as:

$$\varphi \approx \frac{17^{\circ}}{f^{2}_{[GHz]}}. \tag{2.14}$$

At low frequencies this effect cannot be neglected, and at L-band (1.4 GHz) the average rotation is found to be $\varphi = 8.7°$. In most cases it produces an error in the brightness temperature below 0.1 K, but in some cases, it may reach 1 K at large incidence angles [Yueh, 2000; Le Vine and Abraham, 2002; Waldteufel et al., 2004].

Although Faraday rotation estimates by means of the ionosphere total electron content (TEC) can be used, their accuracy may not be enough for the required salinity accuracy. In addition, local ionospheric inhomogeneities can create different Faraday rotations within a single pixel, and this may hamper a proper correction at subpixel level.

As it will be seen, a simple way to avoid this problem is to use the first Stokes parameter, $I = Tx + Ty = Th + Tv$, which is invariant to rotations. The opposite trend at vertical and horizontal polarizations has the additional advantage of minimizing the angular variation of some other effects, despite the radiometric sensitivity is somewhat degraded.

Moreover, moving away from the vertical and horizontal polarization planes of the antennas, there is a geometric rotation of the reference frame that creates a polarization mixing between vertical and horizontal polarizations [Claassen and Fung, 1974]. These rotations, when equal to 45° create a singularity in the retrieval process that largely amplify radiometric errors, rendering the radiometric measurements useless.

2.2.4.2 Space Radiation

The apparent temperature is modified by the contribution of the microwave radiation emitted from the space, as well. Three main phenomena can be considered, and their contribution to the antenna temperature (weighted by the antenna pattern) needs to be taken into account:

- Cosmic radiation level. It is fairly constant, about 2.7 K, and does not affect the quality of the measurement.
- Galactic noise. **A**t L-band presents large variations, from 0.8 K to 40 K [Le Vine and Abraham, 2004] according to the reflection over the Earth's surface. The correction is feasible because the galactic noise is well mapped, although the absolute accuracy of these maps is still questionable and the scattering models present errors.
- Sun glints. It can jeopardize the measurements because the Sun brightness temperature value is higher than 100,000 K. [Camps et al., 2004b; Picard et al., 2004; Reul et al., 2007]. Hence, direct reflections can be avoided by pointing the instrument to the shadow zone of a polar sun-synchronous orbit.

2.2.5 Spatio-Temporal Averaging

Since the radiometric sensitivity achievable is of the order of 2K, it is clear that *SSS* cannot be recovered with the required accuracy from a single measurement. However, if the errors contributing to the uncertainties in T_B are random, the requirements can be accomplished by averaging SMOS individual measurements in both space and time.

The series of independent measurements provided by the multi-angular view (described later) allows retrieving surface parameters with an improved accuracy. This, evidently, will only reduce random errors, but not systematic errors present in the measurements.

For a satellite sensor whit a footprint of about 40x40 km and revisit time of three days at the Equator, a consolidated retrieved product can likely be obtained with 30-day and 1°x1° averages rather than with 10-day and 2°x2° averages. Although the number of samples is similar, the errors in auxiliary data (specifically *SST* and wind speed) are much more correlated in space than in time, so more error reduction is achieved by temporal averaging than by spatial averaging

2.3 Sea Surface Emissivity Modeling

The emissivity of the sea surface depends on both configuration and scene parameters, as already pointed out. Whilst configuration parameters (frequency, look angle and polarization) are set or at least known, the scene parameters (*SSS*, *SST*, wind speed, foam etc.) should be accurately studied to address their magnitude and impact on the emissivity and subsequently on T_B.

The scene-related emissivity variations sources can be distinguished into dielectric and geometric. The first one influences the emissivity properties through the dielectric constant (which embodies the *SSS* information), while the latter one affects the angular spreading or emission of the signal and is parameterized in several ways, as seen, being the most rigorous through the wave spectrum.

The characterization of the sea surface emissivity calls for an accurate modeling, and this section embodies both theoretical (asymptotical) and semi-empirical modeling, describing as well two field experiments carried out to better understand the sea surface emissivity at L-band.

Theoretical models describe thoroughly the physics of the systems and the variables associated to the determination of the brightness temperature. Nevertheless they usually have a complex mathematical description which limits its application in the inverse procedure.

Conversely, semi-empirical models are specifically tuned for the context of the retrieval, and usually come from regression with ground-truth data. The relationship with the measured parameter (T_B) is much simpler, despite suffering of limited applicability and versatility.

2.3.1 Theoretical Modeling

Theoretical modeling of brightness temperature involves studies concerning the dielectric constant model, the spectrum model and an expression describing the electromagnetic interaction with the surface.

2.3.1.1 Dielectric Constant Models

For the ideal case of a flat sea, the emissivity is simply defined by the Fresnel's law in terms of specular reflectivity (Eqns. 2.10, 2.11 and 2.12).

Several models concerning the dielectric constant of the sea water ε_r exist in the literature; the well-known Klein and Swift model [Klein and Swift, 1977], hereafter KS, is widely used even though several new models are available, such as Ellison [Ellison et al., 1998], and Matzler [Matzler, 2006].

Nevertheless, these models are not specifically tuned at L-band and the different values obtained are large enough to produce differences ranging from 0.4 to 1.1 K in the predicted T_B [Dinnat et al., 2003a; Camps et al., 2003a].

Blanch and Aguasca, hereafter BA, performed specific measurements in the 1-2 GHz range [Blanch and Aguasca, 2004]; these results agreed much better with KS model, also in agreement with [Wilson et al., 2004].

Figure 2.10 shows the brightness temperature dependence angular variations at *h* and *v* polarization for a perfectly flat sea surface considering a *SST* of 20° Celsius and a *SSS* of 36 psu.

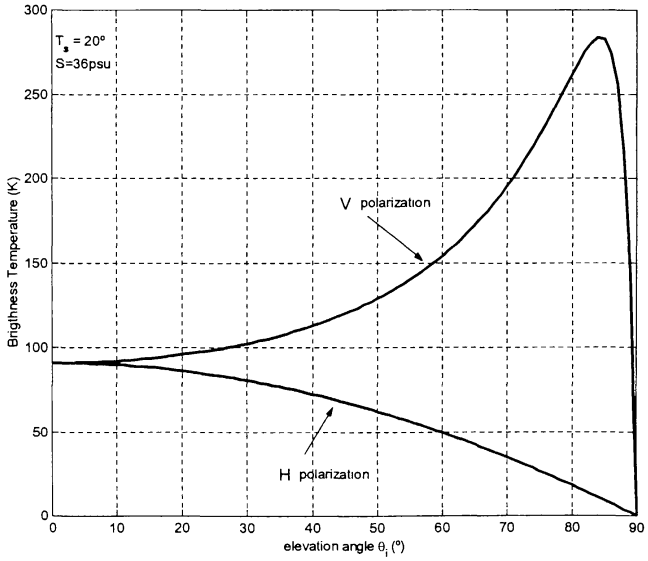

Fig. 2.10 Brightness temperature versus the incidence angle for a perfectly flat sea surface.

2.3.1.2 Sea Surface Emission Forward Models

For a realistic roughened scene the complexity of the electromagnetic description of the surface increase considerably, since it has to be added information regarding the statistical properties of the latter, and the subsequent scattering properties of the scene. The emissivity problem may be dealt with as a problem of bistatic scattering modeling for a rough sea surface.

The presence of wind strongly affects the sea surface emission since it causes waves and, above certain speeds, foam. For partially foam-covered sea surface, according to [Camps et al., 2005a], the emission is given by:

$$e(f,\theta,p,F) = (1-F)\cdot e_w(f,\theta,p) + F\cdot e_f(f,\theta,p), \tag{2.15}$$

where F is the fractional foam coverage, e_w is the emissivity of the wind-roughened sea water and e_f is the emissivity of a totally foam-covered surface. The fractional coverage F depends on the wind speed mainly, but also on *SSS*, *SST*, which affect the water viscosity.

Neglecting the foam contribution, which will be assessed later on, in this paragraph a brief introduction and the range of validity of the different models that approximate the computation of e_w at L-band is examined. Many efforts have been devoted to theoretical forward modeling studies at L-band, evaluating either several emissivity/scattering models or different oceanographic spectra [Vall-llossera et al., 2003; Dinnat, 2003b]

According to the Kirchhoff Model (KM) [Ulaby et al., 1982] a roughened sea surface can be approximated by planes, called "facets", if the correlation length *l* is larger than the wavelength of the incident electromagnetic field, at the horizontal scale, and if the surface height variance σ_η^2 is small compared to the wavelength, at the vertical scale.

On the other hand, Kirchhoff method cannot be used in case of a flat surface or with very small roughness, since the surface must have a minimum standard deviation height.

The Small Perturbation Model (SPM) [Ulaby et al., 1982] is used when both the rms height and the correlation length are smaller than the wavelength of the incident field. The validity margin for this method complements the validity range of the KM.

The Integral Equation Method (IEM) [Fung, 1994] was developed to cover the range where neither Kirchhoff approach nor the SPM give accurate results. Furthermore it reduces to the Kirchhoff or to the SPM according to their validity ranges.

For the thermal radiation of a roughened surface there is an equivalence between the SPM and the Small Slope Approximation (SSA) [Irisov, 1997; Johnson and Zhang, 1999; Reul and Chapron, 2001]. The SSA approach compared to the SPM presents the advantage of being only

constrained on surface slope and not on surface height, making the model applicable to the entire ocean surface.

The Two Scale Model (TSM) [Wentz, 1975; Yueh, 1997] approximates the sea surface as a two-scale surface with small capillary waves on the top of large-scale surfaces. With this approximation the thermal emission is the sum of emissions from individual, slightly perturbed surfaces tilted by the underlying large-scale surface. A version of this model tuned at L-band is available in [Dinnat et al., 2003a].

To properly characterize the sea state [Miranda et al., 2003], different wave spectra are available in literature [Durden and Vesecky, 1985; Donelan et al., 1985; Elfouahily et al., 1997; Kudryavtsev et al., 1999], and have been widely applied in the above mentioned scattering/emission models.

Summarizing, different models and different spectra predict quite different emissivities. According to [Vall-llossera et al., 2003], the best matching with experimental data has been found for the 2-scale method of Yueh [Yueh, 1997] applied with the Durden-Vesecky times 2 spectrum [Durden and Vesecky, 1985] and with KS dielectric constant [Klein and Swift, 1977].

According to [Zanifé et al., 2003], the SSA combined with an appropriate statistical model for the sea surface description is the most accurate first-order asymptotic solution to simulate a rough sea surface at L-band, giving a better understanding of the underlying physics. The spectrum model by Kudryavtsev [Kudryavtsev et al., 1999] provides a physically consistent statistical description at decimetric waves (major surface emitters at L-band), and when used jointly with the SSA model, it seems to provide accurate emissivity predictions [Font et al., 2004]. Simulations using different spectra have demonstrated that the accuracy of the emissivity models is highly dependent on the spectrum.

2.3.2 Semi-Empirical Modeling

Besides the theoretical models, several semi-empirical models have also been developed to describe in a straightforward way the sea surface roughness impact on the sea surface emission. A first approximation lies in considering the total roughened sea surface brightness temperature as the sum of the flat sea brightness temperature plus an empirical contribution related to the sea state:

$$T_B(\theta, pol) = SST \cdot \left(1 - \left|R_{H,V}(\theta, \varepsilon_r(f, SST, SSS))\right|^2\right) + \Delta T_B(\theta, pol). \qquad (2.16)$$

The term $\Delta T_B(\theta, pol)$ in the Eqn. 2.16 represents the deviations of T_B with respect to the flat sea brightness temperature due to the sea surface roughness. The contribution $\Delta T_B(\theta, pol)$

changes in accordance to the semi-empirical model used and it is a function of the incidence angle and of one or more sea state descriptors such as the wind speed, the SWH, the Mean Square Slope (*mss*), and the inverse wave-age (Ω_c).

2.3.2.1 Field Experiments

In order to provide ground-truth measurements, two ESA-sponsored field experiments have been undertaken by the Universitat Politècnica de Catalunya (UPC) of Barcelona, Spain, in cooperation with other institutes. As already mentioned, the brightness temperature dependence on geophysical parameters has to be accurately assessed, and to this aim, semi-empirical models have been developed once *in situ* measurements have been collected.

Measurement campaigns have been carried out with an L-band, automatic, fully-polarimetric, radiometer (LAURA) designed and implemented at UPC (Fig. 2.11) [Villarino, 2004].

WISE (**WI**nd and **S**alinity **E**xperiment) 2000 and 2001 campaigns were devoted to the understanding of the angular dependence of the emissivity of a wind-roughened sea, to better understand the wind and sea state polarimetric impact on the L-band brightness temperatures [Camps et al., 2004a]. They consisted of the acquisition of long time series of T_B altogether with wind speed and significant wave height recording.

The LAURA Radiometer was deployed in REPSOL's Casablanca oil rig (Fig. 2.12), 40 km offshore the coasts of Tarragona (Spain), in a representative site of the Mediterranean hydrographic conditions, in conjunction with other oceanographic and meteorological instrumentation from the Institut de Ciències del Mar (Barcelona, Spain), the Universitat de València (València, Spain), the LODYC (now LOCEAN, Paris, France), and the CETP (Vélizy, France).

The **FROG** (**F**oam, **R**ain, **O**il spills and **G**PS-reflections) 2003 experiment was performed at the IRTA facilities at Poble Nou del Delta (Tarragona, Spain) and was meant to estimate the emission of foam and rain-induced roughness, beside the effects of thin oil film pouring (Fig. 2.13).

Namely, foam emissivity was evaluated in relation with the distribution, size and characteristics of the bubbles, and was characterized as a function of salinity, foam thickness, incidence angle and polarization. These parameters, together with the percentage of foam-covered water, have been used in the development of a semi-empirical model [Camps et al., 2005a]. Over a flat surface rain and oil have a negligible impact on the water surface T_B, but foam has to be included in the emission model at L-band.

In conclusion, the purpose of these field experiments has been the improvement and characterization of the sea surface emissivity semi-empirical models, which until then did not include these effects consistently.

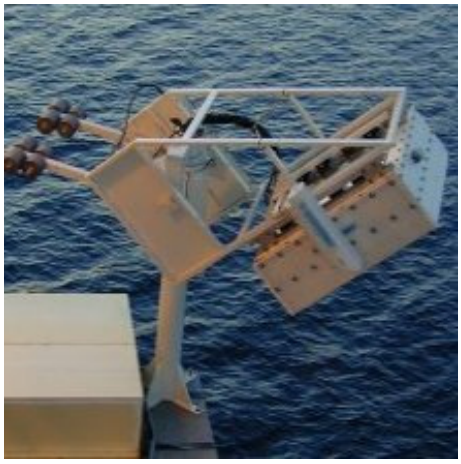

Fig. 2.11 LAURA (L-band AUtomatic RAdiometer).

Fig. 2.12 Casablanca oil rig, WISE field experiments' location. Red circle indicates the position of the LAURA radiometer.

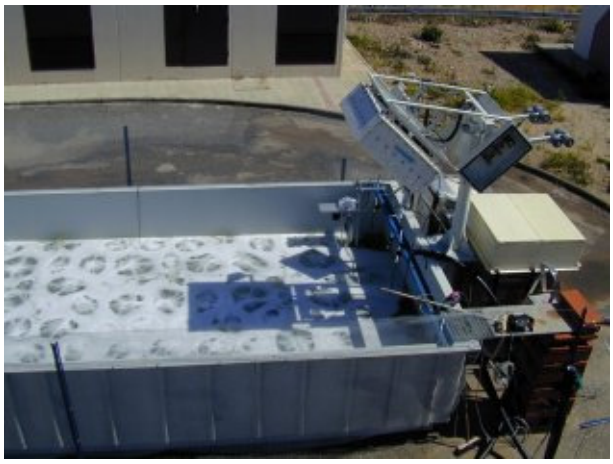

Fig. 2.13 Pond with the foam diffusers switched on in the FROG 2003 experiment.

2.3.2.2 Empirical Sea State Regressions

A simple and commonly used empirical model is the piece-wise linear fit to Hollinger measurements [Hollinger, 1971]:

$$\Delta T_{Bh} = 0.2 \cdot \left(1 + \frac{\theta}{55^{\circ}}\right) \cdot U_{10}, \tag{2.17}$$

$$\Delta T_{Bv} = 0.2 \cdot \left(1 - \frac{\theta}{55^{\circ}}\right) \cdot U_{10}, \tag{2.18}$$

where U_{10} denotes the wind speed at 10 meter height, as said. After WISE 2000 and 2001 experiments, another model was derived to relate the wind speed to the variation of brightness temperature [Camps et al., 2004a]:

$$\Delta T_{Bh} = 0.25 \cdot \left(1 + \frac{\theta}{118^{\circ}}\right) \cdot U_{10}, \tag{2.19}$$

$$\Delta T_{Bv} = 0.25 \cdot \left(1 - \frac{\theta}{45^{\circ}}\right) \cdot U_{10}. \tag{2.20}$$

Whilst another expression involves the use of the significant wave height (*SWH*) [Camps et al., 2004a]:

$$\Delta T_{Bh} = 1.09 \cdot \left(1 + \frac{\theta}{142}\right) \cdot SWH, \tag{2.21}$$

$$\Delta T_{Bh} = 0.92 \cdot \left(1 - \frac{\theta}{51}\right) \cdot SWH. \tag{2.22}$$

A combined U_{10}/*SWH* dependence has been derived in [Gabarró et al., 2004a] as follows:

$$\Delta T_{Bh} = 0.12 \cdot \left(1 + \frac{\theta}{24^{\circ}}\right) \cdot U_{10} + 0.59 \cdot \left(1 - \frac{\theta}{50^{\circ}}\right) \cdot SWH, \tag{2.23}$$

$$\Delta T_{Bv} = 0.12 \cdot \left(1 - \frac{\theta}{40^{\circ}}\right) \cdot U_{10} + 0.59 \cdot \left(1 - \frac{\theta}{50^{\circ}}\right) \cdot SWH \ . \qquad (2.24)$$

2.4 MIRAS Instrument and Interferometric Radiometry by Aperture Synthesis

As said, the SMOS mission unique payload is the MIRAS (Microwave Imaging Radiometer by Aperture Synthesis) instrument: an L-band, two-dimensional, synthetic aperture radiometer with multi-angular and dual/fully-polarimetric imaging capabilities [Martín-Neira and Goutoule, 1997; Camps and Swift, 2002].

Its single payload is a novel concept of L-band radiometer (Fig. 2.14) that measures the brightness temperature of the Earth within a wide field of view and without any mechanical antenna movement. The instrument instantaneously records a whole scene (snapshot) every 1.2 seconds.

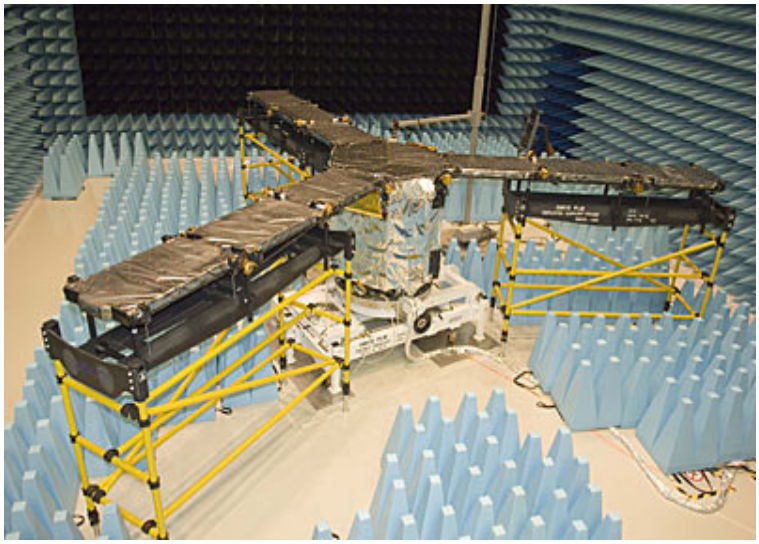

Fig. 2.14 SMOS payload testing [ESA SMOS website].

The instrument has a Y-shaped deployable structure, consisting of 3 coplanar arms, 120° apart each other. The total arm length is about 4.5 m with an angular resolution of approximately 2°. The range of incidence angles is variable (spanning from 0° to almost 65°) within the FOV and depends on the distance between the pixel and the sub-satellite path. Therefore, a particular feature of the MIRAS instrument is its multi-angular imaging capability as the satellite moves over the Earth, a crucial feature for the development of efficient retrieval methods. To achieve an even greater angular excursion and fully exploit its viewing capability the instrument will be put in orbit with the antenna boresight tilted of 32° with respect to nadir.

Real aperture microwave radiometers collect the thermal radiation emitted by a source and present a direct relationship between the power collected and the brightness temperature in a given direction. Nevertheless, to achieve the SMOS performances, a real radiometer would require an antenna size of physical dimensions impossible to cope with in a satellite mission. This is the reason why the salinity estimation by satellite has not been planned until recently. Therefore, it was concluded that the most promising technique was the aperture synthesis radiometry that had successfully been demonstrated in the late 80's [Ruf et al., 1988]. The principle of aperture synthesis employed by the radiometer on SMOS is similar to Earth rotation synthesis developed in radio astronomy [Kraus, 1986] (Fig. 2.15).

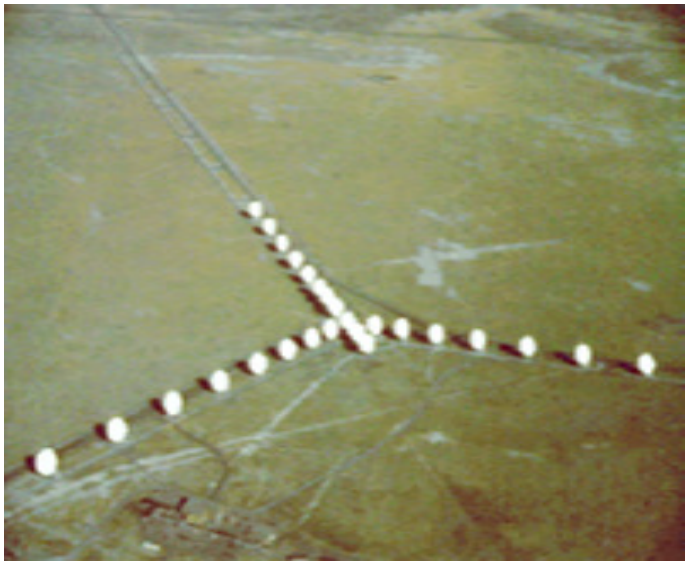

Fig. 2.15 Y-shaped Very Large Array, Socorro, New Mexico, USA [NASA JPL website].

Aperture synthesis permits the use of thinned antenna arrays with performances comparable with an equivalent real aperture antenna of the dimension of the longest baseline distance, being this an advantage self-evident in a satellite mission.

The interferometric radiometer involves an extra step of image reconstruction compared to conventional mapping radiometers that will entail several additional errors; besides random noise errors, in fact, the image reconstruction process induces other radiometric errors (radiometric accuracy and biases) that impact on the *SSS* retrieval accuracy.

To avoid aliasing in the Fourier imaging process, a minimum antenna spacing of 0.57 wavelengths is necessary [Camps et al., 1997]. Nevertheless, antenna size and a limited swath led to an antenna spacing of 0.88 wavelengths [Waldteufel et al., 2003]. Due to the non-compliance of Nyquist criterion, the reconstructed images present aliasing in the spatial frequency domain. These aliases overlap one over each other, thus limiting the instrument actual field of view.

As a consequence, the on-ground alias-free field of view of the instrument has a distorted hexagon-like shape with curved sides, having each pixel different sizes. Due to the motion of the platform, each pixel is measured several times with different spatial and radiometric resolution and incidence angle.

The SMOS field of view is shown in Fig. 2.16 in the (ξ,η) direction cosines domain, where the synthetic brightness temperature image is formed through a Fourier synthesis technique [Camps et al., 1997], and in Fig. 2.17 in cross-track/along-track coordinates [Camps et al., 2005b].

In Fig. 2.16 the SMOS observation geometry is shown. Half space is mapped into the unit circle in (ξ,η) coordinates. The alias-free FOV imaged by the instrument (marked in yellow) is enlarged up to the Earth "aliases" limit by taking into account the sky contribution.

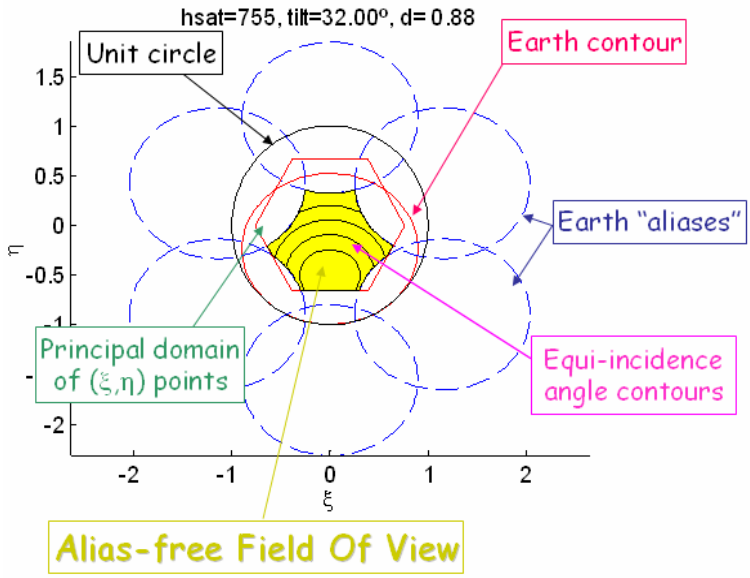

Fig. 2.16 SMOS observation geometry. Half space is mapped into the unit circle in (ξ,η) coordinates. The alias-free Field Of View (AF-FOV) that is imaged by the instrument (in yellow) is enlarged up to the Earth "aliases" limit by taking into account the sky contribution [Camps et al., 2005c].

Figure 2.17 shows how a pixel is imaged under different specific conditions: variable incidence angles (from 0° to 60°, dashed contours centered at nadir) and radiometric sensitivities (from < 3 K to > 5 K, dash-dot lines centered at boresight).

The arrows in Fig. 2.17 indicate the tracks followed by a pixel (it is obviously the satellite moving in the other direction), since it enters in the field of view (top), until it leaves it (bottom). The number of snapshots in which the pixel is imaged varies with the distance to the satellite ground-track. As it increases, pixels are imaged fewer times, the angular variation is reduced, and measurements become noisier, which translates into a degraded performance in terms of the quality of the retrieval. Provided good models exist to account for these varying measuring conditions, the salinity map can be obtained by averaging out all the retrieved values at each snap-shot.

The instrument will be periodically calibrated using a noise injection mechanism in combination with a highly stable noise injection radiometer [Brown et al., 2008].

Engineering studies of the SMOS hardware indicate that the instrument should provide a radiometric accuracy of 1.8 K and a radiometric sensitivity of 2.0 K (rms noise per 1.2 s snapshot) at instrument boresight. The stringent requirements pose technical challenges to achieve the required radiometric accuracy and stability, but recent studies indicate that these performances can be accomplished.

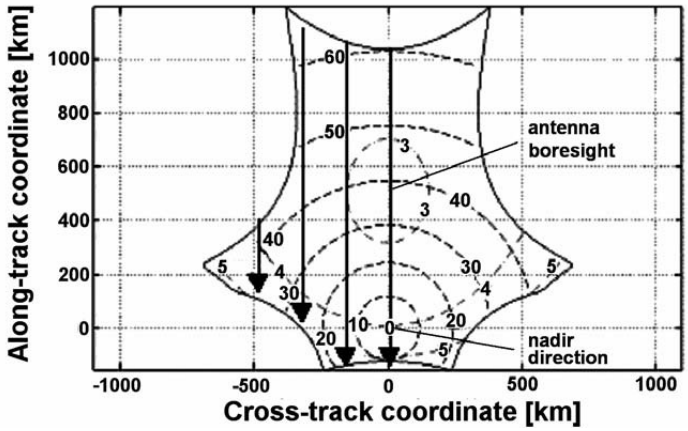

Fig. 2.17 SMOS pixels sampled under different incidence angles and radiometric resolution. Parameters: 21 antennas per arm, d=0.875 wavelengths antenna spacing, β=32° tilt angle, and h = 755 km platform height [Camps et al., 2003a].

Chapter 3
Sea Surface Salinity Retrieval

In the previous chapters the SMOS mission, the basic principles of microwave radiometry, and the rationale of the measurements have been described. In this chapter, the sea surface salinity retrieval procedure starting from the brightness temperature measurements, the so-called inversion scheme, will be analyzed.

Like whatsoever remotely-sensed geophysical parameter estimation, the retrieval of salinity is a minimization problem. In order to ensure a reliable extraction of this variable, all the other parameters affecting the measured brightness temperature will have to be taken into account, filtered or quantified. The overall generated product will thus be *SSS* maps in a single satellite overpass over the Earth, the so-called Level 2 (L2) product.

First, the salinity retrieval problem will be stated, dealing with the cost function to be minimized and the different items involved, as well as the description of the different steps to be performed prior or after the minimization itself. Therefore, the cost function will be analyzed within the context of the SMOS *SSS* retrieval scheme, stressing the relevant issues and pointing out specially those ones that might jeopardize the effectiveness of the retrieval.

Afterwards, a brief compendium of the different studies performed in this context by several research institutes in these last few years will be done, underlining the different approaches, the approximations and the main findings in an ideal evolution timeline of the *SSS* retrieval problem.

In the end, the conclusions and the state of the art of pre-launch salinity retrieval will be summarized, being this the baseline for understanding the studies that will be described in the following chapters.

3.1 Sea Surface Salinity Retrieval: Statement of the Problem

The sea surface salinity retrieval is a complex process that requires the knowledge of other environmental and perturbing factors and an accurate processing of the radiometer measurements. Its complexity is related both to the narrow range of ocean brightness temperatures and to the stronger signature in the measured values of different geophysical parameters (as sea state) other than salinity.

The inversion procedure on a pixel basis involves the transition from Level 1B (Fourier components of brightness temperatures in the antenna polarization reference frame) or Level 1C

(swath-based maps of brightness temperature) data to Level 2 (one-overpass salinity product). It should be stressed, however, that in order to be compared to the mission requirements, the L2 data will have to be processed in turn until Level 3, that is, properly spatio-temporally averaged.

A robust inversion scheme implemented for SMOS *SSS* retrieval from radiometric estimates is based on an iterative convergence algorithm that compares the satellite measured T_BS with the values provided by an L-band forward model.

This algorithm embodies a cost function in which the error ε (variance) between the modeled and the measured data at all incidence angles θ is minimized for each overpass to obtain a set of estimated parameters ($\hat{\vec{P}} = \left[S\hat{S}S, S\hat{S}T, \hat{U}_{10}\right]$) [Camps et al., 2005b].

$$\varepsilon = \frac{1}{\mathrm{N_{obs}}} \sum_n \left\{ \left[\overline{F}_{\mathrm{model}}\left(\theta, \hat{\vec{P}}\right) - \overline{F}_{\mathrm{data}}\left(\theta, \vec{P}\right) \right]^{\mathrm{T}} \left(\overline{\overline{C}}\right)^{-1} \left[\overline{F}_{\mathrm{model}}\left(\theta, \hat{\vec{P}}\right) - \overline{F}_{\mathrm{data}}\left(\theta, \vec{P}\right) \right] \right\} + \\ + \frac{\left(S\hat{S}S - SSS_{ref}\right)^2}{\sigma_{SSS}^2} + \frac{\left(S\hat{S}T - SST_{ref}\right)^2}{\sigma_{SST}^2} + \frac{\left(\hat{U}_{10} - U_{10ref}\right)^2}{\sigma_{U10}^2}, \tag{3.1}$$

where:

- $\mathrm{N_{obs}}$ is the number of observations acquired at a single location in a satellite overpass, which depends on the distance to the satellite's ground track. As the distance increases, the pixel is imaged fewer times, the angular variation is reduced, and the instrument's noise increases, with the corresponding degraded performance in terms of the quality of the retrieved parameters.
- $\overline{\overline{C}}$ is the error covariance matrix that depends on the SMOS operation mode (fully polarimetric or dual polarization [Martín-Neira et al., 2002]), the reference frame (Earth or Antenna), and the pixel position in the field of view [Camps et al., 2005b], and
- $\overline{F}_{\mathrm{model/data}}\left(\theta, \hat{\vec{P}}\right)$ is a vector that contains the modeled or the measured observables, and its structure depends on the formulation of the retrieval problem, which may be versatile provided the appropriate corrections are applied, namely:
  - $\overline{F}\left(\theta, \vec{P}\right) = \left[\mathrm{T_{xx}}\left(\theta, \vec{P}\right), \mathrm{T_{yy}}\left(\theta, \vec{P}\right)\right]^T$, if the problem is formulated in terms of the brightness temperatures in the Antenna reference frame,
  - $\overline{F}\left(\theta, \vec{P}\right) = \left[\mathrm{T_{hh}}\left(\theta, \vec{P}\right), \mathrm{T_{vv}}\left(\theta, \vec{P}\right)\right]^T$, if the problem is formulated in terms of the brightness temperatures in the Earth reference frame, and

- $\overline{F}(\theta,\vec{P}) = \left[\mathrm{I}(\theta,\vec{P})\right]^T = \left[\mathrm{T_{hh}}(\theta,\vec{P}) + \mathrm{T_{vv}}(\theta,\vec{P})\right]^T = \left[\mathrm{T_{xx}}(\theta,\vec{P}) + \mathrm{T_{yy}}(\theta,\vec{P})\right]^T$, if the problem is formulated using the first Stokes parameter.

In the second case, to avoid the singularities that appear in the transformation from the antenna to the Earth reference frame, the MIRAS full-polarimetric mode has been assumed [Martín-Neira et al., 2002]. In the third case, since the first Stokes parameter (*I*) can be computed in either the antenna or the Earth reference frame, the MIRAS dual-polarimetric mode has been assumed, since the radiometric noise is lower and the singularities are avoided [Camps et al., 2002a; Camps et al., 2003a].

3.1.1 Salinity Retrieval Cost Function Features

In the Eqn. 3.1 two classes of terms can be distinguished: the first ones, on the left hand side of the formulation, embody the measured T_B*s* (the observables) and the modeled ones, while the second ones are the so-called background terms, and represent some restrictions which are applied to ease the convergence of the algorithm upon physical *a priori* information.

A maximum-likelihood Bayesian approach is used [Waldteufel et al., 2003], taking advantage of this *a priori* information available about geophysical parameters. SSS_{ref}, SST_{ref}, and U_{10ref} are reference values (with their uncertainties) to be used to nudge the solution, and σ^2_{SSS}, σ^2_{SST} and σ^2_{U10} are the corresponding auxiliary data variances to properly weigh the cost function terms, according to the accuracy of the specific field.

In fact, when implementing a Bayesian approach with a convergence loop, the influence of the *a priori* values (initial conditions) depends on the uncertainty set in these values. A first-guess salinity value is iteratively modified until gathering an optimal fit with the measured T_B*s*. The more the observations in a singe pixel (up to 78 per polarization in the central track of the FOV), the better will be the fit to estimate the *SSS* in this point, thus exploiting the over-determination multi-look SMOS capabilities. It is assumed that the all the parameters will have remained constant in the few minutes of the satellite overpass. The external geophysical parameters that provide additional information will be themselves adjusted during the convergence process [Font et al., 2006].

To assess the importance of the restrictions to nudge the solution, Fig. 3.1 plots the cost function behavior when varying *SSS* and U_{10}, while *SST* has been set to a fixed value, according to [Gabarró et al., 2007]. The cases considered are (a) no constraints considered, (b) only constraint on U_{10}, but not on *SSS*, and (c) constrains in all parameters. They always present a unique minimum, but in the first case the minimum is very broad, complicating the process of retrieval. When just the wind parameter is restricted and the salinity is left free (plot 3.1b), the

range of solutions with meaningful probability is reduced, but is still considerable. The last plot shows, in turn, that if all the constraints are used, the minimum is much better defined. However, the retrieved parameters might tend to the reference values.

Whether restrictions on salinity have to be used or not, and which is the impact on the uncertainty of the *a priori SSS* field is still a matter of debate, as will be thoroughly discussed in the next chapters.

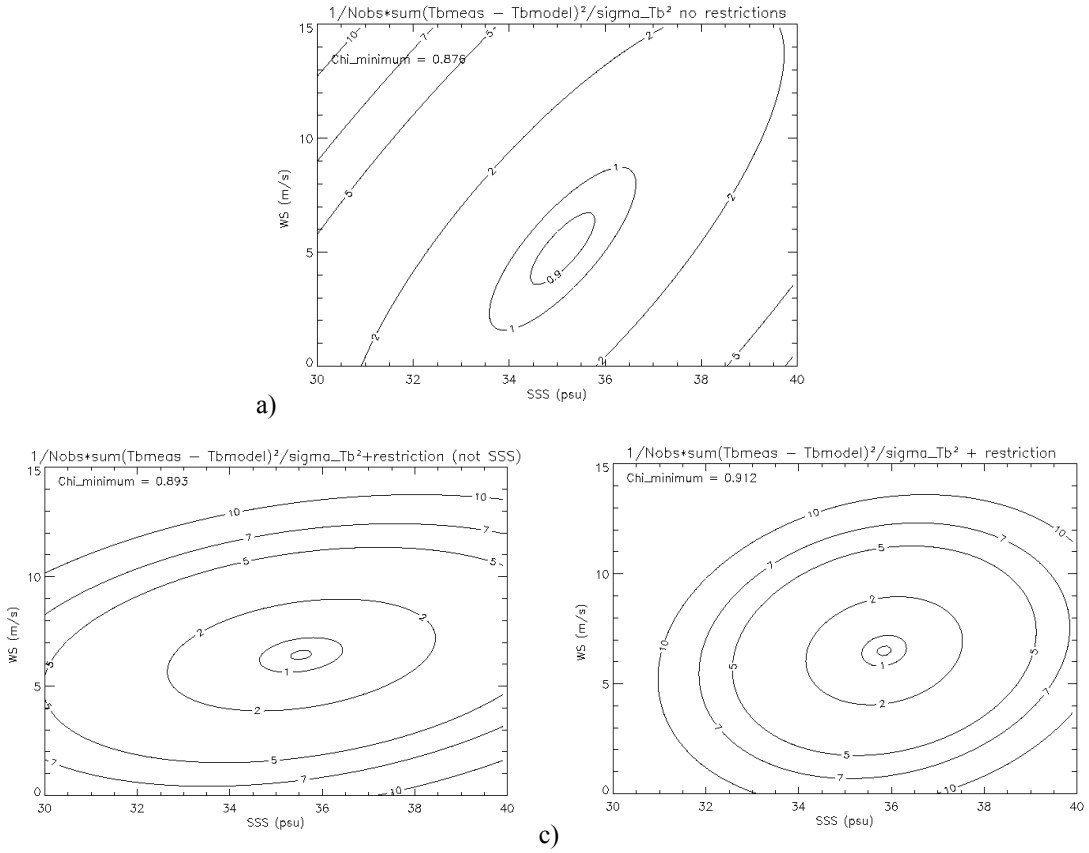

Fig. 3.1 Cost function value contour when varying *SSS* and U_{10} parameters for (a) no constraints, (b) with U_{10} constraints only and (c) when all constraints are used [Gabarró et al., 2007].

A standard nonlinear least-squares routine, the Levenberg-Marquardt method [Marquardt, 1963], is used to retrieve the estimated parameters that minimize the cost function. With the Bayesian formalism, errors on T_B and on retrieved geophysical parameters are assumed to be Gaussian (the covariance matrix of the errors is diagonal). More details can be found in [Waldteufel et al., 2003].

Obviously, since SMOS is not yet flying, the upcoming measured satellites T_B*s* are necessarily simulated. The quality of the retrieval will be strictly related to how realistic these simulations will be and how is dealt with the inherent features of the SMOS brightness temperatures, as will be discussed in the next section. Likewise, the L-band forward modeling of T_B, either theoretical or semi-empirical, was discussed in the previous chapter. It establishes a Geophysical Model

Function (GMF) that constrains the T_B relationship with the parameters to be estimated, thus being a key issue in the goodness of the retrieval.

In other words, through the iterative process the inversion algorithm estimates a set of optimum parameters which minimize the difference among the brightness temperatures with the specified GMF, satisfying at the same time the geophysical constraints imposed on physical bases.

3.1.2 Salinity Retrieval Foregoing Processing Steps

Prior to perform the actual salinity retrieval as descried above, several steps have to be followed, in order to ensure homogeneities among the $T_B s$ to be compared.

On one side, measured (simulated) brightness temperatures will have to be deprived of the inherent scene-dependent bias, and on the other hand, the modeled T_B will have to be rearranged to take into account, apart from the emission from the sea surface, other external effects. Eventually, the geometric transformation from the Earth reference frame (where the forward model has been applied) to the antenna reference frame (where measurements are taken) has to be performed.

For what concerns the modeled T_B, several contributions that modify the signal have to be taken into account, as described in the previous chapter. The modeled T_B at each specific angle will have to be corrected for sky radiation (cosmic and galactic noise) and atmospheric/ionospheric effects. Each contribution is attenuated by absorption in the atmosphere, whilst atmospheric scattering is assumed to be negligible at L-band. As said, Faraday and geometric rotation will have to be included, as well.

The atmospheric and ionospheric effects (upwelling radiation, downwelling radiation scattered over the sea surface, and losses through the atmospheric layer) are sufficiently well modeled [Skou and Hoffman-Bang, 2005].

The Faraday rotation (depolarization due to the propagation through the ionosphere in the presence of the geomagnetic field), in turn, can be either modeled from the knowledge of the ionospheric Total Electron Content (TEC) [Le Vine and Abraham, 2002; Skou et al., 2003; Waldteufel et al., 2004] or avoided by using the first Stokes parameter ($I= Th+Tv=Tx+Ty$) instead of both polarizations separately [Camps et al., 2003a]. The latter presents furthermore the advantage of the cancellation of the geometric rotation effects, even though the number of observables is halved.

Radiation by celestial sources illuminating the ocean surface that are further backscattered towards the radiometer has to be taken into account. The T_B of the cosmic and galactic [Le Vine and Abraham, 2004] radiations can be estimated from sky surveys. The scattered signals are estimated through a proper weighting of the sky T_B illuminating the considered Earth target by the rough sea surface bistatic scattering coefficients estimated at that point.

Once these modifications have been applied, it is possible to compare the resulting T_B modeled with the satellite T_B*s* in the iterative process.

3.2 Sea Surface Salinity Retrieval Issues

At present, the SMOS ocean community is increasingly working towards the consolidation of a robust inversion scheme to enable the *SSS* retrieval from the L-band brightness temperature data. To accomplish the demanding SMOS mission requirements, a full awareness of the *SSS* retrieval issues is needed; among other reasons, this is helpful to assess the quality of the results of a retrieval analysis, evaluating the consequences of the approximations introduced with respect to the future realistic SMOS situation.

Hereafter it is provided a list of the different items involved in the minimization algorithm. Each of the following items will have a certain degree of impact in the retrieval scheme and therefore in the quality of the *SSS* inversion.

- Scene-dependent bias in the simulated T_B:

Three different sources of biases have been identified: errors in the noise injection radiometers (NIR), Sun contributions to the antenna temperature, and imaging under aliasing conditions. A calibration technique has been devised to correct these biases prior to the *SSS* retrieval at each satellite overpass (Fig. 3.2), whose details can be found in [Camps et al., 2005c; Camps et al., 2006; Camps et al., 2008]. Should some residual bias be present in the *SSS* fields, it might be eliminated with a post-processing calibration technique using *in situ SSS* data [Talone et al., 2007a].

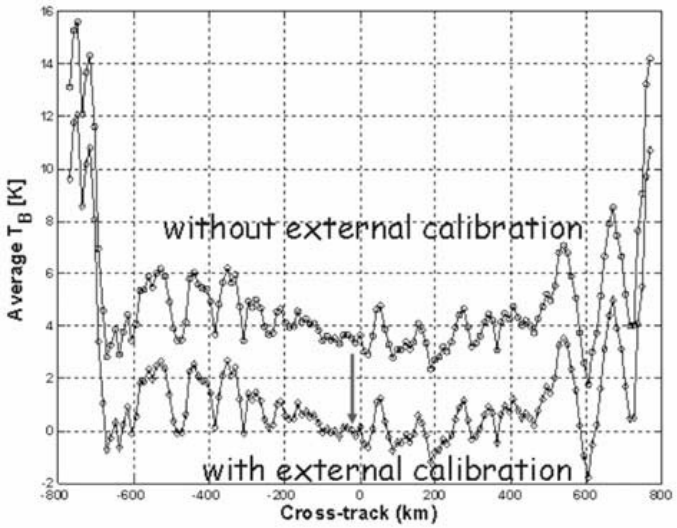

Fig. 3.2 Brightness temperature error versus crosstrack position with (diamonds) and without (circles) external calibration. Brightness temperature biases are significantly reduced by means of this external calibration [Camps et al., 2005c].

- Radiometric sensitivity (thermal noise):

In quasi-realistic simulations, the radiometric noise on brightness temperature will be taken into account through the average normalized antenna radiation pattern of all the receiving elements divided by the obliquity factors, $\frac{t(\theta,\varphi)}{\cos\theta}$, to properly weigh the radiometric measurements according to the noise in each pixel of the 2-D brightness temperature image.

In the boresight direction, the radiometric sensitivity is nearly 2.4 K (dual-polarization mode), and out-of-boresight it is amplified towards the swath edges.

- L-band forward GMF:

Provided that considerable differences might exist in the L-band forward model (see Chapter 2), the choice of an appropriate formulation is decisive.

- Adequate, frequent, and as synchronous as possible sources of auxiliary data:

Auxiliary data are known to be critical, not only for their signature on $T_B s$, but especially for their lack of collocation with SMOS measurements and for the induced salinity error that arise from the uncertainties on the auxiliary field, above all the roughness descriptor.

- Restrictions in the cost function:

As stated, the use of physically-based constraints seem necessary to help the minimization algorithm to converge, although it is not clear whether restrictions on *SSS* should be considered or not, and which is the impact of its uncertainty.

- *Ad-hoc* SMOS imaging configuration:

The geophysical parameter retrieval algorithm must be tailored to reproduce the SMOS imaging characteristics and, in particular, its multi-look and multi-angular imaging capabilities.

- Atmospheric, Galactic and Faraday corrections:

As mentioned, variations on T_B induced by these phenomena might be of some relevance (especially The Faraday rotation).

Likewise, other issues might be taken into account to define more realistic scenarios:

- Different models to be used in direct and inverse formulation.
- Auxiliary parameters different from the original.

The combination and mutual interaction of the above mentioned items might sensibly alter the results and the achievements of a salinity retrieval study; whichever *SSS* error analysis should not be evaluated regardless of the specific retrieval setup configuration.

3.3 Sea Salinity Retrieval Studies

In this section, a very brief overview of the salinity retrieval studies performed by several authors is presented; they can exhibit remarkable differences in the definition of the algorithms and configurations.

These algorithms have been tested using both synthetic data simulated by means of specific simulators (such as the SMOS End-to-end Performance Simulator (SEPS) [SEPS simulator], which will be described in the next Chapter), as well as in situ multi-angular radiometric data acquired during several field experiments (for example, WISE 2000 and 2001, as discussed in the previous chapter, [Gabarró et al., 2004b; Camps et al., 2004a]).

3.3.1 Simulation Studies

Several inversion techniques have been developed and tested so far to retrieve the sea surface salinity from the upcoming SMOS measured brightness temperature data.

The retrieval of *SSS* from radiometric measurements can be performed either through a purely empirical approach, by developing a neural network method using as inputs the SMOS measured T_B and using a learning database involving auxiliary oceanographic data [Ammar et al., 2008; Obligis et al., 2005], or through an iterative convergence scheme that compares the measured values with those provided by an L-band forward model, as said.

In this Ph.D. Thesis it will be considered in detail just the iterative approach, believing that due to the nature of SMOS observations (varying number of observations for each pixel, with different levels of noise) it is the best suited algorithm.

In such algorithms, two main types of forward emissivity models have been considered: semi-empirical relationships (fit to experimental data), or approximate theory for sea surface emissivity (SSA/SPM, TSM, etc).

Relevant studies have dealt with the *SSS* errors induced by uncertainties on auxiliary data [Camps et al., 2002b; Boutin et al., 2004; Camps et al., 2005b; Sabia et al., 2006], or focusing on the effective improvement by spatio-temporal averaging [Camps et al., 2005c, Phillips et al., 2007].

Figure 3.3 shows, as example, the performance of the *SSS* retrieval algorithm with different combinations of auxiliary data restrictions (free parameters, and auxiliary information provided respectively on U_{10}, on *SST*, and on U_{10} and *SST*) as from [Camps et al., 2005b].

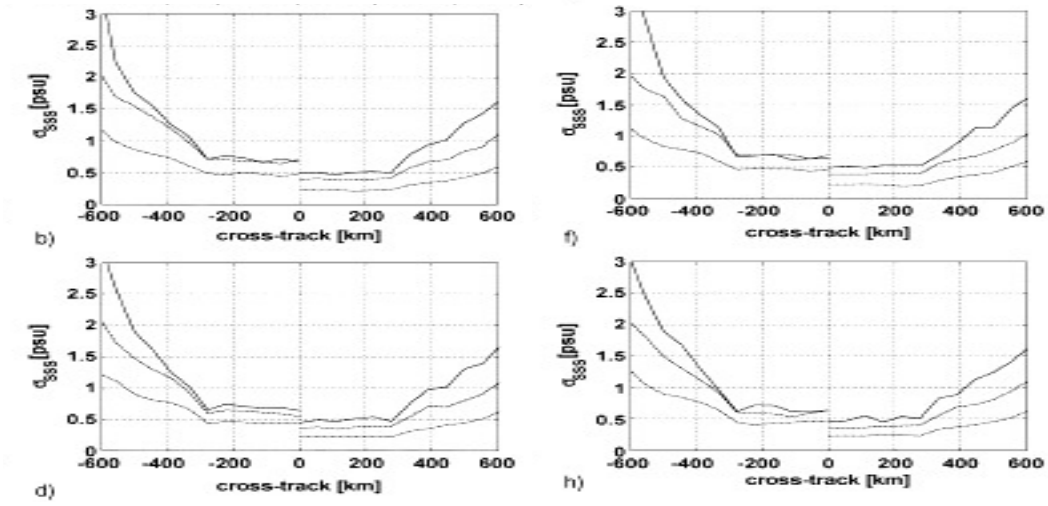

Fig. 3.3 Sea surface salinity retrieval algorithm performance versus pixel position in the swath for a wind speed of 10 m/s and SST of 5 °C (solid line), 15 °C (dashed line) and 25 °C (dotted line). In each plot: first Stokes parameter computed in dual-polarization mode (left side) and *Th* and *Tv* computed in full-polarimetric mode (right side). Case 1 (top left): all parameters as free variables, Case 2 (bottom left): U_{10} auxiliary information, Case 3 (top right): *SST* auxiliary information, and Case 4 (bottom right): U_{10} and *SST* auxiliary information [Camps et al., 2005b].

3.3.2 Experimental Studies

Unlike the simulations studies, in this case sea surface salinity has been retrieved considering as measured $T_B s$ the data acquired during some dedicated field experiments.

Salinity has been successfully retrieved using multi-angular radiometric data collected with a real aperture radiometer during WISE 2000 and 2001 field experiments (see Chapter, 2, Section 2.3) [Gabarró et al., 2004b; Camps et al., 2004].

Moreover, in an attempt to retrieve for the first time sea surface salinity with two-dimensional synthetic aperture brightness temperatures images, the minimization algorithm has been applied to a data set acquired on June 2006 with the AMIRAS (Airborne MIRAS) instrument (Fig. 3.4) aboard the TKK (Helsinki University of Technology) Skyvan flying over lake Lohja, West of Helsinki, Finland [Martin-Neira et al., 2008].

Fig. 3.4 AMIRAS installed on the HUT Skyvan. It is tilted about 24° away from nadir in a similar configuration to that of SMOS [ESA SMOS website].

The interesting feature of this experiment is that the data processing techniques for this small demonstrator (4 antennas each arm) are the same as those that will be used in the MIRAS flight instrument aboard SMOS, from raw visibility samples to calibrated visibilities [Corbella et al., 2005]

3.4 Salinity Processor Prototype

Among the different approaches listed in the previous section, the baseline algorithm chosen by ESA to retrieve sea surface salinity from MIRAS data is embedded into the SMOS Ocean Salinity Level 2 Prototype Processor (L2PP) [Zine et al., 2008] .

The SMOS data processor will generate a sequence of T_B maps that correspond to successive sampling snapshots along an orbit. These values will correspond to a single salinity at a fixed ocean location. Each grid point has to be analyzed to discard incorrect data or flag values that require a specific processing.

As mentioned in Section 3.2, besides the low sensitivity of T_B to salinity, three other major problems make the SMOS determination of *SSS* very challenging:

- The instrument intrinsic limitations (radiometric thermal noise, calibration stability and image reconstruction techniques),
- The need for precise and synchronous sea surface auxiliary information (temperature, roughness) to be estimated from external sources, and,

- The accuracy of the forward model of the sea surface emissivity to be used in the iterative convergence.

With respect to the latter, the different processes that impact on the emission of a roughened surface are not fully described or considered, neither in the available theoretical formulations nor in the semi-empirical models.

Thus, three different roughness model options have been selected for implementation in the salinity retrieval algorithm [Font et al., 2006], to be further checked until identification of an optimal solution for the SMOS *SSS* operational processing chain. Two of them are theoretical models, involving the statistical description of the sea surface and the asymptotic solution for electromagnetic scattering. They are based respectively on the two-scale approach [Dinnat et al., 2002] and the small slope approximation [Johnson and, Zhang, 1999], the latter with a correction accounting for the foam effect [Reul and Chapron, 2003].

The third option is a semi-empirical formulation derived from the few existing data sets, provided by the field campaigns that have measured the L-band polarized emission of the sea surface together with oceanographic and meteorological parameters [Gabarró et al., 2004b; Camps et al., 2004].

As illustrated in Fig. 3.5, the available data reporting roughened sea surface emissivity sensitivities to wind speed does not allow choosing the best adapted correction among these three models.

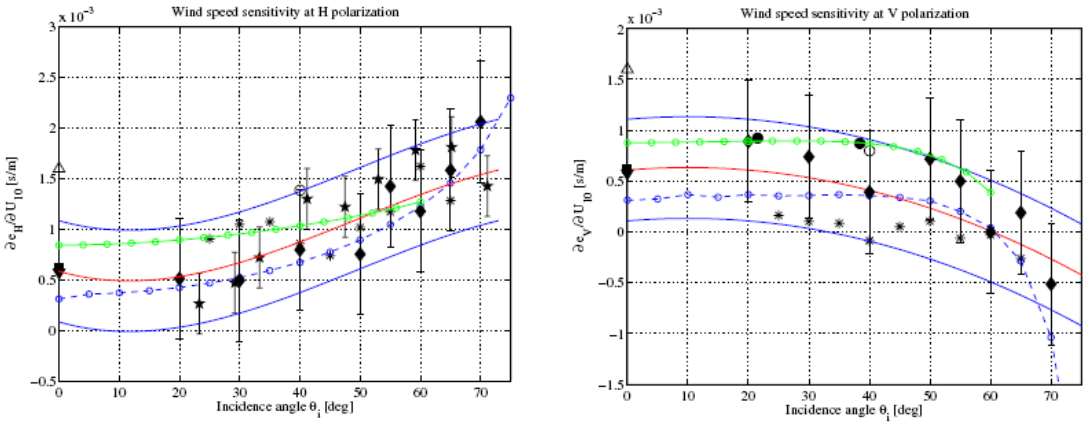

Fig.3.5 Comparison among measured and predicted sensitivities to wind speed at L-band at 10-meter height as function of the incidence angle [Font et al., 2006]. Left: horizontal polarization; Right: vertical polarization. (★ Swift 1976 [Swift, 1976]; ■ Lerner 1977 [Lerner and Hollinger, 1977]; ∗ WISE [Camps et al., 2002a]; ♦ Hollinger 1971 [Hollinger, 1971]; ▼ Webster 1976 [Webster et al., 1976]; ○ Yueh 2001 [Yueh et al., 2001], ● Etcheto 2004 [Etcheto et al., 2004]), (-o-) Predictions from the SSA/SPM (blue) and two-scale (green) models at *SST*=15 °C and *SSS*=35 psu. The red curve shows a best-fit through the observations.

The different selected options for the roughness effect model include the use of different roughness descriptors (e.g. wind speed, wind stress, inverse wave-age or significant wave

height). All the required data will be obtained operationally from the European Centre for Medium-range Weather Forecast (ECMWF).

3.5 Conclusions

In this chapter the salinity retrieval problem has been detailed, underlining its state of the art and the relevant issues; the retrieval of sea surface salinity in the SMOS mission and the different tuning of the minimization algorithm represent the core of this Ph.D. Thesis and are at the basis of the work described in the following chapters. In section 3.4 an overall salinity inversion scheme, the L2PP, has been described, and it has been remarked how several issues need to be completely addressed.

In the following chapters of this thesis, some of these issues will be pointed out, with the aim of establishing at least some hierarchy among them, besides some quantification of the different effects in terms of retrieval accuracy.

Namely, after having described the simulation and processing tools used throughout this work in Chapter 4, in Chapter 5 the impact of several multi-source different auxiliary data on the final *SSS* error will be addressed. This gives a first feeling of the quantitative *SSS* error that should be expected in real upcoming measurements, whilst in the Chapter 6 the potential use of GNSS-R (Global Navigation Satellite Systems-Reflections) derived signals to correct for sea state uncertainty in the SMOS context has been investigated.

Chapter 7 deals with an overall *SSS* Error Budget; all the relevant error sources are listed and consistently binned, and therefore the corresponding effect in terms of the L3 *SSS* error is addressed in different algorithm configurations. An ocean salinity error budget would give a whole perspective of the magnitude of each single contribution and is suitable to furnish a sketch of the problems that will have to be faced and tackled once real SMOS data will be downlinked.

After launch, nevertheless, the algorithm will surely need refinements, either way in the forward model and in finding a closed formulation of the cost function itself, by means of a proper balancing of the different terms.

Chapter 4
Simulation and Processing Tools

In the previous chapter an overall view of the *SSS* retrieval procedure has been provided, spanning from the statement of the problem (the iterative cost function and its related issues) to the studies performed in the SMOS ocean salinity community to address it.
Besides, it has been stressed how several parameters or configuration settings are especially critical, and their assessment requires major efforts in order to ensure an adequate salinity retrieval.
Before going into the details of the retrieval issues that have been studied in this Ph.D. Thesis, in this chapter the software tools that have been used in support of these analyses will be described.
From the simulation side, the SMOS End-to-end Performance Simulator (SEPS) will be presented, which generates the brightness temperature maps to be used in the retrieval, waiting for the true satellite measurements. Afterwards, the inversion procedure as described in the previous chapter is performed by means of the so-called Level 2 Processor, which is in charge of producing the *SSS* maps in a single satellite overpass.

4.1 Simulation Tool

4.1.1 Simulator Main Features

As it has been mentioned, the instrument measured quantities have to undergo a significant amount of processing before getting a useful brightness temperature image. The peculiar features of the MIRAS payload, among which the large number of receivers and the wide FOV of the antennas, required the development of a specifically-tailored instrument error model, calibration and image reconstruction techniques.
In this context, an end-to-end simulator that assesses the performances of this space-borne interferometric radiometer becomes thus a very useful tool, and it is helpful in the instrument design itself, in the development of the calibration strategies and in the inversion techniques.
The SEPS simulator is an *ad hoc* tool that has been mainly developed by the UPC with contributions from the Spanish EADS-CASA Espacio and GMV, and the German DLR [Camps

et al., 2003b], and it is an improved version with a user-friendly interface of the software originally developed in [Camps, 1996] under MATLAB^{TM} code.

It covers the complete simulation of the input brightness temperature maps, the full instrument modeling, the instrumental error correction, and the inversion algorithm to reconstruct the brightness temperatures. The output maps are presented in a graphical format including most of the standard cartographic projections.

The simulator has been developed with the aim of providing an operational tool to predict the system performances. Beyond that, it provides the SMOS ocean salinity scientific community with the realistic simulated T_B inputs needed in the implementation and improvement of the retrieval algorithms.

It has the following capabilities [Corbella et al., 2003]:

- Satellite orbit propagation,
- L-band brightness temperature generation relevant to input geophysical parameters starting from available emission models,
- Accurate instrument modeling,
- Internal calibration by noise injection,
- Image reconstruction algorithm,
- Graphical output projections, and
- System performance evaluation.

Figure 4.1 describes the block diagram of the simulator, stressing which are the products and the variables at each level of the simulation chain.

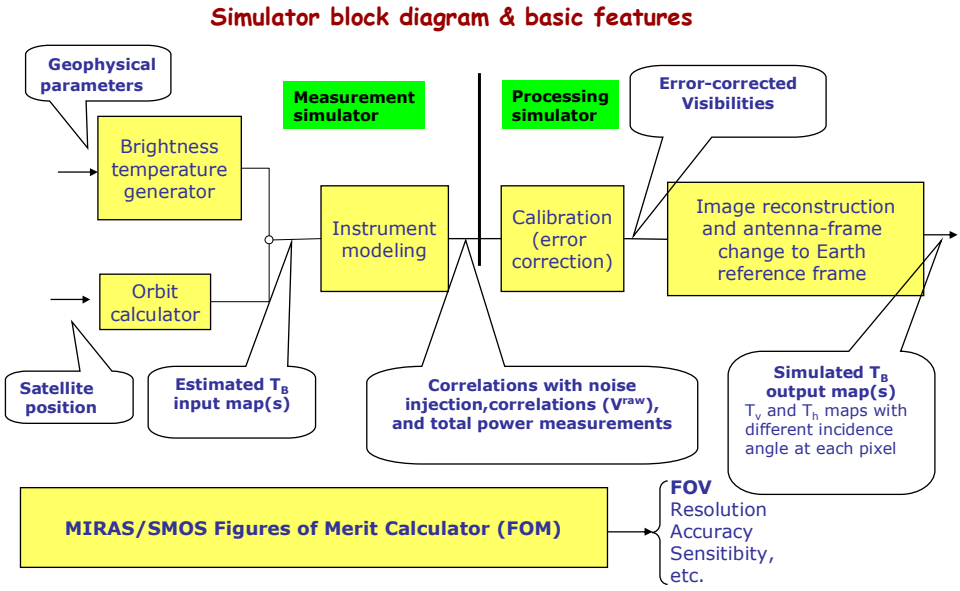

Fig. 4.1 SEPS block diagram highlighting the variables obtained at each step.

The brightness temperature generator computes vertical and horizontal T_Bs by using the expressions available in [Ulaby et al., 1982], and taking into account, for what concerns the sea surface, the following geophysical parameters: ocean salinity, zonal and meridional winds over the oceans, sea surface temperature and ice cover.

Most of these parameters have been extracted from a NASA data set [Meeson et al., 1995; Sellers et al., 1995], mapped with a spatial resolution of 1°x1°, larger than the instrument pixel over Earth's surface. To overcome this problem the resulting brightness temperature pixels are bilinearly interpolated to a thinner 1/12°x1/12° (5 minutes) grid and masked by the NOAA ETOPO5 resolution global digital elevation model [NOAA ETOPO5]. This technique preserves the high-frequency contents given by the coastline.

Recent upgrades not included in the last official release of SEPS are relevant to high resolution data ingestion on specific land or ocean zones [Talone et al., 2007b, Sabia et al., 2007a], and improved image reconstruction algorithm [Camps et al., 2008].

The atmosphere signals (upwelling, downwelling and attenuation) are computed using a first order approximation of Liebe's model for a standard atmosphere, including rain intensity and water vapor concentration maps [Liebe, 1989].

4.1.2 Simulator Panels Description

The following (Fig. 4.2) is the main panel of the SEPS v 4.0 simulator.

Fig. 4.2 SEPS v4.0 main panel.

In the *Scenario management* section, the *Automatic scenario* option allows defining several features of a new simulation. The objective of this functionality is to select a specific geographic zone in which performing the simulation with the corresponding overpassing. This panel appears as in Fig. 4.3.

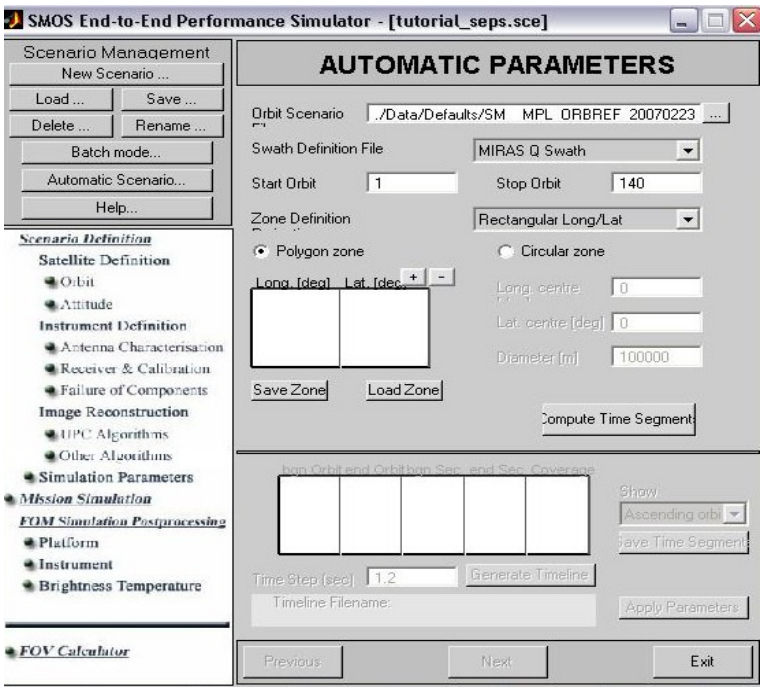

Fig. 4.3 Pre-simulation scenario parameters definition.

The SMOS established orbit is set by default. The simulation can be run choosing in *Swath definition file* among *Nadir, MIRAS-P* and *MIRAS-Q* according to the desired intersection between the sub-satellite point and the geographic zone (see [SEPS simulator], user manual).

Once the orbits are defined (as a reference it can be considered 14 orbits/day and thus 432 orbits/month), the geographic zone can be selected in rectangular boxes providing latitude/longitude coordinates or in azimuth by providing a diameter from a specific point.

The objective of these settings is to calculate the time segments in which the intersection between SMOS and the chosen zone would occur. Subsequently, the corresponding time segments will be detailed, distinguishing between the ascending and descending orbits (Fig. 4.4).

Once the temporal separation among the different snapshots is set (2.4 seconds is the nominal, being 1.2 seconds for each polarization in dual-polarimetric mode), a whole timeline is generated. The orbital and geographical customized simulation parameters are now defined and applied.

The simulator embodies in the *Scenario definition* several other options to be customized according to the purposes of the user; namely, apart from orbital settings, the user can manage

the instrument characteristics, both related to the antennas (array configuration and pattern features) and to the receivers (Fig. 4.5), indicating in particular important features as the calibration settings [Torres et al., 1996; Camps et al., 1999] and the integration time.

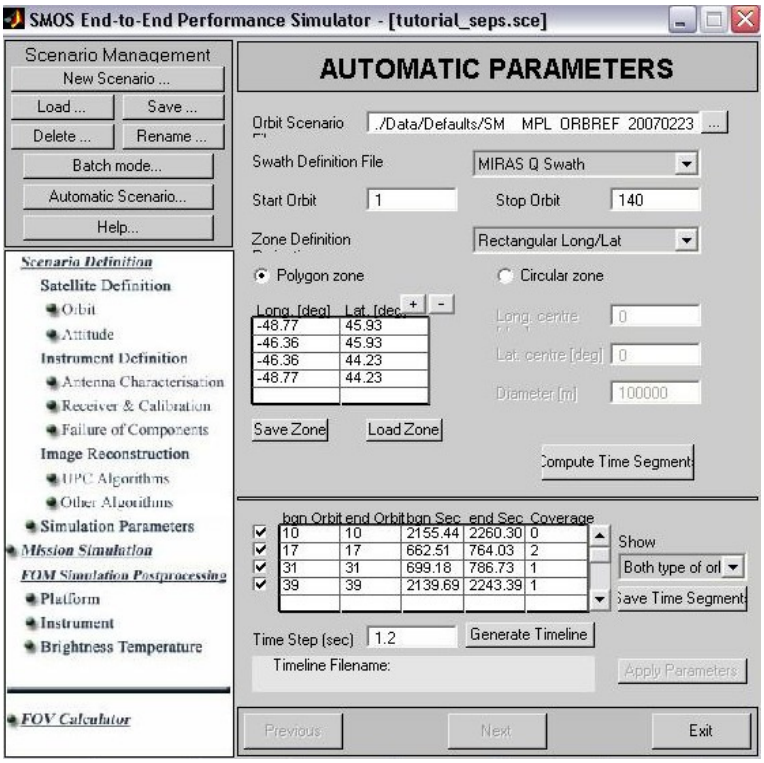

Fig. 4.4 Time segments calculations in the simulation parameters definition.

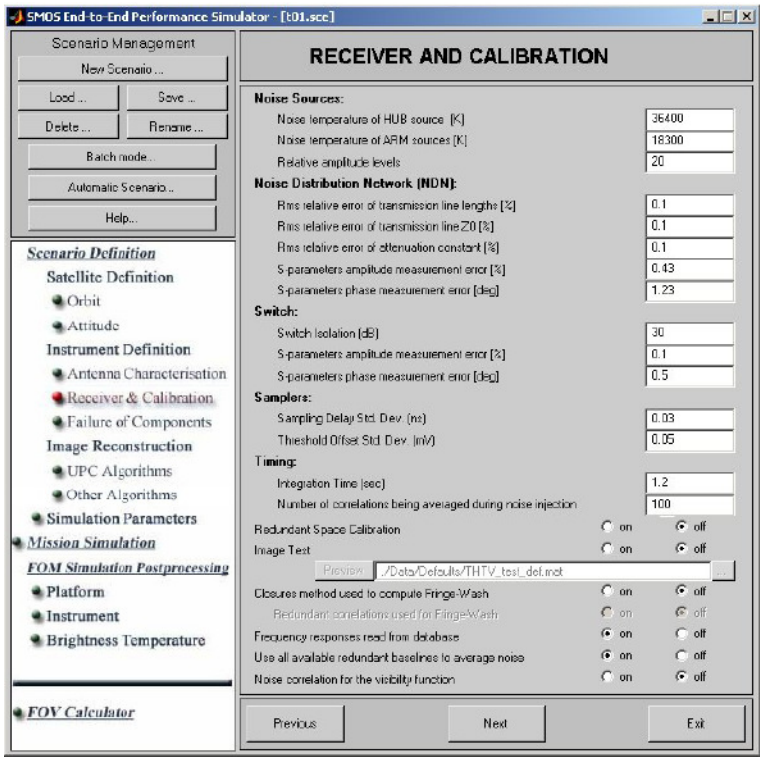

Fig. 4.5 *Receiver and calibration* interface under *Instrument Definition* settings.

Furthermore, the possible failure of components can be monitored in a specific interface of the *Instrument definition* (Fig. 4.6).

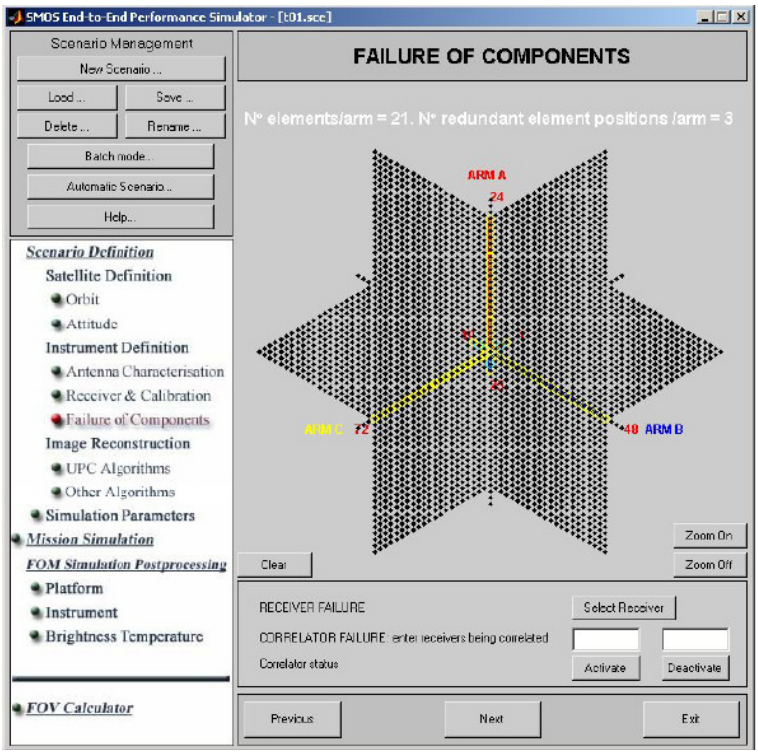

Fig. 4.6 Default appearance of the *Failure of components* interface.

As said, once the visibilities have been estimated and the calibration has been carried out, the brightness temperatures are derived by a complex image reconstruction process [Camps et al., 1998; Camps et al., 2006; Anterrieu et al., 2007; Camps et al., 2008]. In the simulator, the UPC algorithm is used, whose approach has been progressively upgraded in the different versions of the software.

The subsequent modules and options are within the *Simulation parameters* module, which allows further settings of the simulation. The polarimetric mode can be chosen, and the user can decide if taking into account or not the Sun and Moon effects, besides the modeling of the antenna back lobes (Fig. 4.7).

In the sub-module *Modes and timeline* (Fig. 4.8) it is possible to activate the so-called SEPS-light mode, which has some simplifications in the brightness temperature reconstruction (no antenna errors, no fringe-washing errors), but has an enhanced processing speed and allows dramatic improvements in term of CPU time. It has been implemented in order to provide a considerable amount of simulated Level 1C data for the retrieval studies with a shorter computation time, even if less accurate.

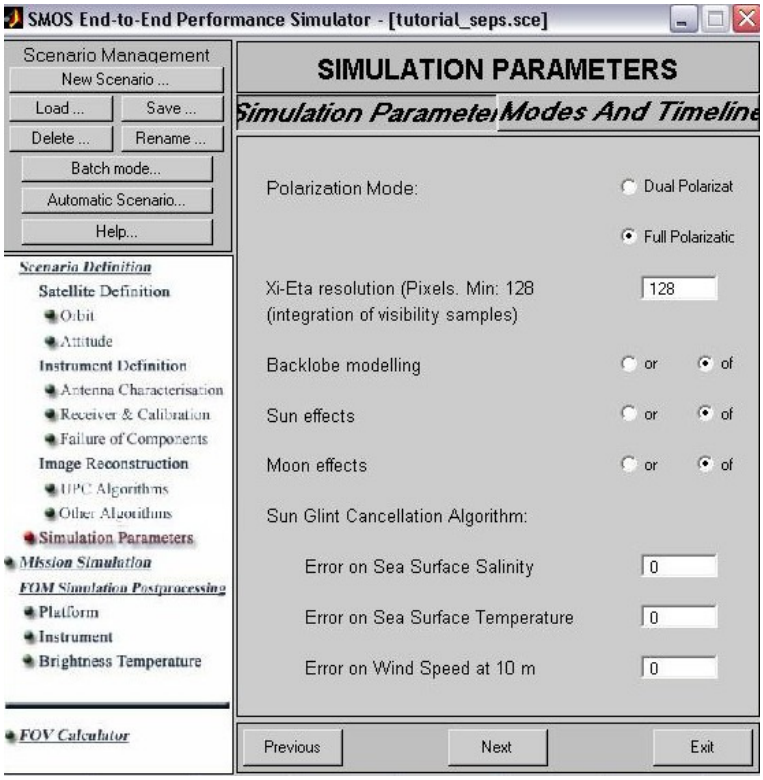

Fig. 4.7 *Simulation parameters* settings.

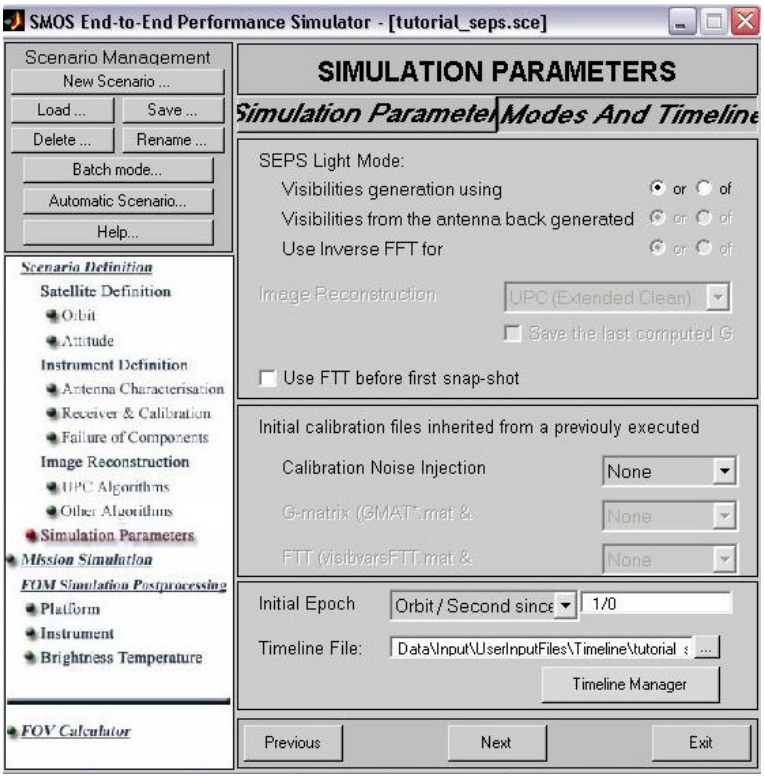

Fig. 4.8 *Modes and timeline* interface with the SEPS-light mode activated.

In the *Timeline manager* sub-section the timeline that will be executed is displayed (Fig. 4.9), and it indicates the selected overpasses, the chosen time step and the number of snapshots

(events) that will be run. A calibration as first event is needed, so it has to be inserted and ticked by the user.

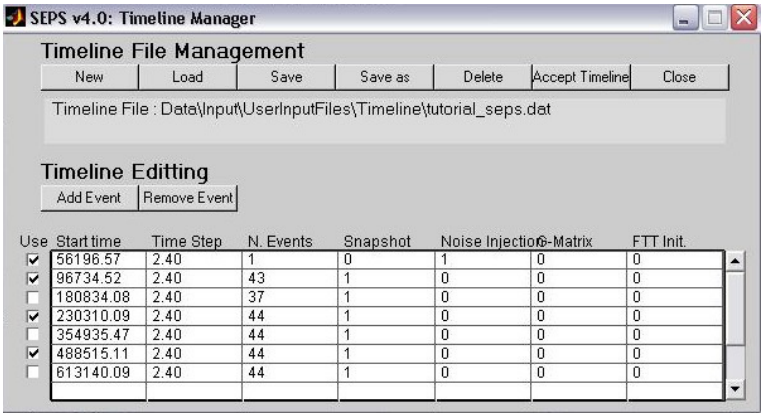

Fig. 4.9 Timeline manager checklist.

The simulation of the defined timeline can then be launched. In the corresponding *Mission simulation* interface, it is possible to establish the resolution cell and project the results in the official ISEA4H9 grid (Icosahedron Snyder Equal Area hexagonal grid of aperture 4 and resolution 9) [Snyder, 1992; Suess et al., 2004], as well (Fig. 4.10).

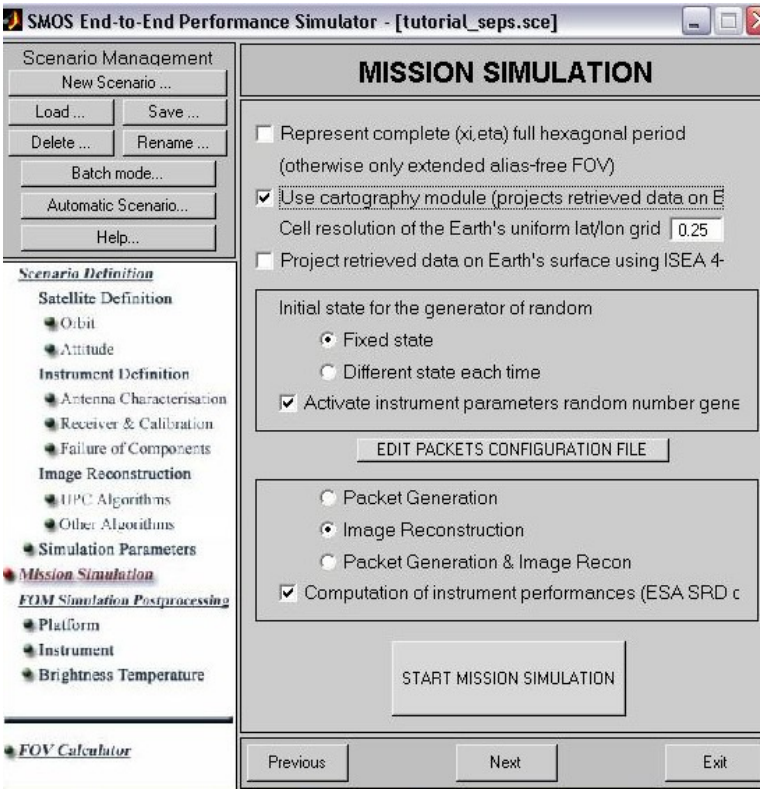

Fig. 4.10 *Mission simulation* panel where the simulation is started.

The simulator includes several post-processing analyses, concerning the platform, the instrument, and more importantly the brightness temperatures images. Figure 4.11 shows an example of the projected sub-satellite point in the simulation.

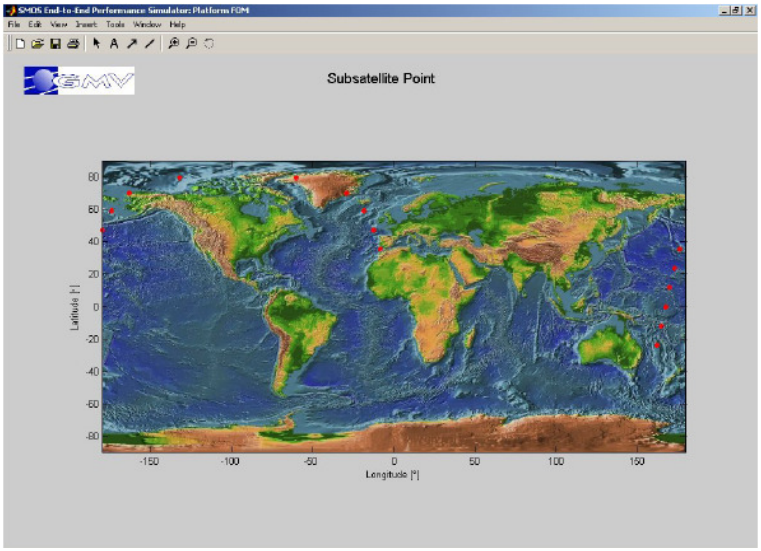

Fig. 4.11 Sub-satellite point (red dots) evolution plot.

With respect to the T_B maps module, it is possible to choose among different options (the reference frame) and projections (cartographic or director cosines). Figure 4.12 illustrates the different cartographic projections onto which brightness temperatures can be plotted.

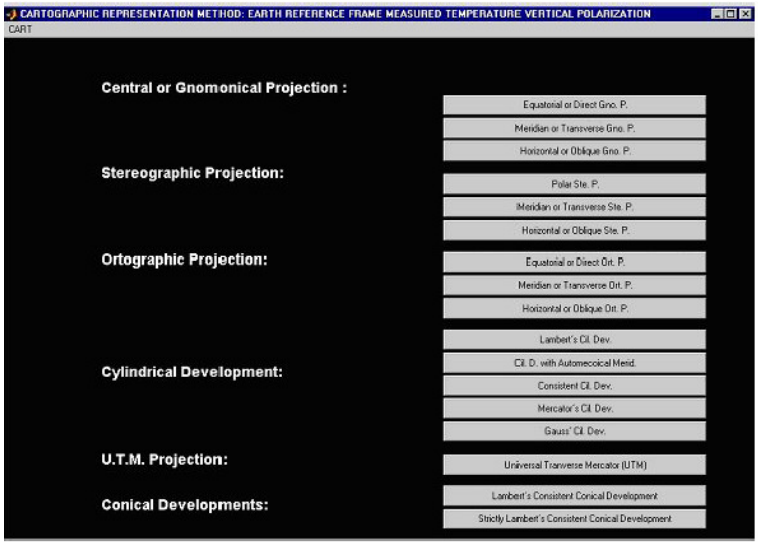

Fig. 4.12 Cartographic projections and developments available.

Figure 4.13 shows a multi-snapshot sample of antenna T_B over an Atlantic zone.

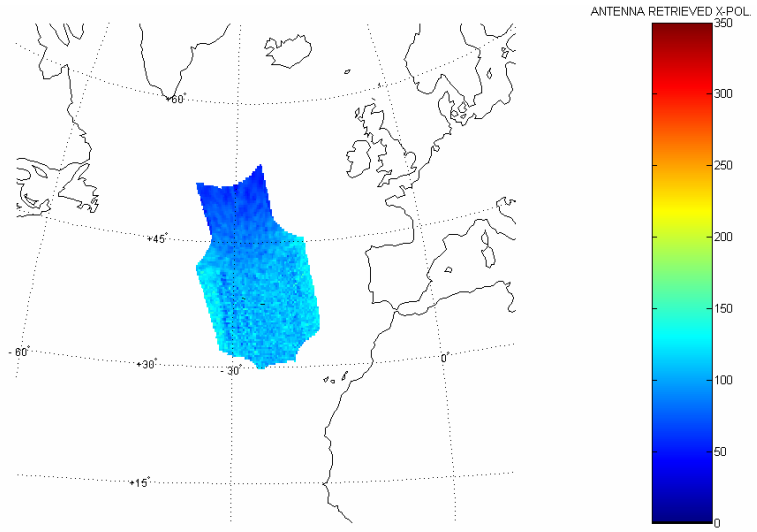

Fig. 4.13 Sample brightness temperatures in the antenna reference frame in several snapshots.

An interesting visual feature of the simulator is the capability of representing different parameters referred to the same field of view, ranging from the incidence angle or the Faraday rotation values, to the $T_B s$ in their corresponding reference frames or at different level. Figure 4.14 represents this feature.

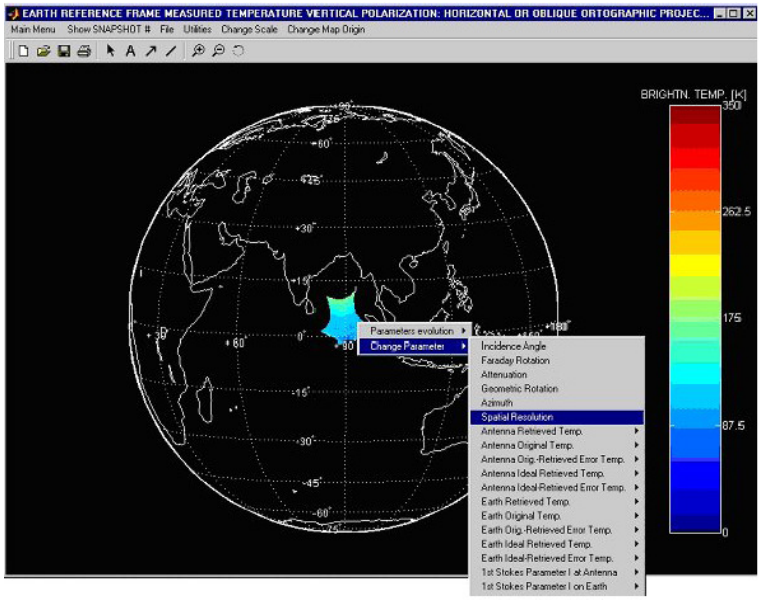

Fig. 4.14 Different available data type to be projected over the map.

Finally, a FOV calculator module allows the computation of different quantities (Fig. 4.15), such as spatial resolution, radiometric sensitivity, field of view over the Earth surface or in direction cosines, and geometrical items like incidence angle or pixel elongation (Fig. 4.16).

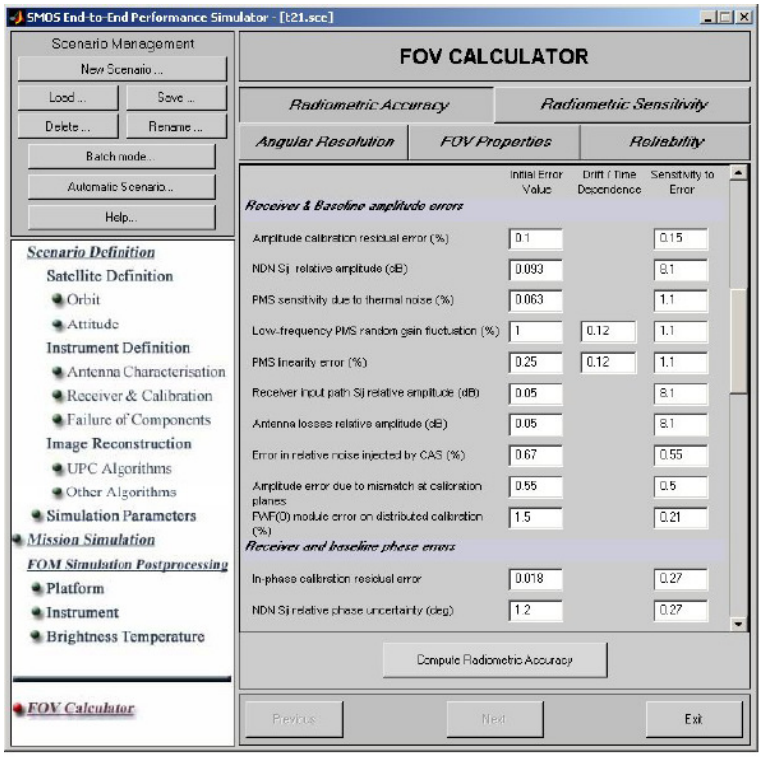

Fig. 4.15 Quantitative representation of the different radiometric and geometric parameters.

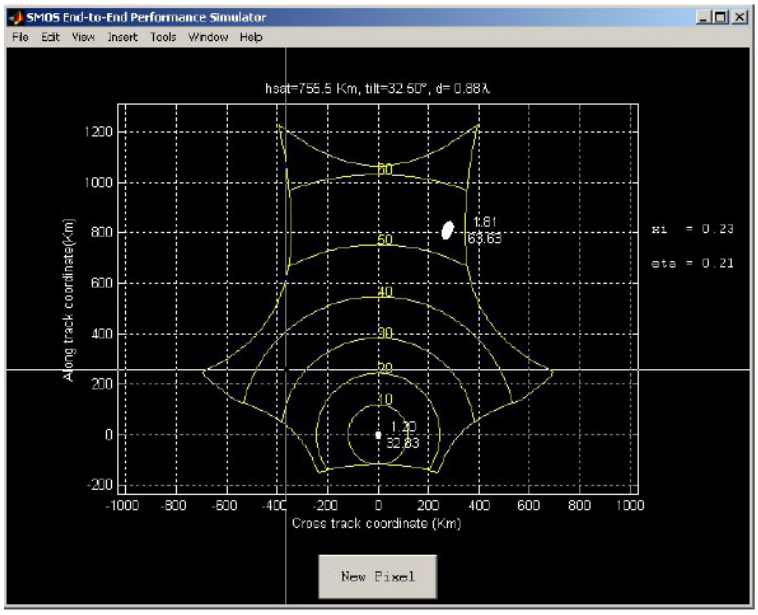

Fig. 4.16 Angular resolution and pixel different shapes projected over the field of view.

Summarizing, SEPS has been used in the technical design trade-off of the instrument and to generate a large number of instrument-like data to be used by the SMOS community for the multi-angular retrieval algorithms. Relying on this simulator, it is possible to shift to the retrieval procedure in the so-called Level 2 processor.

4.2 Level 2 Processing Tool

The Level 2 processor is a software package developed at UPC, and it is used to manage the different sub-modules of the salinity retrieval scheme in order to infer the geophysical parameter of interest. It is used in cascade with SEPS simulator and yields *SSS* maps out of the brightness temperatures once the whole minimization procedure has been applied. Figure 4.17 presents the main panel of this salinity processor.

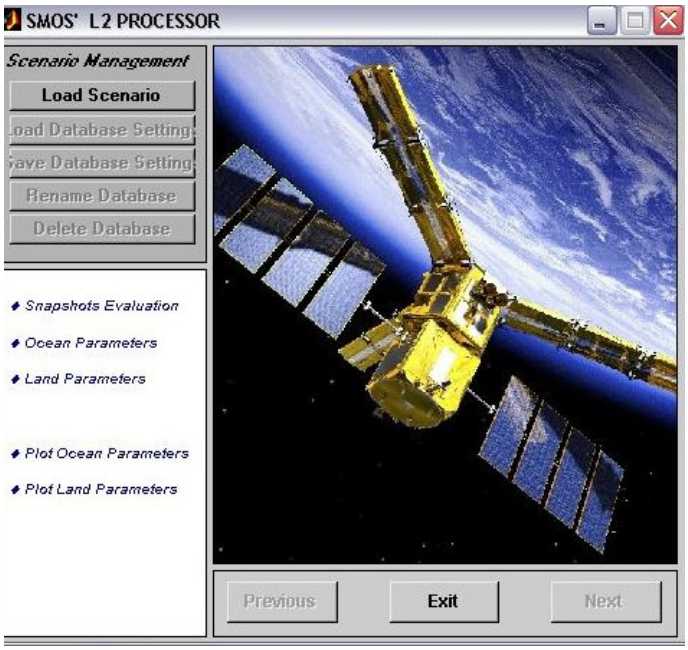

Fig. 4.17 Level 2 processor main panel.

In order to ease the data handling, the Level 2 processor specific approach deals with retrieval in separated boxes of a certain dimension. Thus, height and width of the geographic zone has to be provided. In the advanced setting panel several options to tailor the inversion scheme to retrieve *SSS* in different configurations can be chosen. Firstly, it is possible to define which geophysical parameters retrieve simultaneously. Moreover, the processor allows performing retrieval in the antenna reference frame (*Tx/Ty)*, in the Earth reference frame (*Th/Tv)*, or using the first Stokes parameter (*I*). Figure 4.18 shows the corresponding panel.

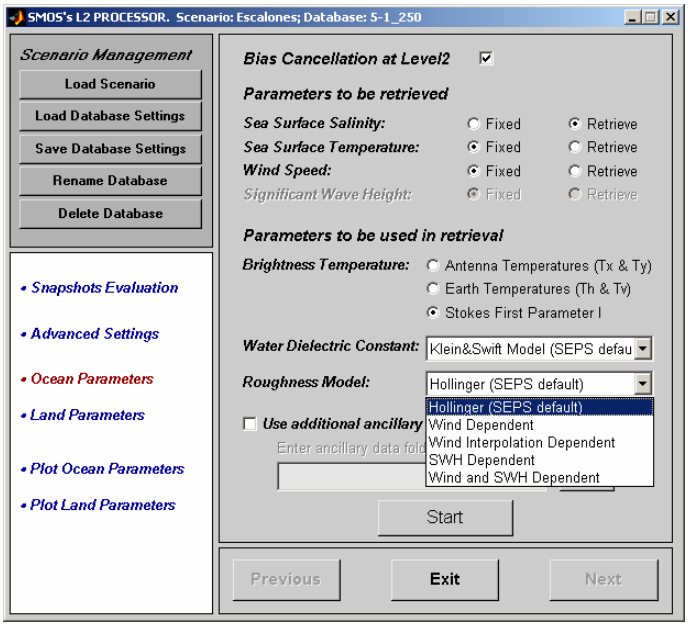

Fig. 4.18 Level 2 processor retrieval options.

Besides, with the latest version it is possible to choose among three dielectric constant models and among several semi-empirical models to perform the inversion. Full flexibility is provided at this stage concerning the selection of the dielectric model or the roughness models, and several other models existing in literature could be easily added. As said, the choice of an adequate and robust forward model, and its related permittivity model, can noticeably influence the accuracy and the results of the retrieval procedure.

Plugging of additional auxiliary parameters is permitted as well. Moreover, L2 processor is in charge of performing bias mitigation/cancellation at brightness temperature level, as coming from SEPS outputs. This external calibration is needed to compensate for brightness temperature biases that arise from the complexity of the payload and of the image reconstruction procedure [Camps et al., 2005c]. Furthermore, as it will be discussed later, the latest version of the ocean salinity Level 2 Processor includes an ARGO buoys krigging data module to cancel residual biases through an average salinity offset correction n [Talone et al., 2007a].

Figure 4.19 represents an example of a salinity retrieval error at Level 2, that is, after a single satellite overpass. Finally, Fig. 4.20 summarizes the main features of the overall SEPS/L2P simulation/retrieval scheme.

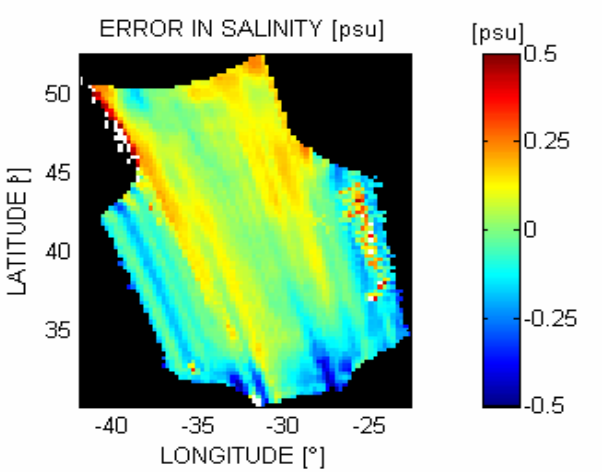

Fig. 4.19 Salinity retrieval error map test using L2 processor.

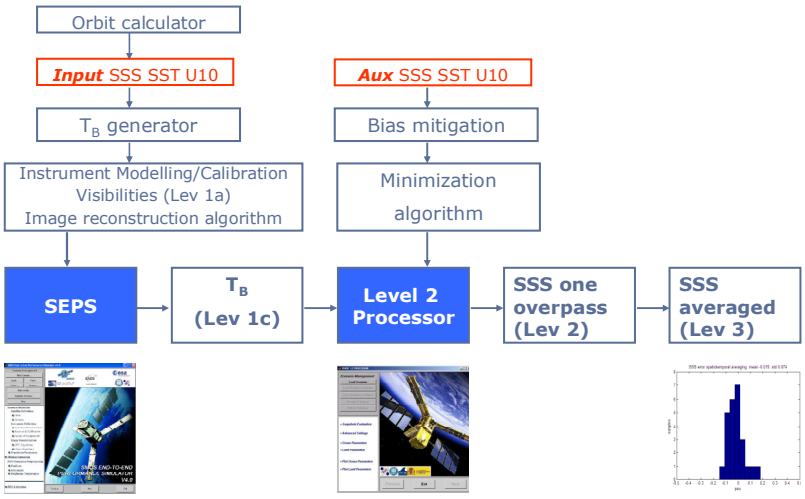

Fig. 4.20 Architecture of the simulation-retrieval cascade performed by means of SEPS/L2p chain.

4.3 Conclusions

In this chapter, the software tools used to simulate the satellite data and retrieve the ocean salinity have been described.

SEPS takes into account the specific features of the instrument, and the related fundamental limitations, such as the poor radiometric sensitivity and accuracy in a single snapshot, the large error near the AF-FOV border and the error amplification and singularities in the translation to pixel reference frame. Brightness temperatures maps generated by SEPS will thus have the realistic bias as induced by the image reconstruction algorithm and the pixel-dependent radiometric accuracy.

The Level 2 processor, in turn, has been developed with the aim of generating routinely salinity retrieval error maps. Such a processor is plugged in cascade with the output brightness

temperature coming from SEPS, and is suitable to be post-processed to get the L3 data that will be the final product analyzed.

The systematic exploitation of the Level 2 processor in conjunction with SEPS will give insights in the study of an optimal SSS retrieval configuration for SMOS and future improvements over current algorithms.

In the next chapters, the attention will be drawn to specific retrieval studies concerning the auxiliary parameters impact on the *SSS* retrieval, and the attempt of establishing an overall *SSS* error budget, quantifying the impact of all the parameters belonging to the inversion procedure.

Chapter 5
Auxiliary Data Impact

The previous chapters were devoted to the overall description of the major issues and concepts related to the SMOS mission; among them, the basic radiometry principles, the need for satellite salinity measurements, and the salinity retrieval statement of the problem. Besides, the simulation and processing software tools available were briefly described.

From this chapter onwards, the research activities pursued in this Ph.D. Thesis are detailed, focusing on some specific issues mentioned in the salinity retrieval chapter. The overall approach is to provide insights on aspects such as auxiliary data impact on *SSS* error or, in a wider context, the definition of a retrieved salinity error budget.

Namely, this chapter deals with the impact on the salinity accuracy of several sources of auxiliary winds and *SSTs* data, stressing two major problems such as the noticeable degradation of the error related to the lack of knowledge of synchronized auxiliary information and the consequences of inaccurate forward modeling in the signal emission parameterization.

In other words, this study, performed within the frame of the ESA's project "Synergetic Aspects and Auxiliary Data Concepts for Sea Surface Salinity Measurements from Space" (hereafter *SynAux*) leaded by the French institute IFREMER, meant to approach a quasi-realistic after-launch salinity retrieval setup. An estimation of the different auxiliary parameters influence has been performed, in order to quantitatively predict to what extent is reasonable to expect to retrieve salinity, once the brightness temperatures will be directly measured by the sensor and no longer generated via simulations. Statistical distributions of the spatio-temporal averaged errors are provided.

5.1 Auxiliary Data Impact Study

Towards the definition of a consolidated retrieved *SSS* product, preliminary assessments should consider the respective quality of Sea Surface Temperature (*SST*) and wind speed (U_{10}) as auxiliary data products, since uncertainties in such auxiliary parameters may themselves induce errors in the retrieval procedure.

The work hereby concerns the analysis of the retrieved *SSS* accuracy linked to the use of the different auxiliary data assimilated into the inversion minimization procedure, underlying the statistical distribution of the error. Several sets of multi-source auxiliary data in a representative mid-Atlantic test zone of 10° of width (defined by longitude 35°W-25°W and latitude 40°N-

50°N) were collected for this purpose on the Level 1C data grid for a complete month of simulated satellite acquisitions.

Level 2 *SSS* products are delivered at each Level 1C grid node, and the impact analysis is then performed by comparing retrieval accuracies at Level 3 relevant to the different auxiliary parameters involved. The retrieval is performed considering several couples of combinations of the auxiliary data available, in order to stress either the *SST* or the U_{10} dependence on salinity retrieval.

The study is performed upon the whole month of the simulated data, in order to infer some statistical information both with respect to the temporal distribution of the errors, and evaluating the spatial variability of the retrieved salinity. Monte Carlo simulations have been performed to estimate some optimum weights to be used in the spatio-temporal averaging procedure.

The work logic is organized as follows. In a first part, the retrieval setup is described, including the auxiliary data sets used, the direct modeling as well as the inversion methodologies. In a second part, the results for the simulations are presented, before splitting the problem in order to distinguish among the different sources of the final salinity error.

5.2 Simulation and Retrieval Strategy

As said, mission requirements for a 2°x2° spatial resolution box after averaging in a 10-day period or for a 1°x1° box after averaging in a 30-day period, are specified by the GODAE committee as a challenging 0.1 psu accuracy [Smith and Lefèbvre, 1997].

In order to evaluate the impact on the retrieved *SSS* of different auxiliary data, a representative mid-Atlantic test zone (Longitude 35° W - 25° W, Latitude 40° N - 50° N) was chosen (Fig. 5.1). In this area there is a small salinity gradient, associated to a strong wind variability, whose effect on the retrieved *SSS* was the main issue under study.

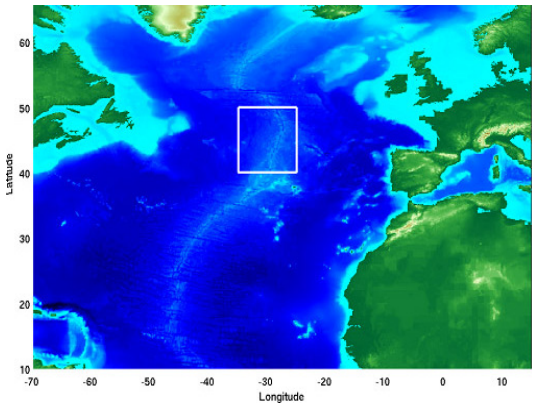

Fig. 5.1 Mid-Atlantic test zone of 10° width (Longitude 35° W - 25° W, Latitude 40° N - 50° N).

5.2.1 Auxiliary Data Set Description

After an in-depth study in other workpackages of the project, the selected auxiliary multi-source data were the following [Reul et al., 2004; Soulat et al., 2004a]:

- **Blended QuikSCAT/NCEP** (National Centre for Environmental Predictions) wind product,
- **ECMWF** (European Centre for Medium-range Weather Forecast) wind product, and
- MWF (Mean Wind Field) **QuikSCAT** satellite wind product,

used as sea surface roughness information (considered as the primary sea state descriptor);

- Météo-France **CMS** (Centre de Météorologie Spatiale) *SST* product, and
- NCEP **Reynolds** *SST* product,

besides the

- **WOA** (World Ocean Atlas) 2001 climatologic *SSS* field.

The auxiliary blended QuikSCAT/NCEP wind product would be a suitable auxiliary wind parameter for SMOS since it combines weather centre products (always available four times a day and close in time to SMOS measurements), with satellite scatterometer data, which inject into the auxiliary product the high-wavenumber scales wind energy missing in the numerical model product. To analyze the impact of comparing such consolidated product to either numerical weather product alone or scatterometer data alone, the ECMWF product and the daily mean wind field QuikSCAT product were provided as additional wind auxiliary data.
Sample of Blended QuikSCAT/NCEP ocean wind is shown in Fig. 5.2 for the selected zone of interest, while Figs. 5.3 and 5.4 show samples of the ECMWF wind and the QuikSCAT wind for the same zone and the same day.

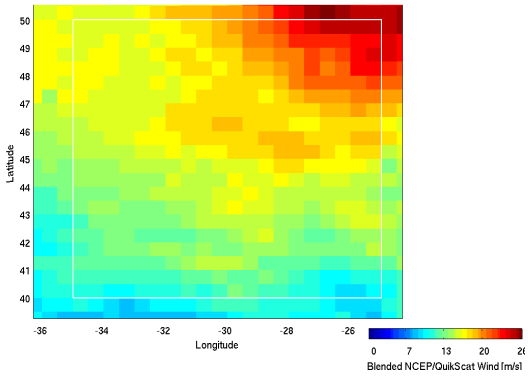

Fig. 5.2 Blended QuikSCAT/NCEP wind fields for the 6th of January 2003.

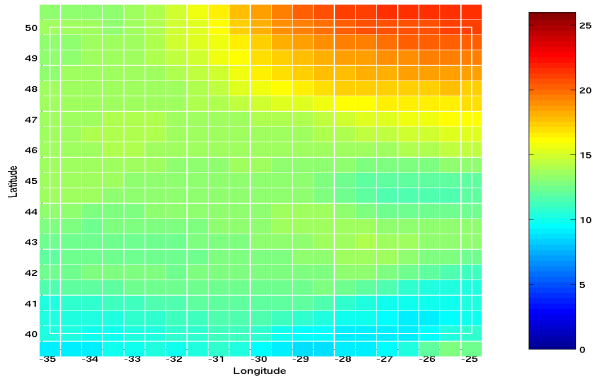

Fig. 5.3 ECMWF wind field for the 6th of January 2003.

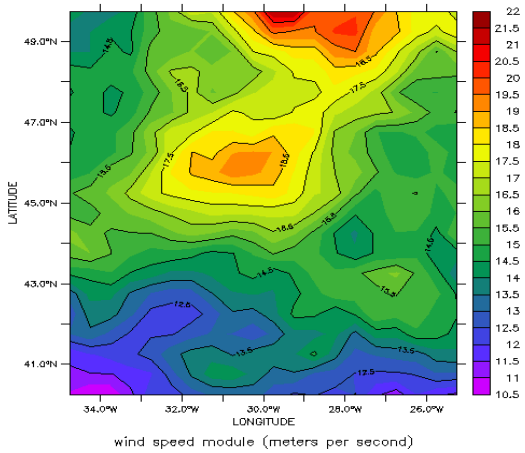

Fig. 5.4 QuickSCAT mean wind field (MWF) product for the 6th of January 2003.

The use of the analyzed and consolidated GHRSST-PP (Global High Resolution Sea Surface Temperature - Pilot Project) type of *SST* data was recommended for the SMOS Level 2 processor [Reul et al., 2004]. However, such data were not yet available operationally. Consequently, the analyzed CMS *SST* product from SAF/OSI (Satellite Application Facility - Ocean and Sea Ice) was provided, since it exhibits strong similarities with the future analyzed GHRSST-PP product.

An example of this product is shown in Fig. 5.5a, left plot. An additional and more traditional *SST* product, the weekly NCEP Reynolds Optimally Interpolated SSTs, was furnished for comparison. The analysis uses both in-situ SSTs and satellite derived SSTs from the NOAA Advanced Very High Resolution Radiometer (AVHRR). The analyzed product for the first week of January is shown in Fig. 5.5b.

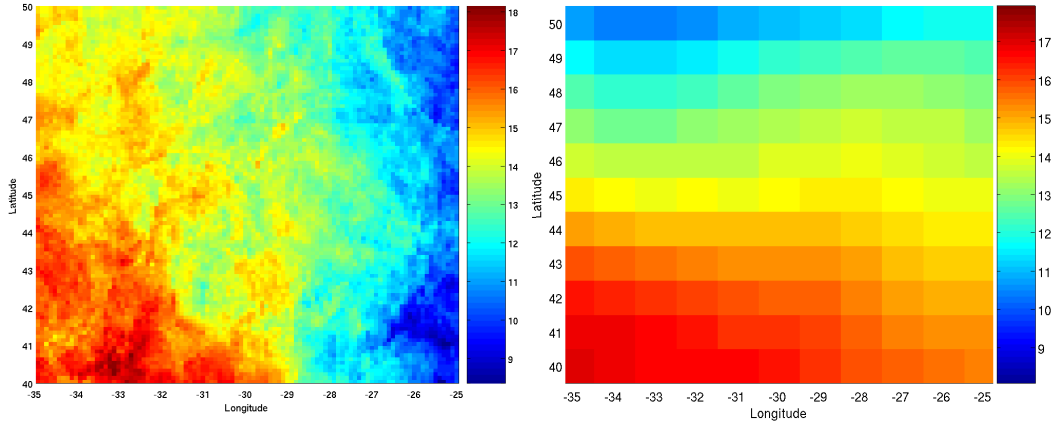

Fig. 5.5 a) SAF/OSI CMS analyzed *SST* product in the selected Mid-Atlantic ocean zone for the 6th of January (in °C). b) Reynolds *SST* for the first week of January.

Finally, the World Ocean Atlas 2001 monthly climatology *SSS* field (Fig. 5.6) was used as salinity input in the selected area. Such field exhibits very little variations (standard deviation of the order 0.2 psu) with a mean value of 35.7 psu; this shall help identifying the impact of only auxiliary *SST* and wind data on the retrieval accuracy.

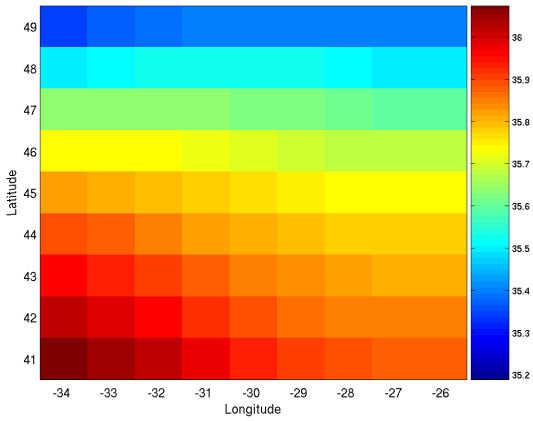

Fig. 5.6 World Ocean Atlas 2001 *SSS* January climatology within the 10° width test zone in the mid-Atlantic Ocean.

Figure 5.7 depicts auxiliary wind products histograms for blended, numerical and satellite-derived wind fields in the selected Mid-Atlantic ocean zone. Table 5.1 sketches how wind fields present different mean values (their histograms being somewhat shifted among each other), with large standard deviations. Both characteristics will affect the retrieved *SSS* accuracy, as will be discussed in the following sections [*SynAux* Report, 2006, WP 1400].

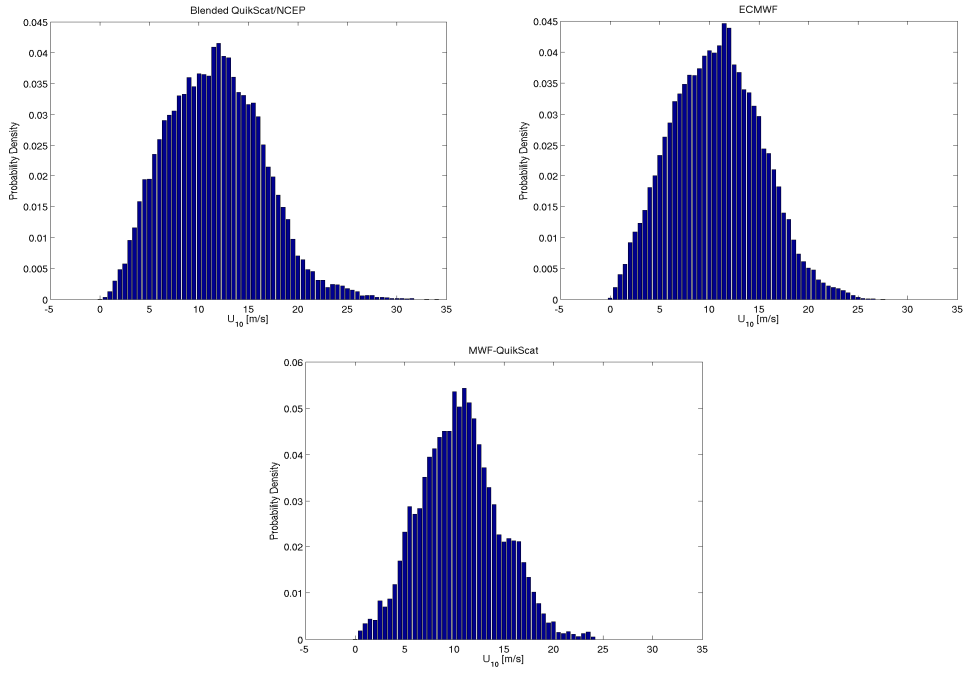

Fig. 5.7 a) Blended wind histogram, b) ECMWF wind histogram, and c) QuikSCAT wind histogram.

Table 5.1 Auxiliary Data Statistics.

Wind Product	Mean Value	Standard Deviation
Blended QuikSCAT/NCEP	11.63 m/s	4.79 m/s
ECMWF	10.70 m/s	4.50 m/s
MWF QuikSCAT	10.57 m/s	4.01 m/s
CMS analyzed	13.50 °C	1.68 °C
Reynolds	13.70 °C	1.69 °C
WOA 2001 *SSS*	35.68 psu	0.22 psu

5.2.2 Generated Brightness Temperature and Auxiliary Data Features

Simulated daily brightness temperatures were generated by IFREMER (Institut Français de Recherche pour l'Exploitation de la Mer) corresponding to the whole month of January 2003, each time the SMOS instantaneous field of view intersected the Region Of Interest (ROI). Level 1C (geocoded) simulated T_B*s* were provided for both satellite ascending and descending passes. Each day an average number of about 500 FOVs intercepted the area. This is illustrated in Fig. 5.8.

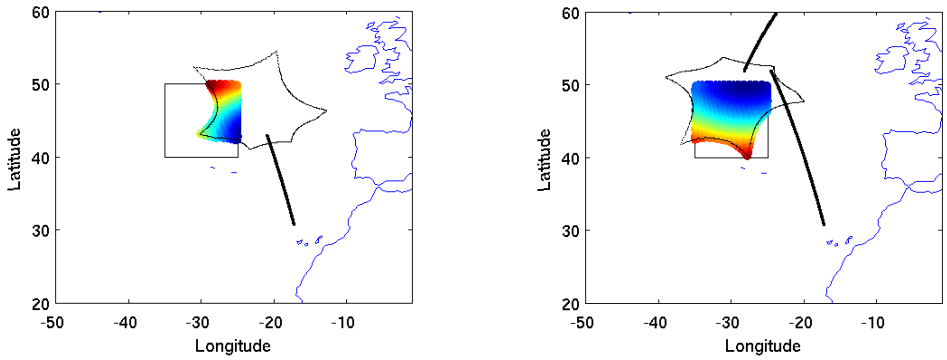

Fig. 5.8 Illustration of the calculated (here T_B in V-pol) SMOS FOV intersections with the Region Of Interest (ROI) for a satellite ascending (left) and descending (right) pass.

Time sampling of data along the orbit was set to the nominal 1.2 seconds step. Each time a FOV crosses the selected zone, the ISEA4H9 grid nodes in the intersection domain were detected, and the auxiliary data closest in time were spatially re-sampled (Fig. 5.9). All auxiliary data sets exhibit a coarser spatial resolution than the ISEA grid, except for the CMS *SST* data. A simple nearest neighbor technique has been used for re-sampling the data.

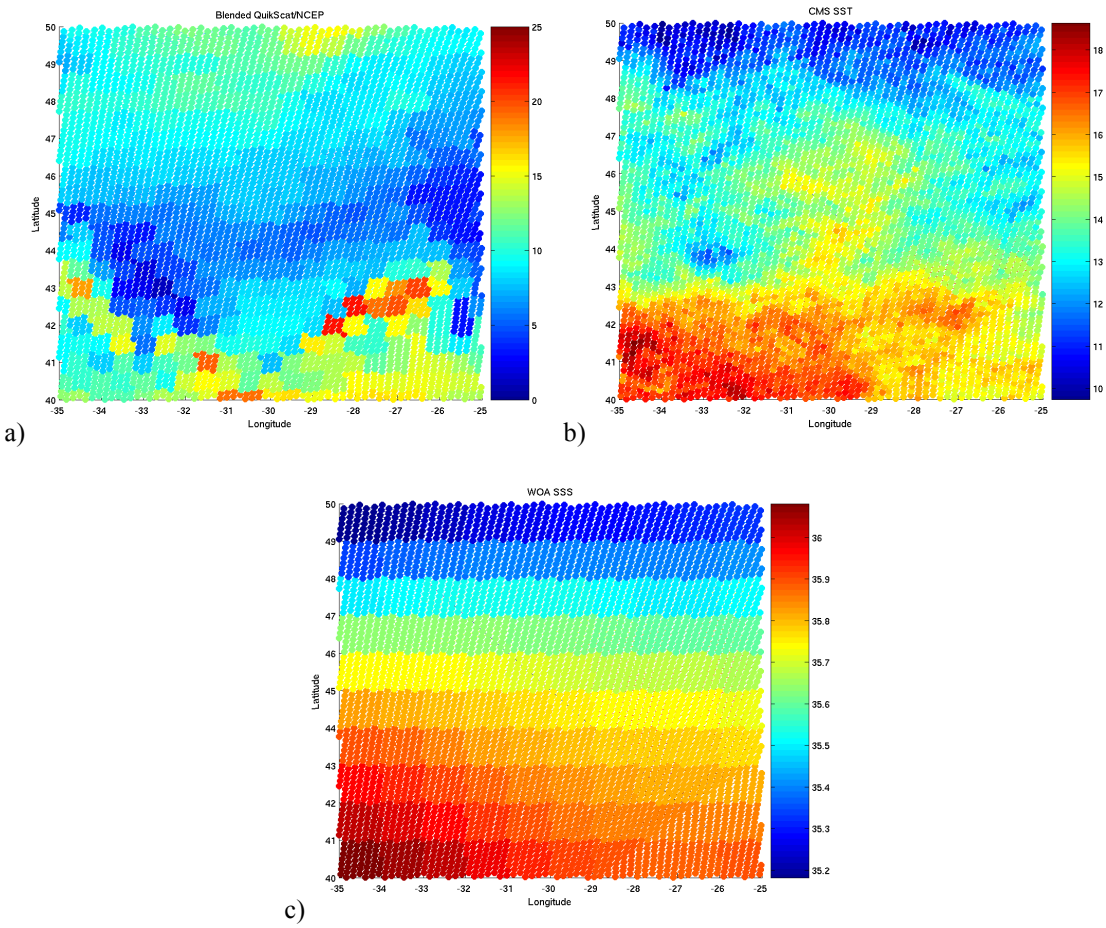

Fig. 5.9 Illustration of the auxiliary data re-sampling procedure on the Level 1C grid for a) blended QSACT/NCEP wind, b) CMS analyzed *SST* and c) WOA *SSS*.

From the SMOS observation geometry (incidence and azimuth angles), and the collected auxiliary data sets, the corresponding brightness temperature fields at H and V polarizations were computed by means of a direct model. These calculations were performed using the aforementioned blended QuikSCAT wind product, together with CMS *SST* and WOA *SSS* climatologic field as geophysical inputs within the Small Scale Approximation (SSA) [Reul and Chapron, 2001] direct model for the effect of sea surface roughness on the L-band emission.

5.2.3 Retrieval Algorithm Features

In this *SSS* retrieval study, several assumptions have been made concerning the sources of geophysical noise. Faraday rotation was considered to be perfectly known, as well as any atmospheric corrections (for a detailed computation of these effects see [Skou and Hoffman-Bang, 2005]), being the estimation of such terms out of the scope of this specific study, which focuses only on the geophysical salinity error. Moreover, a perfectly known sea water dielectric constant model from Klein and Swift [Klein and Swift, 1977] was used both for the direct and the inverse model. In the next chapters, these assumptions will not be considered anymore, and the study will be more realistic.

Retrieved sea surface salinity variability with respect to different auxiliary parameters has been investigated taking into account the particular SMOS configuration, minimizing a cost function as that one described in Eqn. 3.1 by means of the already mentioned Levenberg-Marquardt iterative numerical algorithm with a cubic polynomial line search [Press et al., 1992].

In practice, retrieved *SSS* estimation is not only constrained by the searching ranges, but a variable reference value was provided for each parameter, weighted by the standard deviation (σ_{Aux}) of the corresponding auxiliary field (*SSS*, *SST* and U_{10}).

The main inversion methodology features are the following:

- Multi-parameter retrieval. Sea Surface Salinity, and both reference *SST* and U_{10} are retrieved at once, being adjusted around the reference values to minimize the error.
- Upper and lower boundaries. Physically-based "first guess" searching limits are selected, forcing the solution within the chosen ranges. For instance, salinity must be higher than 0 psu (fresh water) and lower than 40 psu (maximum salinity in open seas).
- *A priori* knowledge of the calculated standard deviation of each auxiliary data set used in the optimization procedure, to nudge the solution once the variability of the auxiliary data is known (Table 5.1). Taking into account that the measurements are neither simultaneous in time, nor collocated in space, the chosen metric has been using the spatial variability of the

wind field, instead of the standard deviation of the error associated to each individual measurement.

- Ten Monte Carlo simulations of each scenario were performed in order to estimate another standard deviation, associated to the retrieval at pixel-level in the swath, to derive some optimum weights ($1/\sigma$) to properly perform the temporal averaging.
- MIRAS operation mode has been both Full-polarimetric and dual-polarimetric; *SSS* retrieval can be performed either in full-pol mode using *Th* and *Tv* or using the first Stokes parameter ($I = Th+Tv=Tx+Ty$) in dual-pol mode to optimize the noise.
- Linear fit to the brightness temperature dependence with wind speed from Hollinger [Hollinger, 1971] is used in the inversion model, unlike the SSA method used to generate the brightness temperatures, to stress the fact that the geophysical function will never be perfectly known.

Even if reasonably similar, the brightness temperature sensitivity to wind speed computed with the SSA method and from the linear fit to Hollinger measurements, still present some discrepancies [Reul and Chapron, 2001; *SynAux* Report, 2006, WP 1400] (Fig. 5.10). As it will be seen in the following sections, this imperfect knowledge of the geophysical model function will introduce a bias and errors in the retrieved *SSS*.

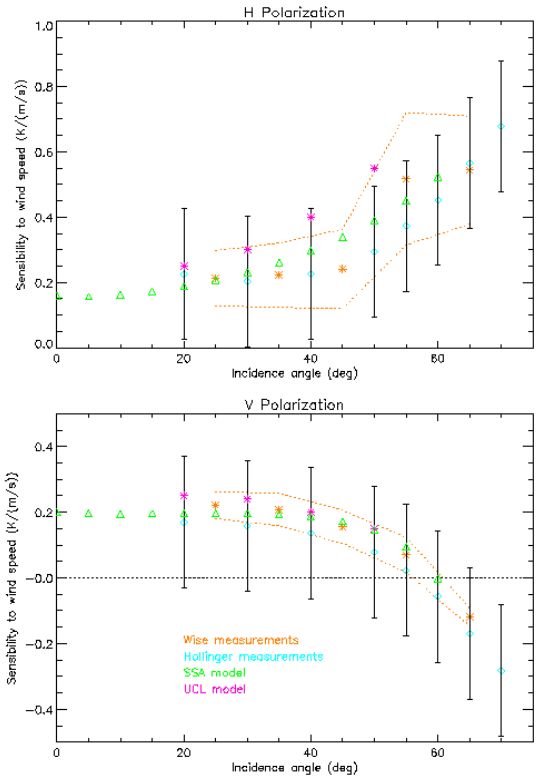

Fig. 5.10 Sensitivity to wind speed provided by model and measurements (Green: SSA model; Cyan: Hollinger model) for a) horizontal polarization and b) vertical polarization [Reul and Chapron, 2001; *SynAux* Report, 2006, WP 1400].

The whole month of simulated T_Bs was analyzed using different combinations of auxiliary data to stress the impact on the retrieved salinity of the different geophysical inputs. The differences with respect to *SST* or U_{10} are then evaluated.

An assessed retrieval configuration has been achieved in two subsequent steps:

- The first attempt dealt with the restricted version of the cost function previously described (Eqn. 3.1). Nevertheless, simulations results showed that such restrictions in the cost function were too constraining. The retrieved salinity values had a mean value equal to the mean reference value, and a standard deviation equal to the variability associated to the input *SSS* field, thus jeopardizing the attempt to study the *SSS* sensitivity to the different auxiliary data. Other simulations were performed either enlarging the climatologic *SSS* rms value or adding a fake bias, and confirmed the previous conclusions. The reason for this behavior seems to lie within the fact that the value considered for the restrictions on *SSS* was very small, thus maximizing the *SSS* restriction predominance in the minimization procedure.
- Analyzing such results, a second approach was satisfactorily identified later as a restricted-like algorithm version, in which the *SSS* was left as a free parameter, but still having restrictions on *SST* and U_{10}. Furthermore, simulations have been done as well without any constraint except for the upper and lower boundaries as previously done in [Camps et al., 2003a, Camps et al., 2005c].

5.3 Salinity Retrieval: Single Overpass

IFREMER-simulated brightness temperatures processing has been approached in order to firstly underline the different configurations single-overpass salinity errors maps and then performing a temporal and spatial averaging analysis in the post-processing.

Displayed salinity errors are shown for the processed data sets by means of selected meaningful results on a daily basis as the average of the ten Monte Carlo scenario realizations. Later on, these realizations will be used to calculate weights to properly evaluate the salinity retrieval at pixel level.

As mentioned before, being the climatologic *SSS* field furnished with an rms accuracy of nearly 0.2 psu, the first version of the study (fully-restricted algorithm) behaved in a way that hid the retrieved variation due to different auxiliary data, hampering the planned analysis. The subsequent second approach has been figured out to solve this problem.

In the latter approach, simulations have been performed for four different auxiliary data couples, the two instrument's operation modes (full-pol and dual-pol), and separated satellite passes

(ascending and descending) resulting in sixteen monthly data sets to be processed. Tracks separation was needed: 1) since vertical *SST* gradients may be different at 6 AM and at 6 PM, and 2) to avoid averaging pixels imaged in a different position within the swath in the two satellite passes. Yet, other simulations were carried out without considering any reference values at all, that is, no auxiliary parameters were introduced in the minimization procedure, which converged without any constraints. Four different configurations were identified aiming at stressing firstly the variability with respect to auxiliary wind (blended wind, ECMWF and QuikSCAT) keeping constant *SST*, and secondly with respect to a different *SST* field (Reynolds), assuming the default blended wind.

Meaningful samples results relevant to the new processing chain are shown hereafter. Figure 5.11a shows error maps (difference between retrieved and original salinity) corresponding to different configurations using the first Stokes parameter measured in dual-pol mode for an ascending pass corresponding to January 29th. The satellite's swath is clearly visible, as well as the *SSS* error variability with respect to the different auxiliary data. Figure 5.11b plots the corresponding number of times each pixel is imaged (N_{obs}, described above).

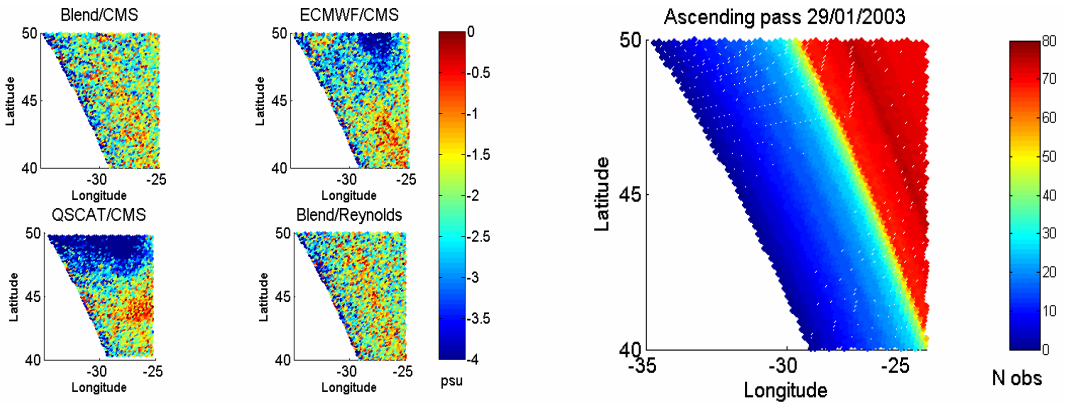

Fig. 5.11 a) Salinity single-overpass error maps for different configurations in dual-pol mode using *I*, and b) number of points used in the retrieval procedure. Both for ascending pass and corresponding to January 29th, 2003.

Figures 5.12a and 5.12b in turn are related to a different day (January 22nd) and to a full-pol mode. Again, *SSS* errors at pixel level are the representative values of single-overpass salinity retrieval. This example was selected to underline how in some days the satellite covered just partially the ROI, with pixels being imaged just very few times. This implied very noisy measurements, leading to the need of a weighted mean to properly perform the temporal averaging.

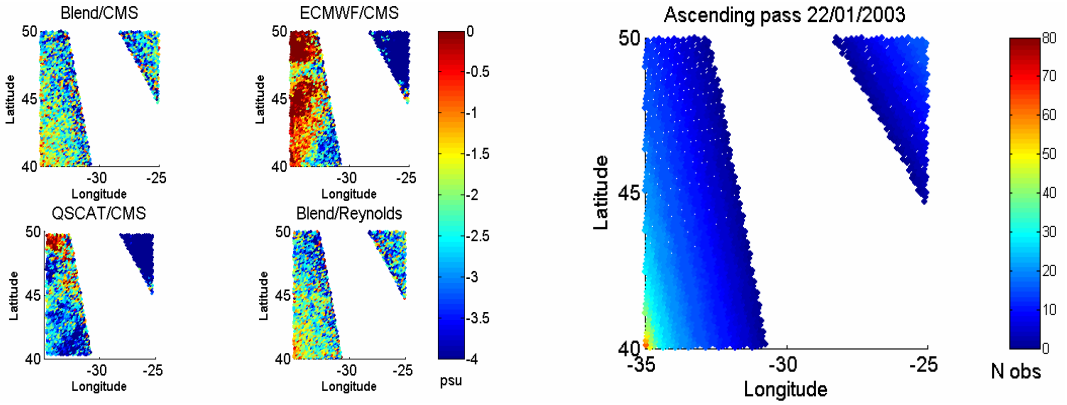

Fig. 5.12 a) Salinity single-overpass error maps for different configurations in full-pol mode using *Th* and *Tv*, and b) number of points used in the retrieval procedure. Both for an ascending pass, corresponding to January 22nd, 2003

Plots relevant to the whole month of data, on a daily-basis, for both passes and instrument modes, are comprehensively listed in Appendix A in [*SynAux* Report, 2006, WP1400].

5.4 Salinity Retrieval: Temporal Averaging

Temporal and spatial averaging with weighted mean along the considered month meant to gather unique values of bias and accuracies for an estimation of the quality of each configuration. Keeping in mind the aim of stressing the variability induced by the different auxiliary parameters, the averaging procedure has been approached as follows. Concerning the temporal averaging, the aforementioned *SSS* errors (single overpass) have been averaged at pixel level along the whole month. However, provided the huge day-to-day variability of these *SSS* errors due to the different pixel positions within the field of view (distance to the satellite's ground-track), a weighted mean was needed.

Such weights were computed as the inverse of the standard deviations of the error calculated from the different realizations of each pixel (ten Monte-Carlo realizations). Thus, each single-pixel retrieval value was used to obtain weights for an adequate evaluation of the monthly error at pixel level. These weights are dependent on the cross-track distance and could be used in the operational processor.

Figure 5.13 is a pictorial representation of such weighting process necessary to perform temporal averaging. Red arrows indicate that weighted mean was conducted along the different daily scenarios, but emphasizing how the same pixel presented noticeable imaging differences throughout the different days and could not be directly averaged along the month.

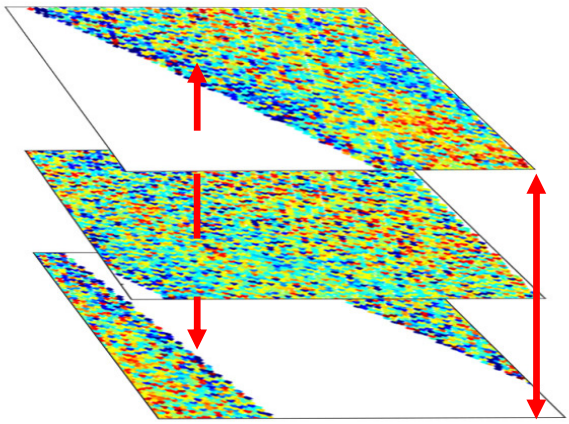

Fig. 5.13 Pictorial view of the pixels imaging differences that led to the weighting process.

Pixels with retrieved *SSS* error farther away than ±2.5 psu from the most probable value were discarded as wrong and not averaged. Afterwards, an overall mean and rms at ROI level allowed computing the expected bias and rms accuracy of each configuration.

Figure 5.14a shows the histogram of the weighted errors within the ROI for the blend/CMS configuration (cfr. auxiliary data listed previously) in the ascending passes. The expected monthly bias and the rms accuracy were underlined, the latter taken as retrieval goodness index in this study. This bias, being quite homogeneous in the whole ROI could be potentially compensated for by means of an external calibration using moored buoys or drifters as proposed in [Camps et al., 2005c; Talone et al., 2007a].

In turn, Fig. 5.14b refers to the same procedure, but relevant to another configuration, that is, using a different wind auxiliary data set, the ECMWF. As it can be seen, this configuration exhibits quite different values from the previous one for the expected bias and the rms accuracy, both the bias and the standard deviation being worse than in the previous configuration. In the final part of the study described in this chapter, the source of such bias will be investigated and analyzed.

It has to be stressed, however, that the blend/CMS configuration represents the ideal case, being the default auxiliary data used in the brightness temperatures generation with the SSA direct model, and all the retrievals obtained using other data combinations are assumed to be worse. On the other hand, one of the goals of the study was to quantitatively check how good this retrieval could be considering that different models to generate and invert the data (more realistic case) are used. Furthermore, taking the default configuration as a baseline, the study focused on the evaluation of the worsening of retrieval accuracy once different auxiliary data set are considered. Addressing *SSS* retrieval using other than default auxiliary data is an attempt to quantify the error accuracy to be realistically expected, at least concerning scene-related issues (apart from other geophysical noise contributions).

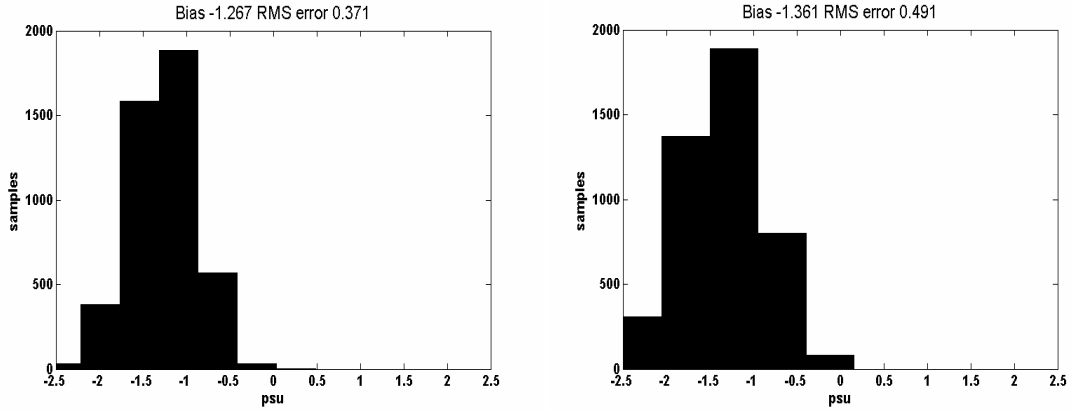

Fig. 5.14 a) Monthly *SSS* weighted errors histogram with ROI bias and rms accuracy referred to blend/CMS configuration in dual-pol mode, and b) Monthly *SSS* weighted errors histogram with ROI bias and *rms* accuracy referred to ECMWF/CMS configuration in dual-pol mode.

5.5 Salinity Retrieval: Spatial Averaging

Once the temporal averaging has been studied for different configurations, a spatial averaging is conducted in 1°x1° and 2°x2° boxes, being identified as suitable spatial resolution. Single-pixel monthly weighted errors coming from temporal processing have been sorted according to their geographic locations within the ROI and then averaged in single boxes.

Figure 5.15a depicts the histogram and the relevant spatio-temporal bias and rms accuracy for a QuikSCAT configuration in dual-pol mode for an ascending pass, while Fig. 5.15b shows a meaningful example relevant to the standard blend/CMS configuration, in a full-pol mode and for a descending pass. Corresponding spatio-temporal retrieved *SSS* accuracy turned out to be one of the best performances in the whole simulation scheme regarding 1°x1° averaging, achieving a value that fulfills the GODAE requirements.

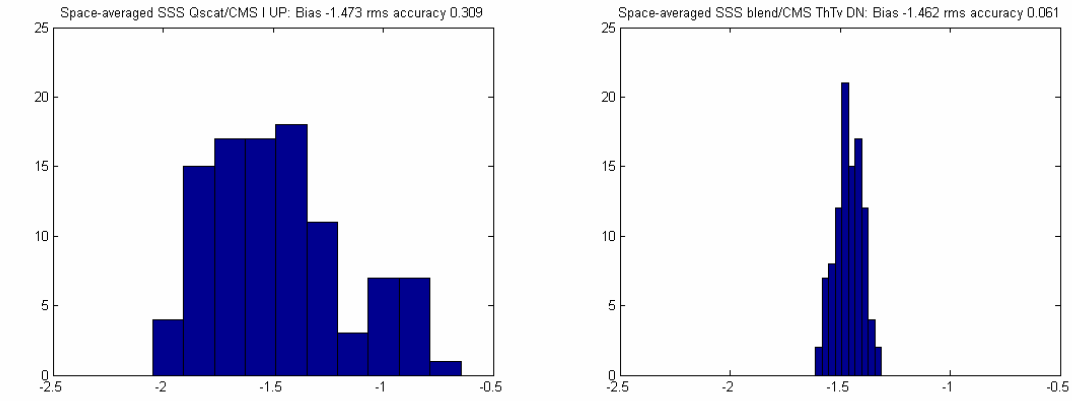

Fig. 5.15 Space-averaged *SSS* histogram with spatio-temporal bias and *rms* accuracy referred to a) QSCAT/CMS configuration in dual-pol mode and b) to blend/CMS configuration in full-pol mode.

Figure 5.16 shows ROI distribution (a) and corresponding histogram (b) for the best configuration leading to minimum rms accuracy in 2°x2° boxes spatial averaging, namely the blended/CMS in full-pol mode and in the satellite descending passes.

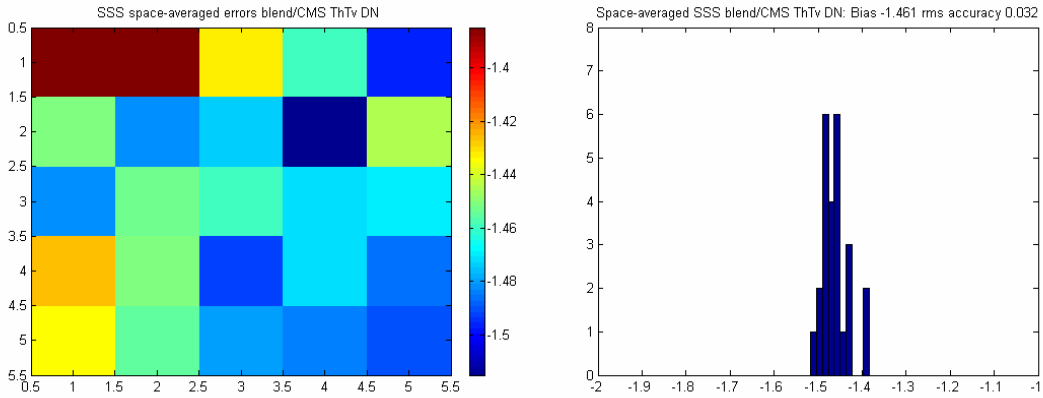

Fig. 5.16 ROI space-averaged (2°x2°) *SSS* errors (a) and corresponding histogram (b) relevant to blend/CMS configuration in full-pol mode for the descending pass**.**

Table 5.2 summarizes the results gathered for each configuration, polarimetric mode and satellite passes. Several considerations arise from the results shown in the table. As expected, concerning the auxiliary wind impact, ECMWF and QuikSCAT winds turned out to be worse than blended wind product, being the latter the default wind used in brightness temperature generation. Nevertheless, quantitative degradation (that is, *SSS* sensitivity to auxiliary wind) with respect to the baseline configuration has been provided.

Concerning the impact of the auxiliary *SST*, a minimum effect is encountered comparing the results using the Reynolds field and the default CMS field. One possible reason is that the rms values considered in the algorithm restrictions for both fields are really close. Furthermore, T_B exhibits a low sensitivity with respect to *SST* around 35 psu.

The use of *Th* and *Tv* measured in full-pol mode provides a slightly better rms accuracy, but a slightly worse bias than using the first Stokes parameter measured as $I=Tx+Ty$ measured in dual-pol mode.

Concerning the unrestricted retrieval algorithm version (no reference values), the use of *I* measured in dual-pol mode provides a lower bias even if, as expected, the rms error is larger. This is arguably useful for future *SSS* retrieved bias correction.

Concerning spatio-temporal *SSS* rms accuracy, as it can be appreciated, the bias is obviously the same, but the rms accuracy has not decreased as expected taking into account the number of available observations. The expected reduction (square root of the number of samples averaged) is not seen since the retrieval often presented errors in the form of patches, which reduced the efficiency of the averaging procedure.

Table 5.2 Monthly-averaged bias and spatio-temporal retrieved *SSS* rms accuracy for the different configurations in psu. In bold: auxiliary data, satellite pass and instrument configuration leading to the smallest *SSS* error. In italic: auxiliary data parameters configurations satisfying GOADE requirements.

Configuration	**Mode**	**Satellite pass**	**Monthly Bias**	**Monthly Rms**	**Rms 1°x1°**	**Rms 2°x2°**
Blend/CMS	Dual (Stokes *I*)	UP	-1.267	0.371	*0.071*	*0.050*
Blend/CMS	Dual (Stokes *I*)	DN	-1.311	0.382	*0.099*	*0.080*
ECMWF/CMS	Dual (Stokes *I*)	UP	-1.361	0.491	0.264	0.248
ECMWF/CMS	Dual (Stokes *I*)	DN	-1.593	0.549	0.293	0.273
QSCAT/CMS	Dual (Stokes *I*)	UP	-1.472	0.546	0.309	0.291
QSCAT/CMS	Dual (Stokes *I*)	DN	-1.530	0.513	0.206	0.162
Blend/Reynolds	Dual (Stokes *I*)	UP	-1.258	0.368	*0.078*	*0.057*
Blend/Reynolds	Dual (Stokes *I*)	DN	-1.316	0.395	*0.102*	*0.081*
No aux data	Dual (Stokes *I*)	UP	-0.860	1.505	0.835	0.737
No aux data	Dual (Stokes *I*)	DN	-0.791	1.195	0.431	0.326
Blend/CMS	Full (*Th*/*Tv*)	UP	-1.447	0.337	***0.055***	*0.036*
Blend/CMS	Full (*Th*/*Tv*)	DN	-1.462	0.331	*0.061*	***0.032***
ECMWF/CMS	Full (*Th*/*Tv*)	UP	-1.512	0.401	0.186	0.166
ECMWF/CMS	Full (*Th*/*Tv*)	DN	-1.679	0.443	0.212	0.198
QSCAT/CMS	Full (*Th*/*Tv*)	UP	-1.584	0.469	0.234	0.220
QSCAT/CMS	Full (*Th*/*Tv*)	DN	-1.622	0.411	0.136	*0.097*
Blend/Reynolds	Full (*Th*/*Tv*)	UP	-1.443	0.346	*0.070*	*0.045*
Blend/Reynolds	Full (*Th*/*Tv*)	DN	-1.453	0.330	*0.056*	*0.035*
No aux data	Full (*Th*/*Tv*)	UP	-3.457	0.902	0.289	0.207
No aux data	Full (*Th*/*Tv*)	DN	-3.295	0.893	0.259	0.211

5.6 Identification of Retrieval Error Sources

Having at disposal the overall spatio-temporal retrieved *SSS* variability scheme, it is interesting to quantitatively and singularly identify the different sources of *SSS* bias and rms accuracy. The goal is to distinguish between the variability associated to the different auxiliary data (main issue addressed in this study) and the additional different contributions involved in the inversion procedure itself.

A master retrieval scenario referred to the ascending passes in dual-pol mode and using the first Stokes parameter was selected, while the possible additional error sources were binned into radiometric noise, direct/inverse model difference, uncertainties on auxiliary data, and auxiliary wind/*SST* difference.

As a first approach, auxiliary data difference was not considered, since *SSS*, *SST* and wind fields were considered constant in the whole ROI (35 psu, 15 °C, and 10 m/s), both to generate brightness temperatures (by means of the Hollinger model), and in the restrictions of the cost function.

The simulation plan is conceived with the purpose of generating a hierarchical sequence of simulations with an increasing complexity, thus furnishing a tool to quantify the multi-source error contributions in the results obtained.

The simplest simulation case to test the reliability of the iterative method did not embody any of the above mentioned potential error sources: there was not radiometric noise, Hollinger linear model was used for both generating $T_B s$ and for inverting data (direct and inverse model), while reference points in the cost function restrictions (actually a varying value with the corresponding uncertainties) were supposed to be exactly known (Type 1). As expected, in such ideal conditions *SSS* retrieval was perfect, only limited by numerical round-off errors, confirming the robustness of the method.

The second step, labeled as Type 2, consisted of adding just the expected radiometric noise. At boresight, the considered noise was of 2.36 K, with a degradation factor towards the swath edges which is a function of the so-called "obliquity factor" and the antenna radiation patterns. The corresponding results exhibit good retrieval, with the expected worsening towards the edges of the swath due to the larger noise and the reduced number of observations. Figure 5.17a and 5.17b show these features referring to the specific case of January 1st.

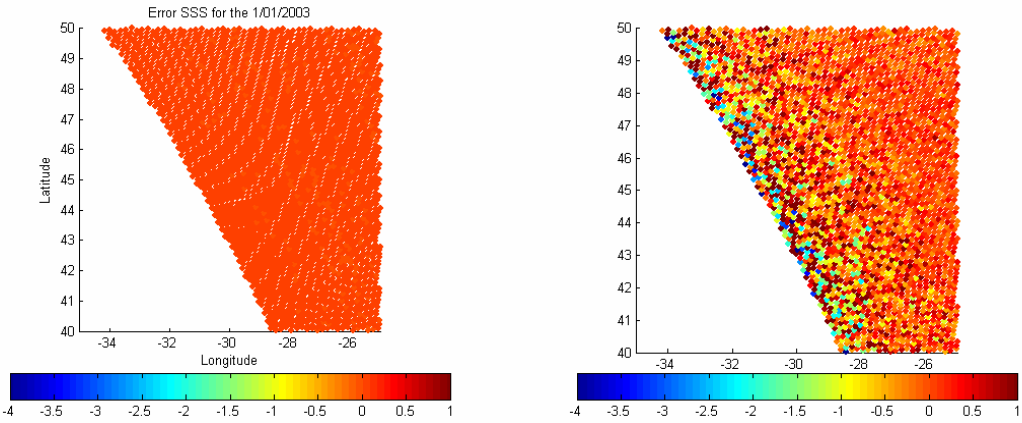

Fig. 5.17 a) *SSS* retrieval in the ideal case (Type 1) and b) *SSS* retrieval with the addiction of radiometric noise (Type 2). Both corresponding to January 1st.

Subsequent simulations were devoted to the understanding of the magnitude of the auxiliary data uncertainties (Type 3). Again, radiometric noise was absent, and direct/inverse models were the same, but the reference points in the cost function are now supposed to be known with some degree of uncertainty, namely concerned to the *a priori* considered standard deviation of the default wind and *SST* fields. The temporally-averaged results shown hereafter emphasize

how this configuration is not responsible for bias introduction in *SSS* retrieval, while it already contributes with a monthly rms *SSS* error of 0.293 psu (Fig. 5.18a). Spatio-temporal averaging reduces such rms error contribution to 0.046 psu in 1°x1° boxes and to 0.025 psu in 2°x2° boxes.

Keeping in mind the increasing degree of complexity to gradually approach the overall setup used in this study, the difference between direct and inverse models was then added to the previous configuration (Type 4), whose potential effect was already foreseen. In this case, auxiliary data are no longer the constant fields used until now in this section, but the default blended wind product and CMS temperature. Figure 5.18b illustrates the monthly-averaged results for this case in which the predominant effect is the appearance of the bias found in the study.

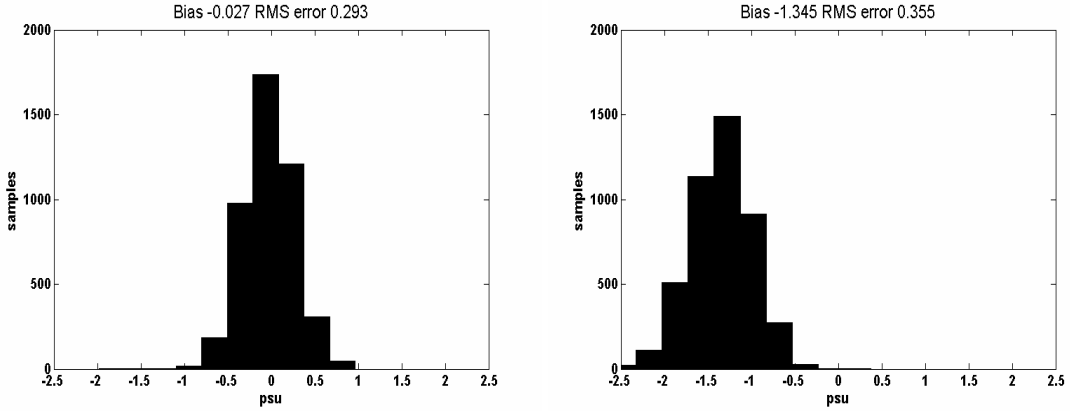

Fig. 5.18 a) Monthly *SSS* weighted errors histogram with ROI bias and rms accuracy referred to Type 3 configuration in dual-pol mode, and b) Monthly *SSS* weighted errors histogram with ROI bias and rms accuracy referred to Type 4 configuration in dual-pol mode.

Table 5.3 compares the spatio-temporal averaged results through Type 1 to Type 6 cases. It is useful to recall that the first one is the ideal case, while the second one evaluates the presence of radiometric noise. Type 3 underlines the reference point uncertainty effect, Type 4 the model difference impact, and finally Type 5 is the already known blend/CMS default configuration (cfr Table 5.2). Two examples of Type 6 different auxiliary data configuration are listed as well. Comparing Types 4 and 5 configurations, the bias appears slightly higher (-1.345 psu) in the first one, whereas the rms accuracy is slightly better (0.355 psu) in time-averaged results, but moderately worse in the space-averaged retrievals, indicating that, as compared to other error sources, the radiometric noise does not affect results heavily. Type 6 case, as reported in Table 5.2, refers to the auxiliary data difference effect, whose magnitude on *SSS* was already a matter of study throughout the chapter.

Table 5.3 Hierarchical error sources identification scheme.

Type	Rad. Noise	Model Diff.	Ref. Point Uncert.	Aux Data Fields	Monthly Bias	Monthly Rms	Rms 1°x1°	Rms 2°x2°	Features
1	No	No	No	Constant	0.000	0.000	0.000	0.000	Ideal
2	**Yes**	No	No	Constant	0.008	0.130	0.033	0.024	Rad. Noise
3	No	No	**Yes**	Constant	-0.027	0.293	0.046	0.025	Ref point effect
4	No	**Yes**	**Yes**	Default	-1.345	0.355	0.083	0.064	Model diff effect
5	**Yes**	**Yes**	**Yes**	Default	-1.267	0.371	0.071	0.050	Blended/CMS
6a	**Yes**	**Yes**	**Yes**	Different	-1.361	0.491	0.264	0.248	ECMWF/CMS
6b	**Yes**	**Yes**	**Yes**	Different	-1.472	0.546	0.309	0.291	QuikSCAT/CMS

As mentioned in the previous sections, if one refers to Type 6 data as "realistic" retrieval case and assuming the different contributions as independent, it is now possible to unwrap the overall *SSS* error coming from different sources. For instance, considering ECMWF monthly accuracy and 1°x1° spatial averaging, ~2% of the final squared error lies in the radiometric noise, an additional ~3% is related to reference point variability, an extra ~7% is due to the model difference, while the remaining ~88% is associated to auxiliary data uncertainty. In the case of QuikSCAT, the degradation effect due to auxiliary data difference is ~92% of the total squared error.

It has to be stressed, however, that part of the *SSS* additional error coming from the last step might be related to unacceptable original/auxiliary wind difference, as well. Figure 5.19a depicts an example of absolute difference between wind used in the T_B generation (default blended QSCAT/NCEP) and auxiliary wind used in the minimization procedure (in this case ECMWF). Such difference can be so high to induce strong discrepancies between the original and the retrieved *SSS*, according to geographical zone. The corresponding *SSS* errors are shown in Fig. 5.19b, in dual-pol mode and referred to ascending pass. Note that *SSS* exhibits remarkable errors in correspondence of the ROI zone characterized for high original/auxiliary wind difference.

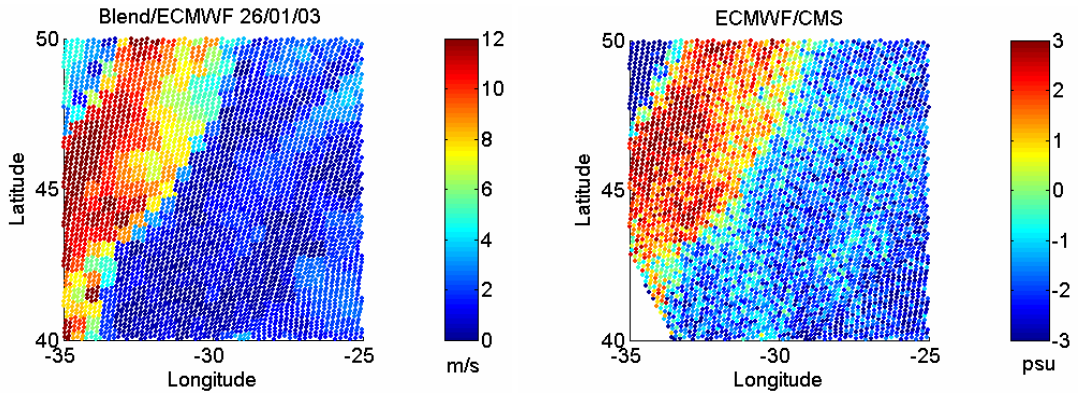

Fig. 5.19 a) Absolute difference in m/s between blended QuikSCAT/NCEP and ECMWF auxiliary winds, corresponding to January 26th, and b) corresponding retrieved *SSS* errors for January 26th, ascending pass, dual-pol and ECMWF auxiliary data.

In summary, the influence of each parameter has been studied starting from an ideal simulation, adding then separately radiometric noise and uncertainties on auxiliary data, respectively. Hence, considering the latter one as always present, the effect of having different model has been investigated. Finally, the progressive impact to *SSS* bias and rms error has been quantified, performing a proper identification of the different error contributions.

Once it is clear that bias encountered in the retrieved salinity lies mostly in the use of a different model for inverting data, a further attempt was made substituting the Hollinger linear fit used in the study so far, with a different empirical model, namely the WISE 2001 [Camps et al., 2004a] one. Results are shown in Fig. 5.20. Bias has been drastically reduced (from -1.267 psu using the linear fit to Hollinger model to -0.497 psu using the WISE 2001 model), indicating that obtaining a good forward model for the roughness effect on sea surface emissivity is a key issue that deserves the maximum attention and effort. Recall that the SSA model was used in the direct model to generate the T_{BS}.

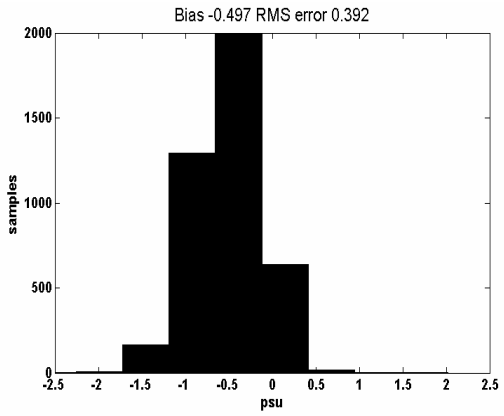

Fig. 5.20 Monthly *SSS* weighted errors histogram with ROI bias and rms accuracy using WISE 2001 model in dual-pol mode.

5.7 Conclusions and Insights

The main goal of this study was to stress the retrieved *SSS* variation induced by the different auxiliary data, providing relevant rms accuracy and bias in a representative area of the North Atlantic Ocean. The assumptions of perfect knowledge of the Faraday rotation and atmospheric processes have been made in the retrieval procedure.

A major scope of this study has been to figure out if GODAE requirements are likely to be accomplished despite the limitations imposed to the retrieval setup. In synthesis, the aim of this study was two-fold:

- To analyze the impact of the use of different auxiliary data sets in the retrieval process, quantifying the sensitivity to the auxiliary fields, as well as to check the quality of the achievable results using different brightness temperature model to generate/invert the data.
- To identify the different *SSS* error contributions through an item-by-item error sources selection meant to distinguish between the auxiliary data impact itself and the additional contributions involved in the inversion procedure. This approach has been the forerunner of a more detailed analysis of the ocean *SSS* error budget, as will be discussed later on in this Ph.D. Thesis.

The use of *Th* and *Tv* measured in full-pol mode has provided a slightly better rms *SSS* error by a varying factor, mostly ranging from 1.1-1.2, but a slightly worse bias than using the first Stokes parameter measured as $I=Tx+Ty$ in dual-pol mode.
The main conclusions of this study can be summarized as follows:

- SSS retrieval in one overpass: rms SSS error is typically around 1 psu (varying depending on the auxiliary data used) increasing up to 4 psu or more at swath edges, in agreement with [Camps et al., 2002b; Camps et al., 2003a; Boutin et al., 2004]. A bias appears in the measurements and must be corrected for by using ground-truth data (e.g. buoys or drifters) [Talone, 2007a].
- Temporally-averaged retrieved SSS (computed as the weighted mean of the retrieved L2 SSS by the inverse of its standard deviation at each pixel position in the swath.): Monthly temporal averaging at pixel level provides a ROI rms error within the range 0.330-0.549 psu, depending on the auxiliary data set used. The use of different sources of auxiliary data for SST has a minimum impact in the SSS retrieval.
- Spatio-temporal averaging of retrieved SSS: In a period of 30 days and in 1°x1° boxes, the retrieved rms SSS error ranges between 0.055 - 0.309 psu. In a period of 30 days and in 2°x2° boxes, the retrieved rms SSS accuracy ranges between 0.032 - 0.291 psu. The best SSS products obtained by spatio-temporal averaging of 30 days satisfy the <0.1 psu error requirement.

Apart from the best case scenario which somehow determines the limits of the retrieval, to address a more realistic case (besides model difference), one should refer to different auxiliary data configurations, since better simulates the upcoming "measured" brightness temperature. In fact, if ECMWF data were used instead (different auxiliary wind), the rms error would increase up to 0.2-0.3 psu (depending on the instrument mode and satellite pass), in accordance to [Camps et al., 2005c]. These studies have shown that without auxiliary data and after spatio-temporal averaging (30 days, 1°x1°) the *SSS* rms error ranges from 0.2 psu at the Equator to 0.7 psu in Polar regions.

An item-by-item error sources analysis has also been performed, in order to isolate the different potential discrepancies sources. Reference point variability, linked to the auxiliary field uncertainty, determines an important part of the final error, even if it does not produce a bias. Direct/Inverse model difference, in turn, seems to be the responsible of bias introduction, besides some extra contribution to the *SSS* error. In this context, radiometric noise does not seem to play a crucial role, since apparently its effect is mostly filtered out in the spatio-temporal averaging procedure. Apart from the intrinsic auxiliary wind/*SST* difference, additional residual error sources lie in biased auxiliary wind field mean values (Table 5.1) and in zonal strong inhomogeneities between winds (Fig. 5.19).

Concerning the bias introduced by model differences, an attempt of replacing the Hollinger model with the WISE 2001 model provided significant bias reduction, stressing how obtaining a good forward model for the roughness effect on sea surface emissivity is still a primary issue of concern.

The auxiliary data information to be supplied is critical; in the next chapter, a potential use of GNSS-R (Global Navigation Satellite System-Reflections) data to collect useful information on the sea state to be handled as external auxiliary information is suggested.

Chapter 6
Auxiliary Data Impact by using GNSS-R Signals

6.1 Global Navigation Satellite Systems-Reflections Auxiliary Data

As already stressed, sea state is the largest contributor to the deviations of the brightness temperature with respect to the flat sea model [Font et al., 2004]. Often, the sea state impact on T_B is estimated using the 10-meter height wind speed (U_{10}), the significant wave height (*SWH*) [Camps et al., 2004a], or both [Gabarró et al., 2004a], but at L-band none of these approaches is fully satisfactory. Furthermore, as described in the previous chapter, using different sources of auxiliary data (mainly U_{10}, as the most readily available parameter to account for sea state) leads to different biases and accuracies in the retrieved salinity fields [Sabia et al., 2006], in addition to the fact that time and space collocation are often critical.

The potential use of GNSS-R (Global Navigation Satellite Systems-Reflections) opportunity signals for altimetry [Martín-Neira, 1993] and sea state determination in terms of the mean square slope (*mss*) has been already tested from ground-based [Martín-Neira et al., 2000; Ruffini et al., 2002; Soulat et al., 2004b; Belmonte-Rivas and Martin-Neira, 2005], airborne [Garrison and Katzberg, 1998; Komjathy et al., 2000; Garrison et al., 2002; Lowe et al., 2002a; Rius et al., 2002; Cardellach et al., 2003; Ruffini et al., 2004; Germain et al., 2004], and space-borne [Lowe et al., 2002b; Gleason et al., 2005] experiments. However, the underlying science needs further refinements to extract meaningful physical quantities that can be successfully used in the remote sensing and oceanographic communities.

Likewise, the potential synergy between GNSS-R *mss* measurements and L-band radiometry has been apparent since long time. It has been proposed that the *mss* derived from GNSS signals reflected by the sea surface could be a potentially appropriate sea state descriptor and could be used to make the necessary sea state T_B corrections to improve the *SSS* estimates.

A hypothetical companion satellite equipped with a GNSS-R receiver could fly in formation with SMOS to provide sea surface roughness estimates (linked through the *mss* measurements), collocated both in time and space, to improve or complement the quality of the salinity retrieval. In fact, the lack of reliable and co-located auxiliary fields for SMOS retrieval is the motivation of this study which is a preliminary assessment of the potential application of GNSS-R signals in the framework of the ocean salinity retrieval. Essentially, the purpose of this study is to explore the capability of parameters extracted from GNSS reflections to substitute for wind speed data in the sea state correction.

This work is in direct relationship with the analysis performed and described in the previous chapter. The methodology applied, the retrieval setup definition and the assessment of the results are oriented to the SMOS *SSS* retrieval framework. The orbit and parameters for the SMOS instrument have been assumed.

This work is divided into three main parts: Section 6.2 describes the simulation strategy, including the determination of the relationship between the *mss* auxiliary data and the wind speed, as well as the *SSS* retrieval setup. Section 6.3 presents and discusses the simulation results concerning the use of the GPS (Global Positioning System) constellation alone. Then, section 6.4 considers an extension of the study including other constellations suitable to be sources of GNSS-R opportunity signals. The study ends with some conclusions and insights for further work in this field.

6.2 Simulation Strategy

The main steps in the simulation strategy are the following: generation of the brightness temperatures in a selected test zone, computation of the specular points within the zone, identification of the empirical non-linear $mss(U_{10})$ relationship, geolocation and association of the derived *mss* values, and *SSS* retrieval scheme definition with GNSS-R auxiliary data.

6.2.1 Brightness Temperature Generation

The brightness temperatures used in this study were the same of the work described in the previous chapter [*SynAux* Report, 2006]. Summarizing, they were provided by IFREMER, in a representative mid-Atlantic 10° width test zone (Longitude 35° W - 25° W, Latitude 40° N - 50° N) for the whole month of January 2003. The following auxiliary data [*SynAux* Report, 2006, WP1100] were used: the *Blended QuikSCAT/NCEP* wind product, the *CMS SAF/OSI SST,* and the *WOA* 2001 *SSS* climatological field, as geophysical inputs to the Small Scale Approximation (SSA) for the sea surface L-band direct emission model [Reul and Chapron, 2001]. These generated $T_B s$ were used as inputs for this study.

6.2.2 Estimation of the GNSS-R Derived Mean Square Slope

The following step was the definition of the relationship between the wind speed and the mean square slope. There are two geometric invariants associated with the *mss* tensor: one

is $\sqrt{\sigma_u^2+\sigma_c^2}$, and the other one is $2\cdot\sigma_u\cdot\sigma_c$, in which σ_u and σ_c are the sea surface slope standard deviations in upwind and crosswind directions, respectively.

The second invariant is chosen since it is the one defined in Geometric Optics theory, and it corresponds to the area of the "slope ellipse", although it degenerates in the case of a sinusoidal sea surface (ellipse completely flat). For the sea surface slope isotropy considered ($\sigma_c/\sigma_u \approx 0.7$, according to the Elfouhaily spectrum [Elfouhaily et al., 1997]), the two definitions provide similar values. In order to get the total $mss = 2\cdot\sigma_u\cdot\sigma_c$, the second moments of the Elfouhaily spectrum are computed. At L-band, the *mss* can be obtained by integrating the sea surface spectrum from a cut-off wave number defined as $2\pi/(3\lambda)$, λ being the electromagnetic wavelength. However, to date there is no unanimity concerning which cut-off wave number in the sea surface spectrum should be chosen in order to correctly reproduce the dependence of the L-band limited *mss* on wind speed, and different formulations can be found in literature [Komjathy et al., 2000; Garrison et al., 2002; Thompson et al., 2005]. Moreover, it is expected that the *mss* actually measured will include other effects affecting the sea state, in addition to the wind speed.

Figure 6.1a shows the optical Cox and Munk [Cox and Munk, 1954] *mss* in comparison to the total *mss* computed from the Elfouhaily spectrum. Figure 6.1b shows, in turn, the mean square slope associated with the L1 GPS frequency (λ=19 cm). As it is shown, not only the value of the *mss* is much smaller, but above 10-12 m/s it decreases as about the logarithm of wind speed.

Due to the absence of a real SMOS satellite in formation that would collect the reflections form GPS satellites constellation (thus estimating the *mss* of the observed scene), the actual *mss* has to be estimated starting by the wind speed field. In order to do that, the *mss* values have been estimated using a cubic empirical relationship with U_{10} (Eqn. 6.1):

$$mss = 5.48\cdot10^{-6}U_{10}^3 - 2.56\cdot10^{-4}U_{10}^2 + 4.48\cdot10^{-3}U_{10} - 1.3\cdot10^{-3}. \qquad (6.1)$$

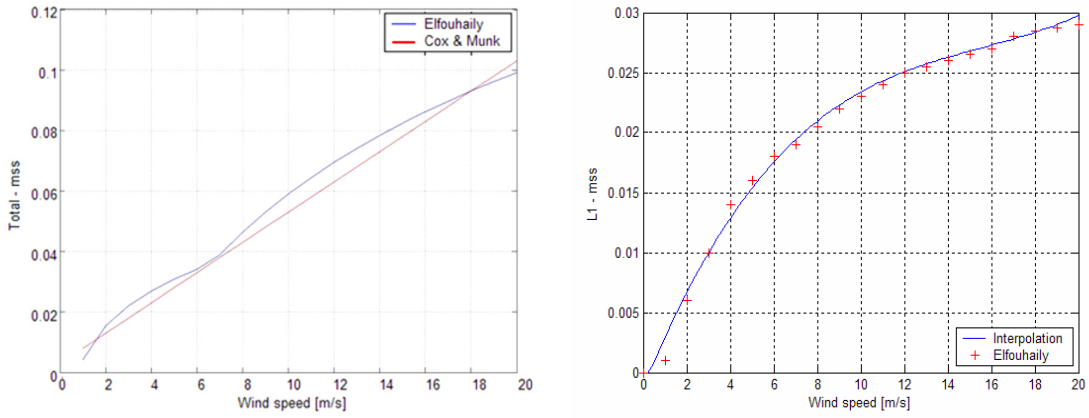

Fig. 6.1 a) Cox and Munk *mss* and total *mss* computed from the Elfouhaily spectrum without cut-off wavenumber, b) The *mss* computed for the L1 GPS frequency (λ=19 cm).

The GNSS-R simulated *mss* will then be obtained from the wind speed reference data (blended *QuikSCAT/NCEP* wind) with the fitting shown in Fig. 6.1b and described by the Eqn. 6.1, plus a given amount of noise assumed to be a zero-mean random Gaussian variable with a standard deviation equal to 0%, 5% or 10% of the *mss* value. Such errors are not the outcome of an *mss* error budget study and no model for the statistics of *mss* retrievals has been considered [Zuffada and Zavorotny, 2001; You et al., 2004]. Instead, these thresholds have been arbitrarily chosen, consistently with the purpose of the study which is limited to analyze whether assuming accurate *mss* fields fulfills or exceeds the mission requirements.

6.2.3 Identification of Specular Reflection Points within the Region of Interest

The specular reflection points have been calculated for the whole month of January 2003 within the test zone in which GNSS reflections would be collected by a hypothetical tandem SMOS satellite. These specular points have been derived by the Spanish company STARLAB with the lowest acceptable temporal resolution for each day of the simulated month, providing hour, minute and second specifications of each reflection for each SMOS instantaneous field of view (IFOV).

In a first configuration, the companion satellite was supposed to fly side-by-side in formation with SMOS, at the same latitude and at a different longitude. Figure 6.2 presents two examples of specular points within the Region of Interest (ROI) for both ascending and descending passes for different days.

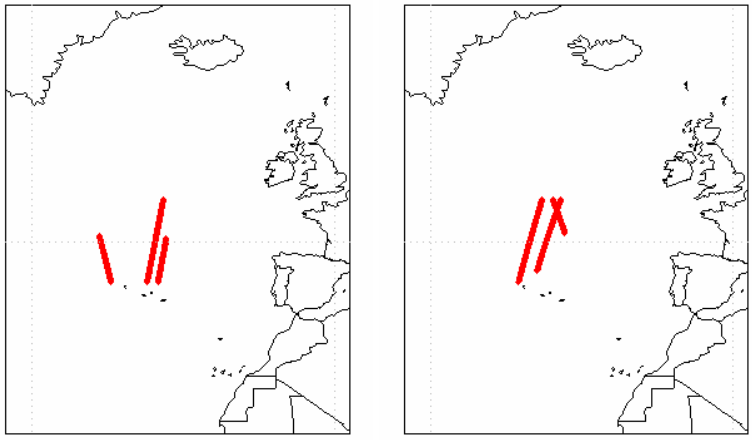

Fig. 6.2 Simulated specular points within the ROI for January 7th (left) and January 19th (right).

Once geocoded to the ISEA4H9 grid to which SMOS data will be referred, these are the only points at which sea surface GNSS-R derived *mss* have been computed within the ROI and used

as auxiliary data for the *SSS* retrieval algorithm. Winds referred to the ascending and descending pass of the satellite were discriminated according to the intersection time of specular points.

6.2.4 Estimation of the *mss* at the Specular Points

Using the blended *QuikSCAT/NCEP* wind speed reference data at the closest time to the tandem satellite passage and the U_{10}-*mss* relationship developed (Eqn. 6.1 and Fig. 6.1b), the *mss* at the specular reflection points within the ROI has been estimated. Then, the generated brightness temperatures have been associated with all the SMOS IFOVs in which these pixels are seen (paragraph 6.2.1).

In this work, the GNSS-R measurements are assumed to be made at the specular point. Actually, the inversion of GNSS-R measurements involves the fitting of a scattering model to the shape of a power-delay (correlation) waveform. The shape of this waveform represents the scattered power from a distributed area on the ocean surface, approximately in the shape of an ellipse with dimensions proportional to the square root of the delay.

However, in this study the values of *mss* have been calculated from an analytical fitting with wind speed data, and not by inversion of the waveform. As previously stated, to focus on the potential improvements in SMOS *SSS* retrievals from GNSS-R measurements, the processing of this signal has been left apart and *mss* values have been used as if they were the outcome of a specific established extraction procedure with a given error.

6.2.5 Salinity Retrieval in terms of the *mss* at the Specular Reflection Points

The *SSS* retrieval scheme considers only the pixels for which a GNSS specular reflection exists. To be consistent with the previous study, the *SSS* retrieval has been formulated both in terms of the brightness temperatures in the Earth's reference frame and referring to the first Stokes parameter. The *SSS* retrieval scheme features are the same used in the *SynAux* study [Sabia et al., 2006]. The cost function to be minimized in this case is:

$$\varepsilon = \frac{1}{\mathrm{N_{obs}}}\sum_{n}\left\{\left[\overline{F}_{\mathrm{model}}\left(\theta,\hat{\vec{P}}\right)-\overline{F}_{\mathrm{data}}\left(\theta,\vec{P}\right)\right]^{\mathrm{T}}\left(\overline{\overline{C}}\right)^{-1}\left[\overline{F}_{\mathrm{model}}\left(\theta,\hat{\vec{P}}\right)-\overline{F}_{\mathrm{data}}\left(\theta,\vec{P}\right)\right]\right\}+ \\ +\frac{\left(S\hat{S}S-SSS_{ref}\right)^2}{\sigma_{SSS}^2}+\frac{\left(S\hat{S}T-SST_{ref}\right)^2}{\sigma_{SST}^2}+\frac{\left(m\hat{s}s-mss_{ref}\right)^2}{\sigma_{mss}^2}. \tag{6.2}$$

SSS_{ref}, SST_{ref}, and mss_{ref} are reference values (with their associated uncertainties) to be used to nudge the solution, and σ_{SSS}, σ_{SST}, and σ_{mss} are the corresponding auxiliary data standard

deviations to properly weigh the cost function terms, according to the accuracy of the specific field. For a detailed description of the other terms, cfr. Chapter 3. Since it has been found that the reference value for *SSS* (SSS_{ref}) restricts the solution too much to the reference value, the constraint on *SSS* has not been included. Again, *SSS* retrievals on a pixel-by-pixel basis are temporally averaged for a whole month, and spatially averaged in blocks of 1°x1° or 2°x2°, in order to reduce the standard deviation of the estimates and obtain results comparable with the mission requirements [Smith and Lefèbvre, 1997].

6.3 Single GNSS-R Opportunity Source: Simulation Results

With the objective of assessing the impact of different error sources and exploit the capabilities of the GNSS-R derived data to characterize the sea state, simulations have been performed at increasing complexity. In this section only the retrieval using the first Stokes parameter computed in dual-pol mode is considered. Moreover, only the specular points calculated by means of the GPS constellation are used.

6.3.1 Salinity Retrieval in the Ideal Case

An ideal scenario has been first built to test the robustness of the iterative method. This simulation was intended to test the reliability of the procedure despite the potential errors introduced by fitting the data either in the $mss(U_{10})$ conversion (due to the unavailability of "true" *mss* fields) or during the $U_{10}(mss)$ derivation (needed to establish a $T_B(mss)$ geophysical model function in the inversion scheme). This method proved to be satisfactory, resulting in perfect *SSS* retrievals, apart from numerical round-off errors.

6.3.2 Salinity Retrieval with Radiometric Noise

Secondly, a simulation that considered only the effect of the radiometric noise present in SMOS measurements has been defined. The noise considered was 2.36 K at boresight, with a degradation factor towards the swath edges which is a function of the so-called "obliquity factor" and the antenna radiation patterns. The goal has been to establish the best-case performance that an ideal instrument only limited by thermal noise could achieve in these conditions. The monthly *rms* error is nearly 0.47 psu, while the bias is negligible (0.013 psu).

6.3.3 Salinity Retrieval with GNSS-R Derived *mss* Errors

As previously discussed, salinity retrieval was studied assuming an uncertainty in the measured *mss* of 5% and 10% of its value. In the beginning of the study 20% error was considered, but this resulted in unreasonably high errors in retrieved *SSS*, due to the specific retrieval setup. However, the use of a homogeneous *mss* value over the whole glistening zone might also be inaccurate, but, to date, no GNSS-R system and algorithms have been proposed to overcome this issue.

Figure 6.3a shows the inverse of Fig. 6.1b, and it is needed to use an *mss* field as input to the semi-empirical forward model to correct for wind speed effects on T_B. It is evident that a 10% error in the *mss* is equivalent to an error in U_{10} much larger than 10%. This is made more explicit in Fig. 6.3b, where, for example, a 10% error in *mss* is equivalent to a 1.5 m/s U_{10} error for *mss* = 0.020 (U_{10} = 7.6 m/s), to a 0.7 m/s U_{10} error for *mss* = 0.015 (U_{10} = 4.6 m/s), and to a 0.25 m/s U_{10} error at *mss* = 0.010 (U_{10} = 3 m/s). Despite the fact that these numbers may seem reasonably accurate, the logarithm-like behavior in the *mss* in Fig. 6.1b strongly influences the variability of U_{10} at high wind speeds. Namely, this is evident especially above *mss* = 0.020 – 0.025, that is, above U_{10}~10 m/s, where a large percentage of wind speed data in the selected zone lies. Such effect will ultimately limit the retrieval capability, since the T_B(*mss*) relationship is derived from an existing T_B(U_{10}) model. It has to be recalled that in this study it has been assumed that the T_B(*mss*) dependence is given by T_B(U_{10}) from [Hollinger, 1971] and U_{10}(*mss*) is derived from Fig. 6.3a.

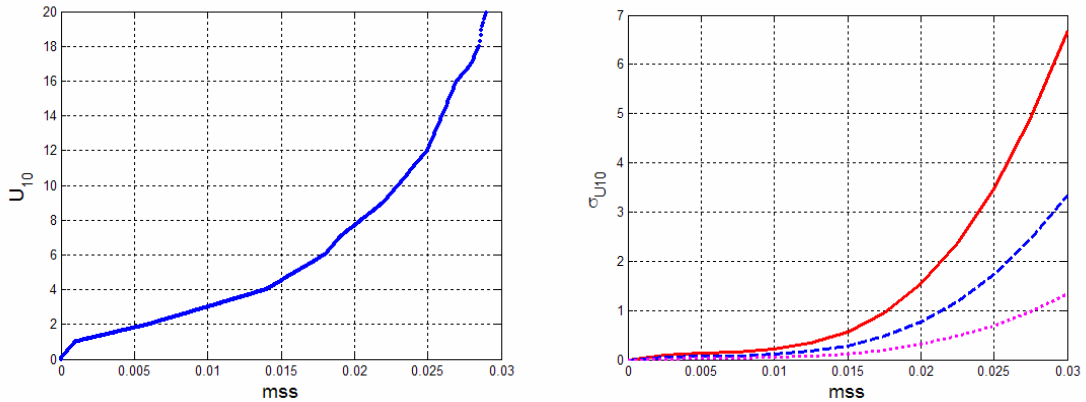

Fig. 6.3 a) Wind speed versus mean square slope, and b) 10% (solid line), 5% (dashed line), and 2% (dash-dot line) *mss* error propagation into U_{10} error.

This approach is sub-optimal in two ways. First, it connects *mss* to U_{10} in the case of GNSS-R, which is known to be an indirect link. Second, it connects U_{10} to T_B, which is another indirect relationship, and not strictly one-to-one, depending T_B on other factors such as the significant wave height, wave age, and presence of foam. Further efforts will have to be devoted to the

definition of a better $T_B(mss)$ model that would encompass the effects mentioned above, and that are instead implicitly considered within the "true" *mss* parameter.

In our case study, the input wind field exhibits the following statistics: $U_{10\,\min}$ = 0.02 m/s, $U_{10\,\max}$ = 33.7 m/s, $U_{10\ \text{avg}}$ = 11.63 m/s and σ_{U10} = 4.79 m/s. It is then clear that the sea state corresponding to the high winds encountered will be measured in most cases with a large uncertainty ($U_{10\ \text{avg}}$ = 11.63 m/s corresponds to *mss* = 0.0246), which will worsen the salinity retrieval performances. That is, simulation results might be somewhat pessimistic, and better results could be obtained in other regions.

Figure 6.4 shows the monthly errors (considering only the specular points) on a pixel-by-pixel basis and the corresponding histogram for those pixels for which a GPS specular reflection existed during the entire month. The retrieved *SSS* exhibits a -1.422 psu bias and a 1.477 psu accuracy. The origin of this bias lies primarily in the difference between brightness temperature direct (SSA) and inverse (Hollinger's [Hollinger, 1971] plus $U_{10}(mss)$ dependence, Fig. 6.3a) models, and also by the fact that a zero-mean Gaussian random error in *mss* does not correspond to a Gaussian random error in U_{10}. This effect was already found in [Sabia et al., 2006] when different $T_B(U_{10})$ models were used.

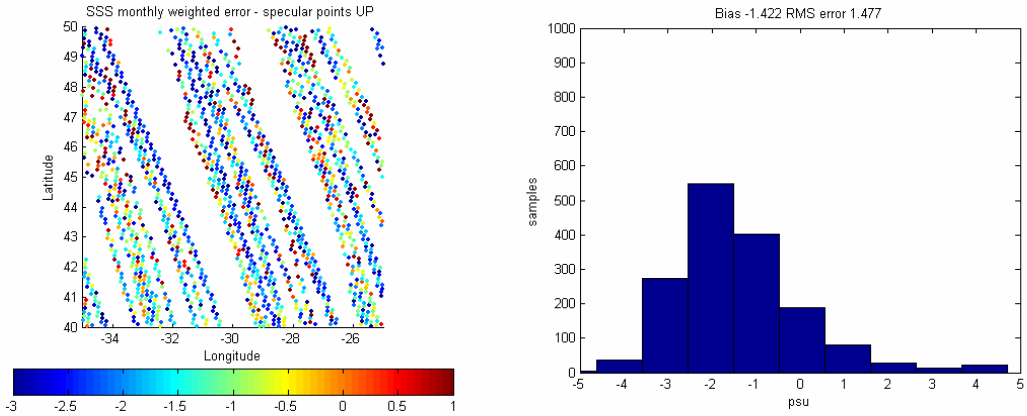

Fig. 6.4 a) Monthly ROI weighted errors relevant to specular points in dual-pol mode for the ascending pass considering 10% *mss* error, and b) corresponding monthly *SSS* weighted errors histogram with ROI bias and *rms* accuracy.

Figure 6.5 shows the monthly averaged errors in *SSS* considering a lower error (5%) in *mss* field estimation. In this case the retrieved *SSS* exhibits a -1.410 psu bias, very similar to the previous case, but a smaller standard deviation of 1.232 psu.

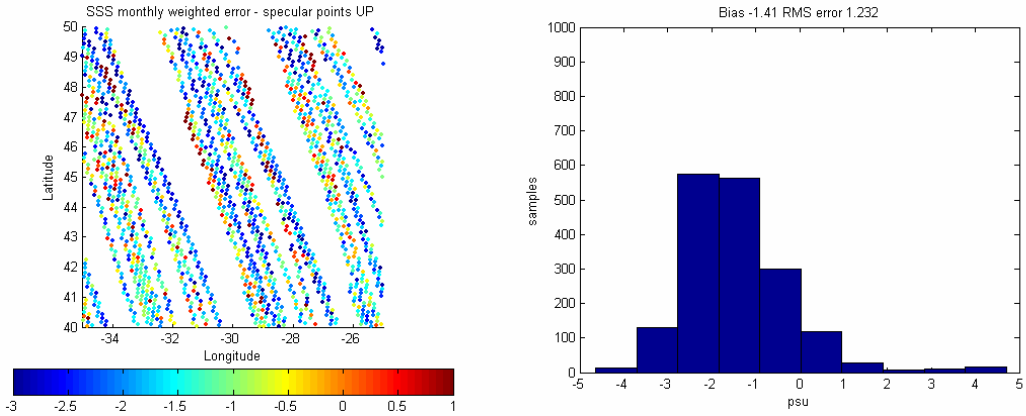

Fig. 6.5 a) Monthly ROI weighted errors relevant to specular points in dual-pol mode for the ascending pass considering 5% *mss* error, and b) corresponding monthly *SSS* weighted errors histogram with ROI bias and *rms* accuracy.

6.3.4 Spatio-Temporal Averaging

According to the approach of the *SynAux* study, temporal averaging was conducted with a proper weighted average procedure to give less weight to the noisier pixels that are farther away from the SMOS ground track. These weights were computed from the standard deviation of the retrievals computed from the 10 Monte Carlo simulations. Spatial averaging was then performed over 1°x1° and 2°x2° boxes. The main results are shown in Table 6.1. Due to the limited number of pixels with measured *mss*, the effectiveness of the spatial averaging is strongly jeopardized, limiting the expected improvement of the retrieval accuracies by using this kind of GNSS-R auxiliary data.

Table 6.1 Single GNSS-R source simulation results.

Configuration	**Satellite pass**	**Monthly Bias**	**Monthly Rms**	**Rms 1°x1°**	**Rms 2°x2°**
Radiometric Noise only	UP	0.013	0.469	0.121	0.045
5% *mss* error	UP	-1.410	1.232	0.595	0.262
10% *mss* error	UP	-1.422	1.477	0.724	0.315

An obvious way to improve the *SSS* retrieval performance would be to increase the number of points in which the *SSS* can be retrieved within the ROI. To do this, an optimal interpolation and extrapolation procedure should be used, but none of the interpolation methods tested (nearest neighbor, bilinear, and MATLAB© v4 interpolation techniques) have produced satisfactory results.

6.4 Multiple GNSS-R Opportunity Sources: Simulation Results

Once the limitations associated with the use of only GPS reflections and the spatial interpolation techniques have been shown, different (existing and future) GNSS constellations will be considered to improve the spatio-temporal coverage (that is, increasing the number of specular reflections) using an optimal averaging strategy.

The constellations considered in this study were the Russian GLONASS (**GLO**bal'naya **NA**vigatsionnaya **S**putnikovaya **S**istema), the future European constellation GALILEO, in addition to points calculated from the Satellite Based Augmentation Systems (SBAS)/INMARSAT telecommunications satellites in geostationary orbit.

In the previous configuration the companion satellite would fly in formation side-by-side with SMOS. In addition, a second configuration has been studied, namely considering a tandem satellite flying 500 km behind the SMOS payload in the same orbit.

In all cases in which *mss* errors greater than 5% were used, the resulting errors in the sea state correction to T_B were found to be too large. Therefore, the following simulations were only conducted for the case of a 5% error in *mss*. In other words, a best-case scenario concerning *mss* estimation was considered, despite the overall *SSS* retrieval scheme was rather realistic and demanding.

The aim of this extension to the previous section is to verify the feasibility of blending information from different GNSS sources to achieve reasonable *SSS* accuracy. Thus, the overall setup of simulations consisted of four constellations, in two configurations with respect to SMOS (tandem satellite side-by-side, hereafter "side" configuration, and behind SMOS, from now onwards "back" configuration), for the two instrument operation modes (*Th* and *Tv* measured in fully polarimetric mode or *I* measured in dual-polarization mode) and for both satellite passes (ascending and descending). This setup resulted in 32 single-constellation simulations. Subsequently, to use as many specular reflection points as possible, a merging of the results from the previous simulations provided the final assessment of this study. Table 6.2 summarizes the results of the single-constellation salinity retrieval in the different configurations mentioned above.

Table 6.2 Multiple GNSS-R source simulation results.

Constellation	Config.	Mode	Satellite Pass	Monthly Bias	Monthly Rms	Rms 1°x1°	Rms 2°x2°	Days with pts.
GPS	Side	*I*	UP	-1.410	1.232	0.595	0.262	25
GPS	Side	*I*	DN	-1.445	1.127	0.522	0.224	19
GPS	Side	*Th*/*Tv*	UP	-1.398	0.997	0.395	0.206	25
GPS	Side	*Th*/*Tv*	DN	-1.422	0.917	0.412	0.174	19
GLONASS	Side	*I*	UP	-1.646	1.295	0.611	0.313	23
GLONASS	Side	*I*	DN	-1.593	1.223	0.680	0.543	11
GLONASS	Side	*Th*/*Tv*	UP	-1.690	1.208	0.564	0.240	23
GLONASS	Side	*Th*/*Tv*	DN	-1.527	0.912	0.473	0.355	11
GALILEO	Side	*I*	UP	-1.660	1.158	0.492	0.276	24
GALILEO	Side	*I*	DN	-1.493	1.370	0.679	0.448	10
GALILEO	Side	*Th*/*Tv*	UP	-1.587	0.994	0.416	0.206	24
GALILEO	Side	*Th*/*Tv*	DN	-1.500	1.123	0.506	0.375	10
SBAS	Side	*I*	UP	/	/	/	/	0
SBAS	Side	*I*	DN	-1.614	1.429	1.396	1.295	8
SBAS	Side	*Th*/*Tv*	UP	/	/	/	/	0
SBAS	Side	*Th*/*Tv*	DN	-1.508	1.133	0.972	0.874	8
GPS	Back	*I*	UP	-1.913	1.016	0.693	0.560	3
GPS	Back	*I*	DN	-1.423	1.175	0.556	0.283	22
GPS	Back	*Th*/*Tv*	UP	-2.020	1.205	0.781	0.616	3
GPS	Back	*Th*/*Tv*	DN	-1.413	0.957	0.374	0.161	22
GLONASS	Back	*I*	UP	-1.907	1.130	0.829	0.635	14
GLONASS	Back	*I*	DN	-1.620	1.275	0.800	0.567	10
GLONASS	Back	*Th*/*Tv*	UP	-1.725	0.906	0.555	0.375	14
GLONASS	Back	*Th*/*Tv*	DN	-1.558	0.915	0.516	0.328	10
GALILEO	Back	*I*	UP	-1.654	1.229	0.771	0.346	4
GALILEO	Back	*I*	DN	-1.458	1.408	1.084	0.765	9
GALILEO	Back	*Th*/*Tv*	UP	-2.073	1.293	0.553	0.349	4
GALILEO	Back	*Th*/*Tv*	DN	-1.354	1.092	0.774	0.626	9
SBAS	Back	*I*	UP	/	/	/	/	0
SBAS	Back	*I*	DN	-1.765	1.288	0.781	0.396	22
SBAS	Back	*Th*/*Tv*	UP	/	/	/	/	0
SBAS	Back	*Th*/*Tv*	DN	-1.920	1.275	0.558	0.345	22

The specular points of the different constellations in both configurations exhibit a wide range of variability in their occurrence in the days considered. Namely, GPS and GALILEO had the largest number of days with available points in the side configuration than in the back one. Conversely, GLONASS and SBAS showed more specular points in the back configuration than

in the side one. Concerning SBAS, specular reflection points were available in both configurations only for the SMOS descending pass. In particular, in back configuration, there is a strong difference between the ascending passes (UP) and the descending ones (DN) regarding the number of points available on each day, especially for the GPS constellation. A possible explanation for this effect is that when the companion satellite is behind SMOS in the ascending passes, it will capture specular reflections only from those GPS satellites present at those latitudes that are more "empty" than in the descending passes (going towards the Equator). This does not hold for GLONASS due to a more homogeneous distribution of the satellites generating reflections within the area under study. Hence, some of these results have to be interpreted carefully, since the number of days with specular points is limited, jeopardizing an effective monthly averaging.

Figures 6.6 and 6.7 show intercomparisons among the monthly biases in the retrieved *SSS* and the corresponding *rms* accuracy after 2°x2° spatio-temporal averaging, respectively. Considering both ascending and descending passes, retrieved *SSS rms* accuracy turned out to be better for the GPS constellation, in both side and back configuration. Conversely, GLONASS and GALILEO exhibited better retrievals for the ascending satellite passes. With respect to the accuracy of the two polarimetric modes, retrieval in fully polarimetric mode using *Th* and *Tv* was better than using the first Stokes parameter in dual-polarization.

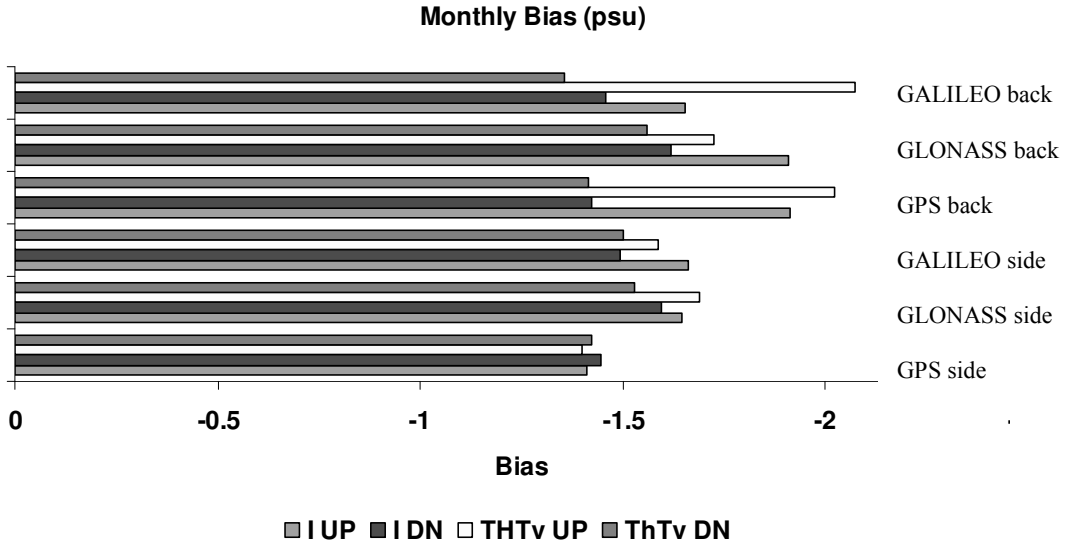

Fig. 6.6 Monthly bias for the different constellations and configurations (right side), for both polarimetric mode and satellite passes (indicated in the legend below).

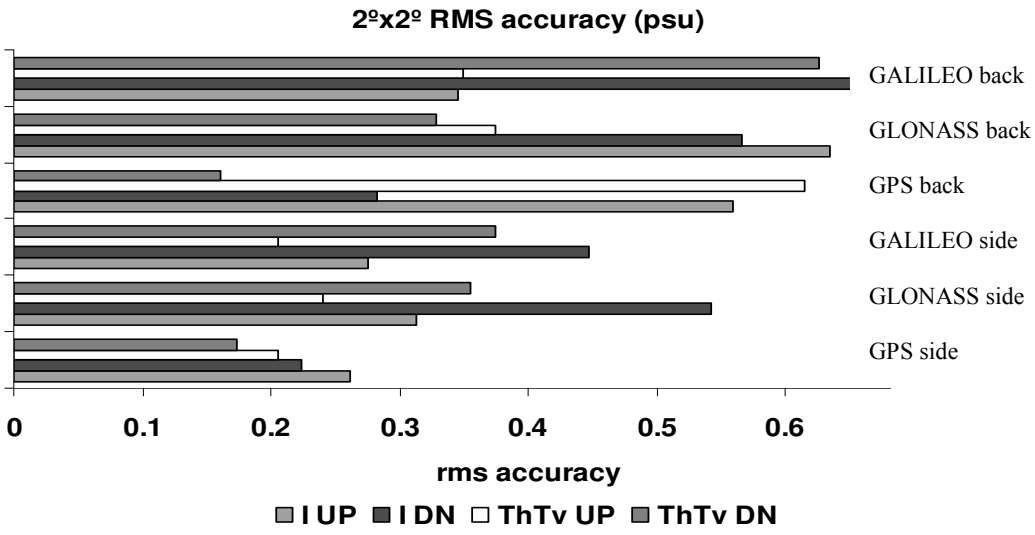

Fig. 6.7 2°x2° rms accuracy for the different constellations and configurations (right side), for both polarimetric mode and satellite passes (indicated in the legend below).

The next step is to combine all the information in Table 6.2 to get a comprehensive retrieval, which considers all the specular points (with their corresponding *mss* fields) that could be collected in the SMOS FOV in the ROI on each specific day. As mentioned, the aim is to increase the number of specular reflection points available to perform better salinity retrieval after spatio-temporal averaging.

Thus, all the single-overpass *SSS* retrievals at the pixel level in the different configurations have been merged to obtain a blended retrieval for each day, and then monthly averaging has been performed as described before. Pixels for which two or more *SSS* values from different constellations were simultaneously available have been averaged. Figures 6.8a through 6.8d show the monthly weighted errors in four cases for fully polarimetric mode, emphasizing the inhomogeneous sampling in the different configurations.

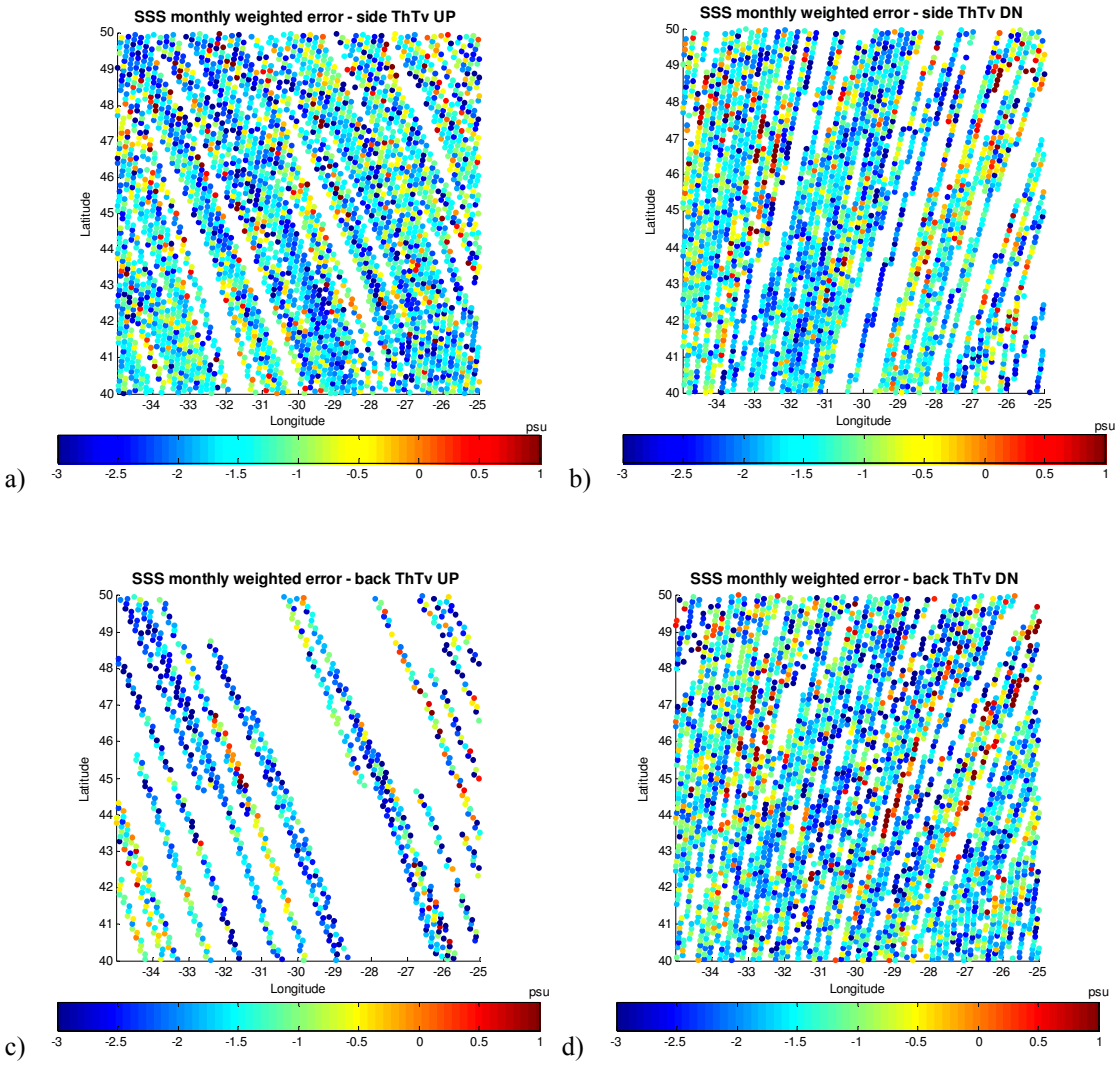

Fig. 6.8 Monthly ROI weighted errors relevant to specular points for multiple blended constellations in full-pol mode for a) side configuration, ascending pass b) side configuration, descending pass c) back configuration, ascending pass and d) back configuration, descending pass.

In most cases, even if the number of sampled pixels has definitely increased, the problem lies in the fact that many of them have never been imaged in the whole month or just a few times, hampering the averaging improvement. In spite of this, the blending of different GNSS-R derived *mss* data is however able to produce an improvement large enough to get closer to the mission requirements (0.1 *psu* accuracy after spatio-temporal averaging) in some cases, with the key advantage of not depending on the availability of simultaneous and collocated wind speed data (or any other appropriate sea state descriptor).

Table 6.3 summarizes the results gathered in the merged constellations approach, for both polarimetric modes, ascending and descending passes, and side and back tandem satellite positions. As is shown, not all the configurations presented an effective improvement with respect to the GPS taken as the default control constellation. However, it should be noticed that the *SSS* retrieved accuracy in 2°x2° boxes is consistent with previously obtained results [Sabia et al., 2006], especially when referring to auxiliary wind data different from those that generated

brightness temperatures. In fact, when dealing with a quasi-realistic situation in which models to generate and invert the data are different, using either wind speed data or *mss* fields different from the original inputs provide similar *SSS rms* error results.

Table 6.3 Coupling of GPS, GLONASS, GALILEO and SBAS Constellations (in bold, configurations achieving an improvement by merging different constellations data).

Constellation	Configuration	Mode	Satellite Pass	Monthly Bias	Monthly Rms	Rms 1°x1°	Rms 2°x2°
Multiple	Side	*I*	UP	-1.590	**1.032**	0.284	**0.169**
Multiple	Side	*I*	DN	-1.507	1.131	**0.453**	0.308
Multiple	Side	*Th*/*Tv*	UP	-1.550	**0.912**	**0.229**	**0.118**
Multiple	Side	*Th*/*Tv*	DN	-1.463	**0.879**	**0.303**	0.210
Multiple	Back	*I*	UP	**-1.882**	1.122	0.722	**0.558**
Multiple	Back	*I*	DN	-1.540	**1.153**	**0.467**	0.292
Multiple	Back	*Th*/*Tv*	UP	**-1.808**	**1.003**	**0.532**	**0.362**
Multiple	Back	*Th*/*Tv*	DN	-1.547	0.999	**0.307**	0.176

6.5 Conclusions and Insights

In this study, the potential improvement by using GNSS-R opportunity signals as auxiliary data in the *SSS* retrieval procedure applied to the SMOS mission has been studied and evaluated [Sabia et al., 2007b].

This analysis is the natural continuation of a study aimed to stress the dependence of the retrieved *SSS* on the different auxiliary data (*SST* and U_{10}) used in the retrieval procedure.

Since neither the *mss* fields, nor their relationship with other geophysical parameters describing the sea state (e.g. wind speed) currently exist, the *mss* values have been derived from the wind speed fields at the GNSS-R specular reflection points that a theoretical SMOS companion satellite flying side-by-side or 500 km behind SMOS would measure. These *mss* values have been used as auxiliary data in the *SSS* retrieval procedure.

The effectiveness of this auxiliary data set was limited by two main factors:

- The limited number of GNSS specular reflection points in each overpass that does not allow efficient spatio-temporal averaging, and
- The assumed large uncertainty in the sea state (in this case parameterized in terms of *mss*(U_{10}) only) introduced by the non-linearity of the *mss* at high U_{10} values (Fig. 6.1b).

In order to overcome these problems, the *mss* fields cannot have an uncertainty larger than 5% of the *mss* value, and several GNSS-R derived *mss* (from GPS, GLONASS, GALILEO and SBAS) have been used to increase the number of specular reflection points. Simulation results show that the GODAE requirements can be nearly achieved in specific configurations: side satellite, use of *Th* and *Tv* and ascending passes.

Using GNSS-R signals seems then to provide unsatisfactory results, since the GODAE requirements are not accomplished except in one case, despite the small error assumed on *mss* retrieved with GNSS-R. On the other hand, keeping this in mind, it has to be emphasized that one of the reasons is the coarse sampling of the zone, mostly due to the fact that only the specular point and not a larger glistening zone has been considered. Future research will consider reflections in such larger glistening zone and not only in the exact moments when the specular reflections take place, but within a narrow temporal window in which the roughness can be assumed to remain unchanged. The number of available *mss* points will thus be increased, and better results should be expected.

As it has been pointed out, a major limitation of this study is the lack of a consolidated relationship between the wind speed and the mean square slope itself. In [Marchán et al., 2008], the use of other observables is proposed, namely the area and the volume of the normalized to the maximum *DDMs* (Delay-Doppler Maps). The choice of different observables to be directly extracted out of the *DDMs* should allow the derivation of a direct relationship with the brightness temperature, thus correcting for the roughness-induced T_B change. Both the wind speed and the *SWH* parameters can be linked to the *DDMs*' shape, although it is known that other sea state descriptors affect the *DDM* shape as well as the T_B.

Eventually, the chosen *SSS* retrieval setup is itself defined as to achieve a quasi-realistic configuration, especially considering that there were no restrictions on salinity. Nevertheless, retrieved *SSS* values with multiple GNSS constellations are of the same order of results obtained in the aforementioned previous study [Sabia et al., 2006], whenever auxiliary winds are different from the original.

The main advantage of GNSS-R signals still lies in the spatio-temporal collocation of the measurements and on the expected improvement in the sampling on one hand (just described) and in the *mss* derivation on the other, thus justifying and motivating continued efforts in this direction.

Chapter 7
Sea Surface Salinity Error Budget

In the previous chapters, an analysis of the impact of the auxiliary data on the salinity accuracy has been performed. These results have been rearranged and used within a wider perspective study: the computation of a retrieved salinity error budget. The basic approach has been already applied in a specific part of the *SynAux* study, whereas the different contributions to the final errors have been isolated and quantified. This concept has been extended with the aim of generating a quantitative binned determination of the salinity accuracy concerning the different error sources. The relevant features are to propagate instrumental errors in terms of salinity accuracy at Level 3, and establish how other factors, such as the Faraday rotation or the Sun contamination, determine errors in the final product.

It should be stressed that the errors are provided at Level 3 to be consistent with the mission requirements and propagate several effects that have been studied at Level 1, and whose final errors contributions were unknown. Nevertheless, the criterion applied to average, both spatially and temporally, the L2 results is straightforward, using a simple weighted average procedure. In turn, it is known that several specific techniques, such as Optimal Interpolation [Bretherton et al., 1976; Wunsch, 1996] or Ensemble Kalman Filter [Evensen and van Leeuwen, 1996], are suitable to optimally average spatially-distributed data or separate different spatial regimes. In the future, in order to obtain the best L3 products, these techniques will have to be applied. At this stage, this is out of the scope of the study, which aims to gather L3 data as a matter of comparison with the GODAE specifications, but further work may be performed to drag further information out of these results.

Another key aspect which has been already mentioned in the salinity retrieval issues chapter is the fact that different retrieval setups lead to different accuracy results, and complete awareness of this issue should be acknowledged. To this end, the error budget study has been conducted in two different configurations: one considers restrictions on salinity, whilst the other lets the salinity be a free parameter. In order to link these results to each other, a study concerning the *a priori* error on *SSS* as tunable has been conducted, spanning from very small error (too constraining restriction in the algorithm), to wide uncertainty which is the last step before a non-constrained configuration.

7.1 Salinity Retrieval Error Budget

Accurate generation of global salinity maps is closely linked to high instrument performances and adequate data processing. To support this, a comprehensive salinity error budget analysis is helpful to identify the magnitude of the error sources associated to the retrieval, and above all to establish a hierarchy of the issues to be tackled in the definition of the upcoming inversion scheme. An error budget study allows studying techniques to cancel/mitigate the bias found in the measurements, and evaluating the impact of specific features such as Sun glint or Faraday rotation in the *SSS* error.

A significant characteristic of this study is that all simulations have been carried out by using the SEPS Simulator. Brightness temperatures maps generated by SEPS have thus the realistic bias induced by the NIR, the image reconstruction algorithm itself, and the pixel-dependent radiometric accuracy. The UPC Level 2 processor software package is used to control the different sub-modules of the salinity retrieval scheme. Moreover, the L2 processor is in charge of performing the bias mitigation/cancellation at brightness temperatures level, as coming from SEPS $T_B s$.

Following the approach of [Yueh et al., 2001], in the framework of the Aquarius mission, an attempt of providing an SMOS error budget table has been performed [Sabia et al., 2007c]. For clarity, error sources have been binned into:

- Instrument and image reconstruction algorithm errors,
- External noise sources, and
- Geophysical (emission model and auxiliary data) errors.

Each of the mentioned items will have a certain degree of impact in the *SSS* retrieval scheme, and separating the different contributions to the final error in *SSS* will be useful in the assessment of the ocean salinity error budget.

The first class of errors accounts for errors arising at Level 1 (brightness temperatures maps), deriving from instrumental features and from the image reconstruction algorithm. A usual distinction is done between the two radiometric noise sources: the radiometric accuracy, that represents a spatial pixel-by-pixel random noise, and the radiometric sensitivity, which is in turn a temporal random noise. A table sketch (Table 7.1) is helpful to clarify this distinction, and to stress the concept of bias in the measurements.

Table 7.1 Instrumental errors divided according to their nature.

Instrumental errors	**Systematic**	**Random**
Space	Bias	Radiometric accuracy
Time	0	Radiometric

7.1.1 Error Budget General Features

A master scenario has been created with the aim of defining a simulation baseline over which the comparisons of the error budget study will be performed, addressing one by one the contribution of each single parameter.

The selected zone is a representative large area in the Mid-Atlantic, similar to that used in the previous studies. Monthly simulations have been considered, propagating and then averaging 10 overpasses over the selected area, resulting into 730 snapshots. To avoid the lower sensitivity of the brightness temperature to *SSS* at colder sea temperatures, the overall simulation has been performed in summertime. The ascending passes have been selected, and simulations have been performed in dual-pol configuration. Retrieval has been performed both in the antenna reference frame (*Tx* and *Ty*), and using the first Stokes parameter (*I*).

Two major differences can be noticed in the analysis approach between this error budget study and both the *SynAux* and the GNSS-R study. While in these two studies the brightness temperatures were generated by IFREMER, in this study the SEPS simulator (described in chapter 4) has been used. This means that the T_BS available in this study are more realistic and suffer from the features related to the instrument, and to the image reconstruction algorithm, which is also part of the objective of the study.

On the other hand, it is important to stress that only constant input/auxiliary data have been considered, in order to let the single contribution of the parameter under study to be unique and evident in the successive simulations. The considered values are: 35 psu for the salinity, 15 °C for the *SST*, and 10 m/s for the wind speed. For the same reasons, the controlled master scenario is simulated without radiometric noise.

The baseline semi-empirical model considered in the simulations is the piece-wise linear fit to Hollinger measurements [Hollinger, 1971], whilst the dielectric constant is parameterized using the Klein and Swift model [Klein and Swift, 1977].

It is fundamental to underline that in this first approach the overall simulation scheme has been conceived considering restriction in *SSS* with a fixed error (σ_{SSS}) of 0.5 psu (weighting factor of the restriction in salinity). This value has been arbitrarily chosen, to avoid constraining the cost function too much. A sensitivity study of the variation of the *SSS* error with respect to the value of σ_{SSS} will be discussed afterwards. Restrictions on *SST* and U_{10} are considered, as well. The values of the expected standard deviations in the cost function are 0.5 °C and 1.5 m/s, respectively. A weighted averaging has been performed in the whole study to ensure homogeneity in the pixel sampling in the different satellite overpasses.

The SEPS simulator has been used in its “light” version, that is, visibilities have been computed by means of an FFT and considering all the antenna patterns to be identical. This will hugely

save computational time, but it will unavoidably introduce some approximations, to the detriment of the full characterization of the instrument features.

Figure 7.1 shows two sample snapshots of SEPS output in the antenna reference frame at X and Y polarizations, while Fig. 7.2 presents a sample of L2 processor *SSS* retrieval.

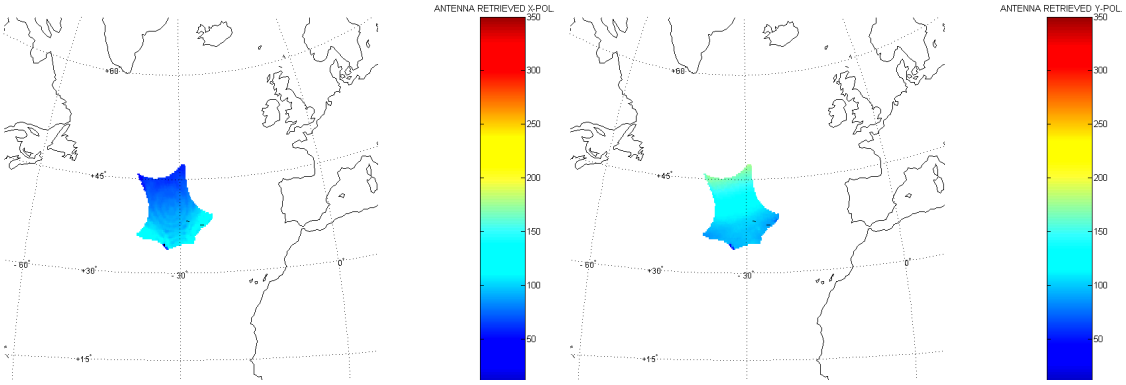

Fig. 7.1 SEPS antenna sample snapshots.

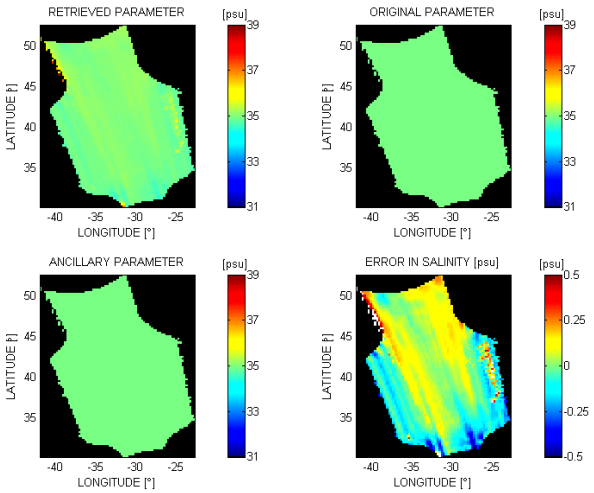

Fig. 7.2 Level 2 processor sample *SSS* retrieval.

The output products of the first part of this study are two tables: the first one is relevant to the bias present in the measurements, whose total effect is just simply added/subtracted to gather the residual offset, and the second one is related the retrieved *SSS* accuracy, whose final error budget is calculated as a quadratic summation.

7.1.2 Instrumental Error Sources

The output coming from the master scenario simulation shows the residual bias present in the measurements and the corresponding *SSS* error variability, specifying the impact of the radiometric accuracy.

Concerning the bias, the values are 0.055 psu in *Tx* and *Ty* retrieval (antenna reference frame), and 0.060 psu using *I* (first Stokes parameter). This is a residual bias component that has not been removed even though the Level 2 bias mitigation algorithm has been applied [Camps et al., 2005c; Talone et al., 2007a].

In these conditions, whereas all the possible sources of errors are taken under control, salinity retrieval cannot be any better than 0.031 and 0.042 psu, respectively. It has to be recalled that these scenarios have been simulated in radiometric ideal case (without thermal noise), but with quasi-realistic instrumental features characterization.

It has to be said that when dealing with almost realistic simulation, a fairly strong bias of 1.5-2 K is still present in the T_B measurements. This systematic L1 bias mainly derives from imperfect calibration and/or drifts in the Noise Injection Radiometer, other than the image reconstruction algorithm itself. This scene-dependent bias has been thoroughly studied and quantified in the past few years [Camps et al., 2005c]. Bias can seriously jeopardize the salinity retrieval; hence, some kind of mitigation/cancellation technique has to be applied. Nevertheless, in the open ocean, it results to be lower and fairly constant within the FOV. Recently, new bias mitigation techniques have been devised, lowering the average bias at FOV down to 1-1.5 K [Camps et al., 2006; Camps et al., 2008]. Salinity bias represents, therefore, the propagation of this effect after spatio-temporal averaging.

Figure 7.3 shows the salinity error (average of the different overpasses) in the selected zone and the corresponding L3 histogram, for both *Tx/Ty* and *I* retrieval. Note how the different overpasses tracks are still visible in the left plots errors as adjacent stripes. The net effect deriving from the evaluation of each single parameter in the following analysis is then calculated by a congruent comparison with these master scenario values.

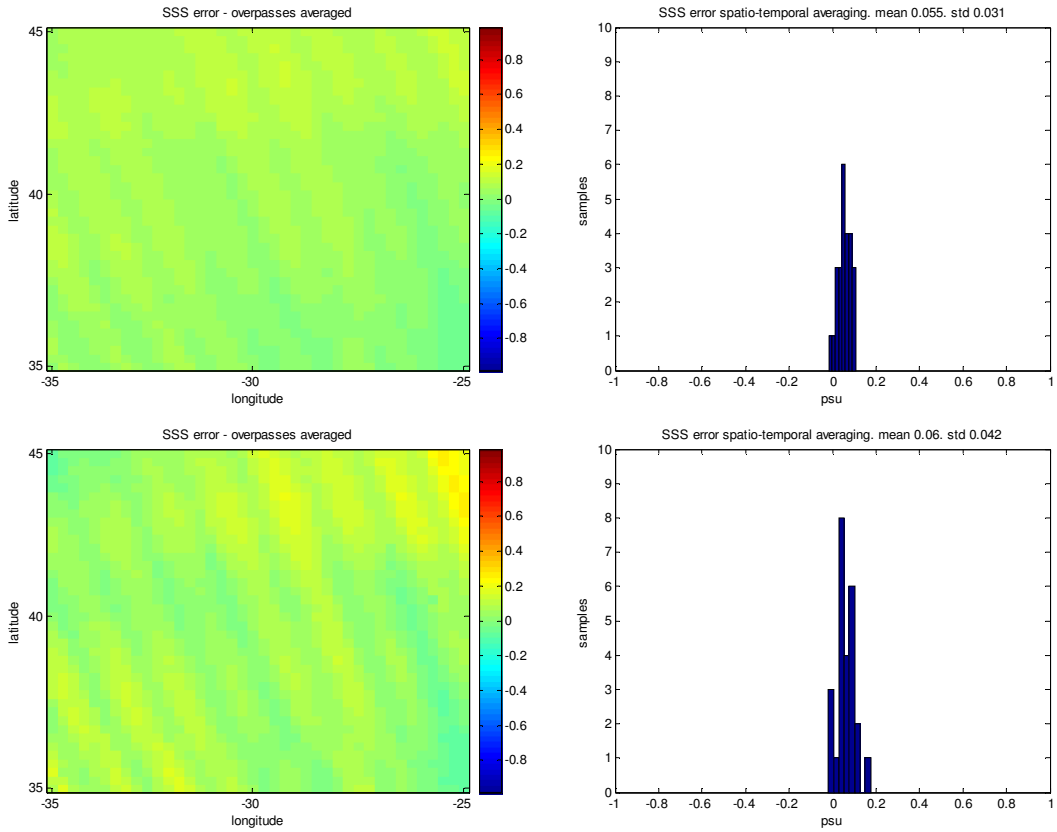

Fig. 7.3 Bias and radiometric accuracy referring to *Tx/Ty* (top) and *I* (bottom) retrieval.

The contribution of the radiometric sensitivity (thermal noise) is not just estimated through a value in the boresight and degradation towards the swath edges, but it has been evaluated as coming from realistic calculations made in SEPS. The comparative effect has been studied considering the nominal integration time (0.158 s) as established in the technical specification of the mission.

As expected, bias contribution is negligible in both configurations due to the nature of this random noise which does not yield any additional systematic error. The quantitative effect of radiometric sensitivity is 0.011 psu in *Tx/Ty* configuration, and 0.021 psu using the first Stokes parameter.

It has to be recalled that the values representing the net effect of each parameter in the tables are calculated as the quadratic difference with the master scenario for what it concerns the accuracy, and by the average of the difference regarding the bias. Figure 7.4 shows the effect of radiometric noise in the final *SSS* error for the both *Tx/Ty* and *I* configurations.

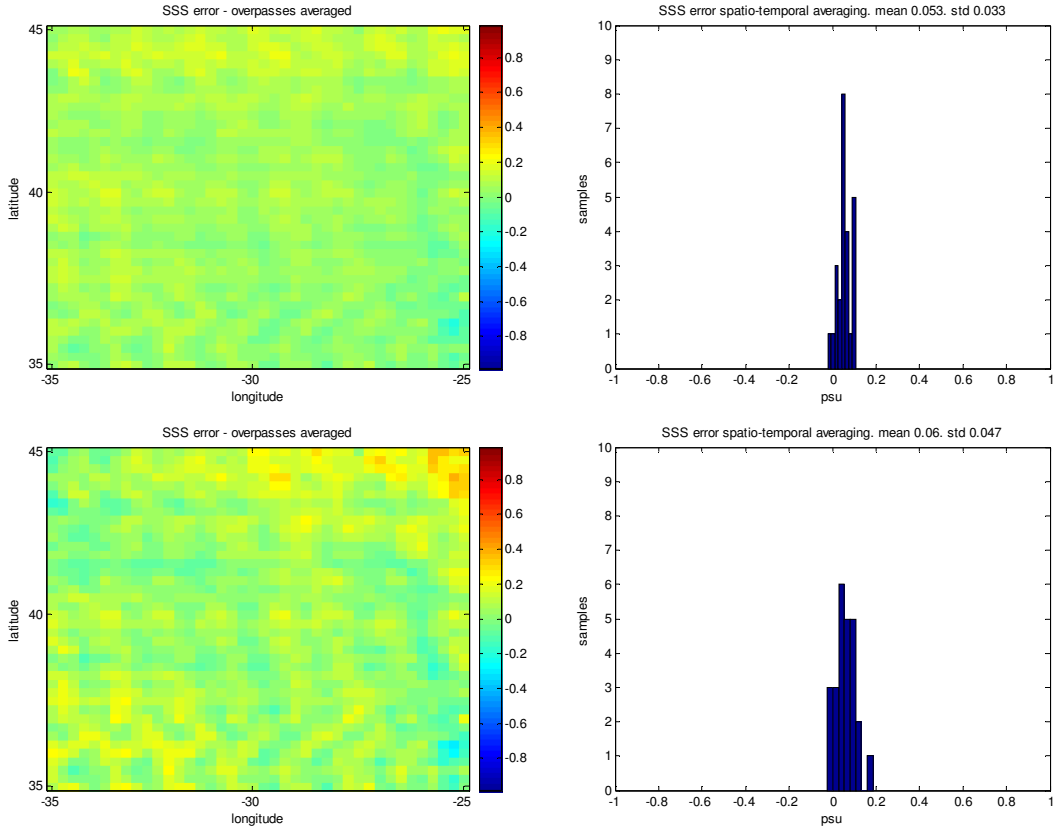

Fig. 7.4 Radiometric sensitivity in *Tx/Ty* (top) and *I* (bottom) configurations.

7.1.3 External Noise Sources

The effect of Faraday rotation has already been studied for the Aquarius mission [Le Vine and Abraham, 2002]. Its contribution might be significant in some circumstances and can, above all, exhibit strong inhomogeneities. It has been studied just for the separated polarizations retrieval, since the effective Faraday rotation using the first Stokes parameter is null (an interesting reason that might push further the application of this parameter [Camps et al., 2003a]). The net contribution to the *SSS* error of this parameter is 0.014 psu, in this specific case, while bias is negligible as can be seen in Fig. 7.5. A further interesting way to address the relevance of Faraday rotation within the final error, is studying which could be its maximum impact, thus providing its effect as a range of values.

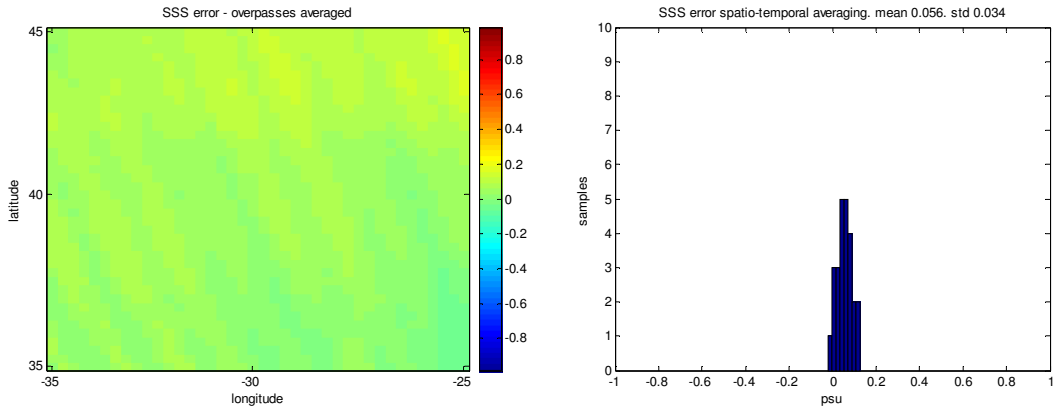

Fig. 7.5 Faraday rotation effect in *Tx/Ty* retrieval.

7.1.4 Geophysical Error Sources

With respect to the geophysical errors and biases arising at Level 2, the subsequent items will address the effect of the emission model choice and the auxiliary data impact. The first contribution studied concerned the dielectric constant model chosen. The already mentioned Klein and Swift model used throughout the whole study has been compared with the more recent Blanch-Aguasca model [Blanch and Aguasca, 2004], derived from measurements specifically tuned at L-band. The idea is to analyze the sensitivity of the retrieved error to a specific change in permittivity parameterizations.

As known from previous studies, a change of the semi-empirical model, (in this case in the dielectric constant parameterization), with respect to the one used for generating the $T_B s$ introduces a negative bias in both polarizations, in this case of -0.046 and -0.066 psu, by using *Tx/Ty* or *I*, respectively. Concerning the accuracy, the results are different by comparing the separated polarizations retrieval and the one using the first Stokes parameter A variation of 0.021 psu is noticed in the first Stokes parameter configuration, whilst in separated polarizations the rms accuracy obtained is slightly better than the master scenario (0.030 versus 0.031) (Fig. 7.6). This is not unrealistic, since the dielectric constant is not a source of noise, which unavoidably would worsen the accuracy, but only a parameterization. In this case, using the Blanch-Aguasca model instead of that one of Klein and Swift, one would obtain a "better" retrieval in *Tx/Ty* of a 0.008 psu.

On the other hand, the two models considered have been studied in a range where both present a good matching, whereas at different SSTs they present stronger discrepancies. In near future, the comparison with other dielectric model is foreseen to provide a full-range of possible variations due to the choice of different models.

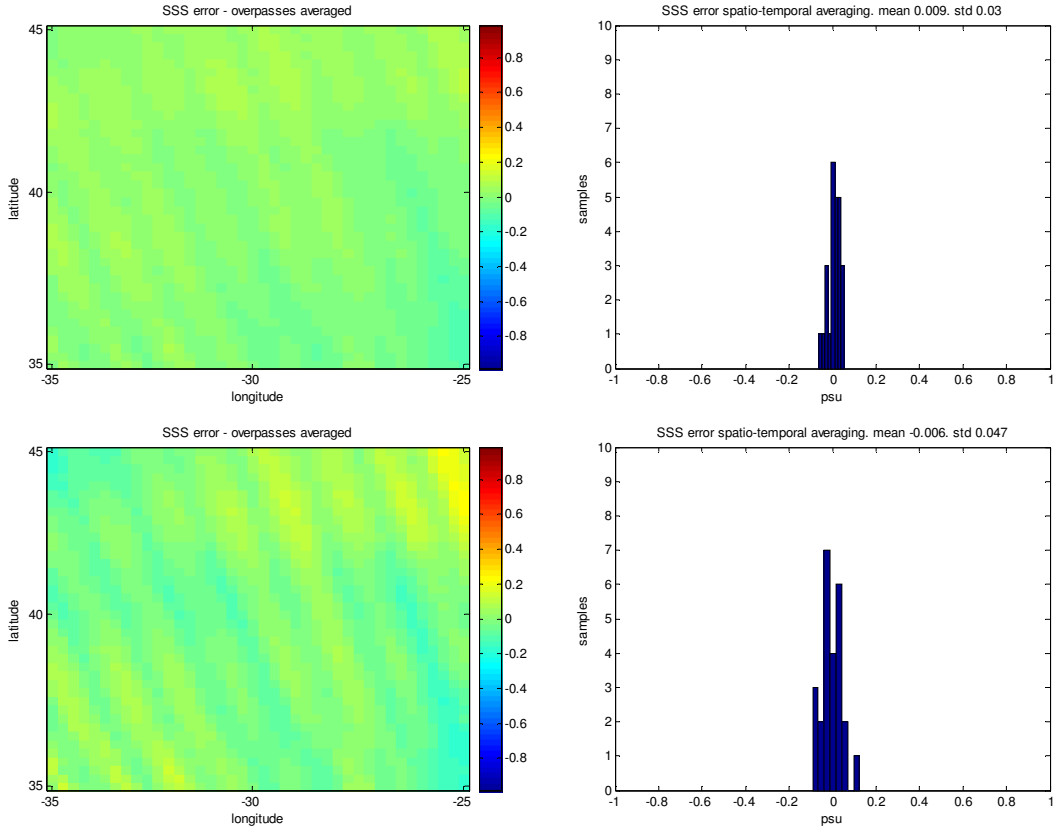

Fig. 7.6 Dielectric constant effect in *Tx/Ty* (top) and using the first Stokes (bottom) parameter.

Another effect that has been studied is that of the presence of foam. Foam is known to be present whenever wind speeds are higher than 7 m/s, which is the case of this simulation. Therefore, the semi-empirical parameterization used might not be complete, because of the lack of the foam emissivity contribution.

The effect of the presence of foam in a different version of the semi-empirical model has been considered according to the work of [Villarino, 2004]. In this case, a comparison has been performed between the classic linear fit to Hollinger measurements and the WISE 2001 field experiment [Camps et al., 2004a] corrected for the foam presence. The WISE foam-free brightness temperature dependencies are as follows:

$$\Delta T_H = 0.25 \cdot \left(1 + \frac{\theta}{118}\right) \cdot U_{10}, \tag{7.1}$$

$$\Delta T_V = 0.25 \cdot \left(1 - \frac{\theta}{45}\right) \cdot U_{10}, \tag{7.2}$$

whilst the foam-induced T_B dependencies are provided from FROG data [Camps et al., 2005a] as a function of the incidence angle and the *SST*:

$$\Delta T_H^{foam}(\theta) \cong \left(1.132 \cdot 10^{-4} \cdot \theta^2 - 9.595 \cdot 10^{-3} \cdot \theta + 2.729 \cdot 10^{-1}\right) \cdot \mathrm{SST}\,, \tag{7.3}$$

$$\Delta T_V^{foam}(\theta) \cong \left(2.224 \cdot 10^{-4} \cdot \theta^2 - 13.234 \cdot 10^{-3} \cdot \theta + 2.567 \cdot 10^{-1}\right) \cdot \mathrm{SST}\,. \tag{7.4}$$

The sea foam coverage fraction can be expressed according to [Monahan and Lu, 1990], but in this study it has been considered the formulation provided by WISE 2001 [Camps et al., 2004a], since it is independent from the air-sea instability:

$$F^{[WISE]} = 0.43 \cdot 10^{-6} \cdot U_{10}^{3.6824}\,, \tag{7.5}$$

the total WISE/FROG sea emissivity model can be expressed as:

$$\Delta T_B(\theta, pol) = F^{[WISE]} \cdot \Delta T_{H,V}^{foam} + \left(1 - F^{[WISE]}\right) \cdot \Delta T_{H,V}^{[WISE]}\,. \tag{7.6}$$

Eventually, the brightness temperature of the sea surface can be modeled as a flat term plus a signal modulation due to the sea state effect as follows:

$$T_B(\theta, pol) = SST \cdot \left(1 - \left|\Gamma_{H,V}(\theta, \varepsilon_r(f, SST, SSS))\right|^2\right) + \Delta T_B(\theta, pol)\,. \tag{7.7}$$

This was done with the aim of investigate if the presence of foam might be of some relevance in terms of the *SSS* error. It has to be said that WISE 2001 fit should already include foam information since they are real data, but measurements over 7 m/s were relatively sparse, and this is exactly the limit above which foam occurrence is higher. This justifies the analysis of foam contribution. On the other hand, it has to be said that foam is just introduced in a linear way, and characterizing only one type of foam [Camps et al., 2005a].

The variation due to the presence of foam is again better than the simulated master scenario accuracy, 0.018 psu using *I*, and 0.026 psu in *Tx/Ty*. Again, being a parameterization, one should not necessarily expect a worsening in the results. Bias is again negative due to the change of the semi-empirical model for what concerns the sea state descriptor: -0.018 and -0.016 psu, by using *Tx/Ty* or *I,* respectively. Figure 7.7 describes its relevance for *Tx/Ty* and *I* cases.

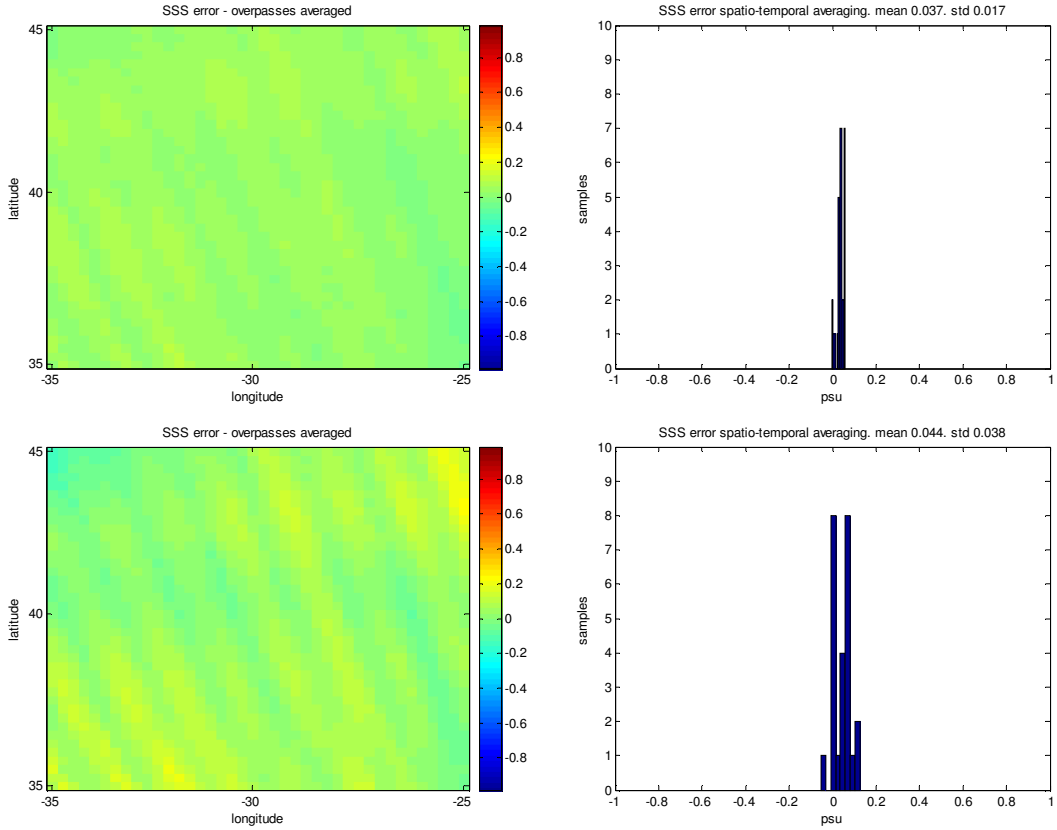

Fig. 7.7 Foam parameterization in *Tx/Ty* (top) and *I* (bottom) configurations.

The following part of the analysis belongs to the previous *SynAux* study, but properly rearranged and tailored to be consistent with this error budget study. As explained, that study concerned the impact of auxiliary data on the *SSS* error and showed a predominant influence of wind speed or, in a wider context, of whichever parameter describing and characterizing the sea state impact on the brightness temperature. Moreover, a first attempt to identify the different error sources was performed. The identification of retrieval discrepancies contributions has been performed by splitting and isolating potential error sources, with an approach which has been the forerunner of the current *SSS* error budget study.

The radiometric noise effect, which was specifically tagged in the *SynAux* study, has been filtered out here in order to have comparable values. Moreover, only spatio-temporally averaged ascending passes of the configurations studied have been considered. The following step has been the removal of the effect of having a different semi-empirical model. A worsening effect is still included in the *SynAux* values, which are the noisy variable reference values that were considered then. On the other end, a compensation effect lies in the fact that these results were obtained using T_B*s* generated by IFREMER without realistic scene-dependent bias. Summarizing, the remaining effects included in those results are the variability of the reference point in the auxiliary data restrictions and the uncertainty on the auxiliary data itself.

An effective way to unwrap the different contributions is to provide range of variations, whereas the lower boundary considers a retrieval using the same auxiliary data as in the $T_B s$ generation and the upper limit reflects the highest excursion found in the error, to be related with using a different auxiliary field.

In the *SynAux* study, the choice of different models introduced a negative bias in the measurements, whose nature is different from the scene-dependent bias commented before. This bias lies in the different model formulation; namely, it is obtained by using the numerical SSA method [Reul and Chapron, 2001] in the direct formulation, and the semi-empirical Hollinger linear fit in the inversion. In [Sabia et al., 2006] it was shown that using instead WISE 2001 model in the inversion lowers down the bias to almost 0.6 psu. This means that this so-called geophysical bias will vary according to the GMF used; to allow comparison between the *SynAux* and the error budget study, this effect has been removed.

The residual geophysical bias related thus to a different auxiliary field is -0.141 psu and -0.214 psu, according to the retrieval configuration (*Tx/Ty* and *I*). Concerning the accuracy, *SST* is capable to introduce an error of 0.026 or 0.028 psu, respectively. Wind speed variation in turn is responsible of the dramatic worsening in the performances of the algorithm as was already known. Depending on the different external wind fields (ECMWF or QuikSCAT) used and their difference with the original field, the results can be as bad as 0.287 psu, far beyond the mission requirements. It has to be stressed, however, that these numbers are related to the specific auxiliary fields considered and different results can be obtained by using other fields. Nevertheless, this quantity is meant to provide a feeling of the impact of such error on the retrieved *SSS*.

The previous GNSS-R study (chapter 6) considered the potential improvement of using opportunity signals and the corresponding *mss* parameters as auxiliary data, instead of using wind speed as sea state descriptor [Sabia et al., 2007b]. The two *mss* values considered in this study are the retrieval in *side* and *back* satellite configuration. Both bias and *rms* accuracy are significantly high. To this end, remember that the effectiveness of this auxiliary data set was primarily limited by the limited number of GNSS specular reflection points in each overpass that did not allow an efficient spatio-temporal averaging and to the uncertain knowledge of the relationship between *mss* and wind speed, both conditions suitable of improvements in the next future. Nevertheless, this technique could be promising considering that at least *mss* values are coincident in space and time with SMOS acquisitions, a fact that is not accomplished with wind speed parameterization.

Summarizing, Tables 7.2 and 7.3 describe the overall *SSS* error budget as commented above and the different contributions as L3 *SSS* error in psu. Results coming from previous studies are illustrated in Italic. Results with stars relate to the foam and dielectric constant issues described before.

Table 7.2 Error budget – Bias.

Items	***Tx/Ty* (psu)**	***I* (psu)**
Instrument and Image Reconstruction Algorithm Bias		
1. Radiometric accuracy	0.055	0.060
2. Radiometric sensitivity	-0.002	0.000
External Noise Bias		
3. Faraday	0.001	N/A
Geophysical Bias		
4. Dielectric constant	-0.046	-0.066
5. Foam	-0.018	-0.016
6 and 7a. Geophysical bias	*-0.141*	*-0.214*
7b. mss	*-0.258*	*-0.292*
8. Total error budget surface	0.054	0.060
9. Total error budget aux parameters	0.054/-0.087	0.060/-0.154
10. Total error budget *mss*	0.054/-0.204	0.060/-0.232

Table 7.3 Error budget – Accuracy.

Items	***Tx/Ty* (psu)**	***I* (psu)**
Instrument and Image Reconstruction Algorithm errors		
1.Radiometric Accuracy	0.031	0.042
2. Radiometric Sensitivity	0.011	0.021
External Noise Errors		
3. Faraday	0.014	N/A
Geophysical Errors		
4. Dielectric constant	0.008*	0.021
5. Foam	0.026*	0.018*
6. Sea Surface Temperature	*0.026*	*0.028*
7a. Wind speed	*0.217*	*0.287*
7b. mss	*0.117/0.362*	*0.167/0.557*
8. Total error budget surface	0.036/0.044	0.047/0.055
9. Total error budget aux parameters	0.036/0.220	0.047/0.291
10. Total error budget *mss*	0.122/0.364	0.173/0.559

7.1.5 Total Error Budget Assessment

The general objective of an error budget study is to provide global values which are a synthetic description of the overall ensemble contributions, and whose magnitude can be in this case directly compared with the SMOS mission requirements.

Firstly, the total sum concerning a flat surface has been considered. The contributions considered for the *Tx/Ty* configuration are radiometric accuracy and sensitivity, plus the Faraday rotation. Dielectric constant and foam parameterization are not considered since they could be conceived, as said, as a different master scenario. The total bias contribution is 0.054 psu. The corresponding minimum accuracy value is 0.036 psu. The upper value of this range is constituted from the added uncertainties in the sea surface temperature variability and it is 0.044 psu. Concerning the retrieval with the first Stokes parameter, the corresponding values are 0.047 and 0.055 psu, both being again the lower and upper bounds of the flat surface error budget considering or not uncertainties on *SST* as coming from *SynAux* study. The considered values are in this case the radiometric sensitivity and accuracy, since Faraday rotation is not an issue for the retrieval using *I*. The corresponding bias is 0.060 psu.

Total error budget referring to the auxiliary parameters consider modelization with or without the impact of the different auxiliary wind speed. Results witness the dramatic worsening (up to 0.291 psu) that one could expect due to the auxiliary wind variability. In the next line of the accuracy table, the total error using *mss* estimates from GNSS-R has the lowest value in correspondence with *side* configuration and the highest value in *back* configuration. Note how the lowest value of total error budget using *mss* is comparable with retrieval using "incorrect" auxiliary wind fields. Total geophysical auxiliary bias spans from the best possibility related to the use of the same semi-empirical formulation to generate/invert the data, to the worst case which is related to the already mentioned effect introduced by different model formulation.

7.2 Extended Ocean Salinity Error Budget

In the previous chapters and in this error budget study it has clearly emerged that the definition of the minimization setup and the tuning of the cost function might have a sensible impact in the simulation results. In order to try to foster consensus on these inversion scheme details, and towards the definition of a consolidated minimization function, this error budget study has been extended to include different retrieval configurations [Sabia et al., 2008].

Namely, whether restrictions on *SSS* have to be inserted or not and which is the covariance of the final *SSS* error with the *a priori SSS* field error (σ_{SSS}) are still a matter of debate. The first part of the following study will thus aim at producing an error budget table in which salinity is not constrained by an additional term. This will provide worse results, but will constitute somehow the worst case scenario that will define the upper value of the salinity retrieval.

It should be remarked that this approach has been already used in both the *SynAux* study and in the following the GNSS-R derived analysis. Nevertheless, neglecting restrictions on salinity here is much more challenging providing SEPS quasi-realistic T_B*s* have been used.

7.2.1 Non-Constrained Error Budget

As above for the restricted-salinity study, Fig. 7.8 show the results concerning the non-constrained weighted master scenario, for both *Tx/Ty* and *I* retrievals.

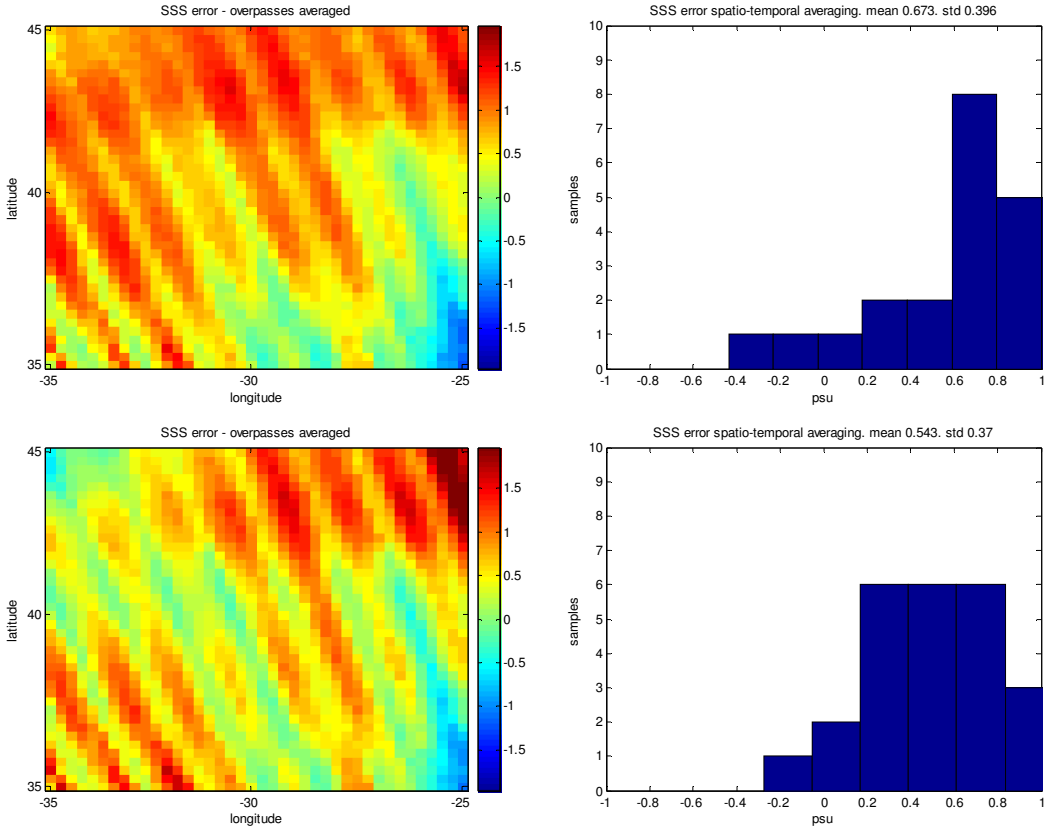

Fig. 7.8 Non-constrained weighted master scenario *Tx/Ty* (top) and *I* (bottom) configurations.

The results indicate a dramatic worsening in the retrieval, as long as the minimization setting is moved towards the non-restricted configuration. As for the restricted configuration case, a weighting procedure taking into account the irregular sampling of the zone has been applied, to enhance the reliability of the retrieval in the pixels with more observations.

Concerning the radiometric sensitivity, the bias is negligible in both cases, while the ratio of its error contribution to the master scenario is of the same of the restricted configuration case. The bias attributed to the Faraday rotation is negligible as well, whilst its net accuracy effect is of 0.157 psu (Fig. 7.9)

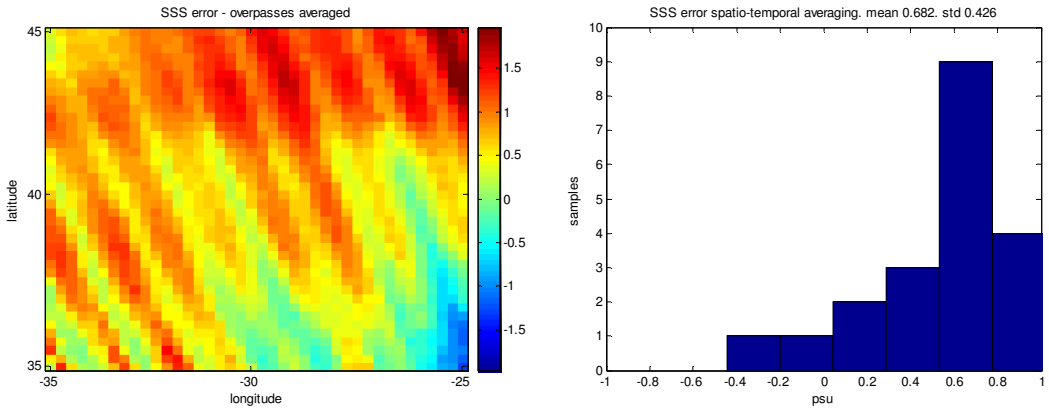

Fig. 7.9 Non-constrained weighted Faraday rotation effect in *Tx/Ty*.

In the non-constrained configuration retrieval, the effect of swapping the semi-empirical model, either changing the dielectric constant model or adding a foam parameterization, is much more evident, as the results embedded in Table 7.4 (bias) and 7.5 (accuracy) witness.

Table 7.4 Extended error budget – Bias.

Items	***Tx/Ty* (psu)**	***I* (psu)**
Instrument and Image Reconstruction Algorithm Bias		
1. Radiometric accuracy	0.673	0.543
2. Radiometric sensitivity	-0.015	0.001
External Noise Bias		
3. Faraday	0.009	N/A
Geophysical Bias		
4. Dielectric constant	-0.614	-0.591
5. Foam	-0.147	-0.135

Table 7.5 Extended error budget – Accuracy.

Items	***Tx/Ty* (psu)**	***I* (psu)**
Instrument and Image Reconstruction Algorithm errors		
1.Radiometric Accuracy	0.396	0.370
2. Radiometric Sensitivity	0.152	0.195
External Noise Errors		
3. Faraday	0.157	N/A
Geophysical Errors		
4. Dielectric constant	0.223*	0.212*
5. Foam	0.301*	0.131*

7.2.2 Auxiliary *SSS* Variability Sensitivity

Since the error on *SSS* auxiliary field (σ_{SSS}) is known to be a critical parameter, it is interesting to address the entire range of variability of the retrieved *SSS* directly related to the variability of

such parameter. Indeed, this would supply direct information of the sensitivity of the *SSS* error to the imperfect knowledge of the reference field itself, with the aim of possibly identifying whether *SSS* restrictions are a bottle-neck for the retrieval and ultimately establish the importance of the constraining terms.

To this end, this parameter is progressively tuned in different simulations starting from very restrictive conditions (σ_{SSS} =0.25 psu) to very large values (up to 6 psu) to approach conditions similar to the non-constrained case. It has to be recalled that the simulation using σ_{SSS} =0.5 psu constitute the restricted master scenario described in the first part of the study. A sample of results in *Tx/Ty* configuration for values of σ_{SSS}= 0.25, 1 and 3.5 psu are shown in Fig. 7.10.

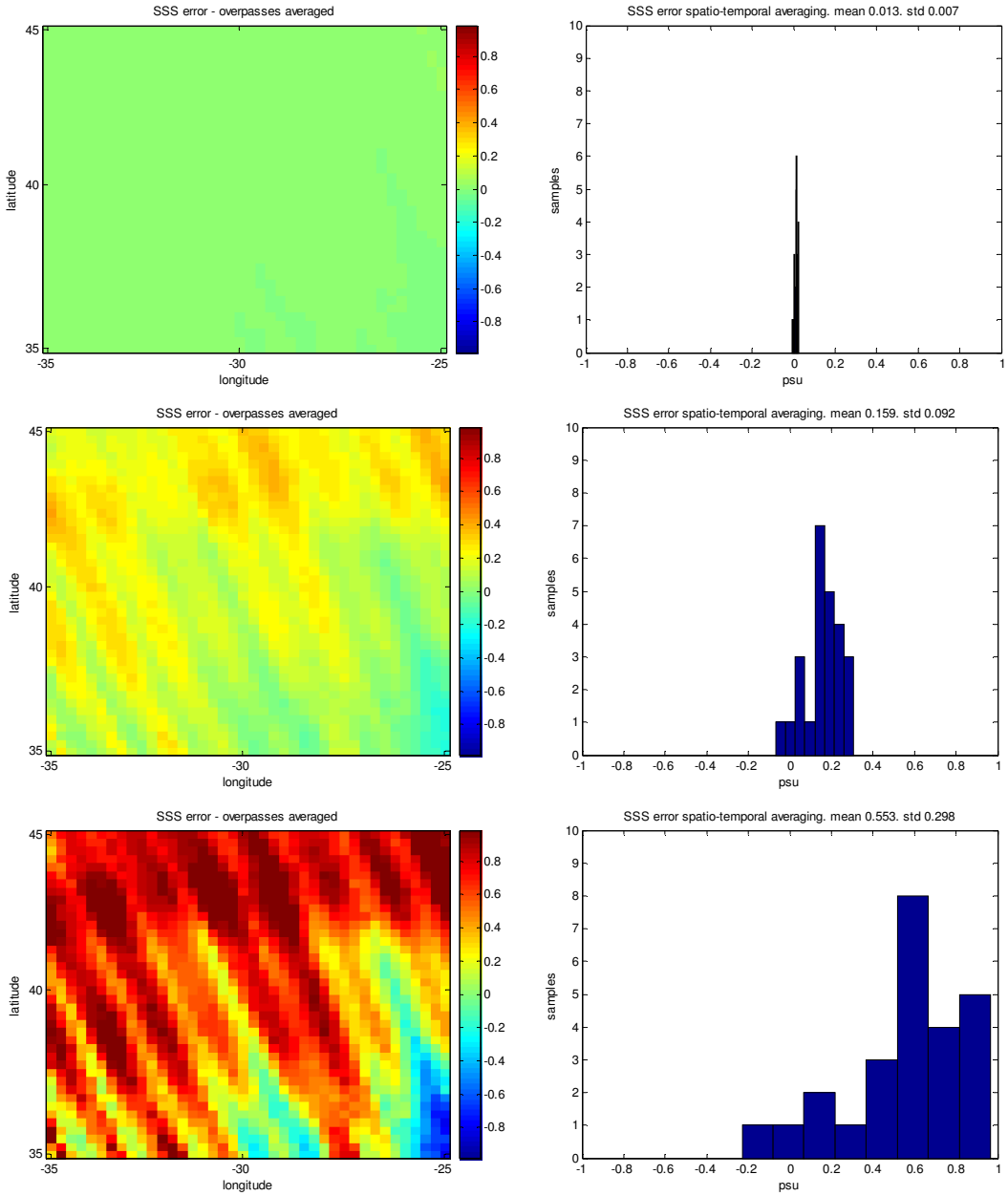

Fig. 7.10 Sample results referred to the sensitivity to the auxiliary field variability in *Tx/Ty*. From top to bottom: σ_{SSS}=0.25 psu, 1 psu and 3.5 psu.

Tables 7.6 and 7.7 illustrate the bias and the *SSS* accuracy results for every step considered in this parameter tuning.

Table 7.6 Auxiliary *SSS* variability sensitivity – Bias.

σ_{SSS} variability - Bias	***Tx/Ty* (psu)**	***I* (psu)**
σ_{SSS} 0.25	0.013	0.016
σ_{SSS} 0.50	0.055	0.060
σ_{SSS} 0.75	0.100	0.120
σ_{SSS} 1.00	0.159	0.182
σ_{SSS} 1.50	0.278	0.289
σ_{SSS} 2.50	0.445	0.413
σ_{SSS} 3.50	0.534	0.468
σ_{SSS} 4.50	0.581	0.495
σ_{SSS} 6.00	0.618	0.515
σ_{SSS} ∞	0.673	0.543

Table 7.7 Auxiliary *SSS* variability sensitivity – Accuracy.

σ_{SSS} variability - Accuracy	***Tx/Ty* (psu)**	***I* (psu)**
σ_{SSS} 0.25	0.007	0.011
σ_{SSS} 0.50	0.031	0.042
σ_{SSS} 0.75	0.058	0.082
σ_{SSS} 1.00	0.092	0.124
σ_{SSS} 1.50	0.159	0.196
σ_{SSS} 2.50	0.257	0.280
σ_{SSS} 3.50	0.310	0.318
σ_{SSS} 4.50	0.339	0.337
σ_{SSS} 6.00	0.361	0.350
σ_{SSS} ∞	0.396	0.370

Note two important features moving towards non-constrained configuration: firstly, after an initial linear behavior the sensitivity tends to saturate. Secondly, at some point there is a cross-over in the bias and accuracy using *Tx/Ty* or *I*, with the latter starting to perform better. Figure 7.11 plots the graphical trends for both bias and accuracy, stressing the results just mentioned. The boundary lines represent the biases and accuracies without restrictions in salinity.

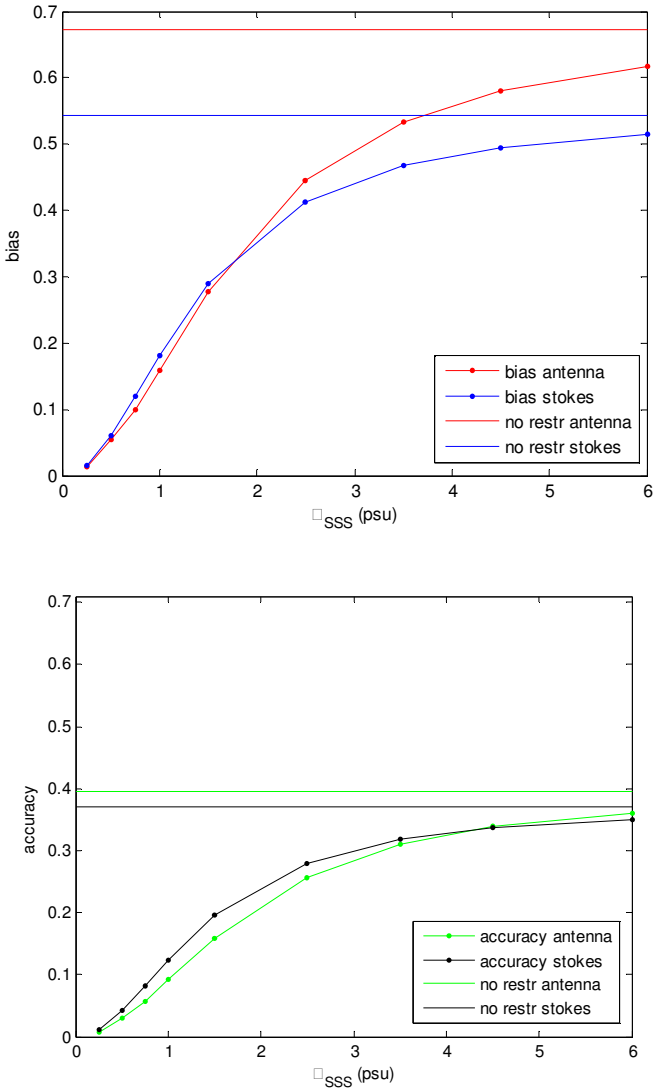

Fig. 7.11 Graphical plots illustrating bias and accuracies of the σ_{SSS} sensitivity study.

The overall final product of the extended error budget analysis is thus a table with restriction on *SSS*, another table without these restrictions, plus a cascade of simulations related only to the master scenario and its evolution as σ_{SSS} increases. The latter would arguably provide some clues on the effective role of *SSS* restrictions.

7.3 Sun Contamination Analysis

The last part of this error budget analysis aims to investigate which is the potential Sun contamination of the SMOS measurements. The Sun impact was originally addressed by considering the corresponding average radiometric noise degradation introduced by the residual error of the sun self-estimation algorithm described in [Camps et al., 2004b].

The problem has now been reanalyzed in a wider perspective in the latest version of the study. The Sun has been directly considered in the simulations, not just referring to the radiometric noise degradation. Two kinds of analyses have been performed: in the first one, the effect of Sun contamination as a whole has been studied, while in the second one the above mentioned Sun self-estimation algorithm has been applied. The first analysis will give insights on the effect of direct Sun not mitigated in the measurements, whilst the latter will provide the residual Sun contamination after its cancellation. Besides, with the aim of providing a complete range of impact of the Sun referred to the solar activities, the considered Sun T_B has been estimated at its minimum and maximum values, respectively [Picard et al., 2004; Reul et al., 2007]. Again, this analysis has been performed in both restricted and non-restricted configuration.

It should be underlined that Sun-contaminated pixels lie in different parts of the 10° width test zone, according to the overpass. This determines a smoothing effect when the *SSS* errors are temporally averaged at pixel level, much more evident in the restricted configuration.

The following figures are sample results referred to retrieval with the first Stokes parameter. In Fig. 7.12 the Sun impact derived by applying or not the Sun self-cancellation algorithm in the restricted configuration is shown.

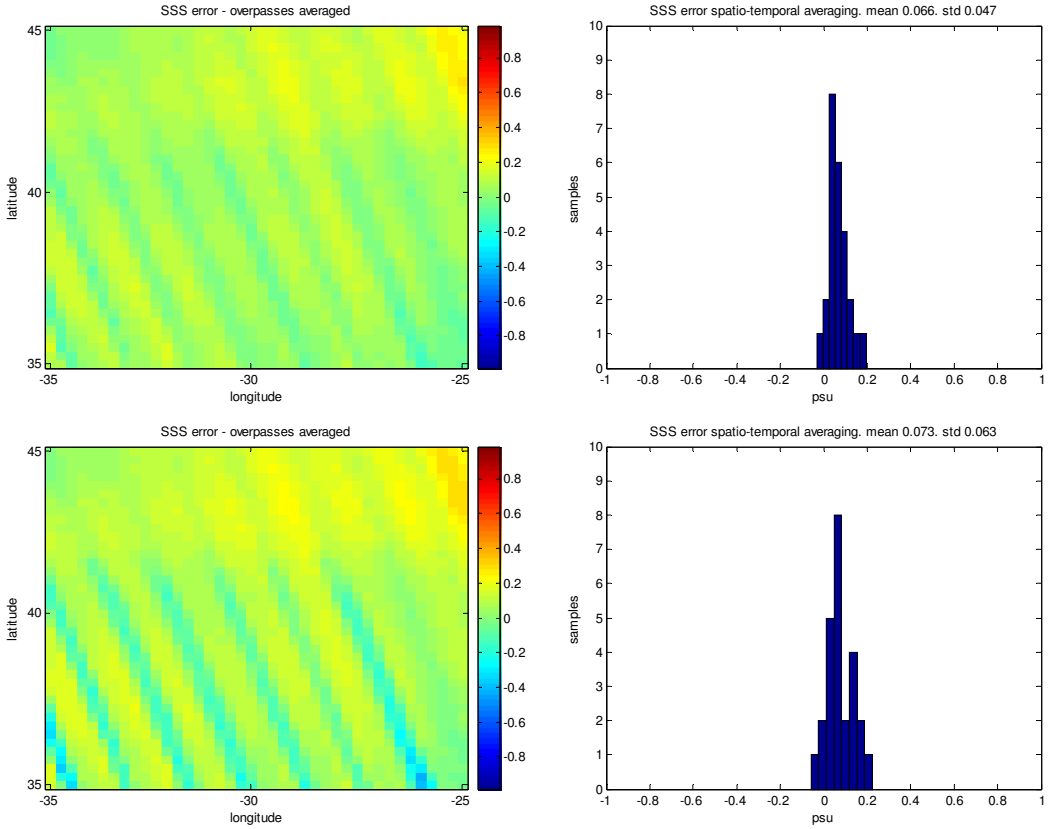

Fig. 7.12 Sample results showing the different Sun impact by applying (top) or not (bottom) the cancellation algorithm using first Stokes parameter in restricted configuration. Sun is at its minimum estimated value.

Figure 7.13 emphasizes the effect of the different Sun T_B at its minimum and maximum value (10^5 and $7{\cdot}10^5$), applying the Sun cancellation, but in non-constrained configuration.

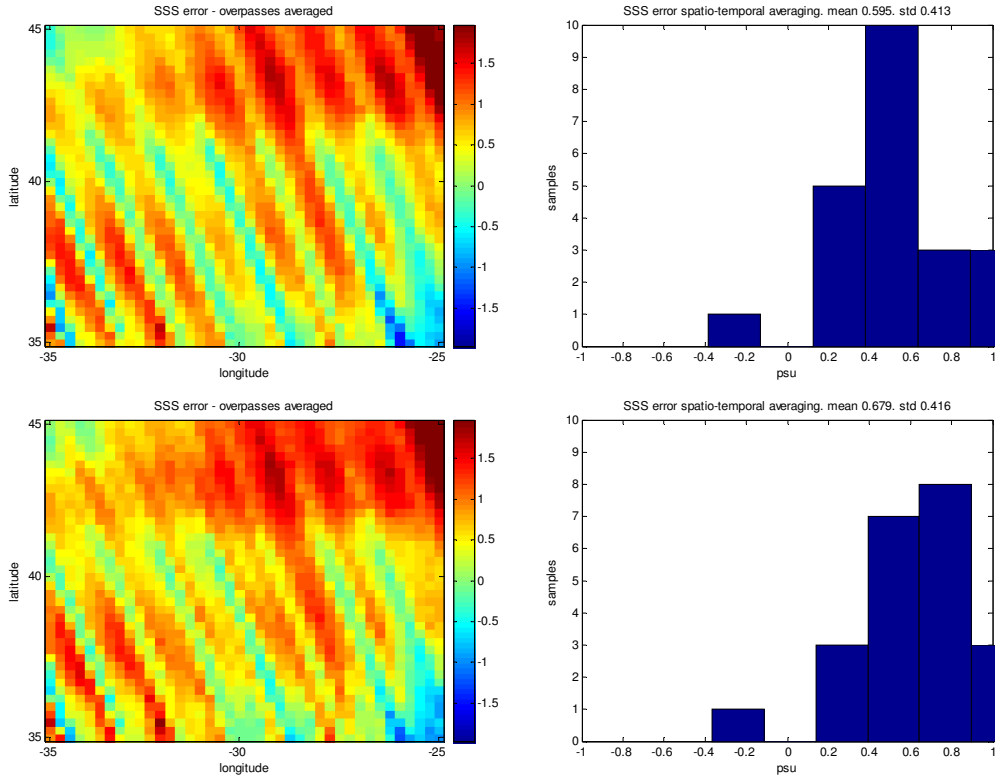

Fig. 7.13 Sample results showing the different Sun impact by estimating its brightness temperature at its minimum (top) and maximum (bottom) value, using first Stokes parameter in non- restricted configuration.

Summarizing, a set of simulations of the quantitative impact of the Sun in both restricted and non-restricted configurations have been performed and the corresponding results are shown in Tables 7.8 and 7.9.

Table 7.8 Sun contamination effect – Bias.

Sun contamination – Bias	***Tx/Ty* (psu)**	***I* (psu)**
Restricted, weighted		
Master restrictions weights	0.055	0.060
Sun MIN, cancelled	-0.002	0.006
Sun MAX, cancelled	0.004	0.017
Sun MIN, NOT cancelled	0.004	0.013
Sun MAX, NOT cancelled	0.012	0.030
Non restricted, weighted		
Master NO restrictions, weights	0.673	0.543
Sun MIN, cancelled, weights	0.067	0.052
Sun MAX, cancelled, weights	0.107	0.136
Sun MIN, NOT cancelled, weights	0.198	0.173
Sun MAX, NOT cancelled, weights	0.767	0.816

Table 7.9 Sun contamination effect – Accuracy.

Sun contamination- Accuracy	***Tx/Ty* (psu)**	***I* (psu)**
Restricted, weighted		
Master restrictions weights	0.031	0.042
Sun MIN, cancelled	0.014	0.021
Sun MAX, cancelled	0.018	0.021
Sun MIN, NOT cancelled	0.034	0.047
Sun MAX, NOT cancelled	0.077	0.118
Non restricted, weighted		
Master NO restrictions, weights	0.396	0.370
Sun MIN, cancelled, weights	0.251	0.184
Sun MAX, cancelled, weights	0.253	0.190
Sun MIN, NOT cancelled, weights	0.382	0.327
Sun MAX, NOT cancelled, weights	0.453	0.427

Looking at the Tables above, a few remarks can be pointed out. In the accuracy table, the impact of the Sun T_B estimation is almost negligible when the cancellation algorithm is applied, whereas its effect is much more evident whenever no corrections are applied. Moreover, despite the direct Sun contamination involves a relatively small percentage of pixels, failing to correct them would imply an important worsening in the results. This effect is enhanced in the non-constrained configuration, as usual.

7.4 Conclusions

In this chapter several activities carried out in the framework of the *SSS* retrieval procedure have been described in the wider context of the ocean salinity error budget, an overall scheme still pending in the SMOS community. Instrumental, external noise sources and geophysical errors have been described, stressing the degree of impact in the comprehensive budget.
Several remarks and considerations stem from this study:

- Salinity retrieval in *Tx/Ty* configuration provides better performances in both bias and accuracy than using the first Stokes parameter in the restricted configuration. The opposite occurs when dealing with non-constrained minimization setting. Further attention will be paid to fully understand these trends, but they seem to be related to the different magnitudes of the background terms in the cost function in the different configurations.

- As already known, the uncertainty on auxiliary wind speed is responsible of an important degradation of the error and it is still the primary issue that will have to be tackled in the prior-to-launch simulation and after-launch retrieval algorithm rehearsal.
- The ideal case (flat surface) error is well within the 0.1 psu prescribed accuracy. Obviously, the uncertainty on the sea state, especially the wind speed characterization that has to be included, will dramatically worsen the results.
- Radiometric sensitivity implies a degradation in the error of almost the same rate for both configurations and polarizations. On the other hand, as expected, this effect is negligible in terms of the bias on the measurements.
- Faraday rotation impact has been studied in the *Tx/Ty* configuration, but it needs further attention considering that it may be variable throughout the seasons and along the position. In the *I* configuration its impact is null.
- Different formulations of the dielectric constant model and of the GMF in general may noticeably modify the results, as it has been further confirmed by using Blanch-Aguasca model and foam inclusion in comparison with the Klein and Swift model and Hollinger linear fit.
- Bias computation indicates that, after a L2 bias cancellation algorithm (necessary anyway due to the bias arising at L1 from realistic image reconstruction algorithm), some residual offset is still present and becomes high in non-constrained configuration.
- The rate of bias and accuracy degradation by tuning the σ_{SSS} parameter has been studied. The cross-over of the retrieval performances and the saturation effect approaching the configuration without restrictions have been described.
- The Sun analysis underlined the need for a proper correction of its contamination; misleading estimation of the Sun T_B is not critical unless in the non-constrained case.

Chapter 8
Sea Surface Salinity Horizontal Variability

Among the issues to be addressed before the SMOS launch, it is interesting to analyze the horizontal *SSS* variability and the prospective capabilities of the retrieved SMOS data to resolve observed oceanographic features. A joint study has been conducted between the UPC Remote Sensing Laboratory and the National Oceanography Centre, Southampton (NOCS), Ocean Observing and Climate department, in the UK.

The purpose of the study is two-fold:

- Probing the capability of SMOS retrieved *SSS* to resolve mesoscale oceanographic features, and
- Testing retrieved *SSS* patterns at increasingly finer spatial resolution.

In other words, this study aims at answering the following questions: "Is any mesoscale (on 50-100 kilometers scale) ocean surface salinity variability detectable in the SMOS retrieved data?" And, if so, "to what extent is it possible to force the *SSS* retrieval, using input data at increasingly higher spatial resolution, without detriment to the accuracy of the retrieval"?

This analysis tries to link previous studies on the role and reliability of auxiliary data (*SST* and wind speed) [Sabia et al., 2006] and the results developed by using comprehensive tools to simulate and process data in the specific SMOS configuration, as the one described in the last chapter [Sabia et al., 2007c; Sabia et al., 2008]. It also provides the first critical and comprehensive assessment of the retrieval capabilities of SMOS in the highly dynamic and challenging Grand Banks region. An extension of this study has been performed in an open ocean Atlantic zone similar to the reference test area previously used.

8.1 Methodology

In order to fulfill the above mentioned tasks, the available tools were:

- OCCAM (Ocean Circulation and Climate Advanced Modeling) project data [OCCAM website] run at NOCS, as source of input/auxiliary data,
- SEPS Simulator, to generate brightness temperature maps, and
- UPC L2 *SSS* processor, to retrieve salinity fields and provide quantitative estimations at different auxiliary data resolution scale.

One year of OCCAM data was available every two days in a zone of roughly 2°x2° located in the North/Western Atlantic (centered at 45° N, 47° W), that exhibited very interesting oceanographic features, especially concerning the salinity fields. The data sets used are at 1, 1/2 and 1/4° resolution, providing for each day meshed values of *SSS*, *SST*, zonal and meridional wind speed. OCCAM data at finer spatial scale resolution are available as well, but at this stage they were considered beyond the scope of the study.

The SEPS Simulator was fed with OCCAM data at different spatial resolutions to generate SMOS-like data, that is, OCCAM T_BS within the selected zone. As seen in Chapter 4, SEPS features include a detailed characterization of the instrument including calibration and radiometric error budget of the system, and an updated image reconstruction algorithm.

One month of brightness temperatures were generated by means of SEPS for ascending or descending overpasses covering the selected OCCAM data zone, once several modifications have been performed within the simulator to allow the ingestion of OCCAM data. Namely, whenever the propagated orbit matched the chosen zone, the available climatology fields formerly used as geophysical inputs in the simulator have been replaced by the OCCAM corresponding values. The average revisit time was nearly 3 days, resulting into 10 overpasses for the considered month, with 73 snapshots each.

L2 processor was in charge of retrieving salinity starting from the brightness temperature maps coming from SEPS. It applies a bias mitigation module and generates as outputs single-overpass Level 2 *SSS* maps.

To be consistent with the requirements established for the SMOS mission, Level 3 data (spatio-temporal averaging at 200x200 km in 30 days) have been produced considering this specific chosen zone as an averaging-box. *SSS* has been retrieved both at Antenna reference frames and using first Stokes parameter. Efforts have been devoted to the optimization of the retrieval module in the L2 processor to adapt it to ingest input from OCCAM.

8.2 Simulations Results

SEPS brightness temperatures maps have been generated in dual-polarimetric mode encompassing the selected OCCAM zone (Fig. 8.1).

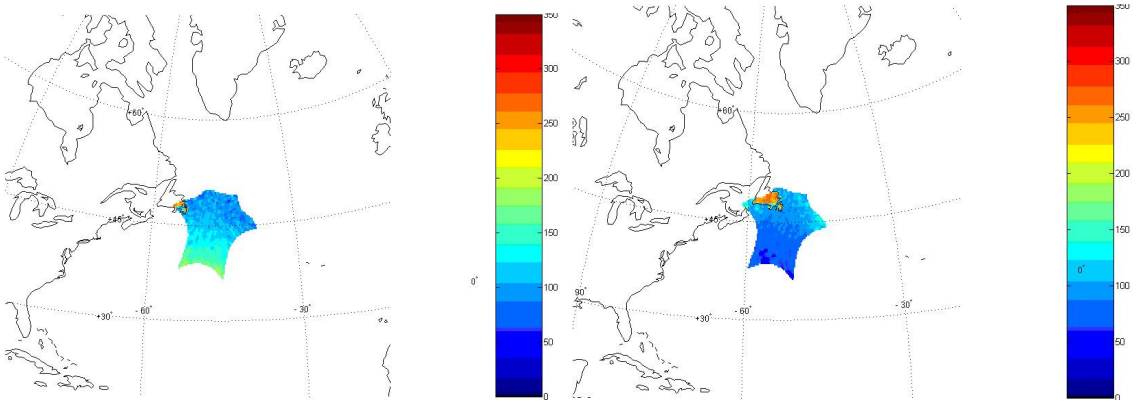

Fig. 8.1 Sample SEPS outputs, at Y-pol (left) and X-pol (right), using 1/2 ° resolution OCCAM data.

Simulations were characterized by a strong bias, due to the nearby presence of the coastline, which needs to be mitigated by the Level 2 processor. As previously described, this scene-dependent bias is a well-known and systematic feature, appearing in every realistic simulation process. However, the magnitude of bias in the field of view is strictly related to the brightness temperature contrast of the scene [Camps et al., 2005c]. In the considered zone the coastline influence (recall that it is an effect at the SMOS FOV scale) is evident, resulting into a huge excursion range of $T_B s$, and thus into a noticeable bias of much larger extent than the standard values corresponding to open oceans.

In addition, in the chosen geographic zone and month (March), the average SSTs were very low which complicated the *SSS* retrieval, since the T_B sensitivity to *SSS* in cold waters decreases sharply [Font et al., 2004]. These issues suggested a rearrangement in the approach followed: the simulated month was shifted towards summertime (July), in order to have warmer SSTs. In this specific zone, the ascending passes would be directly projected towards the land with very strong contamination; to minimize this problem, only the descending passes of the satellite have been considered (Fig. 8.1).

The standard technique of mitigating bias at L2 consists of calculating the difference among the $T_B s$ coming form SEPS and the $T_B s$ obtained directly forwarding an emissivity model, and then subtracting the average value of this bias within the entire FOV (prior to perform the retrieval procedure) [Camps et al., 2005c].

In this case, due to the heterogeneity of the values in the FOV, a specific technique had to be envisaged to reduce the bias, since the standard technique was ineffective. Therefore, the bias was calculated and subtracted straightforwardly only in the OCCAM zone. This provided a reliable technique for the external calibration and subsequent bias cancellation.

According to [*SynAux* Report, 2006], an optimal configuration of the cost function should not constrain the *SSS* parameter, while a priori information should be supplied for what it concerns *SST* and wind fields. The study has been approached consistently but, due to the mentioned

limitations of the zone, it has not been possible to obtain satisfactory results in this configuration. That was not possible even considering a weighted averaging of the *SSS* values, taking into account their relative position in the FOV in the different overpasses.

It should be stressed that the non-constrained configuration was suitable in the *SynAux* and GNSS-R studies described in Chapter 5 and 6, since the T_B*s* considered were not affected by strong biases. In the error budget study (Chapter 7) and in this analysis, where realistic SEPS-generated T_B*s* are considered, the non-constrained configuration provides errors in *SSS* too large. Thus, *SSS* constraints with a standard deviation of 0.5 psu and a reference constant value in the whole area calculated as the mean of the considered *SSS* field constituted the simulation scenario [Sabia et al., 2007a].

Figure 8.2 shows an output of the Level 2 processor referring to a single overpass covering the OCCAM zone. In the left column of the figure the original *SSS* field (top) and the corresponding *SSS* error (bottom), as the difference between retrieved and original, are represented for 1/4° OCCAM resolution.

The selected zone is a small portion of the entire FOV and it is clearly visible because of the contrast with the surrounding zone. This is due to the different input fields leading to different T_B*s*, and to the specific bias correction technique. In the right column a zoom of the figure helps evaluating the magnitude of the *SSS* error. The *SSS* retrieval has been performed in this case in the antenna reference frame, using *Tx* and *Ty*.

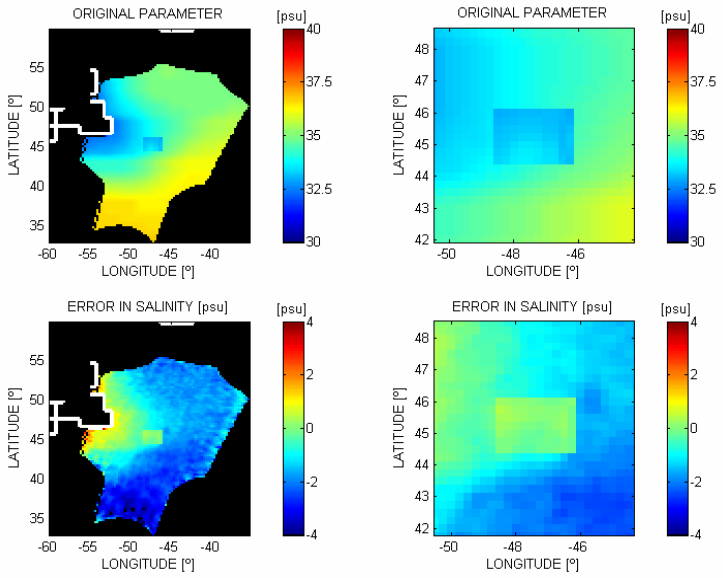

Fig. 8.2 Sample L2 outputs with OCCAM data at 1/4° resolution. Right column: zoom of the original *SSS* and *SSS* error, respectively.

As in the previous studies, to compare results with the SMOS requirements, Level 3 spatio-temporal averaging is needed. The different *SSS* errors have been collected in the different

passes over the OCCAM zone during the month (10 overpasses). Subsequently, the mean value for each pixel have been plotted, and the statistics within the 2°x2° box coincident with the OCCAM zone provided the resulting bias and *rms* accuracy *SSS* product at Level 3.

Figure 8.3 shows the simulation results with the configuration setup just described, for the case of 1° (top row), 1/2° (mid row), and 1/4° (bottom row) input/auxiliary OCCAM data resolution. In the left and right columns, the original and the retrieved sea surface salinity mean fields have been represented, respectively.

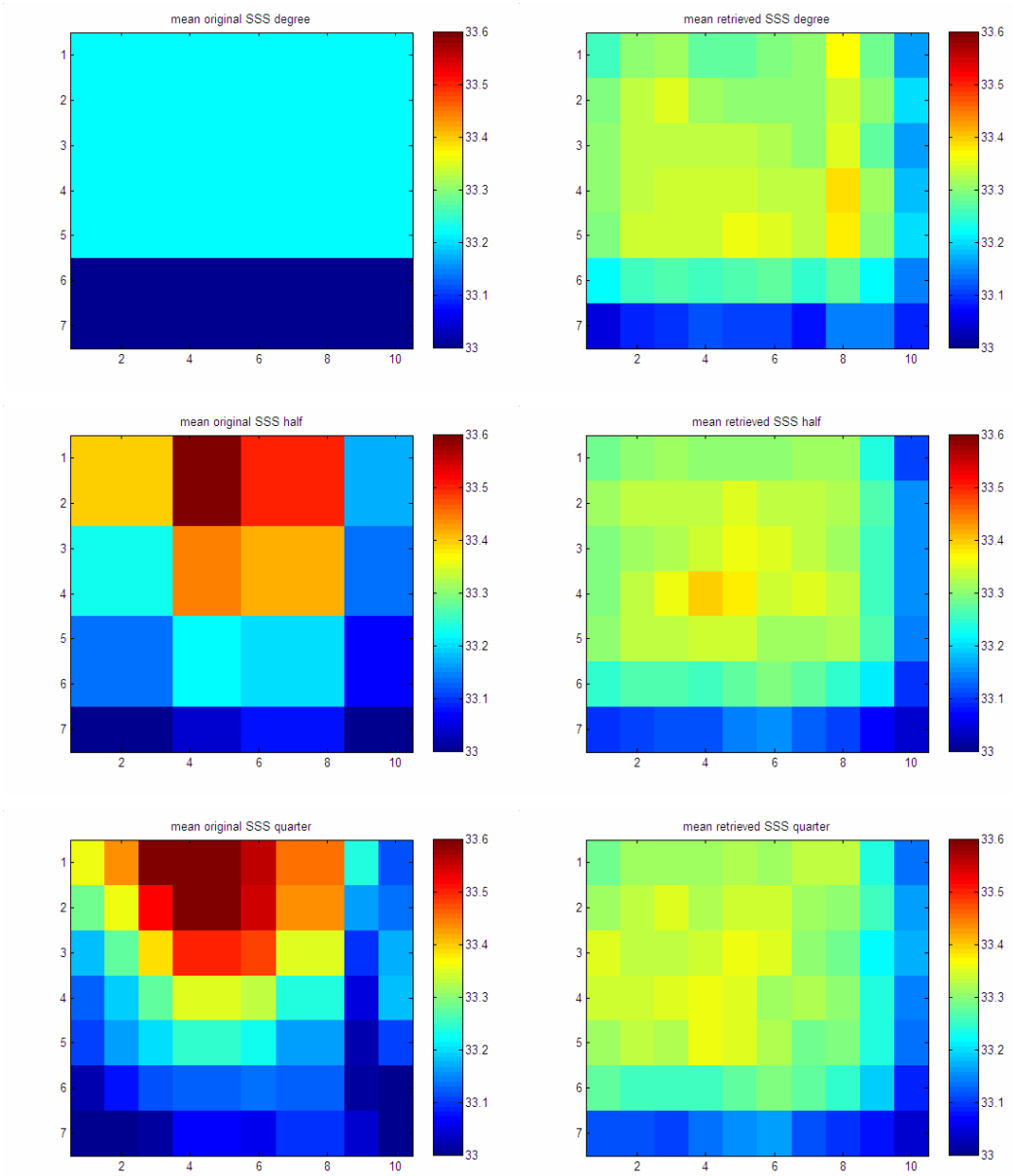

Fig. 8.3 Original (left) and retrieved (right) L3 *SSS* maps, for a 1° (top), 1/2° (mid) and 1/4° (bottom) OCCAM data resolution.

The attention should be drawn to the retrieved *SSS* patterns, whose reproducibility of the original *SSS* features was one of the purposes to be addressed in the study. As it can be seen, in

the cascade 1° - 1/2°- 1/4° the retrieved signature progressively looses the spatial structure of the original fields, reaching the best matching at 1/2° spatial resolution. This suggests that, at a scale of 1/4°, SMOS retrieved *SSS* is no longer capable to reproduce meaningful *SSS* features observed in mesoscale oceanography. It should however be pointed out that 1/4° at these latitudes is already comparable or smaller than the best spatial resolution provided by the SMOS radiometer (30-40 km), although it was not clear if supplying input/auxiliary data at this scale would have been of some benefit both in terms of accuracy of the *SSS* error, or with respect to original features detection.

In Fig. 8.4, the histograms of the *SSS* errors for the different resolutions are provided, along with bias and rms accuracy at L3. The accuracy slightly worsens with increasing resolution, being 0.081 psu at 1°, 0.128 psu at 1/2° and 0.140 psu at 1/4°. These values are within or close to the established mission requirements, even if this is somewhat related to the *SSS*-constrained retrieval setup, a need triggered by the worst-case scenario zone considered.

Apart from the 1° case, residual bias is minimum, since the scene-dependent bias was cancelled in the L2 processor, and no further geophysical bias should be expected since the semi-empirical model function used in the direct and inverse scheme was the same.

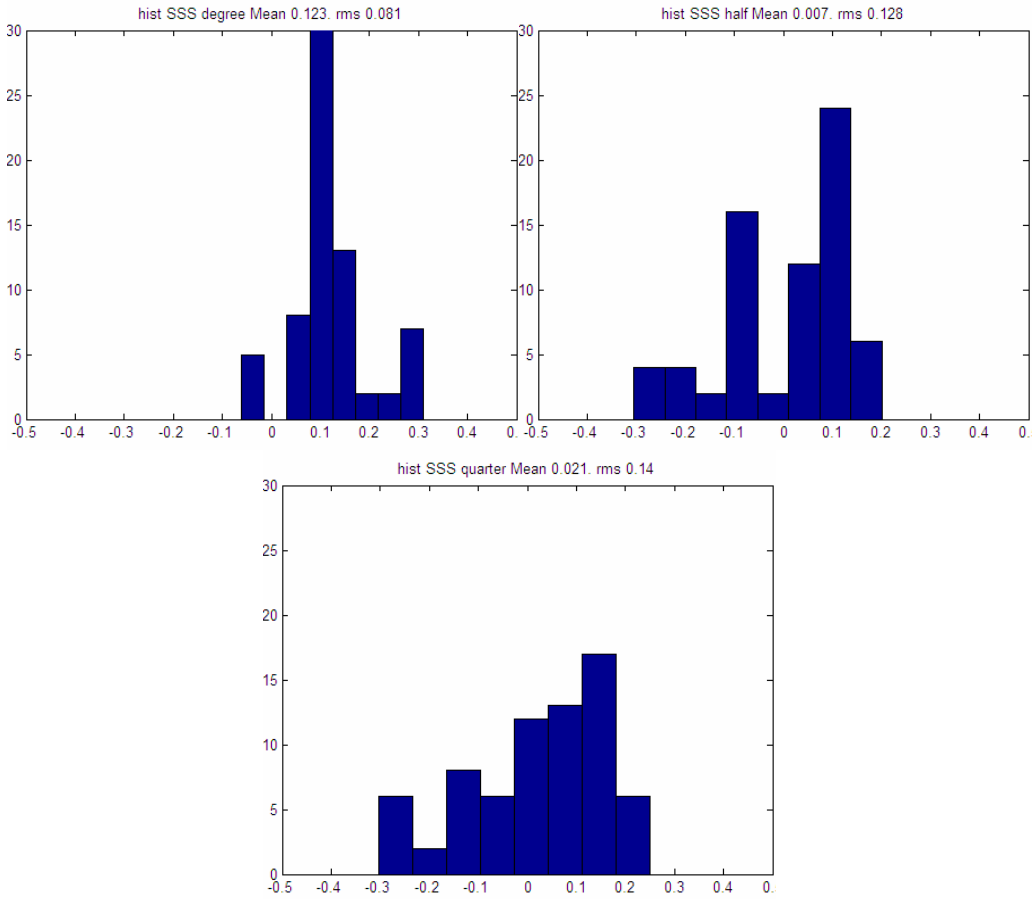

Fig. 8.4 Level 3 error statistics for a 1° (top left), 1/2° (top right) and 1/4° (bottom) OCCAM data resolution.

Therefore, in this particular case, these results seem to limit the actual applicability range of the SMOS retrieved data, perhaps identifying 1/2° as the cut-off resolution scale for several interesting oceanographic phenomena. Again, it has to be stressed that this results are related to the specific test zone, and another case without coastline influence will be discussed later on.
Nevertheless, it is useful to delimitate the lower spatial resolution boundaries of the sensor, and these hints might be helpful in defining proper interpolation nodes at the official SMOS ISEA grid.

8.3 Extended analysis

To evaluate the extrapolations of the former conclusions to other scenarios and configurations, this analysis has been repeated in a different zone. The selected zone was an open ocean area of 10° width comparable to the previous studies test area. Such area presented less challenging conditions, with less bias in the measurements and was devoid of coastline effects.
In this case, only the ascending passes of the satellite have been studied, whilst the bias mitigation applied refers to the standard technique discussed above [Camps et al., 2005c]. Again, the study consists of monthly simulation of 730 snapshots with the same minimization settings than before. SEPS T_B*s* referred to the new zone are shown in Fig. 8.5, while the relevant *SSS* output fields are illustrated in Fig. 8.6

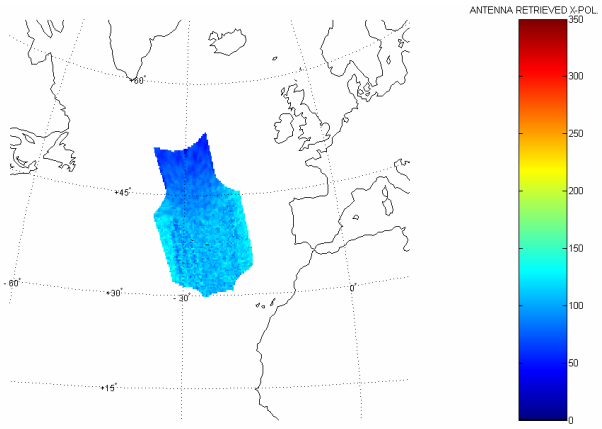

Fig. 8.5 Sample SEPS outputs in the new zone at Y-pol using 1/4° resolution OCCAM data.

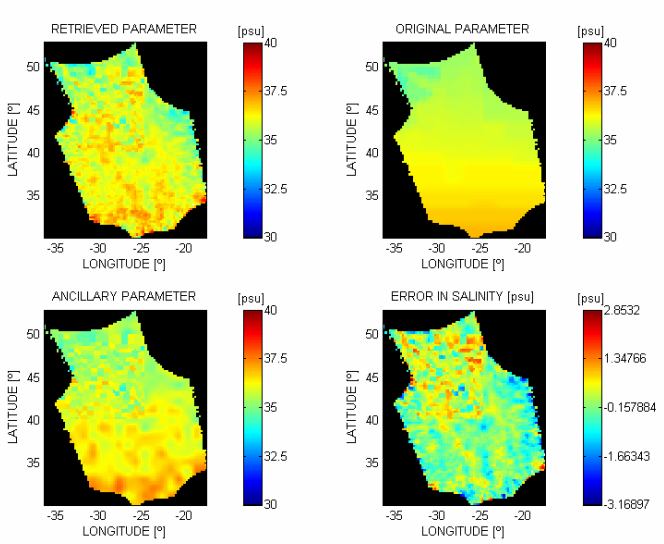

Fig. 8.6 Sample L2 outputs in the new zone with OCCAM data at a 1/4° resolution.

The corresponding results are depicted in Fig. 8.7, for the 1° (ltop), 1/2° (mid) and 1/4° (bottom) cases. The *SSS* original and retrieved fields are represented in the left and right column, respectively.

Conversely to the former zone, this time the retrieved *SSS* is capable of reproducing the original *SSS* patterns even until 1/4°, perhaps better defining some details (like the lower salinity plume in the top left corner) at finer spatial scale.

Figure 8.8 represents the corresponding error histograms. Bias is noticeably higher (ranging from 0.363 to 0.382 psu), but in the former area the offset mitigation had been performed just referring to a small 2°x2° zone. This residual bias unavoidably calls for some external calibration technique. The accuracy slightly improves going towards higher spatial resolution (from 0.182 to 0.161 psu), confirming the capability of reproducing features up to 1/4° scale without detriment in the error.

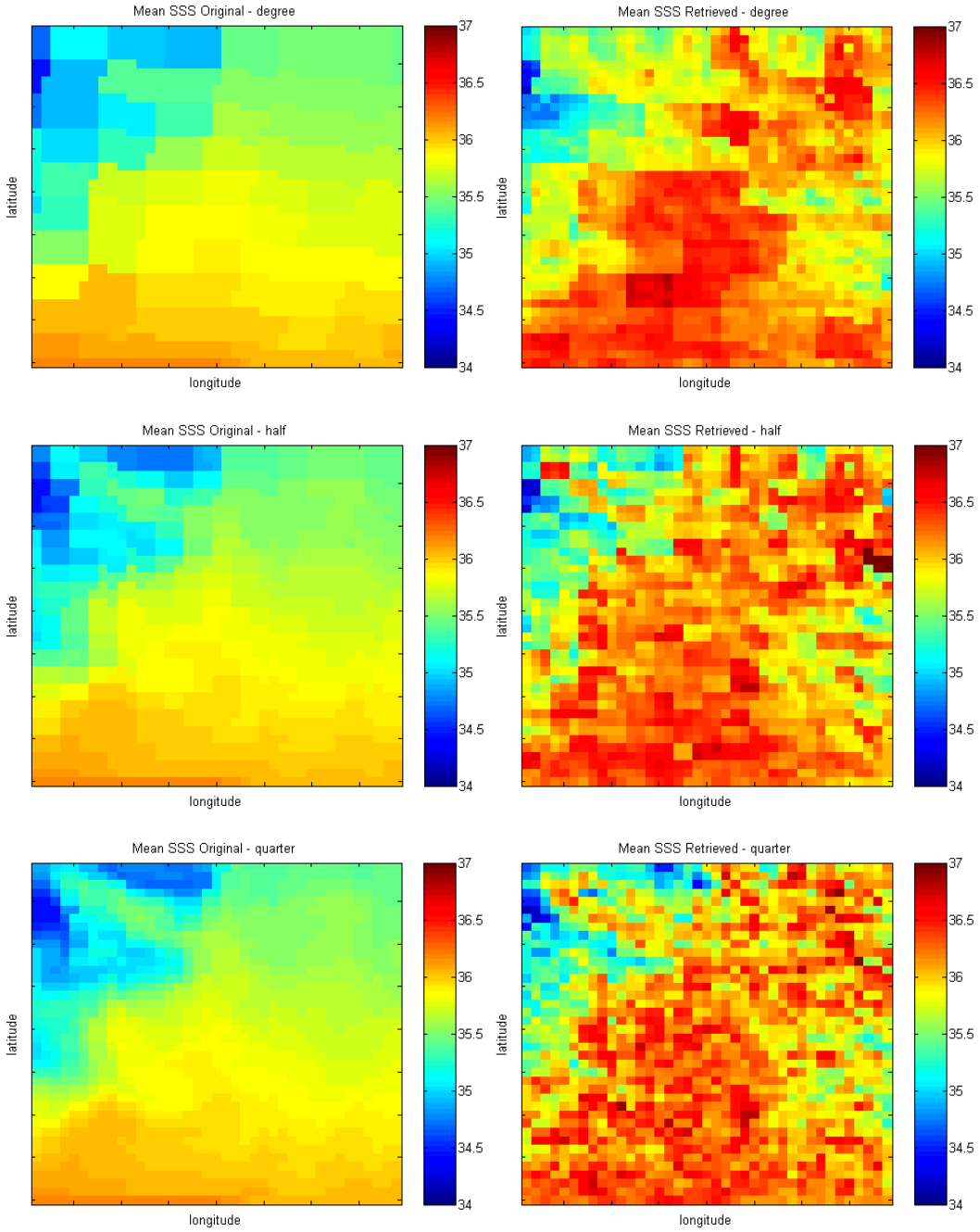

Fig. 8.7 Original (left) and retrieved (right) L3 *SSS* maps, for a 1° (top), 1/2° (mid) and 1/4° (bottom) OCCAM data resolution.

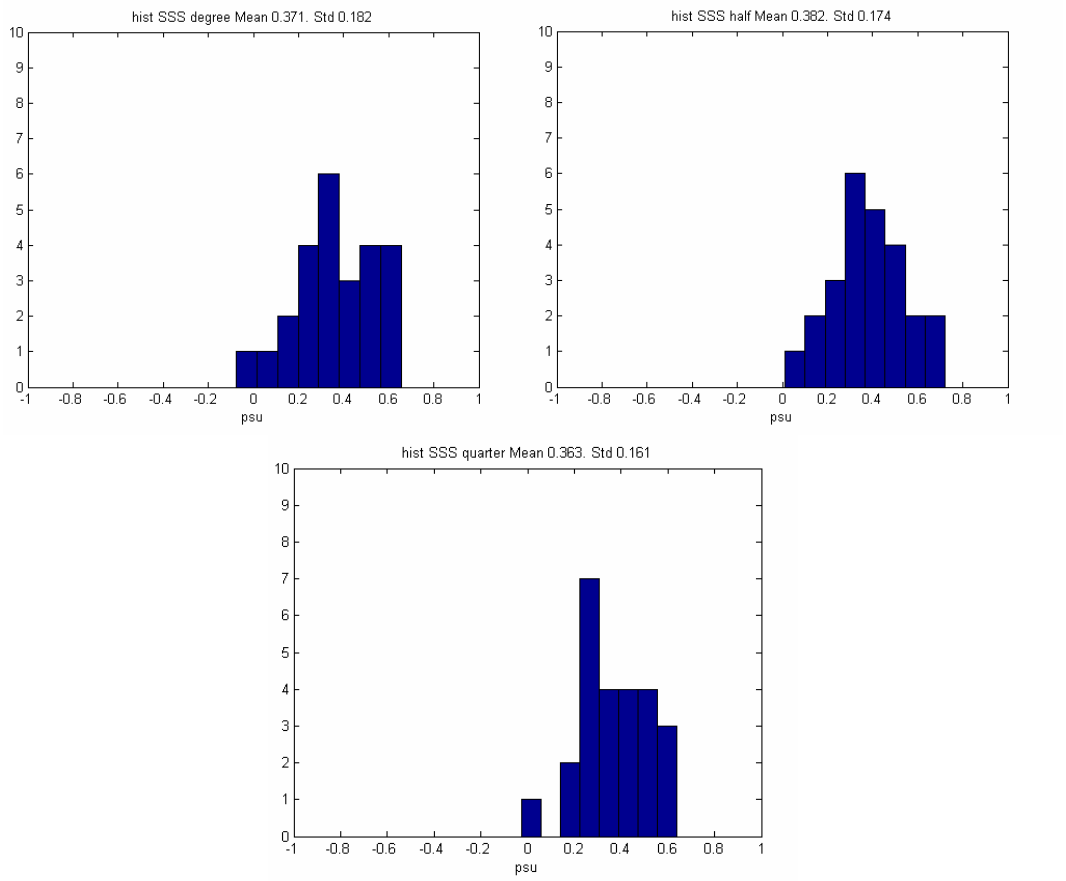

Fig. 8.8 L3 error statistics in the new zone for a 1° (top left), 1/2° (top right) and 1/4° (bottom) OCCAM data resolution.

8.4 Conclusions and Future Lines

The ultimate goal of this study was to evaluate the capability of the SMOS retrieved data to resolve salinity features at different (high resolution) spatial scales.

According to the results, SMOS-resolving capability seems to be limited to the identification of patterns not smaller than 1/2° in size. However, it should be emphasized that these results correspond to the particularly challenging case of a highly dynamic ocean zone with the influence of land.

In turn, in an open ocean zone without the coastline influence and a smaller bias, using spatial high resolution data until 1/4° may be of some benefit to monitor finer scale oceanographic features without suffering particular error degradation. It is not yet clear whether is possible or not to push further the spatial resolution in such open ocean zones.

Despite this analysis needs further refinements on other test zones, it seems that in coastal areas the cut-off scale to distinguish *SSS* patterns is set to 1/2°, while in open ocean is possible to push further the retrieval up to 1/4°. Residual bias has to be corrected by some external salinity

calibration techniques. This study may be of some help in identifying proper interpolation nodes at the SMOS ISEA grid [Suess et al., 2004].

Chapter 9
Conclusions and Open Issues

In this Ph.D. Thesis several studies have been performed towards the determination of an ocean salinity error budget within the ESA SMOS mission. After having described in the first two Chapters the motivations of the mission, the rationale of the measurements and the basic concepts of microwave radiometry, the salinity retrieval main features have been covered in Chapter 3.

The salinity retrieval issues whose influence is critical in the inversion procedure are:

- Scene-dependent bias in the simulated T_B,
- Radiometric sensitivity (thermal noise) and radiometric accuracy,
- L-band forward geophysical model function definition,
- Auxiliary data uncertainties,
- Restrictions in the cost function, especially on salinity term, and
- Adequate L3 spatio-temporal averaging.

A straightforward concept stems from the statement of the salinity retrieval problem: different tuning and setting of the minimization algorithm lead to different results, and complete awareness of that should be assumed. Based on this consideration, the core of this Ph.D. Thesis, the error budget determination, has been progressively approached by evaluating the extent of the impact of different variables and parameterizations in the salinity accuracy.

In Chapter 5 the impact of several multi-source different auxiliary data on the final *SSS* error have been addressed. This gives a first feeling of the quantitative *SSS* error that should be expected in real upcoming measurements, whilst in Chapter 6 the potential use of GNSS-R derived signals to correct for sea state uncertainty in the SMOS context has been investigated.

Chapter 7 concerned the overall *SSS* Error Budget; where the error sources are consistently binned, and the corresponding effect in terms of the L3 *SSS* error have been addressed in different algorithm configurations.

Chapter 8 has shown the results of a *SSS* horizontal variability study, performed by using input data at increasingly variable resolution, and assessing the capability of retrieved *SSS* to reproduce mesoscale oceanographic features.

Main results and insights deriving from these studies are discussed afterwards.

9.1 Auxiliary Data Impact

The main goal of this study has been to stress the retrieved *SSS* variation induced by the different auxiliary data, providing relevant rms accuracy error and bias in a representative area of the North Atlantic Ocean. A major scope of this study has been to figure out if GODAE requirements are likely to be accomplished despite the limitations imposed to the retrieval setup. This study aimed at:

- Analyzing the impact of different auxiliary data sets in the retrieval process, quantifying the sensitivity to the auxiliary fields, as long as to check the quality of the achievable results using different brightness temperature model to generate/invert the data.
- Identifying the different contributions through an item-by-item error sources selection meant to distinguish between the auxiliary data impact itself and the additional contributions involved in the inversion procedure.

The main conclusions of this study can be summarized as follows:
In a period of 30 days and in 1°x1° boxes, the retrieved rms *SSS* error ranges between 0.055 - 0.309 psu. In a period of 30 days and in 2°x2° boxes, the retrieved rms *SSS* accuracy ranges between 0.032 - 0.291 psu. The best *SSS* products obtained by spatio-temporal averaging of 30 days satisfy the <0.1 psu error requirement.
Apart from the best case scenario, to address a more realistic case one should refer to different auxiliary data configurations, since better simulates the upcoming "measured" brightness temperature. If ECMWF data were used instead (different auxiliary wind), the rms error would increase up to 0.2-0.3 psu (depending on the instrument mode and satellite pass), still in accordance to other studies.
An item-by-item error sources analysis has also been performed, in order to isolate the different potential discrepancies sources. Reference point variability, linked to the auxiliary field uncertainty, determines a significant part of the final error, even if it does not produce bias. Direct/Inverse Model difference, in turn, seems to be the responsible of the bias introduction, besides some extra contribution to the *SSS* error. In this context, radiometric noise does not seem to play a crucial role, since apparently its effect is mostly filtered out in the spatio-temporal averaging procedure.
Concerning the bias introduced by model differences, an attempt of replacing the Hollinger model with the WISE 2001 model provided significant bias reduction, stressing how obtaining a good forward model for the roughness effect on sea surface emissivity is still a primary issue of concern.

9.2 Auxiliary Data Impact by using GNSS-R Signals

The potential improvement of using GNSS-R opportunity signals as auxiliary data in the *SSS* retrieval procedure applied to the SMOS mission has been studied and evaluated. This analysis is the natural continuation of the previous auxiliary data impact study.

Since neither the *mss* fields do exist nowadays, nor is its relationship with other geophysical parameters describing the sea state (e.g. wind speed) completely understood, the *mss* values have been in a first instance derived from the wind speed fields available. These data have been computed in the GNSS-R specular reflection points that a theoretical companion satellite flying aside or 500 Km behind SMOS would measure. These *mss* values have then been used as auxiliary data in the *SSS* retrieval procedure.

The effectiveness of this auxiliary data set was limited by two main factors:

- The limited number of GNSS specular reflection points in each overpass that does not allow an efficient spatio-temporal averaging, and
- The assumed large uncertainty in the sea state (in this case parameterized in terms of *mss*(U_{10}) only) associated to the *mss* measurement error and the saturation of the *mss* at high U_{10} values.

In order to overcome these problems the *mss* fields cannot have an uncertainty larger than 5% of the *mss* value, and several GNSS-R derived *mss* (from GPS, GLONASS, GALILEO and SBAS) have been used to increase the number of specular reflection points. The GODAE requirements can be nearly achieved in some specific configurations: side satellite, use of *Th* and *Tv* and ascending passes.

Nevertheless, retrieved *SSS* multiple constellations values are of the same order of results obtained in the *SynAux* study, if referred to auxiliary wind different than the original. Systematic measurements to determine the relationship between the T_B and the *mss*, among other geophysical parameters, must be performed to improve the quality of the estimation of the *mss*.

9.3 Sea Surface Salinity Error Budget

The activities carried out in the framework of the *SSS* retrieval procedure have been described in the wider context of an ocean salinity error budget, an overall scheme still pending in the SMOS community. Instrumental, external noise sources and geophysical errors have been described, stressing the degree of impact in the comprehensive budget.

Several remarks and considerations stem from this study:

- Salinity retrieval in *Tx/Ty* configuration provides better performances in both bias and accuracy than using the first Stokes parameter in the restricted configuration. The opposite happens when dealing with non-constrained minimization setting. Further attention will be paid to fully understand these trends, but they seem to be related to the different magnitudes of the background terms in the cost function in the different configurations.
- As already known, the uncertainty on auxiliary wind speed is responsible of an important degradation of the error and is still the primary issue that will have to be tackled in the prior-to-launch simulation and after-launch retrieval algorithm rehearsal.
- The ideal case (flat surface) error is well within the 0.1 psu prescribed accuracy. Obviously, the uncertainty on the sea state, that will have to be included, will dramatically worsen the results.
- Radiometric sensitivity implies degradation in the error of almost the same rate for both configurations and polarizations. On the other end, as expected, this effect is negligible in terms of the bias on the measurements.
- Different formulations of the dielectric constant model and of the GMF in general may noticeably modify the results, as it has been further confirmed by using Blanch-Aguasca model and foam inclusion in comparison with the Klein and Swift model and Hollinger linear fit.
- Bias computation indicates that, after a L2 bias cancellation algorithm (necessary anyway due to the bias arising at L1 from realistic image reconstruction algorithm), some residual offset is still present and becomes high in non-constrained configuration.
- The rate of bias and accuracy degradation by tuning the σ_{SSS} parameter has been studied. The cross-over of the retrieval performances and the saturation effect approaching the configuration without restrictions have been described.
- The Sun analysis underlined the need for a proper correction of its contamination; failing to estimate the Sun T_B is not critical except in the non-constrained case.

9.4 Sea Surface Salinity Horizontal Variability

The ultimate goal of this study has been the evaluation of the SMOS capability to resolve salinity features at different (high resolution) spatial scales. According to the results, the SMOS-resolving capability in coastal areas seems to be limited to the identification of patterns not smaller than 1/2° in size. However, it should be emphasized that these results correspond to the particularly challenging case of a highly dynamic ocean zone with the influence of land.

In turn, in an open ocean zone without coastline influence and less bias, using spatial high resolution data until 1/4° may be of some benefit to monitor finer scale oceanographic features without suffering a significant degradation in the salinity error.
This analysis needs further refinements on other test zones, and residual bias has to be corrected by some external salinity calibration techniques. This study may be of some help in identifying proper interpolation nodes at the SMOS ISEA grid.

9.5 Open Issues

An ocean salinity error budget gives a whole perspective of the magnitude of each single error contribution and is suitable to furnish a sketch of the problems that will have to be addressed and tackled once real SMOS data will be downlinked.
After launch, nevertheless, the algorithm will surely need refinements, either way in the forward model and in finding a closed formulation of the cost function itself.
In fact, once the real data will be available, it will be possible to tailor properly an adequate GMF to the SMOS data; to this end, a semi-empirical formulation including several sea state descriptors will have to de adjusted to the downlinked T_BS.with the aim of improving the salinity retrieval.
Likewise, a key issue is a proper balancing of the different terms of the cost function, since throughout this Ph.D. Thesis clearly emerged that the different tunings and settings of the inversion algorithm do have an impact on the results. Firstly, it will have to be considered that the correlations among the brightness temperatures may introduce errors in the minimization procedure, and the actual numbers of independent T_BS measurements should be identified. Some work has already been performed in this direction in [Talone et al., 2008], identifying an effective weight to balance the observational term in the cost function.
Furthermore, with respect to the background terms, a sensitivity study will ensure that the different constraining terms are homogeneous, both among them and when compared to the observational/modeled terms. A balancing of the cost function will be achieved by introducing empirical weights to each single term of the function.
Bias mitigation is still an issue, and further efforts will have to be devoted to this topic, either improving the L2 bias mitigation algorithm or applying some external calibration techniques. Eventually, advanced optimization techniques will be used to properly average the single-overpasses SMOS data into the GODAE-like boxes. These techniques might allow identifying the correlations that are likely to occur in the salinity fields and try to improve the overall retrieval.

References

[Ammar et al., 2008]

Ammar, A., S. Labroue, E. Obligis, C.E. Mejia, M. Crepon, and S. Thiria, Sea Surface Salinity Retrieval for the SMOS Mission Using Neural Networks*, IEEE Trans. Geosci. Remote Sens, 46 (3)*, 754-764, 2008.

[Anterrieu, 2007]

Anterrieu, E., On the Reduction of the Reconstruction Bias in Synthetic Aperture Imaging Radiometry (Corrected), *IEEE Trans. Geosci. Remote Sens*, 45 (4), 1084-1093, 2007.

[Belmonte-Rivas and Martin-Neira, 2005]

Belmonte-Rivas, M., and M. Martin-Neira, Coherent GPS Reflections from the Sea Surface, *IEEE Geosci. Remote Sensing Lett*, *3 (1)*, 28–31, 2006.

[Berger et al., 2002]

Berger, M., A. Camps, J. Font, Y. Kerr, J. Miller, J. Johannessen, J. Boutin, M. Drinkwater, N. Skou, N. Floury, M. Rast, H. Rebhan, and E. Attema, Measuring Ocean Salinity with ESA's SMOS Mission, *ESA Bulletin, 111,* 113-121, 2002.

[Bingham et al., 2002]

Bingham, F.M., S.D. Howden, and C.J. Koblinsky, Sea Surface Salinity Measurements in the Historical Database, *J. Geophys. Res., 107*, 8019, 2002.

[Blanch and Aguasca, 2004]

Blanch, S., and A. Aguasca, Seawater Dielectric Permittivity Model from Measurements at L-Band, *Proceedings of the International Geoscience and Remote Sensing Symposium (IGARSS),* Anchorage, Alaska, USA, 1362-1365, 2004.

[Boutin et al., 2004]

Boutin, J., P. Waldteufel, N. Martin, G. Caudal, and E. Dinnat, Surface Salinity Retrieved from SMOS Measurements over Global Ocean: Imprecisions Due to Sea Surface Roughness and Temperature Uncertainties," *J. Atmos. Ocean. Technol*., *21 (9),* 1432-1447, 2004.

[Bretherton et al., 1976]

Bretherton, F., R. Davis, and C. Fandry, A Technique for Objective Analysis and Design of Oceanographic Experiments Applied to MODE-73, *Deep-Sea Research, 23*, 559-582, 1976.

[Browin et al., 2008]

Brown, M., F. Torres, I. Corbella, and A. Colliander, SMOS Calibration, *IEEE Trans. Geosci. Remote Sens, 46 (3),* 646-658, 2008.

[Camps, 1996]

Camps, A., Application of Interferometric Radiometry to Earth Observation, *Ph.D. Dissertation, Universitat Politècnica de Catalunya*, 1996.

[Camps et al., 1997]

Camps, A., J. Bará, I. Corbella, and F. Torres, The Processing of Hexagonally Sampled Signals with Standard Rectangular Techniques: Application to 2D Large Aperture Synthesis Interferometric Radiometers, *IEEE Trans. Geosci. Remote Sens.,* 35 (1), 183-190, 1997.

[Camps et al., 1998]

Camps, A., J. Bará, F. Torres, and I. Corbella, "Extension of the CLEAN Technique to the Microwave Imaging of Continuous Thermal Sources by means of Aperture Synthesis Radiometers, *Prog. Electromagn. Res., 18,* 67–83, 1998.

[Camps et al., 1999]

Camps, A., F. Torres, I. Corbella, J. Bará, and F. Monzón, Automatic Calibration of Channels Frequency Response in Interferometric Radiometers, *Electron. Lett., 35*, 115 –116, 1999.

[Camps and Swift, 2002]

Camps, A., and C.T. Swift, "New techniques in microwave radiometry for earth remote sensing," in Review of Radio Sci. 1999–2002, W. R. Stone, Ed. Piscataway, NJ: IEEE Press, pp. 499–518, 2002.

[Camps et al., 2002a]

Camps, A., J. Font, J. Etcheto, V. Caselles, A. Weill, I. Corbella, M. Vall-llossera, N. Duffo, F. Torres, R. Villarino, L. Enrique, A. Juliá, C. Gabarró, J. Boutin, E. Rubio, S.C. Reising, P. Wursteisen, M. Berger, and M. Martin-Neira, Sea Surface Emissivity Observations at L-band: First Results of the Wind and Salinity Experiment WISE 2000, *IEEE Trans. Geosci. Remote Sens., 40 (10),* 2117-2129, 2002.

[Camps et al., 2002b]

Camps, A., N. Duffo, M. Vall-llossera, B. Vallespín, Sea Surface Salinity Retrieval Using Multi-angular L-band Radiometry: Numerical Study Using the SMOS End-to-end Performance Simulator, *Proceedings of the International Geoscience and Remote Sensing Symposium (IGARSS), Toronto, Canada,* 2, 1123-1125, 2002.

[Camps et al., 2003a]

Camps, A., I. Corbella, M. Vall-llossera, N. Duffo, F. Torres, R. Villarino, L. Enrique, F. Julbé, J. Font, A. Julià, C. Gabarró, J. Etcheto, J. Boutin, A. Weill, V. Caselles, E. Rubio, P. Wursteisen, and M. Martín-Neira, L-Band Sea Surface Emissivity: Preliminary Results of the WISE 2000 Campaign and its Application to Salinity Retrieval in the SMOS Mission*" Radio Sci., 38 (4), 8071,* 2003.

[Camps et al., 2003b]

Camps, A., I. Corbella, M. Vall-llossera, N. Duffo, F. Marcos, F. Martínez-Fadrique, and M. Greiner, The SMOS End-to-end Performance Simulator: Description and Scientific Applications, *Proceedings of the International Geoscience and Remote Sensing Symposium (IGARSS), Toulouse, France,* 13-15, 2003.

[Camps et al., 2004a]

Camps, A., J. Font, M. Vall-llossera, C. Gabarró, I. Corbella, N. Duffo, F. Torres, S. Blanch, A. Aguasca, R. Villarino, L. Enrique, J. Miranda, J. Arenas, A. Julià, J. Etcheto, V. Caselles, A. Weill, J. Boutin, S. Contardo, R. Niclós, R. Rivas, S.C. Reising, P. Wursteisen, M. Berger, and M. Martín-Neira, The WISE 2000 and 2001 Field

Experiments in Support of the SMOS Mission: Sea Surface L-Band Brightness Temperature Observations and their Application to Multi-Angular Salinity Retrieval, *IEEE Trans. Geosci. Remote Sens.,* 42 (4), 804-823, 2004.

[Camps et al., 2004b]

Camps, A., M. Vall-llossera, N. Duffo, M. Zapata, I. Corbella, F. Torres, and V. Barrena, Sun Effects in 2-D Aperture Synthesis Radiometry Imaging and their Cancellation, *IEEE Trans. Geosc. Remote Sens., 42 (6)*, 1161-1167, 2004.

[Camps et al., 2005a]

Camps, A., M. Vall-llossera, R. Villarino, N. Reul, B. Chapron, I. Corbella, N. Duffo, F. Torres, J. Miranda, R. Sabia, A. Monerris, and R. Rodríguez, The Emissivity of Foam-Covered Water Surface at L-Band: Theoretical Modeling and Experimental Results from the FROG 2003 Field Experiment, *IEEE Trans. Geosci. Remote Sens., 43 (5),* 925-937, 2005.

[Camps et al., 2005b]

Camps, A., M. Vall-llossera, N. Duffo, F. Torres, and I. Corbella, Performance of Sea Surface Salinity and Soil Moisture Retrieval Algorithms with Different Ancillary Data Sets in 2D L-Band Aperture Synthesis Interferometric Radiometers, *IEEE Trans. Geosci. Remote Sens., 43 (5),* 1189-1200, 2005.

[Camps et al., 2005c]

Camps, A., M. Vall-llossera, L. Batres, F. Torres, N. Duffo, and I. Corbella, Retrieving Sea Surface Salinity with Multi-angular L-band Brightness Temperatures: Improvement by Spatio-temporal Averaging, Radio Sci., 40 (2), 2005.

[Camps et al., 2006]

Camps, A., M. Vall-llossera, I. Corbella, N. Duffo, F. Torres, Improved Image Reconstruction Algorithms for Aperture Synthesis Radiometers, *Proceedings of the International Geoscience and Remote Sensing Symposium (IGARSS), Denver, Colorado, USA,* 1168-1171, 2006.

[Camps et al., 2008]

Camps, A., M. Vall-llossera, I. Corbella, N. Duffo, and F. Torres, "Improved Image Reconstruction Algorithms for Aperture Synthesis Radiometers, *IEEE Trans. Geosci. Remote Sens.,46 (1),* 146-158, 2008.

[Cardellach et al., 2003]

Cardellach, E., G. Ruffini, D. Pino, A. Rius, A. Komjathy, and J.L. Garrison, 2003 Mediterranean Balloon Experiment: Ocean Wind Speed Sensing from the Stratosphere Using GPS Reflections, *Remote Sens. Environ., 88 (3),* 351-362, 2003.

[Claassen and Fung, 1974]

Claassen, J.P., and A.K. Fung, The Recovery of Polarized Apparent Temperature Distributions of Flat Scenes from Antenna Temperature Measurements, *IEEE Trans. Antennas Propagat, 22*, 433–442, 1974.

[Corbella et al., 2003]

Corbella, I., A. Camps, F. Martínez, F. Marcos, F. Torres, M. Vall-llossera, N. Duffo, and J. Bará, End-to-end Simulator of 2D Interferometric Radiometry, *Radio Sci., 38 (3)*, 8058, 2003.

[Corbella et al., 2005]

Corbella, I., F. Torres, A. Camps, A. Colliander, M. Martin-Neira, S. Ribo, K. Rautiainen, N. Duffo, and M. Vall-llossera, MIRAS End-to-end calibration: application to SMOS L1 processor, *IEEE Trans. Geosci. Remote Sens., 43 (5),* 1126-1134, 2005.

[Cox and Munk, 1954]

Cox, C., and W. Munk, Measurements of the Roughness of the Sea Surface from Photographs of the Sun's glitter," *J. Opt. Soc. Amer., 44,* 838-850, 1954.

[Debye, 1929]

Debye, P., Polar Molecules, *Dover Reprint, originally pub. Reinhold Publishing Corp.*, 1929.

[Delcroix et al., 1996]

Delcroix, T., C. Henin, V. Porte, and P. Arkin, Precipitation and Sea-Surface Salinity in the Tropical Pacific Ocean, *Deep-Sea Res., 43,* 1123–1141, 1996.

[Dinnat et al., 2002]

Dinnat, E., J. Boutin, G. Caudal, J. Etcheto, and P. Waldteufel, Influence of Sea Surface Emissivity Model Parameters in L-band for the Estimation of Salinity, *Int. J. Remote Sen.s, 23,* 5117-5122, 2002.

[Dinnat et al., 2003a]

Dinnat, E., J. Boutin, G. Caudal, and J. Etcheto, Issues Concerning the Sea Emissivity Modeling at L-band for Retrieving Surface Salinity, *Radio Sci., 38 (4),* 8060, 2003.

[Dinnat, 2003b]

Dinnat, E., De la Détermination de la Salinité de Surface des Océans à Partir de Mesures Radiométriques Hyperfréquence en Bande L, *Ph.D. Thesis, Université Pierre et Marie Curie, Paris, France,* 2003.

[Donelan et al., 1985]

Donelan, M.A., J. Hamilton and W.H. Hui, Directional Spectra of Wind Generated Waves," *Philos. Trans. R. Soc. London, Ser. A, 315,* 509-562, 1985.

[Durden and Vesecky, 1985]

Durden, S.L., and J.F.Vesecky, A Physical Radar Cross-Section Model for a Wind-Driven Sea with Swell, *IEEE J. Oceanic Engineering, 10 (4)*, 445-451, 1985.

[ECMWF website]

European Centre for Medium-range Weather Forecasts.
Online at: [http://www.ecmwf.int/research/era/ERA-40_Atlas/docs/section_B/parameter_emp.html]

[Elfouhaily et al., 1997]

Elfouhaily, T., B. Chapron, K. Katsaros, and D. Vandermark, A Unified Directional Spectrum for Long and Short Wind-driven Waves, *J. Geophys. Res., 102 (7)*, 15781–15796, 1997.

[Ellison et al., 1998]

Ellison, W., A. Balana, G. Delbos, K. Lamkaouchi, L. Eymard, C. Guillou and C. Prigent, New Permittivity Measurements of Sea Water, *Radio Sci., 33 (3),* 639-648, 1998.

[Emery and Wert, 1976]

Emery, W.J., and R.T. Wert, Temperature-Salinity Curves in the Pacific and their Application to Dynamic Height Computation, *J. Phys. Oceanogr, 6*, 613-617, 1976.

[Envisat website]

ESA Envisat website. Online at: [http://www.envisat.esa.int/]

[EO Portal website]

Earth Observation Portal.
Online at: [http://directory.eoportal.org/pres_SMOSSoilMoistureandOceanSalinityMission.html]

[ESA SMOS Brochure, 2004]

ESA SMOS Brochure, SMOS: ESA's Water Mission, *BR-224*, 14, 2004.
Online at: [http://esamultimedia.esa.int/docs/br_224.pdf]

[ESA SMOS website]

ESA SMOS website. Online at: [http://www.esa.int/esaLP/LPsmos.html]

[Etcheto et al., 2004]

Etcheto, J., E. Dinnat, J. Boutin, A Camps, J. Miller, S. Contardo, J. Wesson, J. Font, and D. Long, Wind Speed Effect on L-Band Brightness Temperature Inferred from EUROSTARRS and WISE 2001 Field Experiments, *IEEE Trans. Geosci. Remote Sens., 42 (10)*, 2206-2213, 2004.

[Evensen and van Leeuwen, 1996]

Evensen, G., and P.J. van Leeuwen, Assimilation of Geosat Altimeter Data for the Agulhas Current Using the Ensemble Kalman Filter with a Quasigeostrophic Model, *Monthly Weather Review, 124 (1)*, 85-96, 1996.

[Font et al., 2004]

Font, J., G. Lagerloef, D. Le Vine, A. Camps, and O.Z. Zanife, The Determination of Surface Salinity with the European SMOS Space Mission, *IEEE Trans. Geosci. Remote Sens.*, *42 (10)*, 2196-2205, 2004.

[Font et al., 2006]

Font, J., J. Boutin, N. Reul, P. Waldteufel, C. Gabarró, S. Zine, J. Tenerelli, F. Petitcolin, and J.L. Vergely, An Iterative Convergence Algorithm to Retrieve Sea Surface Salinity from SMOS L-Band Radiometric Measurements, *Proceedings of the International Geoscience and Remote Sensing Symposium (IGARSS), Denver, Colorado, USA,* 1697-1701, 2006.

[Font et al., 2008]

Font, J., A. Camps, and J. Ballabrera-Poy, Microwave Aperture Synthesis Radiometry: Paving the Path for Sea Surface Salinity Measurement from Space, *Barale V., Gade M. Eds., Remote sensing of the European seas, Springer Science Dordrecht*, 2008.

[Font and Camps, 2008]

Font, J., and A. Camps, SMOS: La Medición de Salinidad desde el Espacio, *Teledetección de los océanos: fundamentos y aplicaciones, Chapter 14, C.García-Soto Ed., Editorial Tébar,* 2008.

[Fung, 1994]

Fung, A.K., Microwave Scattering and Emission. Models and Their Applications, *Boston, MA: Artech House*, 1994.

[Gabarró et al., 2004a]

Gabarró, C., J. Font, A. Camps, M. Vall-llossera, and A. Julià, A New Empirical Model of Sea Surface Microwave Emissivity for Salinity Remote Sensing;" *Geophys. Res. Lett., 31*, LO1309, 2004.

[Gabarró et al., 2004b]

Gabarró, C., M. Vall-llossera, J. Font, and A. Camps, Determination of Sea Surface Salinity and Wind Speed by L-Band Microwave Radiometry from a Fixed Platform, *Int. J. Remote Sens*, *25 (1),* 111-128, 2004.

[Gabarró et al., 2007]

Gabarró, C., M. Portabella, M. Talone and J. Font, Analysis of the SMOS Ocean Salinity Inversion Algorithm, *Proceedings of the International Geoscience and Remote Sensing Symposium (IGARSS), Barcelona, Spain*, 971-974, 2007.

[Garrison and Katzberg, 1998]

Garrison, J.L., and J.L. Katzberg, Effects of Sea Roughness on Bistatically Scattered Range Coded Signals from the Global Positioning System, *Geophys. Res. Lett., 25 (13)*, pp, 1998.

[Garrison et al., 2002]

Garrison, J.L., A. Komjathy, V.U. Zavorotny, and S.J. Katzberg, Wind Speed Measurement Using Forward Scattered GPS Signals, *IEEE Trans. Geosci. Remote Sens., 40 (1),* 50 - 65, 2002.

[Germain et al., 2004]

Germain, O., G. Ruffini, F. Soulat, M. Caparrini, B. Chapron and P. Silvestrin, The Eddy Experiment II: GNSS-R Speculometry for Directional Sea-Roughness Retrieval from Low Aircraft, *Geophys. Res. Lett., 31 (21)*, 2004.

[Gleason et al., 2005]

Gleason, S., S. Hodgart, S. Yiping, C. Gommenginger, S. Mackin, M. Adjrad, and M. Unwin, Detection and Processing of Bistatically Reflected GPS Signals from Low Earth Orbit for the Purpose of Ocean Remote Sensing, *IEEE Trans. Geosci. Remote Sens., 43 (6),* 1229–1241, 2005.

[Hollinger, 1971]

Hollinger, J.P., Passive Microwave Measurements of Sea Surface Roughness, *IEEE Trans. Geosci. Electron., 9 (3),* 165- 169, 1971.

[Irisov, 1997]

Irisov, V.G., Small-Slope Expansion for Thermal and Reflected Radiation from a Rough Surface, *Waves in Random Media, 7*, 1-10, 1997.

[Johnson and Zhang, 1999]

Johnson, J.T., and M. Zhang, Theoretical Study of the Small Slope Approximation for Ocean Polarimetric Thermal Emission, *IEEE Trans. Geosci. Remote Sens.*, 37 (5), 2305-2316, 1999.

[Kerr et al., 2001]

Kerr, Y., P. Waldteufel, J.P. Wigneron, J.M. Martinuzzi, J. Font, and M. Berger, Soil Moisture Retrieval from Space: The Soil Moisture and Ocean Salinity (SMOS) Mission, *IEEE Trans. Geosci. Remote Sens., 39 (8),* 1729–1735, 2001.

[Klein and Swift, 1977]

Klein, L.A., and C.T. Swift, An Improved Model for the Dielectric Constant of Sea Water at Microwave Frequencies, *IEEE J. Oceanic Eng., 2 (1),* 104-111, 1977.

[Koblinsky et al., 2003]

Koblinsky, C.J., P. Hildebrand, D. Le Vine, and F. Pellerano, Sea Surface Salinity from Space: Science Goals and Measurement Approach, *Radio Sci.*, *38 (4)*, 8024, 2003.

[Komjathy et al., 2000]

Komjathy, A., V. Zavorotny, P. Axelrad, G.H. Born, and J.L. Garrison, GPS Signal Scattering from Sea Surface: Wind Speed Retrieval Using Experimental Data and Theoretical Model, *Remote Sens. Environ., 73,* 162–174, 2000.

[Krauss, 1986]

Kraus, J.D., Radio Astronomy, *Delaware, OH, Cygnus-Quasar,* 1986.

[Kudryavtsev et al., 1999]

Kudryavtsev, V.N., V.K. Makin, and B. Chapron, Coupled Sea Surface-Atmosphere Model Spectrum of Short Wind Waves, *J. Geophys. Res., 104 (4)*, 7625-7639, 1999.

[Lagerloef et al., 1995]

Lagerloef, G.S.E., C.T. Swift, and D.M. Le Vine, Sea Surface Salinity: The Next Remote Sensing Challenge, *Oceanography, 8,* 44–50, 1995.

[Lagerloef, 2000]

Lagerloef, G.S.E, Recent Progress toward Satellite Measurements of the Global Sea Surface Salinity Field. Satellites, Oceanography and Society, *D. Halpern, Elsevier Oceaongraphy Series, 63,* 367, 2000.

[Lerner and Hollinger, 1977]

Lerner, R.M., and J.P. Hollinger, Analysis of 1.4 GHz Radiometric Measurements from Skylab, *Remote Sens. Environ., 6,* 251- 269, 1977.

[Le Vine and Abraham, 2002]

Le Vine, D.M., and S. Abraham, The Effect of the Ionosphere on Remote Sensing of the Sea Surface Salinity from Space: Absorption and Emission at L-Band, *IEEE Trans. Geosci. Remote Sens.*, *40 (4),* 771-782, 2002.

[Le Vine and Abraham, 2004]

Le Vine, D.M., and S. Abraham, Galactic Noise and Passive Microwave Remote Sensing from Space at L-Band, *IEEE Trans. Geosci. Remote Sens.*, 42 (1), 119-129, 2004.

[Le Vine et al., 2007]

Le Vine, D.M., G.S.E. Lagerloef, F.R. Colomb, S.H. Yueh, and F.A. Pellerano, Aquarius: An Instrument to Monitor Sea Surface Salinity From Space, *IEEE Trans. Geosci. Remote Sens., 45 (7), Part 1,* 2040 - 2050, 2007.

[Levitus, 1982]

Levitus, S., Climatological Atlas of the World Ocean, *NOAA Prof. Paper 13, U.S. Govt. Printing Office, Washington, D.C.,* 173, 1982.

[Levitus et al., 1994]

Levitus, S., R. Burgett, and T.P. Boyer: World Ocean Atlas 1994, *Silver Spring, Md, NOAA NESDIS, 3, Salinity*, 1994.

[Levitus et al., 1998]

Levitus, S., T.P. Boyer, M.E. Conkright, T. O'Brien, J. Antonov, C. Stephens, L. Statoplos, D. Johnson, and R. Gelfeld, World Ocean Database, *Natl. Oceanogr. Data Cent., Silver Spring, Md., NOAA/NESDIS 18,* 1998.

[Liebe, 1989]

Liebe, H.J., MPM: An Atmospheric Millimeter Wave Propagation Model, *Int. J. Infrared Millimeter Waves, 10 (6),* 631– 650, 1989.

[Lowe et al., 2002a]

Lowe, S., C. Zuffada, Y. Chao, P. Kroger, J.L LaBreque, and L.E. Young, 5-cm Precision Aircraft Ocean Altimetry Using GPS Reflections, *Geophys. Res. Lett.*, 29, 4359–4362, 2002.

[Lowe et al., 2002b]

Lowe, S., J. LaBrecque, C. Zuffada, L.J. Romans, L.E. Young, and G.A. Hajj, First Spaceborne Observation of an Earth-reflected GPS signal, *Radio Sci., 37 (1),* 1007*,* 2002.

[Marchán et al., 2008]

Marchán, J.F., N. Rodriguez, A. Camps, X. Bosch, I. Ramos and E. Valencia, Correction of the Sea State Impact in the L-band Brightness Temperature by Means of Delay-Doppler Maps of Global Navigation Satellite Signals Reflected over the Sea Surface, *IEEE Trans. Geosci. Remote Sens., 46 (10),* 2008.

[Marquardt, 1963]

Marquardt, D.W., An Algorithm for Least-Squares Estimation of Non-Linear Parameters, *SIAM, J. Appl. Math., 11 (2),* 431–441, 1963.

[Martín-Neira, 1993]

Martín-Neira, M., A Passive Reflectometry and Interferometry System (PARIS): Application to Ocean Altimetry, *ESA Journal, 17,* 331-355, 1993.

[Martín-Neira and Goutoule, 1997]

Martín-Neira, M., and J.M. Goutoule, A Two-Dimensional Aperture-Synthesis Radiometer for Soil Moisture and Ocean Salinity Observations, *ESA Bull., 92,* 95–104, 1997.

[Martín-Neira et al., 2000]

Martin-Neira, M., P. Colmenarejo, G. Ruffini, and C. Serra, Ocean Altimetry Using the Carrier Phase of GNSS Reflected Signals, *Proceedings of Ocean Winds 2000, Plouzané, France, CERSAT News, 11,* 2000.

[Martín-Neira et al., 2002]

Martín-Neira, M., S. Ribó, and A.J. Martín-Polegre, Polarimetric Mode of MIRAS, *IEEE Trans. Geosci. Remote Sens., 40 (8),* 1755–1768, 2002.

[Martín-Neira et al., 2008]

Martín-Neira, M., I. Cabeza, C. Pérez, M.A. Palacios, M.A. Guijarro, S. Ribó, I. Corbella, S. Blanch, F. Torres, N. Duffo, V. González, S. Beraza, A. Camps, M. Vall-llossera, S. Tauriainen, J. Pihlflyckt, J.P. González, and F. Martin-Porqueras, AMIRAS—An Airborne MIRAS Demonstrator, *IEEE Trans. Geosci. Remote Sens., 46 (3),* 705-716, 2008.

[Mätzler, 2006]

Mätzler, C., Thermal Microwave Radiation: Applications for Remote Sensing, *Ed. IEEE, London, UK,* 2006.

[Meeson et al., 1995]

Meeson, B.W., F.E. Corprew, J. McManus, D. Myers, K.S.J.W. Closs, D. Sunday, and P.J. Sellers, ISLSCP Initiative I-Global Data Sets for Land-Atmosphere Models 1987–1988 [CD-ROM], *NASA, Greenbelt, Md.,* 1995.

[Michel et al., 2005]

Michel, S., B. Chapron, J. Tournadre, and N. Reul, Global Analysis of Sea Surface Salinity Variability from Satellite Data, *Oceans – Europe,* 11-16, 2005.

[Miranda et al., 2003]

Miranda, J.J., M. Vall-llossera, A. Camps, N. Duffo, I. Corbella, and J. Etcheto, Sea State Effect on the Sea Surface Emissivity at L-Band, *IEEE Trans. Geosci. Remote Sens., 41 (10),* 2307-2315, 2003.

[Monahan and Lu, 1990]

Monahan, E.C., and M. Lu, Acoustically Relevant Bubble Assemblages and Their Dependence on Metereological Parameters, *IEEE J. Oceanic Eng., 15,* 340–349, 1990.

[NASA JPL website]

NASA Jet Propulsion Laboratory. Online at: [http://deepspace.jpl.nasa.gov/dsn/history/dsn67.html].

[NOAA ETOPO5]

NOAA National Geophysical Data Center. Online at: [http://www.ngdc.noaa.gov/mgg/fliers/93mgg01.html].

[Obligis et al., 2005]

Obligis, E., S. Labroue, A. Ammar, S. Thiria and M. Crepon, Neural Networks to Retrieve Sea Surface Salinity from SMOS Brightness Temperatures, *Proceedings of the International Geoscience and Remote Sensing Symposium (IGARSS), Toulouse, France,* 2568-2571, 2005.

[OCCAM website]

OCCAM global ocean model. Online at: [http://www.noc.soton.ac.uk/JRD/OCCAM]

[Phillips et al., 2007]

Phillips, S., C. Boone and E. Obligis, The Role of Averaging for Improving Sea Surface Salinity Retrieval from the Soil Moisture and Ocean Salinity (SMOS) Satellite and Impact of Auxiliary Data, *J. Atmos. Ocean. Technol., 24 (2),* 255-269, 2007.

[Picard et al., 2004]

Picard, B., N. Reul, P. Waldteufel, and E. Anterrieu, Impact of Solar Radiation on Sea Surface Salinity Remote Sensing By Space-borne Synthetic Aperture Imaging Radiometers, *Proceedings of the International Geoscience and Remote Sensing Symposium (IGARSS), Anchorage, Alaska, USA,* 1926-1929, 2004.

[Press, 1992]

Press, W., S. Teukolsky, W. Vetterling, and B. Flannery, Numerical Recipes in C: The Art of Scientific Computing, *2nd ed., Cambridge Univ. Press, New York,* 1992.

[Reul and Chapron, 2001]

Reul, N., and B. Chapron, SMOS Salinity Data processing Study: Improvements in Emissivity Models, *Final Report, WP 1100, ESA Contract 15165/01/NL/SF,* 2001.

[Reul and Chapron, 2003]

Reul, N., and B. Chapron, A model of Sea-Foam Thickness Distribution for Passive Microwave Remote Sensing Applications, *J Geophys Res., 108,* 3321-3331, 2003.

[Reul et al., 2004]

Reul, N., M. Srokosz and B. Chapron, Synergetic Aspects and Auxiliary Data Concepts for Sea Surface Salinity Measurements from Space, *Final Report, WP1200: Sea Surface Temperature Auxiliary Data Processing Scheme, ESA ESTEC 18176/04/NL/CB,* November 2004.

[Reul et al., 2007]

Reul, N., J. Tenerelli, B. Chapron, and P. Waldteufel, Modeling Sun Glitter at L-Band for Sea Surface Salinity Remote Sensing with SMOS, *IEEE Trans. Geosci. Remote Sens., 45 (7),* 2073-2087, 2007.

[Rius et al., 2002]

Rius, A., J.M. Aparicio, E. Cardellach, M. Martín-Neira, and B. Chapron, Sea Surface State Measured Using GPS Reflected Signals, *Geophys. Res. Lett., 29 (23),* 2002.

[Robinson, 1994]

Robinson, I.S., Satellite Oceanography: An Introduction for Oceanographers and Remote Sensing Scientists, *Wiley & Sons,* 1994.

[Ruf et al., 1988]

Ruf, C.S., C.T. Swift, A.B. Tanner, D.M. Le Vine, Interferometric Synthetic Aperture Microwave Radiometry for the Remote Sensing of the Earth, *IEEE Trans. Geosci. Remote Sens.*, *26 (5)*, 597-611, 1988.

[Ruffini et al., 2002]

Ruffini, G., M. Caparrini, B. Chapron, F. Soulat, O. Germain, and L. Ruffini, Oceanpal: An Instrument for Remote Sensing of the Ocean and Other Water Surfaces Using GNSS Reflections, *Proceeding of EuroGOOS, Athens, Greece*, 2002.

[Ruffini et al., 2004]

Ruffini, G., F. Soulat, M. Caparrini, O. Germain, and M. Martin-Neira, The Eddy Experiment: Accurate GNSS-R Ocean Altimetry from Low Altitude Aircraft, *Geophys. Res. Lett., 31 (21),* 2004.

[Sabia et al., 2006]

Sabia, R., A. Camps, M. Vall·llossera, and N. Reul, Impact on Sea Surface Salinity Retrieval of Different Auxiliary Data within the SMOS Mission, *IEEE Trans. Geosci. Remote Sens., 44 (10),* 2769-2778, 2006.

[Sabia et al., 2007a]

Sabia, R., C. Gommenginger, A. Camps, M. Srokosz, Retrieved Sea Surface Salinity Spatial Variability using High Resolution Data within the Soil Moisture and Ocean Salinity (SMOS) Mission, *Proceedings of the International Geoscience and Remote Sensing Symposium (IGARSS), Barcelona, Spain,* 1330-1333, 2007.

[Sabia et al., 2007b]

Sabia, R., M. Caparrini, A. Camps, and G. Ruffini, Potential Synergetic Use of GNSS-R Signals to Improve the Sea State Correction in the Sea Surface Salinity Estimation: Application to the SMOS Mission, *IEEE Trans. Geosci. Remote Sens., 45 (7),* 2088-2097, 2007.

[Sabia et al., 2007c]

Sabia, R., A. Camps, M. Vall-llossera, M. Talone, J. Font, Towards an Ocean Salinity Error Budget Estimation within the SMOS Mission, *Proceedings of the International Geoscience and Remote Sensing Symposium (IGARSS), Barcelona, Spain,* 38-41, 2007.

[Sabia et al., 2008]

Sabia, R., A. Camps, M. Vall-llossera, M. Talone, Extended Ocean Salinity Error Budget Analysis within the SMOS Mission, *Proceedings of the International Geoscience and Remote Sensing Symposium (IGARSS), Boston, Massachusetts, USA,* 2008.

[Sellers et al., 1995]

Sellers, P., et al., An Overview of the ISLSCP Initiative I-Global Data Sets [CD-ROM], *NASA, Greenbelt, Md.,* 1995.

[SEPS simulator]
SMOS End-to-end Performance Simulator. Online at [http://www.smos.esa.int/SEPS/]

[Silvestrin et al., 2001]
Silvestrin, P., M. Berger, Y. Kerr, J. Font, ESA's Second Earth Explorer Opportunity Mission: The Soil Moisture and Ocean Salinity Mission - SMOS. *IEEE Geosci. Remote Sens. Newsletter, 118,* 11-14, 2001.

[Skou, 1981]
Skou, N., Microwave Radiometer Systems: Design and Analysis, *Artech House*, 121, 1981.

[Skou, 2003]
Skou, N., Faraday Rotation and L-band Oceanographic Measurements, *Radio Sci., 38 (4)*, 8059, 2003.

[Skou and Hoffman-Bang, 2005]
Skou, N., and D. Hoffman-Bang, L-band Radiometers Measuring Salinity from Space: Atmospheric Propagation Effects, *IEEE Trans. Geosci. Remote Sens., 43 (10),* 2210 -2217, 2005.

[Smith and Lefèbvre, 1997]
Smith, N., and M. Lefèbvre, The Global Ocean Data Assimilation Experiment (GODAE). *Monitoring the Oceans in the 2000s: An Integrated Approach, International Symposium, Biarritz, France,* 1997.

[SMOS SRD, 2002]
SMOS Scientific Requirements Document, *ESA*, 2002.
Online at: [http://esamultimedia.esa.int/docs/EOQ66_SMOS.pdf]

[Snyder, 1992]
Snyder, J.P., An Equal-area Map Projection for Polyhedral Globes, *Cartographica, 29 (1),* 10–21, 1992.

[Soulat et al., 2004a]
Soulat, F., N. Reul, B. Chapron and M. Srokosz, Synergetic Aspects and Auxiliary Data Concepts for Sea Surface Salinity Measurements from Space, *Final Report, WP1300: Processing Schemes for Sea Surface Roughness, ESA ESTEC 18176/04/NL/CB,* 2004.

[Soulat et al., 2004b]
Soulat, F., M. Caparrini, O. Germain, P. Lopez-Dekker, M. Taani, and G. Ruffini, Sea State Monitoring Using Coastal GNSS-R, *Geophys. Res. Lett., 31 (21),* L21303, 2004.

[Suess et al., 2004]
Suess, M., P. Matos, A. Gutierrez, M. Zundo, M. Martin-Neira, Processing of SMOS Level 1c Data onto a Discrete Global Grid**,** *Proceedings of the International Geoscience and Remote Sensing Symposium (IGARSS), Anchorage, Alaska, USA,* 1914 – 1917, 2004.

[Swift, 1976]
Swift, C.T, Microwave Radiometer Measurements of the Cape Cod Cannal, *Radio Sci., 9 (7),* 641-653, 1976.

[Swift and Mcintosh, 1983]

Swift, C.T., and R. Mcintosh, Considerations for Microwave Remote Sensing of Ocean-Surface Salinity, *IEEE Trans. Geosci. Remote Sens., 21 (4)*, 480-491, 1983.

[*SynAux* Report, 2006]

Synergetic Aspects and Auxiliary Data Concepts for Sea Surface Salinity Measurements from Space, *ESA ESTEC 18176/04/NL/CB, Final Report,* 2006.

Online at: [ftp://ftp.estec.esa.nl/ftp/pub/vr/VRO/GS_Study_18176_FR.pdf]

[Talone et al., 2007a]

Talone, M., A. Camps, J. Font, and R. Sabia, Towards a Coherent Sea Surface Salinity Product from SMOS Radiometric Measurements and ARGO Buoys, *Proceedings of the International Geoscience and Remote Sensing Symposium (IGARSS), Barcelona, Spain,* 3959-3962, 2007.

[Talone et al., 2007b]

Talone, M., A. Camps, A. Monerris, M. Vall-Ilossera, P. Ferrazzoli, and M. Piles, Surface Topography and Mixed-Pixel Effects on the Simulated L-Band Brightness Temperatures, *IEEE Trans Geosci. Remote Sens., 45, (7),* 1996-2003, 2007.

[Talone et al., 2008]

Talone, M., A. Camps, C. Gabarró, R. Sabia, J. Gourrion, M. Vall·llossera, B. Mourre, and J. Font, Contributions to the Improvement of the SMOS Level 2 Retrieval Algorithm: Optimization of the Cost Function, *Proceedings of the International Geoscience and Remote Sensing Symposium (IGARSS), Boston, Massachusetts USA,* 2008.

[Thompson et al., 2005]

Thompson, D.R., T.M. Elfouhaily, and J.L. Garrison, An Improved Geometrical Optics Model for Bistatic GPS Scattering from the Ocean Surface, *IEEE Trans Geosci. Remote Sens., 43 (12),* 2810-2821, 2005.

[Torres et al., 1996]

Torres, F., A. Camps, J. Bará, I. Corbella, and R. Ferrero, Onboard Phase and Modulus Calibration of Large Aperture Synthesis Radiometers: Study Applied to MIRAS, *IEEE Trans. Geosci. Remote Sens.*, 34 (4), 1000–1009, 1996.

[Ulaby et al., 1982]

Ulaby, F., R.K. Moore, A.K. Fung, Microwave Remote Sensing. Active and Passive. Vol I: Microwave Remote Sensing Fundamentals and Radiometry, *Addison-Wesley Publishing Company*, 1982.

[UNEP website]

United Nation Environmental Programme - Climate. Online at: [http://www.grida.no/climate/vital/32.htm].

[Vall-llossera et al., 2003]

Vall-llossera, M., J. Miranda, A. Camps and R. Villarino, Sea Surface Emissivity Modelling at L-Band: An Inter-Comparison Study, *Proceedings of the First results Workshop on EuroSTARSS/WISE/LOSAC Campaigns, ESTEC Publication Division, Noordwijk, the Netherlands, SP-525,* 143-153, 2003.

[Villarino, 2004]

Villarino, R., Empirical Determination of the Sea Surface Emissivity at L-band: A contribution to ESA's SMOS Earth Explorer Mission, *Ph.D. Thesis Dissertation, Universitat Politècnica de Catalunya, Barcelona, Spain,* 2004.

[Waldteufel et al., 2003]

Waldteufel, P., J. Boutin and Y. Kerr, Selecting an Optimal Configuration for the Soil Moisture and Ocean Salinity Mission, *Radio Sci., 38 (3),* 8051, 2003.

[Waldteufel et al., 2004]

Waldteufel, P., N. Floury, E. Dinnat, and G. Caudal, Ionospheric Effects for L-band 2-D Interferometric Radiometry, *IEEE Trans. Geosci. Remote Sens., 42 (1),* 105-118, 2004.

[Webster et al., 1976]

Webster, W.J., T.T. Wilheit, D.B. Ross, and P. Gloersen, Spectral Characteristics of the Microwave Emission from a Wind-Driven Covered Sea, *J. Geophys. Res., 81 (18),* 3095-3099, 1976.

[Wentz, 1975]

Wentz, F., A Two-scale Model for Foam-free Sea Microwave Brightness Temperature, *J. Geophys. Res., 80 (24),* 3441–3446, 1975.

[Wilson et al., 2004]

Wilson, W.J., S.H. Yueh, S.J. Dinardo, and F. K. Li, High-Stability L-band Radiometer Measurements of Saltwater, *IEEE Trans. Geosci. Remote Sens., 42 (9),* 1829-1835, 2004.

[Wunsch, 1996]

Wunsch, C., The Ocean Circulation Inverse Problem, *Cambridge University Press*, 442, 1996.

[You et al., 2004]

You, H., J.L. Garrison, G. Heckler, and V.U. Zavorotny, Stochastic Voltage Model and Experimental Measurement of Ocean-Scattered GPS Signal Statistics, *IEEE Trans Geosci. Remote Sens., 42 (10)*, 2160-2169, 2004.

[Yueh, 1997]

Yueh, S.H, Modeling of Wind Direction Signals in Polarimetric Sea Surface Brightness Temperatures; *IEEE Trans. Geosci. Remote Sens., 35 (6),* 1400-1418, 1997.

[Yueh, 2000]

Yueh, S.H., Estimates of Faraday Rotation with Passive Microwave Polarimetry for Microwave Remote Sensing of Earth Surfaces, *IEEE Trans. Geosci. Remote Sens., 38, (5, Part 2),* 2434 – 2438, 2000.

[Yueh et al., 2001]

Yueh, S.H., R. West, W. Wilson, F.K. Li, E. Njoku, and Y. Rahmat-Samii, Error Sources and Feasibility for Microwave Remote Sensing of Ocean Surface Salinity, *IEEE Trans. Geosc. Remote Sens, 39 (5)*, 1049-1060, 2001.

[Zanifé et al., 2003]

Zanifé, O.Z., N. Reul, B. Chapron, E. Obligis, C. Boone, S. Labroue, H. Sagen, and G. Evensen, SMOS Salinity Data Processing Study, *Rep. CLS-IFREMER-NERSC, ESA Contract 15165/01/NL/SF*, 2003.

[Zine et al., 2008]

Zine, S., J. Boutin, J. Font, N. Reul, P. Waldteufel, C. Gabarró, J. Tenerelli, F. Petitcolin, J.L. Vergely, M. Talone, and S. Delwart, Overview of the SMOS Sea Surface Salinity Prototype Processor, *IEEE Trans. Geosc. Remote Sens, 46 (3),* 621-645, 2008.

[Zuffada and. Zavorotny, 2001]

Zuffada, C., and V.U. Zavorotny, Coherence Properties of the GPS Signal Scattered off the Ocean on the Accuracy of Remote Sensing of Sea Surface, *Proceedings of the International Geoscience and Remote Sensing Symposium (IGARSS), Sydney, Australia,* 3332–3334, 2001.

List of Publications

International Journal Papers

1. Camps, A., M. Vall-llossera, R. Villarino, N. Reul, B. Chapron, I. Corbella, N. Duffo, F. Torres, J. Miranda, **R. Sabia**, A. Monerris, and R. Rodríguez, The Emissivity of Foam-Covered Water Surface at L-Band: Theoretical Modeling and Experimental Results from The FROG 2003 Field Experiment, *IEEE Trans. Geosc. Remote Sens, 43 (5)*, 925-937, 2005.

2. Vall-llossera, M., A. Camps, I. Corbella, F. Torres, N. Duffo, A. Monerris, **R. Sabia**, D. Selva, C. Antolín, E. López-Baeza, J.F. Ferrer, and K. Saleh, SMOS REFLEX 2003: L-Band Emissivity Characterization of Vineyards, *IEEE Trans. Geosc. Remote Sens, 43 (5),* 973-982, 2005.

3. **Sabia**, **R.**, A. Camps, M. Vall-llossera, and N. Reul, Impact on Sea Surface Salinity Retrieval of Different Auxiliary Data within the SMOS Mission, *IEEE Trans. Geosc. Remote Sens.*, 44 (10), 2769-2778, 2006.

4. **Sabia**, **R.**, M. Caparrini, A. Camps, and G. Ruffini, Potential Synergetic Use of GNSS-R Signals to Improve the Sea State Correction in the Sea Surface Salinity Estimation: Application to the SMOS Mission, *IEEE Trans. Geosc. Remote Sens.*, *45 (7),* 2088-2097, 2007.

5. Camps, A., J. Font, M. Vall-Ilossera, I. Corbella, N. Duffo, F. Torres, S. Blanch, A. Aguasca, R. Villarino, C. Gabarró, L. Enrique, J. Miranda, **R. Sabia**, and M. Talone, Determination of the Sea Surface Emissivity at L-Band and Application to SMOS Salinity Retrieval Algorithms: Review of the Contributions of the UPC-ICM, *Radio Sci., 43, RS3008,* 2008.

National Journal Papers

1. Migliaccio, M., **R. Sabia** and M. Marrazzo, On the Electromagnetic Scattering of Sea Surfaces, *A.I.T Informa-Rivista Italiana di Telerilevamento, 26-28,* 17-22, 2003.

2. **Sabia**, **R.**, A. Camps, M. Vall-llossera, R. Villarino, J. Miranda, A. Monerris, and M. Zapata, Sea Surface Salinity Retrieval within the ESA Soil Moisture and Ocean Salinity (SMOS) Mission, *Atti della Fondazione Giorgio Ronchi, LX (4),* 597-604, 2005.

International Conference Proceedings

1. Marrazzo, M., **R. Sabia** and M. Migliaccio, IEM Sea Surface Scattering and the Generalized P-Power Spectrum, *Proceedings of the International Geoscience and Remote Sensing Symposium (IGARSS), Toulouse, France,* 2003.

2. **Sabia**, **R.**, M. Vall-llossera and M. Migliaccio, Sea Surface Emission at L-band Using the IEM Method, *Proceedings of the International Geoscience and Remote Sensing Symposium (IGARSS), Toulouse, France,* 2003.

3. Vall-llossera, M., A. Camps, E. López-Baeza, C. Antolín, D. Selva, A. Monerris, **R. Sabia**, F. Ferrer and K. Saleh, SMOS REFLEX 2003: Preliminary Results of Soil Moisture Dependence of the L-band Brightness Temperature of Vineyards Measured with the LAURA Radiometer, *Proceedings of NATO-CCMS and Science Committee Workshop "Desertification in the Mediterranean Region: A Security Issue", Valencia, Spain,* 2003.

4. Vall-llossera, M., A. Camps, I. Corbella, F. Torres, N. Duffo, D. Selva, S. Monerris, **R. Sabia**, C. Antolín, E. López-Baeza, F. Ferrer and K. Saleh, SMOS Reflex'03: L-Band Radiometric Characterization of Vineyards, *Proceedings of MicroRad '04, Rome, Italy,* 2004.

5. Camps, A., M. Vall-llossera, R. Villarino, I. Corbella, N. Duffo, F. Torres, R. Rodriguez, **R. Sabia** and A. Monerris, Foam-covered and Rain-roughened Sea Surface Emissivity at L-band: Results from the FROG 2003 Experiment, *Proceedings of MicroRad '04, Rome, Italy,* 2004.

6. Villarino, R., A. Camps, M. Vall-llossera, J. Miranda, **R. Sabia**, A. Monerris, R. Rodríguez, F. Campoy, J. Fernández, I. Corbella, N. Duffo, F. Torres and J. Arenas, Sea Surface Emission at L-band: Results from the WISE/FROG Field Experiments, *Proceedings of the International Geoscience and Remote Sensing Symposium (IGARSS),* Anchorage, Alaska, USA, 2004.

7. **Sabia**, **R.**, A. Camps, N. Reul, and M. Vall-llossera, Impact on Sea Surface Salinity Retrieval of Multi-source Auxiliary Data within the SMOS mission, *Proceedings of the International Geoscience and Remote Sensing Symposium (IGARSS),* Seoul, Korea, 2005.

8. Monerris, A., M. Cardona, M. Vall-llossera, A. Camps, **R. Sabia**, R. Villarino, E. Alvarez, and S. Sosa, Soil Moisture Retrieval Errors using L-band Radiometry Induced by the Soil Type Variability, *Proceedings of the International Geoscience and Remote Sensing Symposium (IGARSS),* Seoul, Korea, 2005.

9. **Sabia**, **R.,** A. Camps, M. Vall-llossera, and N. Reul, Retrieved Sea Surface Salinity Dependence on Multi-source Auxiliary Data within the SMOS Mission, *Proceedings of MicroRad '06, San Juan, Puerto Rico,* 2006.

10. Camps, A., M. Caparrini, **R. Sabia**, and G. Ruffini, Sea Surface Salinity Retrieval from Space: Potential Synergetic Use of GNSS-R Signals to Improve the Sea State Correction and Application to the SMOS Mission, *Proceedings of MicroRad '06, San Juan, Puerto Rico,* 2006.

11. Monerris, A., M. Vall-llossera, A. Camps, **R. Sabia**, R. Villarino, M. Cardona, E. Álvarez, and S. Sosa, Soil Moisture Retrieval Using L-band Radiometry: Dependence on Soil Type and Moisture Profiles. Results from the MOUSE 2004 Field Experiment, *Proceedings of MicroRad '06, San Juan, Puerto Rico,* 2006.

12. Camps, A., J. Font, M. Vall-llossera, R. Villarino, C. Gabarró, L. Enrique, J. Miranda, I. Corbella, N. Duffo, F. Torres, S. Blanch, A. Aguasca, **R. Sabia**, From the Determination of Sea Emissivity to the Retrieval of Salinity: Recent Contributions to the SMOS Mission from the UPC and ICM, *Proceedings of the International Geoscience and Remote Sensing Symposium (IGARSS),* Denver, Colorado, USA, 2006.

13. **Sabia, R.**, C. Gommenginger, A. Camps, M. Srokosz, Retrieved Sea Surface Salinity Spatial Variability using High Resolution Data within the Soil Moisture and Ocean Salinity (SMOS) Mission, *Proceedings of the International Geoscience and Remote Sensing Symposium (IGARSS), Barcelona, Spain,* 2007.

14. **Sabia, R.**, A. Camps, M. Vall-llossera, M. Talone, J. Font, Towards an Ocean Salinity Error Budget Estimation within the SMOS Mission, *Proceedings of the International Geoscience and Remote Sensing Symposium (IGARSS), Barcelona, Spain,* 2007.

15. Camps, A., M. Talone, J. Font, **R. Sabia**, Towards a Coherent Sea Surface Salinity Product from SMOS Radiometric Measurements and Argo Buoys, *Proceedings of the International Geoscience and Remote Sensing Symposium (IGARSS),* Barcelona, Spain, 2007.

16. Talone, M., A.Camps, B. Mourre, **R.Sabia**, M.Vall.llossera, C.Gabarró, and J.Font, The Impact of Combining SMOS and ARGO Data on the SMOS Level 3 Product: the Repercussions on the Coastal Vicinity Effect, *Proceedings of MicroRad '08, Florence, Italy,* 2008.

17. Talone, M., A.Camps, C.Gabarró, **R.Sabia**, M.Vall.llossera, B. Mourre, and J.Font, Contributions to the Improvement of the SMOS Level 2 Retrieval Algorithm: Optimization of the Cost Function, *Proceedings of the International Geoscience and Remote Sensing Symposium (IGARSS),* Boston, Massachusetts, USA, 2008.

18. **Sabia**, **R.,** A. Camps, M. Vall-llossera, Extended Ocean Salinity Error Budget Analysis within the SMOS Mission, *Proceedings of the International Geoscience and Remote Sensing Symposium (IGARSS),* Boston, Massachusetts, USA, 2008.

National Conference Proceedings

1. **Sabia**, **R.**, A. Camps and M. Vall-llossera, The ESA's SMOS Mission and Sea Surface Salinity Retrieval Issues, *Proceedings of the IEEE GRS South Italy Chapter GOLD Conference 2004, Naples, Italy,* 2004.

2. Camps, A., M. Vall-llossera, **R. Sabia**, J. Font, and N. Reul, La Medida de la Salinidad de los Océanos con la Misión SMOS de la ESA, *Proceedings of the XI Congreso Nacional de Teledetección, Tenerife, Spain,* 2005.

3. Monerris, A., M. Vall-llossera, A. Camps, **R. Sabia**, A. Martínez-Vázquez, I. Ledesma, and M. Piles, Field Experiments to Improve the Soil Emission Models at L-band: Contribution of the UPC to the ESA SMOS Mission, *Proceedings of Recent Advances in Quantitative Remote Sensing II, Valencia, Spain,* 2006.

4. **Sabia**, **R.,** C. Gommenginger, A. Camps, and M. Talone, Recent Insights in Sea Surface Salinity Estimation within the Soil Moisture and Ocean Salinity (SMOS) Mission, *Proceedings of the IEEE GRS South Italy Chapter GOLD Conference 2006, Bari, Italy,* 2006.

5. **Sabia**, **R.,** A. Camps, M. Talone, and M. Vall-llossera, The SMOS Mission Retrieval Scheme: the Ocean Salinity Error Budget, *Proceedings of the IEEE GOLD Remote Sensing Conference 2008, Roma, Italy,* 2008.

Acknowledgments-Agradecimientos-Ringraziamenti

I can't remember how many times I thought about this moment…the exact moment of writing the acknowledgements of my Ph.D. Thesis. It is probably not difficult to understand why. I always thought that by the time I would have written these acknowledgements, I would have managed to finish my work…and (eventually) here we are! It has been a long, challenging, difficult yet joyful and amazing time! An entire period of my life I spent in this wonderful city surrounded by nice people and good friends.
I hardly believe I will have the opportunity to communicate my gratitude in such an official document in the future, thus I will take advantage of this one. As I already did in my Laurea Thesis, instead of acknowledgements in the usual way I'd rather like to nominate and give credits to the people I felt close, for the valuable support and for having spent time and life together. I would like to do that in different languages, it is kind of weird, but it gives me the feeling of a more immediate communication.

En primer lugar, quiero agradecer mi director de tesis, Adriano Camps, por haberme dado la posibilidad, en el lejano 2003, de realizar mi doctorado aquí. He tenido la suerte que me llevara un director con capacidades y talante científico fuera del común, y profesionalmente he recibido grandes enseñanzas y he aprendido mucho de él. Sobre todo he recibido pasión por el trabajo, método, determinación, y lo más importante, estímulos a jugar limpio y con la correcta actitud científica. No obstante seamos diferentes, valoro muchísimo todo lo que me ha enseñado en estos años, su dedicación a la investigación y a las personas con quien trabaja.
Quiero también agradecer a mi otra directora de tesis, Mercè Vall-llossera, por el soporte técnico y moral, además de la amabilidad y la disponibilidad demostrada en estos 5 años.
En general, quiero agradecer el Departamento de Teoría de la Señal y Comunicaciones de la UPC por darme la posibilidad de cursar mis estudios aquí, poniendo a disposición recursos y estructuras.
Quisiera agradecer también el SMOS BEC del Instituto de Ciencias del Mar, donde he estado trabajando part-time este año, especialmente los directores Jordi Font y Xicu Torres, y mis nuevos colegas de allí Baptiste, Jeróme, Alfredo, Caro, Maria, Mariona, Miguel y Sofia.
En las reuniones del martes se ha ido alternando mucha gente, y entre todos quiero agradecer espacialmente los chicos y chicas radiometricos con quien he estado trabajando codo a codo en estos años. En primer lugar Sandra, mi amiga y compañera de mesa en esta larga aventura que hemos empezado y acabado juntos; Marco, compañero de salinidad y sobre todo persona extremamente disponible y de buen rollo y con quien es un placer trabajar, y sin dejar a lado Maria y José Miguel.
Y ahora una larga lista de agradecimientos a las personas que he encontrado en estos largos y maravillosos años aquí en Barcelona.
Cronológicamente es justo empezar con las primeras personas que han cuidado de mí en los primeros meses en esta ciudad, cuando todavía hablaba ingles y solo chapurreaba algo de Castellano. Estas personas, Jorge, Ramón y Miguel, han sido muy importantes para mi en un periodo intenso cual es irse a vivir solo al extranjero. Por la misma razón estoy muy agradecido a Eduard, Stan y Alex, por mucho tiempo hemos sido un cuarteto de comidas y hemos pasado momentos muy agradables.
El despacho D3-114 quedará para siempre como parte importante de mi vida. En ello he vivido casi todo el tiempo de mi doctorado y he compartido miles de momentos de los más variados. Tengo gran admiración de las personas que he conocido allí: listas, preparadas, determinadas, en definitiva con la relación calidad-sueldo más alta que haya visto. En este despacho del Gran Hermano, hemos trabajado mucho a la vez que disfrutado un montón. Ha habido risas, cariño, tensiones, amistad, carreras de sillas, amigos invisibles, cafés, soporte mutuo, en una palabra todas las cosas de la vida, y quizás sea por esto que este sitio queda tan radicado en mis recuerdos y pensamientos.
Además de Sandra, concretamente quiero dar las gracias a Luca, mi buen amigo Italiano con quien he compartido muchas cosas y siempre con el placer (y la solidariedad) de verse en el mismo barco de extranjeros; Mariví, una chica muy dulce y con quien en los años he desarrollado amistad y confianza, y Txema, compañero de equipo, del Barça y de viajes low-cost. También quiero agradecer Gerard, Juanfer, y Omar por las muchas risas y anécdotas.
Pablo y Hugo no han sido solamente compañeros y amigos de despacho. Al venir aquí no esperaba encontrar personas de otro país con las cuales llegar a conectar tanto, por tanto tiempo, y tan bien. Con Pablo he dividido la pasión por la música, el fútbol, el Napoli, conciertos, hemos vivido juntos, hablado de todo, y compartido muchísimos momentos. Con Hugo hemos llegado a vivir todo el día junto, entre despacho y piso, y hemos salido, montado fiestas, visto muchas pelis, y charlado siglos. Ambos son de estos amigos que espero no perder nunca.

Hay muchas otras personas de la UPC que quiero mencionar. Ante todo, Raquel y Bea, mis dos amiguitas guays, dos chicas majas, amables y de enorme compañía que he descubiertos en los últimos dos años, y luego Mica, Sergi, WikiPere, Gemma, Oscar, Vero, Benji, Chordi y el PauTeam.
Entre los compis de piso, el mítico comité "Bruc 68", especialmente Victor Papá, gran compañero de piso y amigo, cuyas aforismas siempre marcarán la pauta, y Leila y Flora, a pesar de no vernos mucho.
Y luego las muchas otras personas que he conocido o con quien he vivido aquí en Barna dividiendo tantos buenos momentos. Mi amiga Bianca ante todos, por ser tan simpática y solar, y luego Kike, Sugey, Orit, Melina, Annabarbara, Pilar, Juan, Giacomo, Cesar.
También quiero agradecer los *Cabin Crew Prepare for Landing*; quizás el éxito nos quede muy lejos, pero el buen rollo y los momentos agradables pasados tocando la música que nos gusta no tienen precio.
Y por acabar, un gracias a los jugadores del equipo *D4*, de parte de su humilde portero. De no ser por el cada vez más acuciante problema del fondo físico, no tendríamos que habernos conformado solo con la Copa del 2007.

Furthermore, I would like to thank the National Oceanography Centre of Southampton, UK, Ocean Observing and Climate Department, where I spent 4 months in 2006 in my European Ph.D. stage. I would like to thank especially Christine Gommenginger, my tutor there, for hosting me, and supporting my work in a friendly and cheerful environment. I would like to remember as well my English flatmates Emma, Doug, Phil and my Greek friends Thanos, Aggie and Haris.

Ed é giunto il momento dei ringraziamenti in Italiano.
Dal punto di vista accademico é giusto cominciare con la persona che mi ha iniziato al Telerilevamento, fin da quel folle piano di studi del 1999, ovvero Maurizio Migliaccio. A lui devo i primi insegnamenti, gli sproni, e la possibilitá di essere venuto qui a Barcelona, cosa per la quale gli sono e gli saró eternamente grato.
Voglio poi ricordarmi dei miei amici italiani, e devo iniziare dicendo che sono orgoglioso, davvero, del fatto che pur vivendo all'estero ed essendo dispersi in varie cittá e ciascuno con i propri impegni, quando non con famiglie a carico, tra visite, vacanze e weekend siamo sempre riusciti a stare in contatto. Per me questo é un motivo di vanto, segno che quando i rapporti sono forti e intensi non ci sono distanze e tempi che tengano.
Voglio iniziare dagli AMICI, e quindi Ciro, Sergio, Roberto, Valerio, Simone, Alberto e Clara, in ordine sparso cosí non litigano, tanto loro lo sanno che sono tutti primi, e poi anche i carissimi Andrea, Paola, Gianluca, Angelina, Tatore, Giovanna e Luca.
Le parole piú belle, stavolta si, sono per la mia fidanzata/compagna/amica/confidente Novella. Nonostante le distanze, il nostro rapporto di intesa, sintonia, divertimento, complicitá e benessere é tale che il termine di sola coppia sta financo stretto. Lei é la persona che vorrei accanto nella mia vita.
E per finire la mia famiglia. Mia madre é ancora una volta sul gradino piú alto per l'amore, la dedizione, la cura, e l'appoggio che mi ha sempre dato, da vicino prima come da lontano adesso, forse la cosa piú bella che posso dirle é che sogno un giorno di poter essere un genitore come é stato lei per me. Umberto, degno compagno di mia madre, per l'affetto, l'equilibrio e la partecipazione che sento nella mia vita. Di Fausto mi sono perso parte della sua crescita, ma mi sento ricompensato nel vederlo con orgoglio crescere sempre meglio e sentire ogni volta che siamo e resteremo sempre un duo.
Voglio ringraziare anche mio padre, per i suoi consigli, l'interesse e la determinazione che mi ha inculcato e trasmesso. Fabio, Stefano e Cristina, con il solo rammarico di non passare piú tempo insieme. E poi Emma e Claudia, i miei zii, cuginetti e la mia cara nonna Isabella.

Sin todos ellos no lo habría conseguido.
Senza tutti loro non ci sarei riuscito.

Grazie di cuore